A Pre-Tensioned Bent System for Accelerated Bridge Construction in Seismic Regions

Ólafur Sveinn Haraldsson

A dissertation
submitted in partial fulfillment of the
requirements for the degree of

Doctor of Philosophy

University of Washington

2015

Reading Committee:

Marc O. Eberhard, Co-Chair
John F. Stanton, Co-Chair
Laura N. Lowes
Neil M. Hawkins

Program Authorized to Offer Degree:

Civil & Environmental Engineering

University of Washington

Abstract

Ólafur Sveinn Haraldsson

Supervisory Committee Co-Chairs:
Professors Marc O. Eberhard and John F. Stanton

Nearly all bridge bents (intermediate supports) are constructed of cast-in-place reinforced concrete. Such bridges have served the nation well in the past, but to meet current design expectations, they need to be improved in three areas: 1) speed of construction, 2) seismic resiliency, and 3) durability.

Building on previous research at the University of Washington (Hieber et al. 2005, Wacker et al. 2005, Pang et al. 2010, and Haraldsson et al. 2013), a new pre-tensioned bent system has been developed to address these needs. The system consists of 1) precast technology that reduces construction time, 2) unbonded pre-tensioning that minimizes post-earthquake displacements, and 3) high-performance materials that extend the bridge's life-span.

Davis et al. (2012) tested a version of the system using conventional concrete in the plastic hinge regions. They found that pre-tensioning improved the system's re-centering capabilities but led to earlier bar buckling and bar fracture than in previously tested RC columns. In order to delay bar buckling and bar fracture, the system was modified to include Hybrid Fiber Reinforced Concrete (HyFRC) in the plastic hinge regions. This composite concrete has been shown to exhibit superior durability and cracking resistance (Ostertag et al. 2007).

The effect of the HyFRC on the pre-tensioned bent system was investigated both with quasi-static and dynamic tests. The quasi-static tests showed that using HyFRC in the plastic hinge region increased column ductility; in all cases the column maintained more than 80% of its strength up to a drift ratio of 10%. The HyFRC also delayed spalling of the concrete, but it did not significantly increase the drift ratios at the onset of bar buckling and bar fracture. The shake-table tests of a cantilever column, which was designed to re-center up to a drift ratio of 3.0%, showed that the new system had lower expected residual drifts than columns constructed with

conventional cast-in place methods. The pre-tensioned column had a residual drift of 0.23% after experiencing a peak drift ratio of 5.5%. In contrast, the companion reference column, constructed using cast-in-place technology, had a residual drift ratio of 0.83% after experiencing a peak drift ratio of 5.7%.

A numerical model in OpenSees was developed and calibrated with a set of 34 RC quasi-static, cyclic tests. This model was calibrated using a concrete constitutive model that takes into account concrete early reloading, developed as part of this research, and used commonly used steel constitutive models; Giuffre-Menegotto-Pinto's (Steel02) model, and Moehle and Kunnath's (ReinforcingSteel) model. The simulations showed improved accuracy in comparison to previous research (e.g., Berry and Eberhard 2007), and showed that the response of the system was affected more by the chosen steel model than by the concrete model. The results of these simulations were used to make predictions of the response of five columns tested on the UC Berkeley shake table. These simulations showed that models built using the proposed strategy predict peak displacements quite accurately, especially at the yield and design level, but do not accurately capture residual displacements.

TABLE OF CONTENTS

LIST OF FIGURES

Figure Number **Page**

LIST OF TABLES

Table Number **Page**

Acknowledgements

My dissertation work would not have been possible without the help and guidance from many individuals. Over the past 7 years, I have grown in many ways through working on various projects at the University of Washington as well as opportunities to collaborate with other institutions: to work with people from different background and to learn from each and every one of them in different ways.

I am grateful to have had the opportunity to work with both Dr. John F. Stanton and Dr. Marc Eberhard. They have guided me in fundamental ways that I am extremely grateful for, especially by their extremely detail-oriented approach in science and engineering. They have also on the other hand, showed me the importance of collaborative works and provided me precious opportunities to work with leading groups in earthquake engineering. I want to acknowledge both Dr. Laura Lowes and Dr. Neil Hawkins for serving on my committee. Their insights and suggestions were extremely helpful to me. In terms of modeling, Dr. Michael Berry at Montana State University was extremely helpful to me when I was starting doing numerical modeling.

The support from my family and my colleagues in the department has been extremely meaningful for me to be where I am today. Dr. Bjarni Bessason at the University of Iceland has always been there to provide encouragement to pursue my dreams in academia. My grandparents, Ólafur Kristinn Hermannsson and Ragnheiður Brynjólfsdóttir, and my parents, who have always supported me in pursuing my own passion in knowledge and science, make me feel safe in this long journey of exploration.

Last but not least, this work was not possible with generous funding. I have been fortunate of having been funded by the Valle Scholarship of the University of Washington, Federal Highway Administration through the Highways for Life Program, and Pacific Earthquake Engineering Center, and Landsvirkjun Power. The support of all agencies is gratefully acknowledged.

1 INTRODUCTION

1.1 Need for New Bridge Technologies

Reinforced concrete bridge construction technologies in seismic regions have changed little since the mid-1970s, when ductile details were introduced after the San Fernando earthquake. Nearly all bridge bents (intermediate supports) in seismic regions are now constructed of cast-in-place reinforced concrete. Such bridges have served the nation well in the past, but to meet current design expectations, they need to be improved in three main areas:

- speed of construction
- seismic resilience
- durability

Speed of construction is becoming increasingly important in urban areas, because bridge construction causes traffic delays that are costly for society and increase greenhouse gas emissions, in particular CO_2. Columns and cap-beams that are cast-in-place require time-consuming shoring, form construction, reinforcement placement, concrete casting and curing. To perform these tasks, it is often necessary to close lanes, and in some cases, reroute traffic.

Cast-in-place bridge bents are also susceptible to earthquake-induced structural damage, such as column reinforcing bar buckling, bar fracture and residual displacements. These types of damage can lead to bridge closure for inspection or repair, and occasionally to bridge replacement. The possibility of closing important transportation lifelines after an extreme event is not acceptable, because the functioning of these lifelines is essential to the resilience of urban communities.

Current construction technologies are also insufficiently durable. The long-term durability of cast-in-place systems is reduced by cracking due to both restraint of drying shrinkage and alkali-silica reaction. Cracking allows the ingress of moisture and de-icing salts, which can lead to corrosion of the reinforcement. New structural systems and construction methods are needed to improve the performance of bridges in these three areas.

One solution for reducing construction-related delays is to precast structural elements off site and then assemble them rapidly once they arrive on site. Seismic performance can be improved by reducing post-earthquake residual displacements through the use of prestressing in the precast bridge columns. The prestressing is designed to bring the system to its original plumb position when the lateral load is removed. Durability of the system can by enhanced by the selection of high-performance materials to improve the system structural performance and minimize corrosion. Precasting also has other benefits, such as improved construction quality due to in-plant QC, and better worker safety due to the shorter time spent on site.

1.2 Non-Prestressed Precast Bent System

The pre-tensioned bent system builds on previous research at the University of Washington (Hieber et al. 2005a, 2005b, Wacker et al. 2005, Stueck et al. 2007, Stueck et al. 2009, Pang et al. 2008, Pang et al. 2010, Haraldsson et al. 2013a, 2013b, and Tran et al. 2013). This research focused on developing a new bridge bent system that reduced on-site construction time. The chosen approach was to precast structural elements off site and then assemble them rapidly on site. Connections were developed for the foundation-to-column and column-to-cap beam interfaces, since these are the most convenient places to join precast members together. Unfortunately, these same locations experience the largest moments and inelastic deformations during a seismic event. The focus of this research endeavor was to design connections that facilitated ease of construction while maintaining seismic resistance equal to, or better than, cast-in-place construction.

Figure 1-1 shows a "Large-Bar" connection between a precast column and a precast cap-beam (Pang et al. 2008, 2010). In this connection, longitudinal bars project from the top of the column and are grouted into ducts in the precast cap-beam. This concept had been tested previously by others (e.g., Matsumoto et al. 2008), however these designs tended to require a large number of fit-ups on site and correspondingly small construction tolerances. For example, a 5-ft diameter column is reinforced with 18-No. 11 bars would require ducts to be small to accommodate the horizontal beam reinforcement and thus small tolerances. The Large-Bar connection uses fewer but larger bars. The same 5-ft diameter column could be reinforced with 6-No. 18 bars grouted into 8.5-in. diameter ducts in the cap-beam. This configuration simplifies

fit-up on site. Stueck et al. (2007, 2010) showed that bars of this diameter could be developed in grouted ducts entirely within the depth of the precast cap-beam

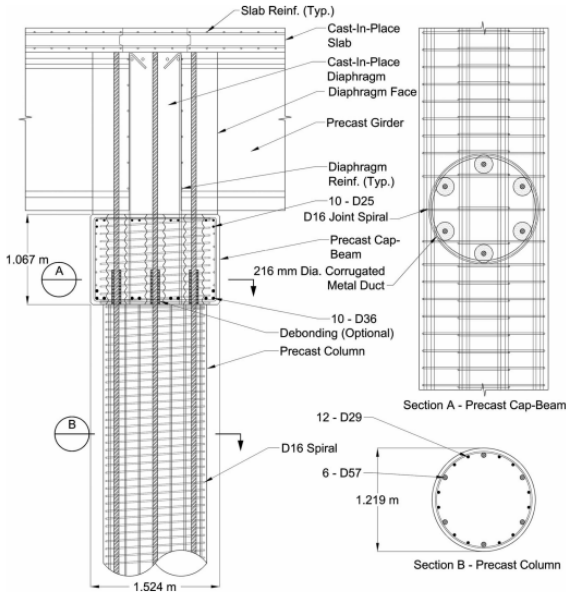

Figure 1-1. Large-Bar connection (Pang et al. 2008, 2010)

Haraldsson et al. (2013a, 2013b) developed a "Wet Socket" connection to connect a precast column to a cast-in-place spread footing. The concept is shown in Figure 1-2. The details of this connection differ from those of conventional, cast-in-place system in several ways.

- First, no reinforcement crosses the interface between the footing and the column, so the only resistance to vertical load (gravity and vertical component of an earthquake load) comes from shear friction across the precast to cast-in-place interface. That interface is intentionally roughened to facilitate this load transfer.
- Second, the longitudinal column bars are not bent out at the bottom, as seen typical cast-in-place construction, but achieve their anchorage by headed anchors. This choice simplifies transportation and handling, and reduces hazard posed by protruding bars.

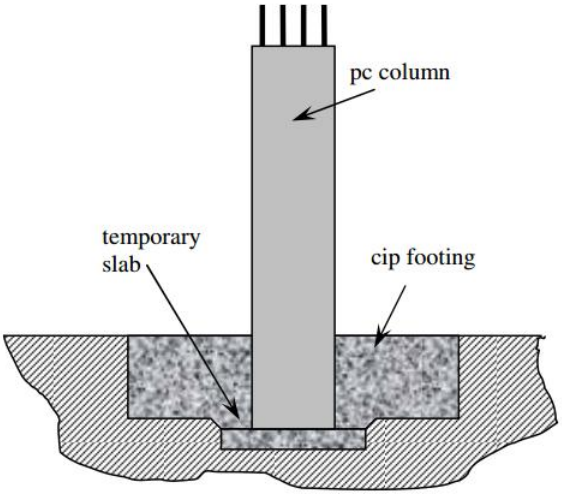

Figure 1-2. Socket connection concept

The pre-tensioned bent system builds on the successes of these connections to achieve accelerated construction over cast-in-place systems. The top of the pre-tensioned, precast column is cast with protruding mild reinforcement and a reduced diameter section of the column, which is used to bond the strands. The reduced diameter section of the column and the reinforcing bars are grouted into individual ducts in the cap-beam. The bottom connection, identical to that used in the non prestressed system, consists of embedding a roughened segment of the precast column into the cast-in-place spread footing.

1.3 Research Objectives

The primary goals of this research were to:

- Develop a new resilient precast bridge bent system that is suitable for Accelerated Bridge Construction in seismic regions,
- Evaluate the performance of that new system, and
- Calibrate a column model to a set of reinforced concrete columns tests to more accurately capture column behavior under seismic loading. Furthermore, develop modeling recommendations for estimating peak and residual displacements for reinforcing columns under dynamic loading.

1.3.1 Development of Pre-tensioned Bent System

Pre-tensioning offers the possibility of improving the resilience of the system by reducing its residual, post-earthquake displacements. In the pre-tensioned version of the system, the precast column contains pre-tensioned strands that are unbonded within the clear height of the column and bonded within the top and bottom connections. The prestressing strands are designed to remain elastic, and thus to bring the bent system back to its original plumb position following an earthquake. To remain elastic, the additional strains due to the earthquake loading must be small, and debonding achieves this by distributing the elongation over a long length of strand. To dissipate energy, bonded mild reinforcement crosses the crack planes located at the beam-to-column and column-to-footing interfaces.

Prior to the research described in this dissertation, Davis et al. (2012a, 2013b) tested two 42% scaled unbonded pre-tensioned subassemblies that represented a column-to-footing and a beam-to-column connection, respectively. They showed that the columns hinged and no damage occurred in the connection regions, as is required by current standards (e.g., AASHTO LRFD 2011, AASHTO GS 2011, and Caltrans SDC v1.6). The two specimens' cyclic responses were identical, and both columns re-centered to less than 1% residual drift following a peak drift of 10%. However, the columns suffered spalling and bar buckling at lower drift ratios than did previously tested RC specimens in earlier test programs (Pang et al. 2008, Pang et al. 2010, Haraldsson et al. 2013a, and Haraldsson et al. 2013b). This early buckling and spalling was attributed to the additional compressive stress on the concrete introduced by the prestressing.

The new pre-tensioned bent system is shown in Figure 1-3. This new version is intended to increase the resilience of the system by using Hybrid Fiber Reinforced Concrete (HyFRC) shells located in the plastic-hinge regions. Plastic-hinge regions are the locations where the rotations are concentrated, and at which high strains are induced in the concrete and steel. HyFRC is a special concrete mixture that contains high dosages of two different types of fiber, and has also been shown to exhibit superior durability and cracking resistance compared to conventional concrete (Yi and Ostertag 2004, Grupp et al. 2007, Ostertag et al. 2007, and Jen et al. 2011). Placement of the HYFRC in the plastic hinge regions was expected to delay spalling of the concrete and buckling of longitudinal bars, which are the two most significant forms of damage

(Kumar et al. 2011). Various schemes were considered for incorporating the HyFRC into the pre-tensioned bent system. The main reasons for choosing a shell configuration was because HyFRC is an expensive material, so they were placed were they are needed, and the shell configuration facilitates passing the strands down in the middle of the column. section.

The day-to-day durability of the system is enhanced by the fact the column is under constant compression from the pre-tensioning, which inhibits ingress of moisture, by the use of epoxy-coated coated strands, and by the ability of the HyFRC to inhibit shrinkage cracking.

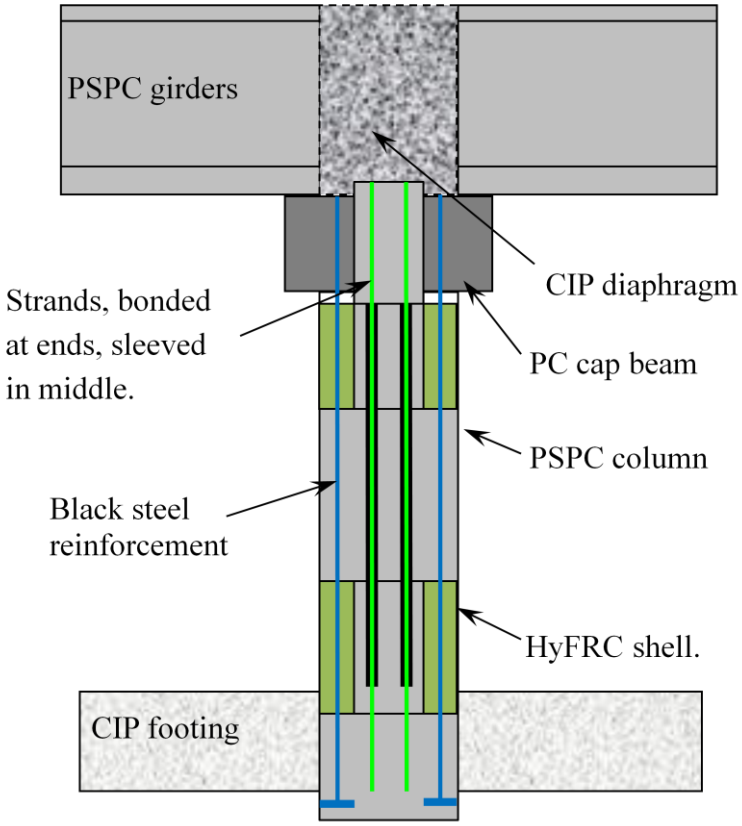

Figure 1-3. Pre-tensioned bridge bent system

1.3.2 Performance Evaluation

As part of the evaluation of the system's seismic performance, it was necessary to determine whether the pre-tensioned system is more resilient than a conventional bent system, and in particular, to know whether the introduction of HyFRC reduces residual displacements and damage such as spalling, bar buckling, bar fracture). Therefore, quasi-static tests, shake-table

tests and analyses were evaluated. Some of the tests had been conducted previously by others, some new quasi-static tests were conducted, and two new shaking table tests were conducted.

The quasi-static tests considered included previous tests of conventional reinforced concrete columns (Pang et al. 2008, Pang et al. 2012, Haraldsson et al. 2013a, and Haraldsson et al. 2013b), and new tests of pre-tensioned columns with and without HyFRC (Davis et al. 2012a, 2013b and Finnsson et al. 2013, respectively).

In 2012, two shake-table tests were conducted at UC Berkeley as part of a larger research initiative on resilient bridge columns. The program consisted of four test specimens. One of them was a conventional, cast-in-place column detailed according to current standards and practice (Caltrans SDC v1.6) and served as a reference. The second column in that series relevant to the present work was a precast, pre-tensioned column with a HyFRC shell in the plastic hinge region.

1.3.3 Modeling Recommendations

Prior to the advent of unbonded prestressing in structural systems (Stone at al. 1993) residual displacements after an earthquake were unavoidable and their magnitude depended largely on the details of the ground motion. The unbonded prestressing technology provided a physical means for reducing residual displacements, but they have proved to more difficult to predict than peak displacements. The reason is that peak displacements are relatively insensitive to the model used (recall the "equal displacements rule" that states that an elastic and an inelastic system will undergo the same peak displacement), but the residual displacement calculation depends on the ability to reproduce correctly both the loading and unloading behavior paths. That is a significantly greater challenge.

Not surprisingly, current numerical models predict residual displacements poorly. To improve their prediction, a new concrete constitutive model was developed as part of this research for the OpenSees analysis platform. The constants within it were chosen to optimize the fit with measured residual displacements of the quasi-static of the bridge columns. The model was then used to predict the responses, including residual displacements, of the five reinforced concrete columns that had been tested dynamically on the shaking table. The findings, and

recommendations for how best to use the model, are presented in this thesis for the guidance of designers.

1.4 Scope

This document consists of ten chapters. This chapter describes the motivation for the research, the background for the development of the pre-tensioned bent system, and the research objectives. Chapter 2 summarizes previous research, conducted at the University of Washington and elsewhere, that is relevant to the development of the precast pre-tensioned bent system. Chapter 3 describes the development of the pre-tensioned bent system. In Chapter 4, the quasi-static experiments on subassemblies relevant to this research are described and evaluated. Chapter 5 presents the new concrete constitutive model and addresses numerical strategies to predict accurately quasi-static responses of experimental tests. Design of the shake table test specimens, shake-table test setup, instrumentation, test program, experimental results and evaluation of test results are discussed in chapter 6 through 8. Chapter 9 evaluates the results of Chapter 5 by predicting peak and residual displacements of shake-table tests performed by researchers at the University of California-Berkeley (Hachem et al. 2003, and Schoettler et al. 2013), and Chapter 10 provides a summary of this research and conclusions.

2 OVERVIEW OF PREVIOUS RESEARCH

This chapter summarizes some of the previous research that is relevant to the development of the precast, pre-tensioned bridge bent system. The review is organized into three sections that address key features of the developed system: (1) accelerated bridge construction, (2) self-centering bridge systems, and (3) high-performance materials.

2.1 Accelerated Bridge Construction (ABC)

Many bridges in the United States have been identified as being either functionally or structurally deficient (FHWA 2008). To remedy these deficiencies, extensive bridge construction will be needed in the near future. Current methods of construction using cast-in-place concrete will exacerbate traffic congestion, which is already a costly problem, especially in urban areas.

New bridge systems and construction methods are needed to address these challenges. One means of accelerating bridge construction is to precast bridge elements off site and then assemble them rapidly once they arrive on site. This technology can minimize traffic disruptions and environmental impacts, improve constructability and worker safety, increase quality and durability, and lower life-cycle costs (Wacker et al. 2005, Pang et al. 2008). Precast, prestressed concrete girders have been used for over 60 years and now constitute the most common bridge superstructure type throughout the country. In contrast, precast concrete technology has seldom been used in bridge substructures, especially in seismic regions.

According to modern U.S. bridge design philosophy in seismic regions, the superstructures and foundations are to remain elastic through a seismic event, and therefore the inelastic deformations are to occur in the bridge columns (AASHTO Guide Specifications 2011). The rationale underlying this philosophy is that yielding in the cap-beams increases the risk of bridge collapse, and that foundation inspection and repair are difficult and costly. The substructure is therefore the only remaining location in which inelastic behavior can be accepted. Furthermore, confined bridge columns typically have a large reserve axial strength capacity, so even if a column that suffered plastic hinging during an earthquake, it would still have a large enough axial capacity to support the superstructure (Pang et al. 2008).

The seismic performance of a bridge bent is controlled largely by the column connections to the foundation and to the cap-beam. During an earthquake, these interfaces experience the largest moments and thus the inelastic deformation reversals occur there. The interfaces need to accommodate them without significant loss of strength and, in a cast-in-place system, this can be achieved by making the reinforcement continuous from the column to the cap beam or footing, and by supplying sufficient confinement. However, in a precast substructure the site connections are typically made at these interfaces in order to facilitate fabrication and transportation. Thus those connections must be designed for two criteria: ease and speed of assembly on site, and seismic robustness. In the past, connections that have proved advantageous in one aspect have performed poorly in the other, so history has shown that designing to satisfy both criteria at once is challenging. Research has therefore been focused on developing seismically resistant connections that are also easy to assemble.

The following two subsections discuss research that has been performed for bridge substructures both in non-seismic (Section 2.1.1) and seismic areas (Section 2.1.2). Greater emphasis is placed on bridges in seismic areas, since they are more relevant to the research of the precast, pre-tensioned bent system. An extensive literature review and evaluation of existing precast concrete substructure technologies in seismic regions can be found in reports by Weinert (2011) and Marsh et al. (2011).

2.1.1 Precast Bents for Rapid Construction in Non-seismic Regions

Most research in precast ABC for non-seismic regions in the United States has focused on connecting beams and columns at their interfaces, a strategy that facilitates fabrication and transportation of precast pieces. One of the first research efforts in the US was in Florida State in the early 1990s. LuBuono, Armstrong and Associates (1996) on behalf of the Florida State Department of Transportation conducted a survey to investigate the feasibility of using precast elements for bridge substructures. Most state departments reported back concern about the connection between precast components. The report also gives a summery on the responses from the survey related to the advantages and disadvantages of various precast concrete components.

Billington et al. (1999, 2001) proposed a precast segmental substructure system suitable for short- and moderate-span bridges that have columns up to 60-ft tall. The intent was to provide an

alternative to a cast-in-place substructure system. The system concept is that the column is segmental with segments that are match cast for a better fit. Figure 2-1 shows the system concept for a single column pier. Before a new segment is lowered down on an existing segment and post-tensioned together, post-tensioning bars are coupled and epoxy placed on the faces of the adjoining segments. Once the "precast template" is secured in the right height, the precast cap-beam is lowered down and post-tensioned vertically to the pier.

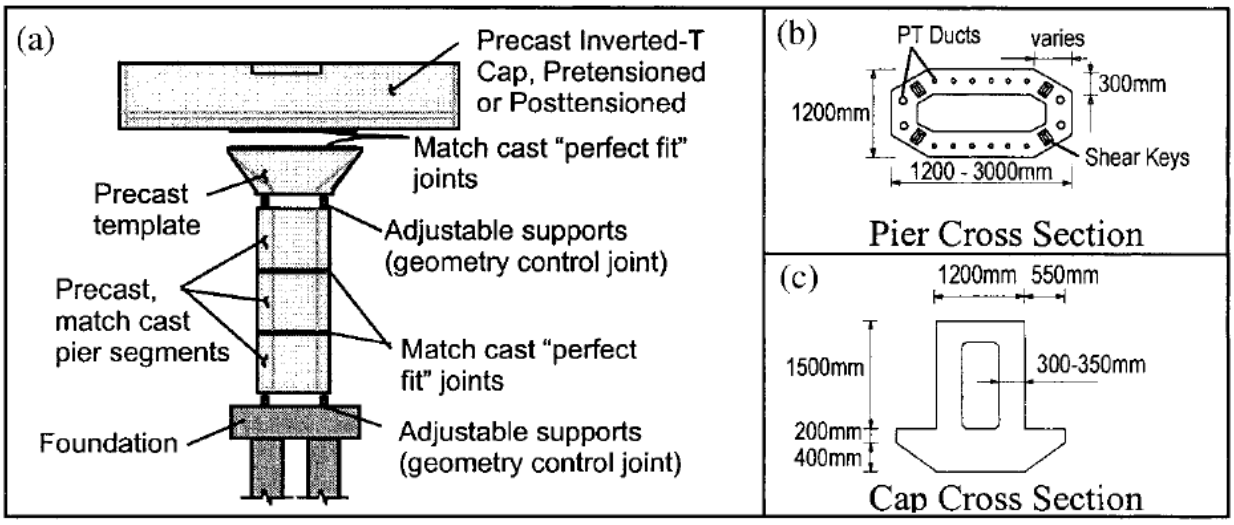

Figure 2-1. Single-column pier composed of precast components (Billington et al. 2001)

Matsumoto et al. (2001, 2008) developed a bent-cap system to connect a precast cap-beam to a cast-in-place column. This test program explored four kinds of connections at full scale, which included grout pockets, grouted ducts, grouted sleeve couplers, and bolted connections. Figure 2-2 shows the connection details explored. The tests showed that all four connections would perform sufficiently well for non-seismic regions. The Texas Department of Transportation (TxDOT) has up to this day built several bridges by precasting the cap-beams and connecting them to columns using the grouted ducts option, and therefore was able to reduce construction time. An example of a successful project is the PCI-award-winning State Highway 66 crossing over Lake Ray Hubbard near Dallas, Texas (Matsumoto et al. 2008).

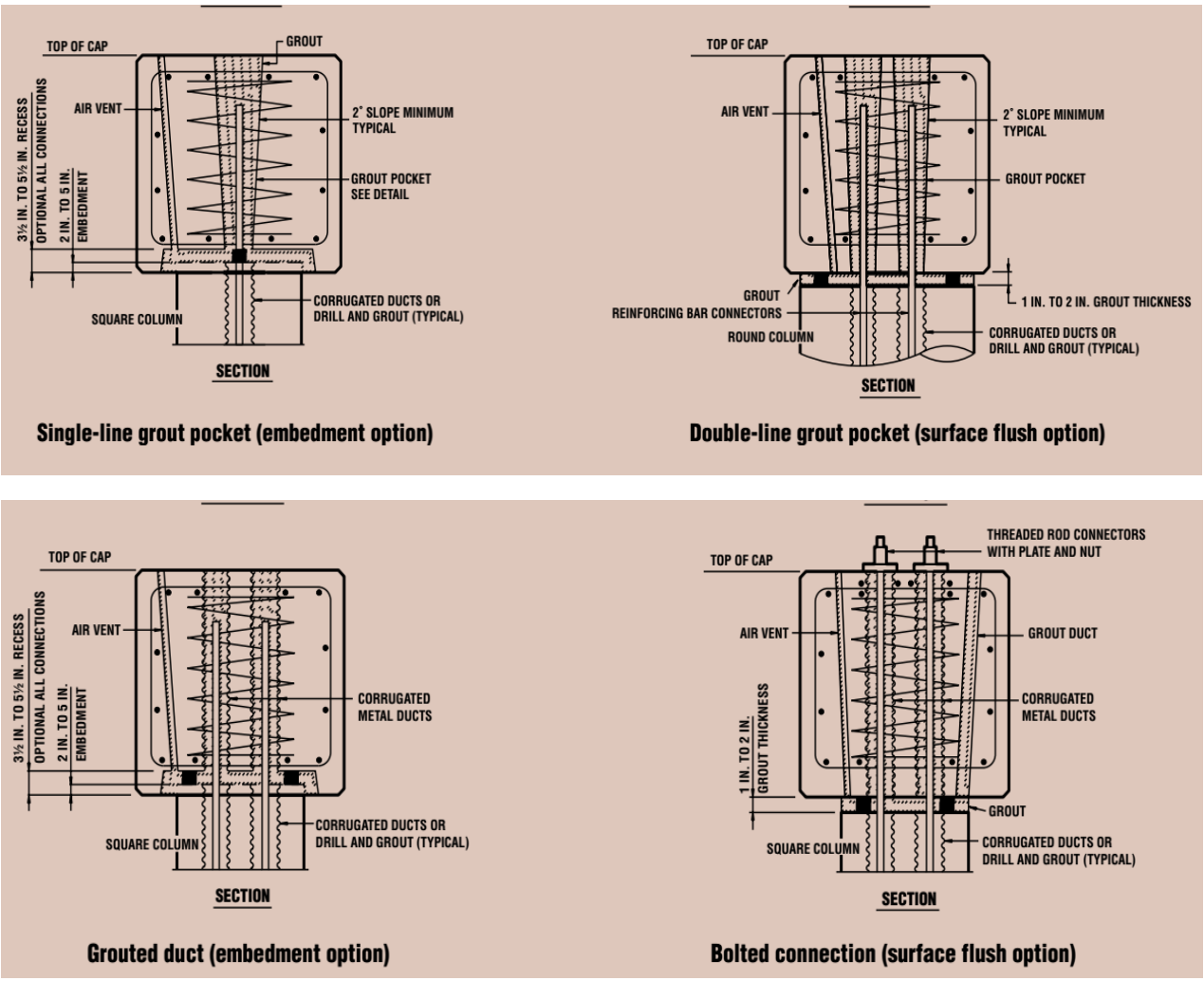

Figure 2-2. Beam-to-column connection details explored by Matsumoto et al. (2008)

2.1.2 Precast Bents for Rapid Construction in Seismic Regions

2.1.2.1 Concept Development of Precast Substructure System

Hieber et al. (2005a) wrote an extensive review of the use of precast technologies. The report also includes considerations and recommendations that are important for seismic regions, such as western Washington State. The same researchers proposed a precast emulative cast-in-place system to investigate further. Figure 2-3 shows the proposed system.

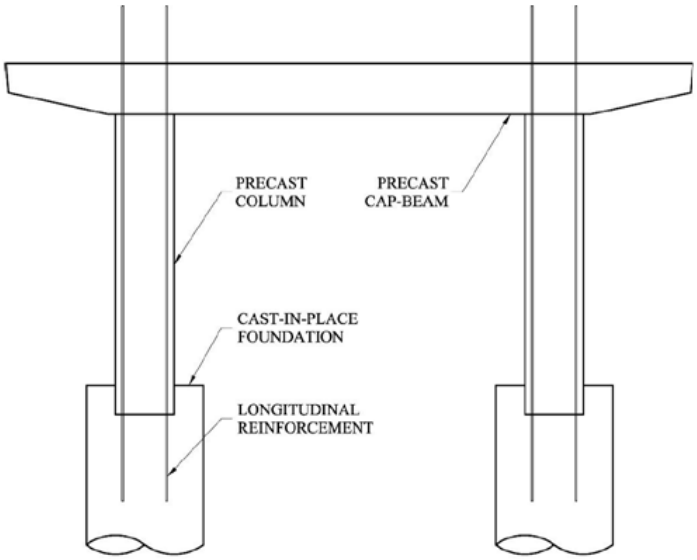

Figure 2-3. Proposed precast bridge bent system (Hieber et al. 2005b)

The system assumed drilled shaft foundations since they are more common in Washington State. The base of the precast column has protruding longitudinal bars and the column is plumbed into the foundation. The column then sits on a temporary support leg until the transition zone is cast. Two potential column-to-cap beam connections were proposed: a "complete opening connection and a "slotted opening. Figure 2-4 shows plan views of these connections. These researchers also developed methodologies to design bridges using the precast construction concept, which included both displacement-based and forced based design procedures (Wacker et al. 2005).

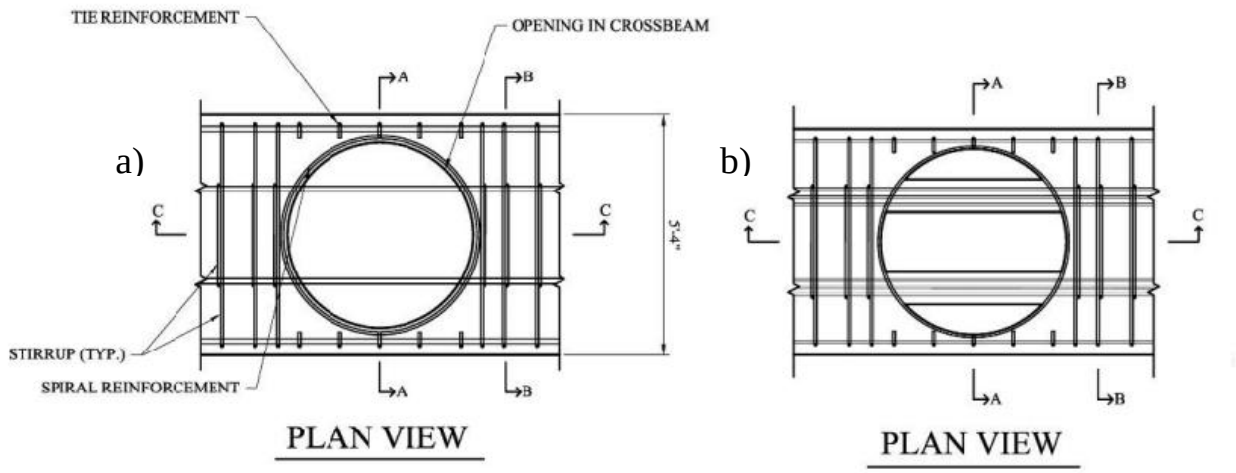

Figure 2-4. Proposed column-to-cap beam connections: a) "complete opening", and b) "slotted connection (Hiebert et al. 2005b)

2.1.2.2 Column-to-Cap Beam Connection

University of Washington ABC research on developing a complete precast concrete bent system started with a state-of-the art report by Hieber et al. (2005a) and was followed by two reports that focused on the development and design of precast substructures for seismic regions (Hieber et al. 2005b, Wacker et al. 2005). In 2006, a suite of candidate beam-to-column connections were developed, evaluated, and rated by considering fabrication difficulties, construction, and structural behavior. The seven connection types reviewed were 1) Ducts, 2) Large-bars, 3) Large opening, 4) Solid column (RC), 5) Solid column (PSC), 6) Concrete-filled tube, and 7) Slotted Column. Information about this work can be found in Pang et al. 2008.

The Large-Bar Connection, shown in Figure 2-5, was selected to be investigated further (Pang et al. 2008, 2010). The connection concept is to use larger column bars instead of many smaller ones. Larger but fewer bars allow the use of larger ducts in the cap-beam, which provide greater construction tolerances and consequently make on-site construction easier. In this design, six No.18 column bars protrude from the top of the column and are grouted into 8.5-in. diameter metal ducts in the cap-beam.

Steuck et al. (2007, 2009) conducted full-scale pullout tests on No. 18 bars grouted into ducts and showed that the extra length available in bent's diaphragm only increases the

robustness of the connection. The tests showed that No. 18 bars yielded and fractured at the embedment lengths of a $6d_b$ (6 times bar diameter) and $14d_b$, respectively. This meant that No. 18 can be fully developed in a duct in a height that is available in a typical bridge cap-beam. Steuck's findings were consistent with those of Raynor et al. (2002), who found that high bond stresses were achieved by No. 8 and No. 10 bars grouted into metal ducts.

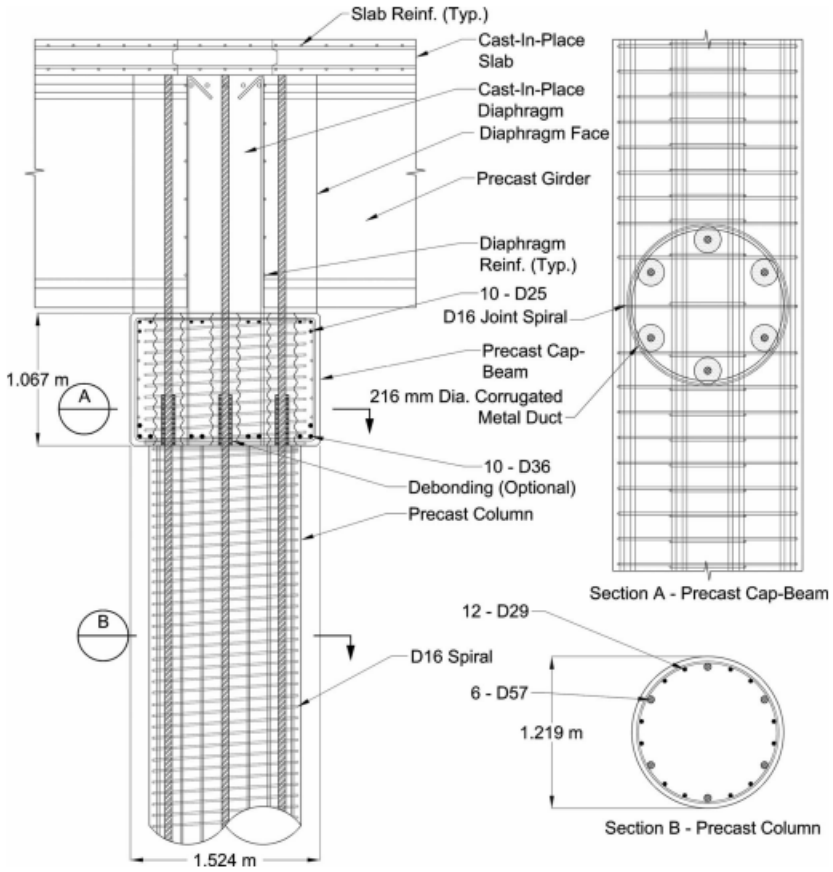

Figure 2-5. Full-Scale Large-Bar Connection (Pang et al. 2008, 2010)

Pang et al. (2008, 2010) conducted cyclic tests on four, at 42%-scale, specimens to investigate the structural performance of the Large-Bar connection. The test specimens represented a 4-ft diameter prototype column. All specimens had columns with a 20-in. diameter and 60-in. length, which resulted in a span-to-depth ratio of 3. One specimen represented a typical cast-in-place construction and was built with 16 No. 5 longitudinal bars and served as a reference specimen. The other three columns tested variations of the Large-Bar connection concept. In one specimen, the bars were fully bonded in grouted ducts, and in the other two the

bars were partially debonded over the grouted length. The bars were debonded to reduce the strain concentration at the interface between the column and cap-beam.

The tests showed that the Large-Bar connection behaves similarly to a typical cast-in-place connection. Furthermore, deliberate debonding had little to no effect on the performance of the precast column. The connection that was originally fully bonded underwent partial debonding through "strain penetration" during the load cycles and its performance matched that of the two debonded connections. It is possible that a larger difference between the performances would have been seen if the loading had resembled a pulse ground motion rather than a cyclic load of progressively increasing amplitude.

The National Cooperative Highway Research Program (NCHRP) initiated Project 12-74 on "Development of Precast Bent Cap Systems for Seismic Regions." The project goals were to come up with design methodologies, connections details, designs and construction specifications, commentary, and illustrative design examples. This test program investigated both emulative (of a cast-in-place connection) and hybrid connections that consist of an unbonded prestressing for self-centering and mild reinforcement for energy dissipation (Matsumoto 2009, Restrepo et al. 2011).

Matsumoto (2009) tested four column-to-cap beam connections at 42 % scale. All columns had the same overall geometry (20-in. diameter column and 35-in. high, resulting in a span-to-depth ratio of 1.75.). One specimen served as a reference cast-in-place construction for the other three emulative test specimens, which were one connection with grouted ducts (similar to the Large-Bar Connection, except with many smaller bars grouted into ducts) and two that tested a "pocket" connection, one designed for full ductility and one for limited ductility. The "pocket" concept is to precast the cap-beam with an opening created with a corrugated pipe (Figure 2-6). The grouted duct connection and the pocket connection designed for full ductility showed emulative structural response to the cast-in-place reference specimen. Even though the pocket connection designed for limited ductility showed significant joint shear damage, emulative structural response was concluded (Matsumoto 2009, Restrepo et al. 2011).

Figure 2-6. Assembly of the "pocket" connection (Matsumoto 2009)

2.1.2.3 Column-to-Foundation Connections

The grouted duct connection described in Section 2.1.2.2 can be completed from above by pouring the grout down into the duct, but the solution is less easy to implement for a footing. Thus, Haraldsson et al. (2013a) developed a "wet" Socket connection that connects a precast column to a cast-in-place spread footing, in which a precast column is placed in the excavation and the footing concrete is cast around it with no steel passing between the two concretes. All the stresses are transferred by shear at the roughened interface. The wet socket concept was also adapted by Tran et al. (2013a) for drilled shafts.

Figure 2-7 shows the construction sequence, assuming that the Large-Bar Connection is being used at the top of the column. Once the footing has been excavated (Step 1 in Figure 2-7), the precast column is brought to site, plumbed, leveled, and braced (Step 2). Top and bottom footing reinforcement is then placed around the column, and the footing is cast (Step 3). The final step is to connect the column to the cap-beam (Step 4). In comparison with conventional cast-in-place construction, the primary advantage of this system that a footing and column can be built in little more time than is needed to cast the footing alone. The socket connection also provides unlimited construction tolerances. Some flexibility is possible in the sequence of steps. For example, the footing reinforcement can be placed prior to setting the column.

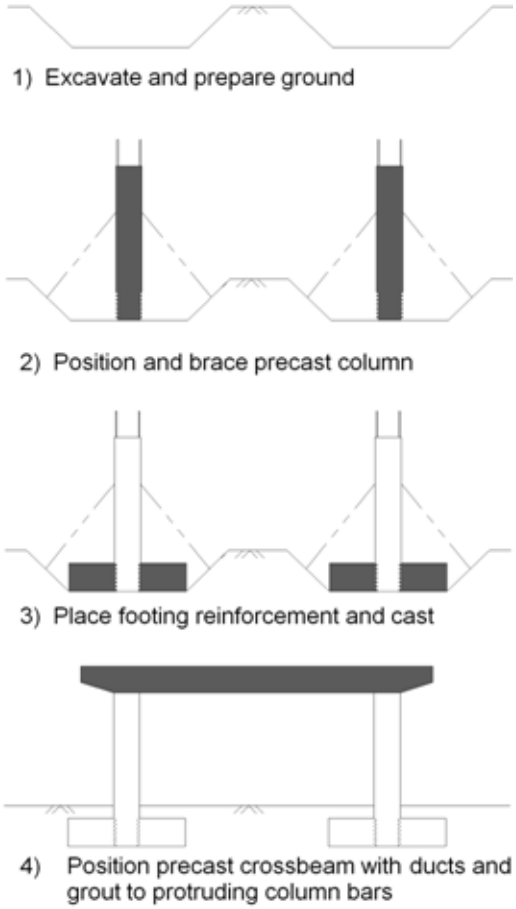

Figure 2-7. Construction sequence of the wet socket spread footing (Haraldsson et al. 2013a, 2013b)

Figure 2-7 shows the construction sequence, assuming that the Large-Bar Connection is being used at the top of the column. Once the footing has been excavated (Step 1 in Figure 2-7), the precast column is brought to site, plumbed, leveled, and braced (Step 2). Top and bottom footing reinforcement is then placed around the column, and the footing is cast (Step 3). The final step is to connect the column to the cap-beam (Step 4). In comparison with conventional cast-in-place construction, the primary advantage of this system that a footing and column can be built in little more time than is needed to cast the footing alone. The socket connection also provides unlimited construction tolerances. Some flexibility is possible in the sequence of steps. For example, the footing reinforcement can be placed prior to setting the column.

The column longitudinal bars are straight and are terminated with mechanical anchors instead of being bent out into the foundation, as is common with cast-in-place construction. This

straight bar configuration provides a much simpler and more direct flow of forces into the foundation than is possible with traditional cast-in-place bent-out bar detail. A strut-and-tie model of connection is illustrated in Figure 2-8. The figure shows also that, for the bent-out bar detail, the force in the diagonal strut must be transferred by bond into the curved region of the bar. That mode of transfer is relatively weak, and a diagonal crack forms in the footing when the bond fails. By contrast, with the headed bar in the socket detail, the forces are transferred through a direct bearing via CCC-node, which connects three compression struts.

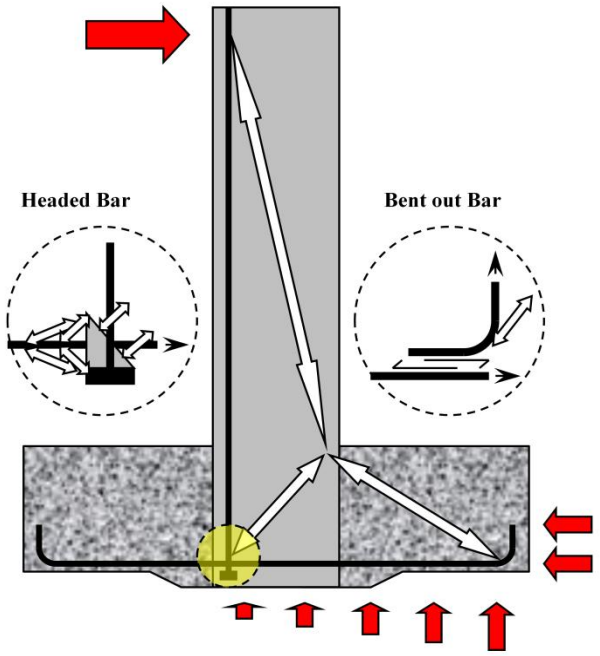

Figure 2-8. Strut-and-tie model (Haraldsson et al. 2013b)

Haraldsson et al. (2013a, 2013b) constructed two socket specimens. Both were at 42% scale and had the same overall geometry as previous tests conducted by Pang et al. (2008, 2010). The specimens had a footing height equal to $1.1D_c$, where D_c is the column diameter. In the first specimen, the reinforcement was detailed to comply as closely as possible with current codes and design practice. At the bottom of the precast column, slots in each direction were formed in each direction to allow the bottom reinforcement of the footing to pass through and engage with the tension steel in the column. Caltrans's minimum prescriptive ties for footing joint shear were included (Caltrans 2010). The need for them was originally determined from footings built with bent-out longitudinal column bars, and they were believed to be unnecessary with headed bars

because of the better performance of the critical node shown in Figure 2-8. They were included to avoid spurious failure modes in the test, but the low strains recorded in them, and the absence of diagonal cracks in the footing, showed that they did in fact contribute nothing. Three sets of four diagonal bars (12 No. 4 bars in all) were stacked, in the bottom, in the horizontal plane around the column to provide the normal forces needed to induce shear friction resistance between the column and the footing, in case the column started to push through the footing.

In the second specimen, the column slots were eliminated and the amount of secondary reinforcement, such as Caltran's prescriptive footing ties and the diagonal stacked bars, were reduced. The footing ties were halved, and the diagonal bars were reduced to one set (4-No.4). These changes made the connection easier to construct. The amount of flexural reinforcement in both footings was controlled by minimum requirements. The difference between the two specimens is shown in Figure 2-9.

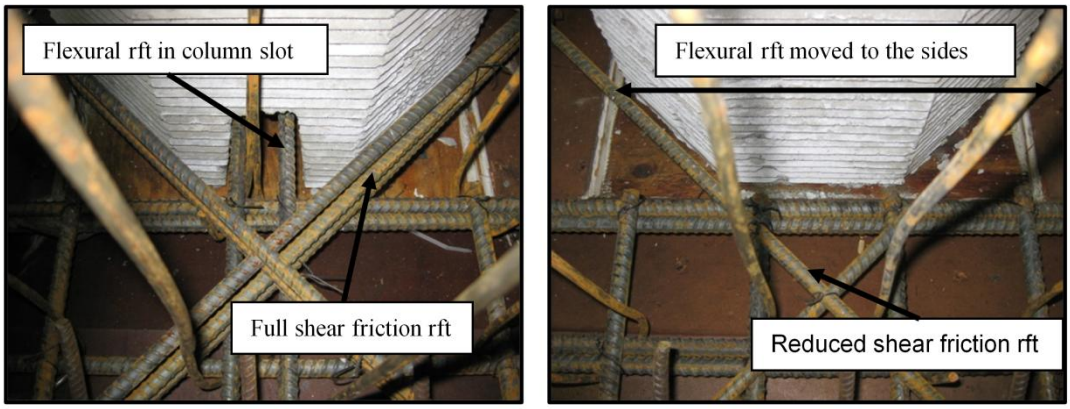

Figure 2-9. Base detail comparison of specimens

The cyclic tests revealed that the socket connection can be designed to behave as well as a comparable cast-in-place column-to-footing connection. In some ways the socket connection behaved better; the footing experienced no cracking at all, in contrast to the diagonal "joint shear cracking" usually seen in test using bent-out bars. In one test, after the cyclic loading program was complete, the column was loaded axially to try to induce a push-through or punching shear failure of the footing. (A large void was left beneath the column, which resisted vertical load solely by shear stress on the cip-pc interface). The load reached 3.5 times the factored column load (scaled to lab scale) before the column itself failed explosively in the already-damaged plastic hinge region. The footing did not even crack.

Haraldsson et al. (2013a, 2013b) concluded that the socket connection can be simplified for thick footings (footing height$\geq 1.1D_c$). The bottom flexural steel can be moved to the sides of the column instead of going through column base slots, the prescriptive footing ties can be omitted, and the shear friction steel can be reduced to one set of diagonal bars to avoid existence of unreinforced concrete in the corners (if the column section is circular or octagonal). In fact, the shear friction steel proved unnecessary for resisting shear friction during testing as they experienced little stress. The basis for these recommendations is that the footings barely cracked in flexure, and nearly all moment was carried by the concrete.

Janes (2011) tested a third specimen with a thinner footing ($h_{footing} = 0.5D_c$). The goal was to force failure into the connection region and thereby to provide information about the mechanics in the region. The thin footing failed as intended, in its last cycle (at a peak drift ratio of 10%), due to combined punching shear and moment transfer. This is a failure mode that is not considered by the AASHTO LRFD Design Specification (AASHTO LRFD 2011). In contrast to the AASHTO LRFD, the ACI 318-11 Building Code has indeed a procedure for thin slabs on top of columns. Detailed information about these three socket spread footing tests can be found in Haraldsson et al. 2013a.

Tran et al. 2013a adapted the socket connection concept to drilled shafts. The construction sequence is shown in Figure 2-10. The ground is drilled, and a reinforcing cage is placed into the hole. Then the shaft is cast all the way up to the transition zone (Step 1). After the precast column is positioned and braced (Step 2), the transition zone is cast (Step 3). Once the concrete in the transition zone has gained strength, the cap-beam can be lowered down on the columns (Step 4).

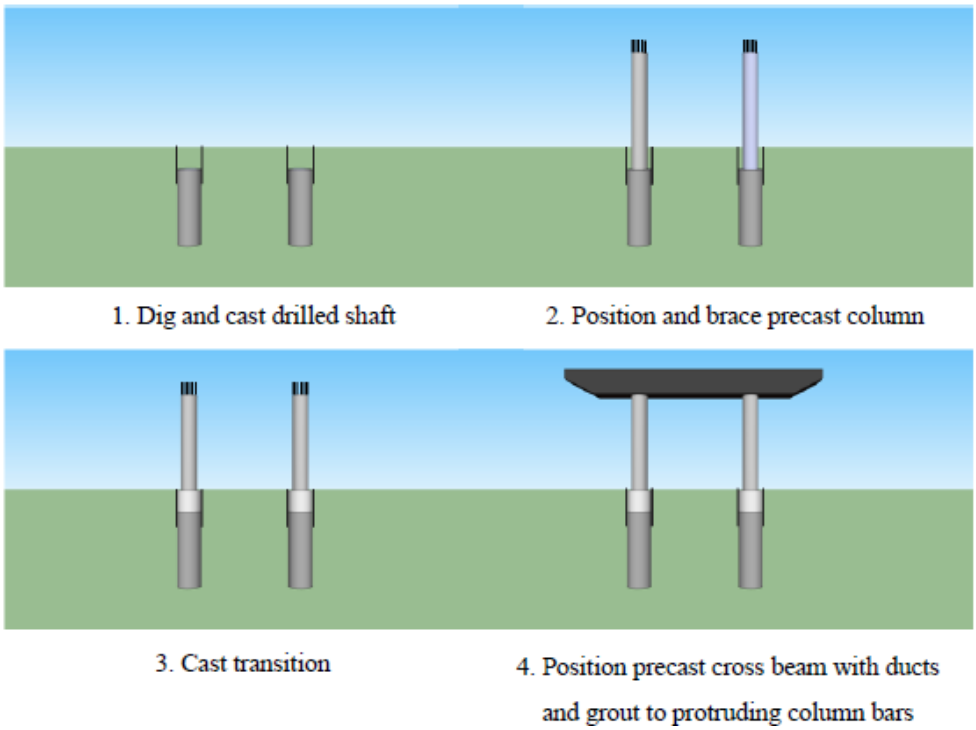

Figure 2-10. Construction sequence of the socket drill shaft connection (Tran et al. 2012)

Two drilled shaft specimens were constructed and tested at 28 % scale, which represented a prototype column with a diameter of 6 ft and a 9-ft diameter shaft. These dimensions were chosen to make the drilled shaft and the column as close as possible in diameter, while at the same time satisfying WSDOT Bridge Design Manual (BDM) 2008 criterion of $D_{shaft} - D_{column} \geq 2.0\,ft$ (WSDOT 2008). The prototype column diameter was larger than the 4-ft diameter prototype columns considered by Pang et al. 2008, and Haraldsson et al. 2013a. Nonetheless, the specimens' geometry (20-in. diameter column with a span-to-depth ratio equal to 3) matched previous tests conducted at the University of Washington (e.g., Pang et al. 2008, 2010, and Haraldsson et al. 2013a, 2013b).

The difference between the two drilled shaft specimens considered by Tran et al. (2013a) was the amount of shaft spiral reinforcement. The first specimen tested was detailed such that the shaft spiral conformed to WSDOT BDM (2008) for non-contact splices. The specimen experienced plastic hinging in the column, as is required in a standard design. The other specimen, which had half of the spiral reinforcement in the shaft, failed in the transition region of the shaft, as was intended.

2.2 Self-Centering Bridge Systems for Seismic Regions

The concept of using prestressing (through unbonded post-tensioning) was first developed on ductile concrete moment-resisting frames in buildings, at the University of Washington, by Ishizuka et al. (1984). This concept was further developed for building frames in a testing program at NIST (Stone et al, 1995, Stanton et al. 1997), then through the Precast Seismic Structural Systems (PRESSS) Research Program (Nakaki et al. 1999). The system concept is to reinforce the beams with an unbonded post-tensioning tendon and bonded mild reinforcement.. The tendon remains elastic and provides the system restoring force, and the mild reinforcement dissipates energy by yielding alternately in tension and compression. Both types of reinforcement contribute to the flexural strength. Figure 2-11 shows the concept for building frames.

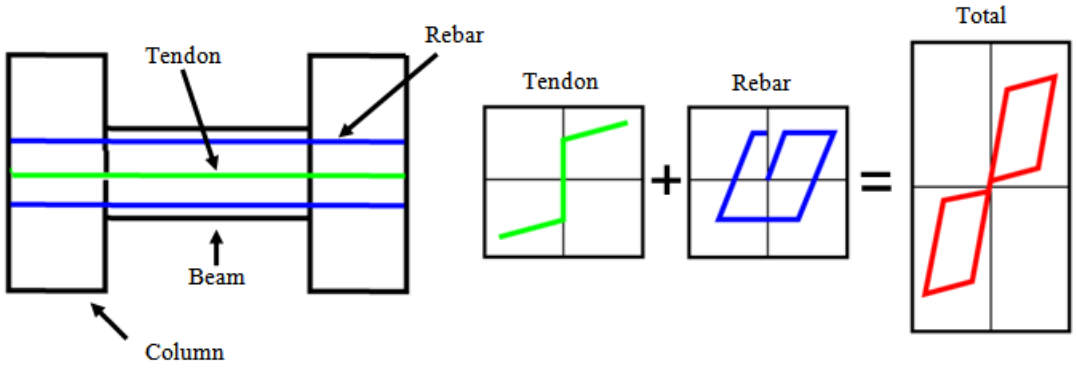

Figure 2-11. Beam-to-column connection concept with unbonded post-tensioning tendon and mild reinforcement

This design approach allowed the beams to rock against the column, and nearly all deformations occurred at that interface. The combination of elastic tendon and mild reinforcement minimized the damage in the beams themselves (Stanton et al. 1997). Priestley and Tao (1993), Stone et al. (1995) Priestley and MacRae (1996), Cheok et al. (1998), and El-Sheikh et al. (1999) all studied post-tensioned connections and found them to be satisfactory for seismically active regions. Furthermore, they showed that residual displacements were negligible for systems that incorporated unbonded post-tensioning.

The self-centering concept was recently adapted to bridge pier systems to minimize post-earthquake residual displacements. In building frames, the beams are post-tensioned and cracks

appear in the beams at the column faces when the beam rocks against the column. The elastic force in the tendon tends to close the crack, thereby bringing the frame back to plumb.

In a bridge application, the columns rather than the beams are prestressed. The system is thus similar to the building one except that it is rotated 90 degrees. However, there are two features that differ significantly in the two applications. First, in the bridge, the self-weight of the superstructure adds to the effects of prestressing and helps the re-centering, provided that the displacements are small enough (i.e., less than a column diameter) in which case the P-delta effects remain positive. Second, beams in frames exhibit "beam growth" (e.g., Kim et al. 2002), which causes the end columns in a frame to be loaded more heavily than the interior ones and cracks to be induced in the floor that could lead to unseating if precast floor elements are used. In a bridge, it is the columns that "grow" during seismic loading. The result is that the deck level might rise by an inch or so during the ground motion, but this is unlikely to be noticed by travelers. For transverse loading, all columns undergo equal displacements and grow by the same amount, so no additional forces are induced by the growth. For longitudinal loading, additional forces are induced only at the end spans (because the abutment does not rise or fall), and those additional forces are small because the spans are typically longer than the column heights and the girders are simply supported at the abutments.

The next two subsections will discuss experimental work and numerical analysis performed on self-centering systems.

2.2.1 Experimental Work

One of the first studies using the self-centering concept on bridge substructures was conducted by Hewes and Priestley (2001). They tested four, large-scale precast segmental bridge columns under quasi-static loading. Two of the test specimens had an aspect ratio of 6.0, and two had an aspect ratio of 3.0. Figure 2-12 shows the reinforcement details for the specimens with the high aspect ratio. The column segments were connected together with unbonded prestressing strands which were anchored in the foundation and in the cap-beam. All specimens included a steel jacket at the base of the column for added confinement. They found out that residual displacements were small in all specimens. They were in the order of 0.10 to 0.30% drifts after being laterally displaced up to a 6.0% drift.

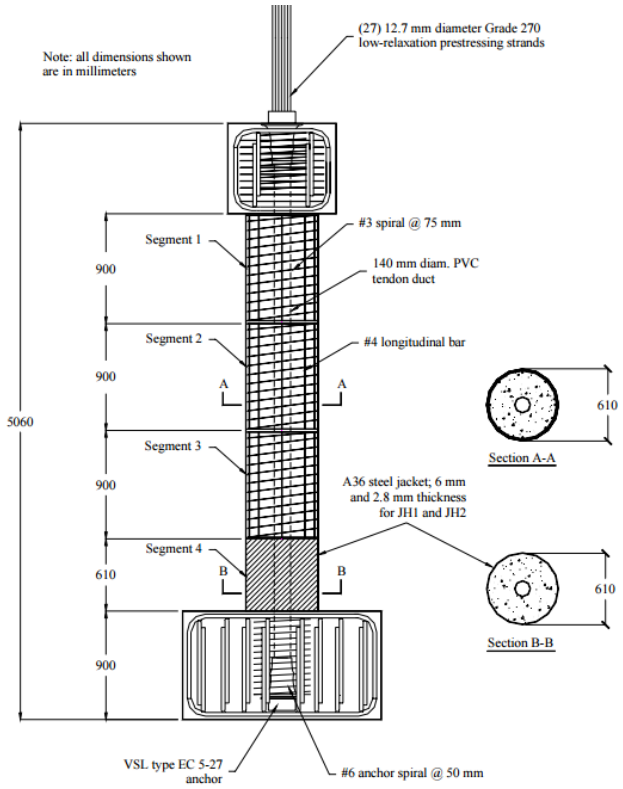

Figure 2-12. Reinforcement details for specimens with an aspect ratio 6.0 tested by Hewes and Priestley 2001)

Rouse and Billington (2003) tested six, large-scale segmental columns joined with unbonded post-tensioning strands, in which they tried different materials to minimize the damage in the plastic-hinge zone. Figures 2-13 and 2-14 show the system concept and the test setup, respectively. Two of the specimens had conventional concrete in the plastic hinge region, whereas four specimens had high performance fiber-reinforced cement-based composite (HPFRCC). All specimens showed re-centering through the use unbonded post-tensioning. By including HPFRCC in the plastic hinge region, additional hysteretic energy dissipation and ductility was observed compared to the ones with conventional concrete. Similarly, Billington and Yoon (2004) conducted small-scale, cyclic-load tests by coupling post-tensioning strands with a ductile fiber-reinforced cement-based composite (DFRCC) to limit damage in the hinging region. DFRCC is a class of HPFRCC that shows strain hardening behavior of in pure tension. Their tests showed that the DFRCC dissipated more energy and suffered less damage than traditional concrete. All specimens had minimal residual displacements at the end of the test program.

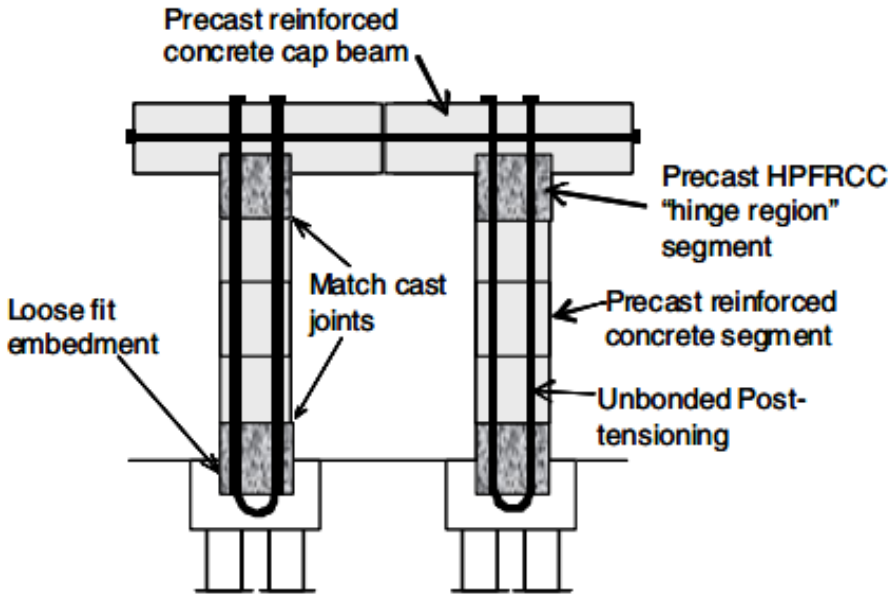

Figure 2-13. System concept developed by Rouse and Billington 2003

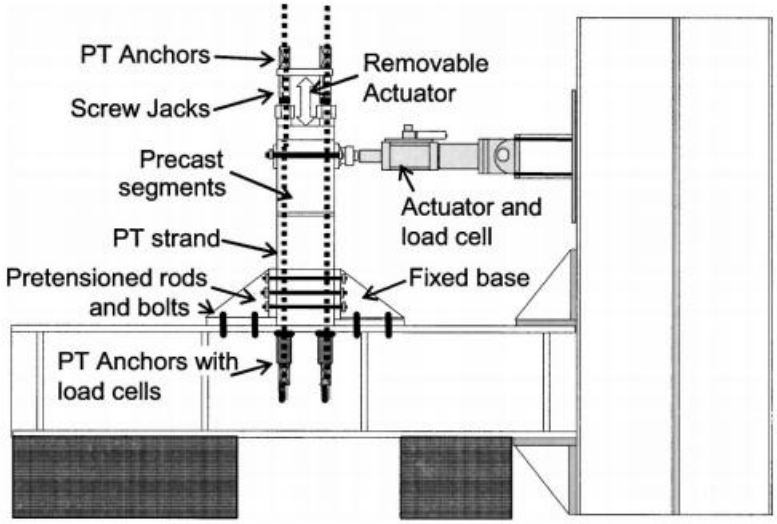

Figure 2-14. Test setup by Rouse and Billington 2003

Ou et al. (2006) investigated four unbonded post-tensioned precast segmental bridge columns. Figure 2-15 shows the elevation of the specimens. The column segments were connected with unbonded strand tendons. The first specimen did not include mild reinforcement across the segments joint but the remaining three specimens were connected with traditional mild

reinforcement for energy dissipation. The mild reinforcement was intentionally unbonded over a short region to reduce strain concentrations. All three columns showed good re-centering.

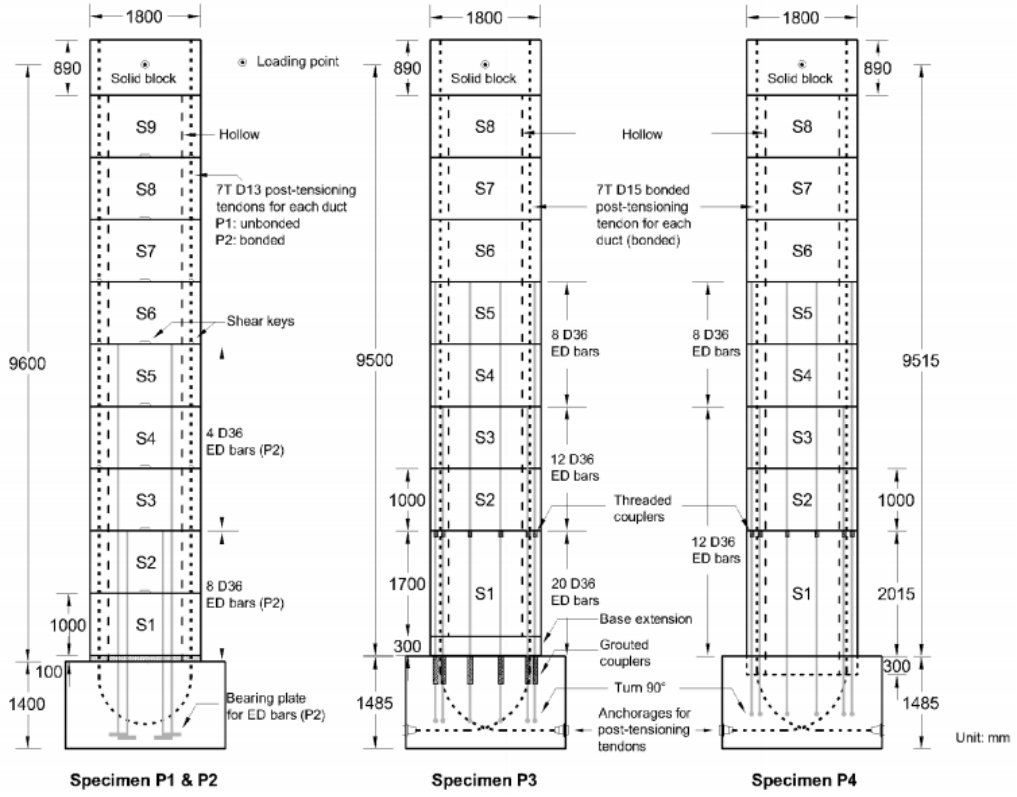

Figure 2-15. Elevation of specimens tested by Ou et al. 2006

Jeong et al. (2008) tested on a shake table four single-column specimens and one two-column bent specimen. The single-column specimens and the bent were tested at 22% scale, based on 6 ft dia. columns in the prototype. The single-column specimens were post-tensioned with a single Williams bar and had an aspect ratio of 6. For the single column tests, the parameters looked at were bonding vs. unbonding of mild reinforcement in the plastic-hinge region, amount of prestressing, and finally the effect of steel jacketing on the plastic hinge region. The specimens were subjected to two component near-field horizontal ground excitation in four steps with an increased intensity. All single column specimens showed similar re-centering capability with residual drifts of less than 0.1% (after the design-level ground motion). Researchers noted the effect of increasing prestressing which decreased both maximum and residual displacements, and increased damage in the plastic hinge region.

Cohagen et al. (2008) incorporated an unbonded post-tensioning William bar into the Large-bar beam-to-column connection developed by Pang et al. (2008, 2010). Two test specimens were constructed and were tested under quasi-static loading. The specimens' geometry and test program were identical to that previously used by Pang et al. (2008, 2012). The primary goal of the investigation was to study the effects on re-centering of relative proportions of prestressed and mild reinforcement. The columns showed a better re-centering capability after 2% drift than a comparable non-prestressed one tested by Pang et al. (2008). Both specimens had increased damage at the interface at higher drift ratios which was attributed to the force increase in the post-tensioning.

Motaref et al. (2010) included an elastomeric bearing in the plastic hinge zone in a post-tensioned segmental column. Two cantilever column designs were tested at 33% scale on a shake table based on a 5ft dia. prototype. Both columns, had an aspect ratio of 4.5 (to the center of mass), and were post-tensioned with a high-strength bar. The first segment (of five), which was 20-in. high, differed between the specimens. One column was constructed with conventional concrete in the plastic hinge region and 10 No. 4 headed dowels, thus forcing the column to rock at the interface between the first and the second segment. This was done to facilitate comparison between the two specimens. The other column, shown in Figure 2-16, had an 8-in. elastomer pad near the interface with 8 No. 5 bars that crossed through it. The segment above was cast-in-place with the elastomer and the height of the segment was 12 inches. Motaref et al. (2010) observed that both columns were able to re-center, but the behavior of the column with the elastomer in the hinging region, was better in terms of column damage, energy dissipation, and lateral-load and peak drift capacity. The elastomer and reinforcement configuration showed 14% more energy dissipation than the one that consisted of regular concrete and dowels. Furthermore, the elastomer specimen maintained strength up to 14% drift, whereas the other went to 11% drift. The inclusion of elastomer in bridge columns leads to a complex construction. The elastomer assembly has to be cast in the foundation, which introduces risks of alignment problems and takes additional time. As detailed by Motaref et al., it cannot be classified as an ABC connection.

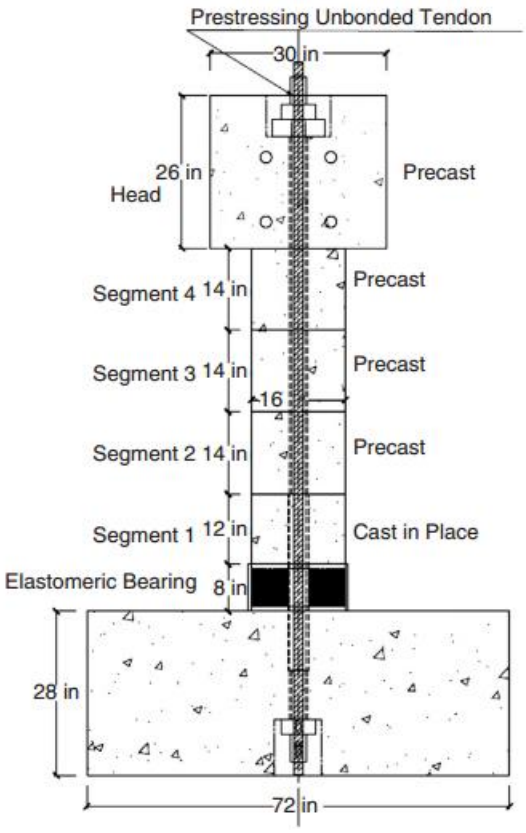

Figure 2-16. Specimen with elastomer at the base tested by Motaref et al. 2010)

As part of the NCHRP 12-74, (described earlier in 2.1.3) Tobolski (2010) tested three post-tensioned column specimens with the same 42%-scale specimen geometry and aspect ratio, equal to 2.3, as Matsumoto (2009). Restrepo et al. 2011 summarizes the test program.

All specimens were connected to a precast cap-beam using the grouted-duct option, as described by Matsumoto (2009). The aspect ratio The first specimen served as a conventional hybrid specimen (reinforced concrete with unbonded post-tension). The second was a post-tensioned concrete-filled tube with mild reinforcement at the interfaces. Figures 2-17 and 2-18 show the elevation and the test setup of the third specimen, respectively. It was a "dual-shell" system which combines two steel tubes with cast-in-place concrete infill between them and unbonded post-tensioning tendon at the center. The interior pipe was a corrugated metal pipe that acts as a stay-in form. The intent of the dual-shell system was to reduce the weight of the column. All specimens were post-tensioned with a single seven wire strand. Mild reinforcement

to be grouted into ducts in the cap-beam, for energy dissipation, was provided in the “dual-shell” specimen..

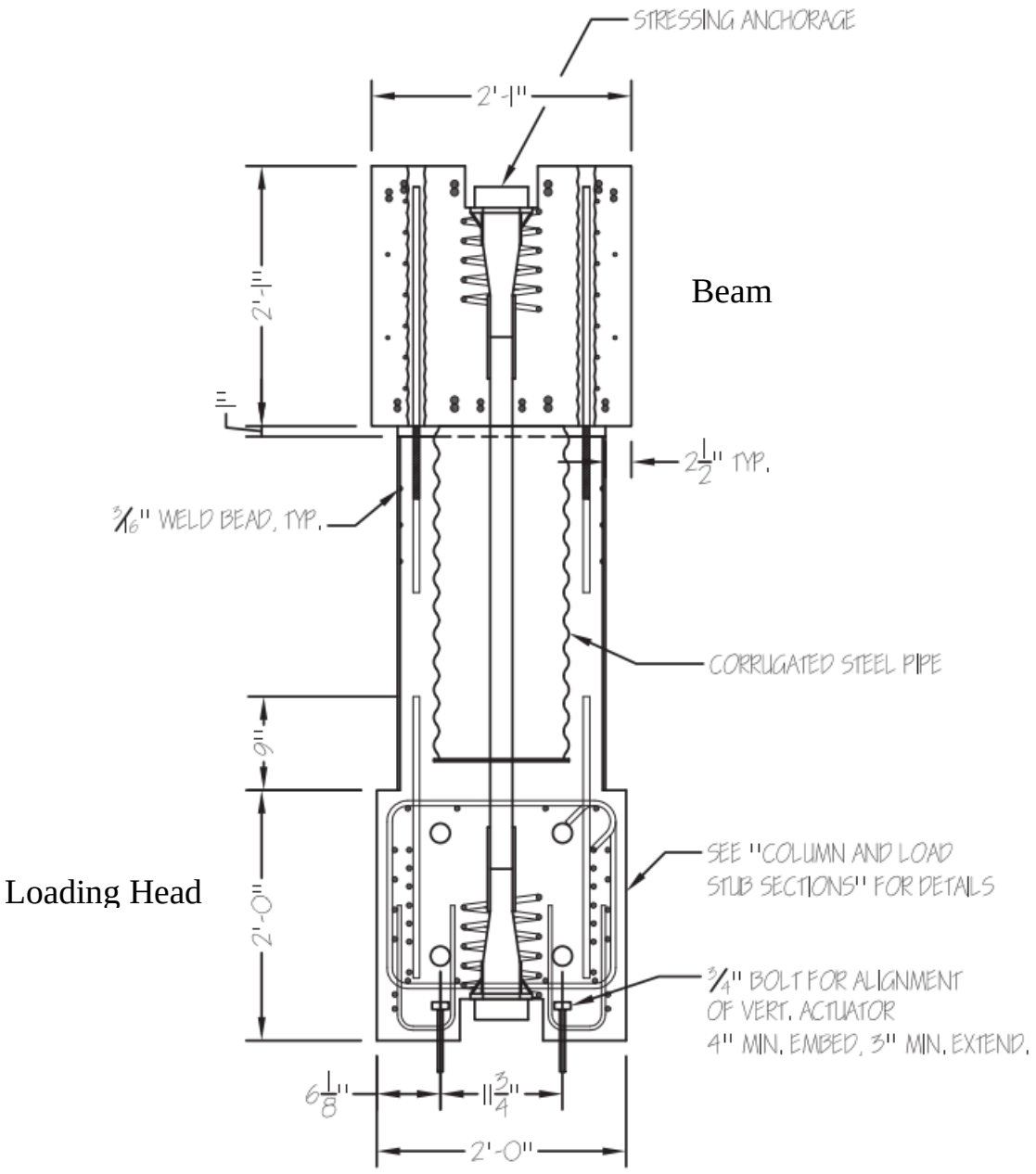

Figure 2-17. Elevation of “dual shell” column tested by Tobolski et al. 2010

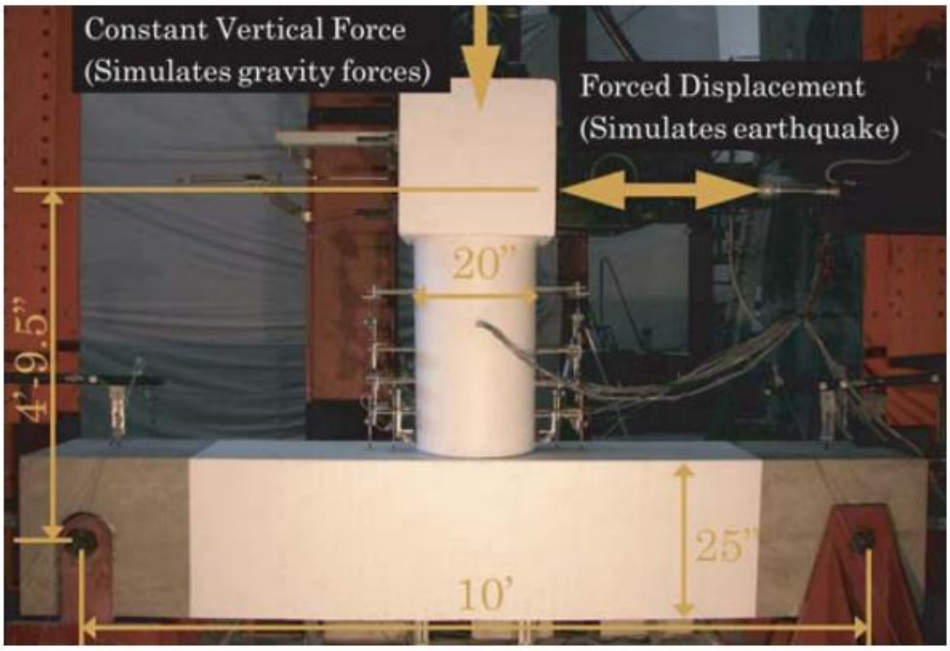

Figure 2-18. Test setup of specimens tested by Tobolski (Restrepo 2011)

All three specimens re-centered and satisfied the test program's criterion of not yielding the post-tension tendon until after the 2.5% design drift. The grout bedding layer (at the interface between the column and the cap-beam) experienced crushing, but it was concluded that fiber-reinforced grout could enhance the overall performance and improve the re-centering of the system (Restrepo et al. 2011).

Figure 2-19. Top view of the "dual-shell" column

2.2.2 Modeling of Self-Centering Systems

Several analytical studies have been performed to simulate self-centering systems and to properly predict residual displacements.

Kwan and Billington (2003a, 2003b) used finite-element analysis to study the monotonic, cyclic, and seismic behavior of a post-tensioned bridge pier system. They looked into the influence of the amount of unbonded post-tensioning on residual displacements. The study showed that peak displacements of a system with only unbonded post-tensioning during dynamic analysis were 20% up to 30% greater than in a model with bonded mild reinforcement detailed to have the same strength. This behavior of the unbonded post-tensioned system is attributed to its low energy-dissipation capacity.

Sakai and Mahin (2004) reached similar conclusions after performing dynamic analysis in OpenSees on single post-tensioned (PT) columns. But, even though the displacement demands were greater for the PT columns, they had smaller residual drifts. To minimize post-earthquake residual displacements, the amount of mild reinforcement is reduced, compared to a conventionally built column, for a prestressing bar or strands.. Thus, the design challenge is to optimize the amount of unbonded prestressing, for re-centering, to bonded mild reinforcement, for energy dissipation. They also performed quasi-static cyclic analysis on both traditional RC columns and post-tensioned columns in OpenSees and looked at the effect of various parameters, such as axial force, prestressing force, and confinement.

Hieber et al. (2005b) performed pushover and dynamic analysis in OpenSees on both the precast emulative bent system and the precast hybrid system (shown in Figure 2-20). Parameters investigated included column aspect ratio, longitudinal reinforcement ratio (for RC bents), equivalent reinforcement ratio (for hybrid frames), axial-load ratio, and re-centering ratio (for hybrid frames). The re-centering ratio was defined with the following equation:

$$\lambda_{re} = \frac{P_{axial} + A_p f_{po}}{A_s f_y} \qquad 2\text{-}1$$

where P_{axial} is the column axial load, A_p is the total area of the prestressing strands or bars, f_{po} is the initial prestressing in the strands or bars, A_s is the total area of mild reinforcement, and f_y is the yield strength of the bar.

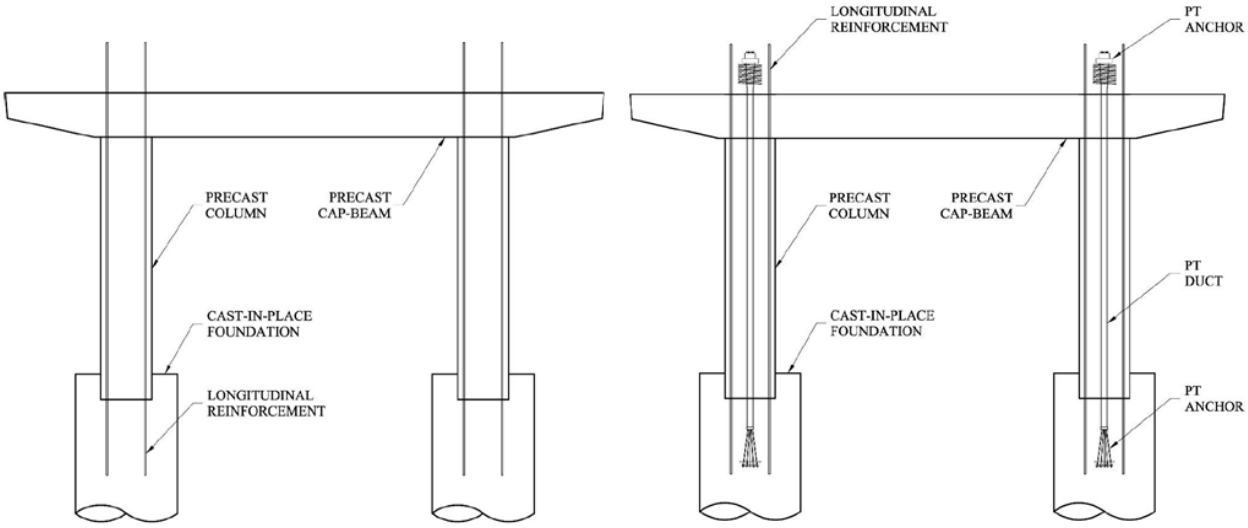

Figure 2-20. Proposed precast bridge bent systems by Hieber et al. 2005b

Analysis showed that replacing mild reinforcement with unbonded post-tensioning has the potential of minimizing residual displacements. Hieber et al. (2005b) concluded that the maximum drift ratio was nearly independent of the re-centering ratio. However, increasing the re-centering ratio reduced the residual displacements.

Jeong et al. 2008 analyzed their shake table test specimens (five single columns and one bent) in OpenSees. The analyses found that the peak responses of the columns were independent of specific material models (concrete or steel model), but the residual displacements were very sensitive to the hysteresis models used.

Lee and Billington (2009) also modified a concrete constitutive material model to account for imperfect crack closure and used it to simulate self-centering fiber-reinforced columns. This concept was originally proposed by Stanton (1979). They found that inclusion of the imperfect crack closure feature improved estimates of residual displacements.

Yazgan and Dazio (2011a, 2011b) studied the accuracy with which peak and residual displacements could be predicted in RC structures. They looked at section hysteresis models such as fiber-section model in OpenSees using both force-based and displacement-based elements and compared their results to real test data. Other models investigated were a bilinear and a modified Takeda (Takeda et al. 1970). Simulations using fiber-sections showed that peak displacements can be accurately predicted "if the hysteresis model takes into account stiffness

degradation" (Yazgan and Dazio 2011). In contrast to the peak response, residual displacements were typically underestimated using fiber-sections. This underestimation was attributed to the accumulation of small errors during the time history. They showed that the residual displacement predictions are more sensitive than the maximum displacements to various model parameters, especially the viscous damping ratio.

2.3 High-Performance Materials

The durability of the pre-tensioned bridge bent system is enhanced by the presence of the Hybrid Fiber Reinforced Concrete (HyFRC) shells in the column's plastic hinge regions, and the epoxy-coated prestressing strands. The following sections will discuss research on high-performance materials relevant to the development of the pre-tensioned bent system.

2.3.1 High-Performance Concrete

High performance fiber reinforced composites are damage-resistant in uniaxial tension and bending. Applications of high performance fiber reinforced composites in service and under investigation are found in areas where high strain demands are expected, such as coupling beams (Kanda et al. 1998, Canbolat et al. 2005), frame joints (Parra-Montesinos et al. 2005), and to repair and retrofit of structures (Kyriakides and Billington 2008, Billington et al. 2011).

Various researchers have conducted tests on high-performance concrete in research for bridge columns. Billington and Yoon (2004), as previously mentioned, incorporated a ductile fiber-reinforced cement-base composite (DRFCC) with unbonded post-tensioned precast columns in the plastic hinge regions. "DRFCC consists of Portland cement, water, silica fume or fly ash, fine sand, and a low percentage by volume (about 2%) of randomly oriented polymeric fibers" (Billington and Yoon 2004). Material tests on DRFCC have shown that it has typically higher ductility, strain hardening behavior in pure tension, and more energy dissipation under cyclic loading than other traditional concrete or others fiber-reinforced composite (FRC) materials. Figure 2-21 compares DRFCC to a mortar test in uniaxial tension. Column tests on square columns showed that DRFCC suffers less damage than traditional concrete and has the potential for dissipating more energy.

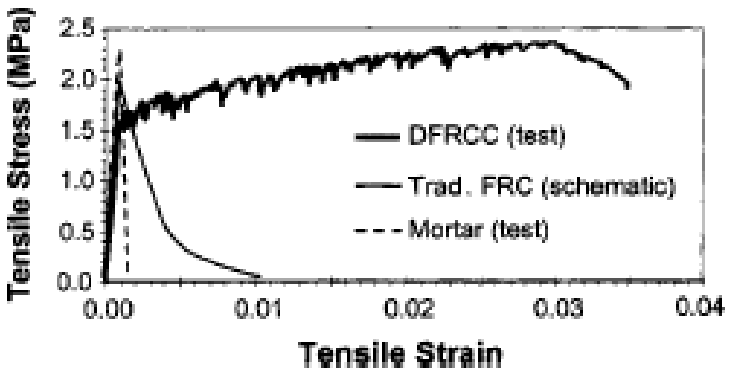

Figure 2-21. Uniaxial tensile response of DRFCC, FRC (schematic curve), and mortar (Billington and Yoon 2004)

Hybrid fiber reinforced concrete (HyFRC) was utilized in the development of the pre-tensioned bent system. HyFRC differs from DRFCC by including both steel fibers and coarse aggregates. Flexural beam tests conforming to ASTM C1609 showed that the HyFRC has more deflection hardening behavior in bending and superior damage resistance at relatively low fiber volume fraction than conventional concrete. Figure 2-22 shows flexural test results for both beams with traditional concrete and HyFRC using two different reinforcement ratios (Blunt and Ostertag, 2009a, 2009b, Trono et al. 2011).

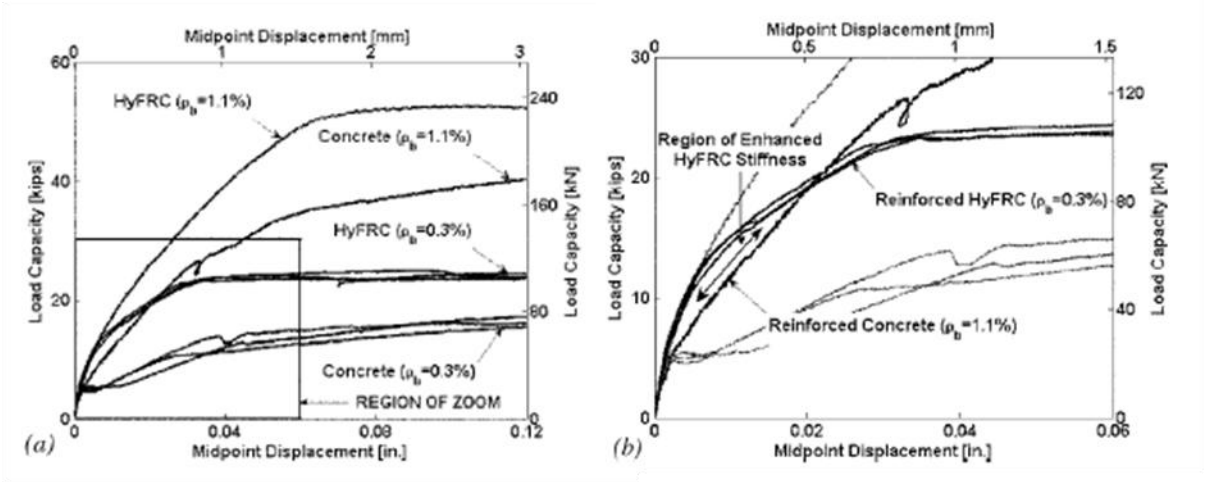

Figure 2-22. a) Flexural behavior of various reinforced beams with different reinforcement ratio, ρ_b and b) enlarged region from a) to show the the region of enhanced stiffness due to the HyFRC (Blunt and Ostertag 2009b)

The HyFRC uses both "micro"-fibers and conventional steel "macro"-fibers to provide crack control. Yi and Ostertag (2004), Grupp et al. 2007, Ostertag et al. 2007, and Jen et al. 2011 all showed that HyFRC exhibits superior durability and cracking resistance to conventional concrete. Kumar et al. (2011) tested two cantilever bridge column specimens under quasi-static loading. The columns were scaled 22% from a prototype column. The columns had 16-in. diameter circular cross section with an aspect ratio of 4.2. The HyFRC concrete delayed spalling of the concrete cover up to a drift ratio of 3.6% even at half the transverse reinforcing ratio (ρ_{spiral} = 0.37%) when compared to a conventional concrete column that had twice as much transverse reinforcement (about ρ_{spiral} = 0.7%-0.8%). In the conventional column, extensive spalling was observed at a drift ratio of 4.0%. The spall height was equal to the column diameter.

2.3.2 Epoxy-Coated Prestressing Strands

One of the objectives in development of the pre-tensioned bent system was to have an enhanced durability. After the pre-tensioning strands are released, they put the precast column under constant compression, which prevents ingress of moisture. To further reduce the potential for corrosion of the strands, epoxy-coated strands were chosen for the system. The following discusses research on epoxy-coated strands.

LeClaire et al. (1996) investigated the effects of temperature on the bond strength of epoxy-coated strand. Freshly cast concrete can reach 120-140°F as a result of heat of hydration of concrete alone. Steam curing (to increase the rate of hydration) of precast members can raise the heat to 150-180°F. They tested twenty-four test specimens of ½" diameter epoxy coated and uncoated (or "black") strands under direct tension. The test setup is shown in Figure 2-23. Each specimen was embedded for 3 inches in an 8-in. concrete cube that was in an environmentally controlled chamber.

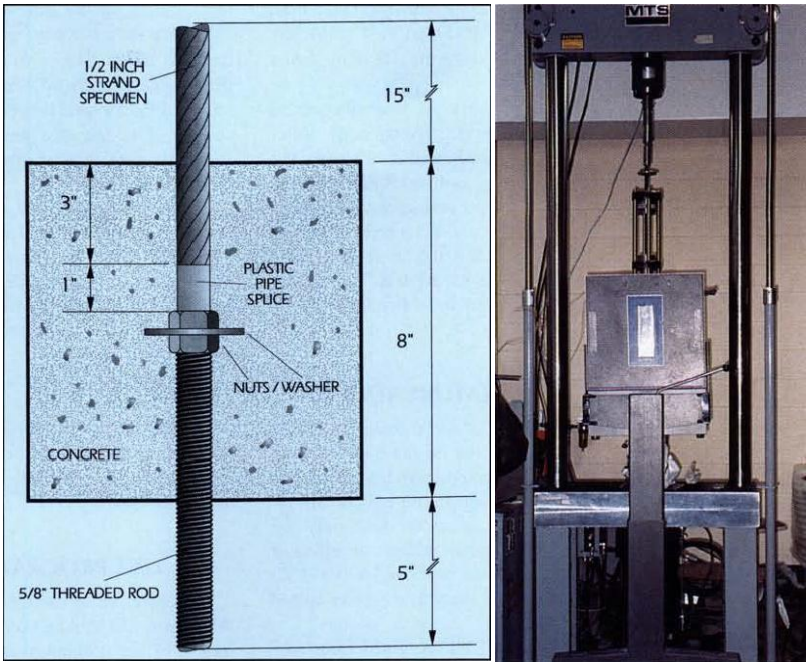

Figure 2-23. Schematic test setup (left) and test setup with environmental control chamber (right) (LeClaire et al. 1996)

They concluded that bond capacity starts to drop at a temperature higher than 125°F, and severe loss of bond was experienced at temperatures between 160 and 175°F. This was attributed to reduction of interface bond between the epoxy and the steel strands. Furthermore, LeClaire et al. recommended that internal temperature of a precast member should not exceed 160°F when de-tensioning epoxy-coated prestressing strands.

Brearly Jr. and Johnsson (1990) investigated grit density's (i.e., roughening) effect on epoxy coated strand's bond with concrete. Figure 2-24 shows three different grit densities on epoxy coated strand. They conducted fifty-two pull-out tests on 270-ksi, seven-wire strand in concrete. The strand diameters they tested included 3/8-in., 1/2-in., and 0.6-in. diameter strands. Each set tested consisted of uncoated black strand and four types of epoxy coated strand that differed in grit densities ranging from no grit, low grit density, medium grit density, and high grit density (Figure 2-24). Each test specimen was cast into an 8 in. x 8 in. x 12 in. concrete prism, in the center along the 12 in. axis, as shown in Figure 2-25. Their tests showed that grit-impregnated epoxy-strands had higher bond stress than uncoated strands and that the bond stresses were higher as the grid was denser.

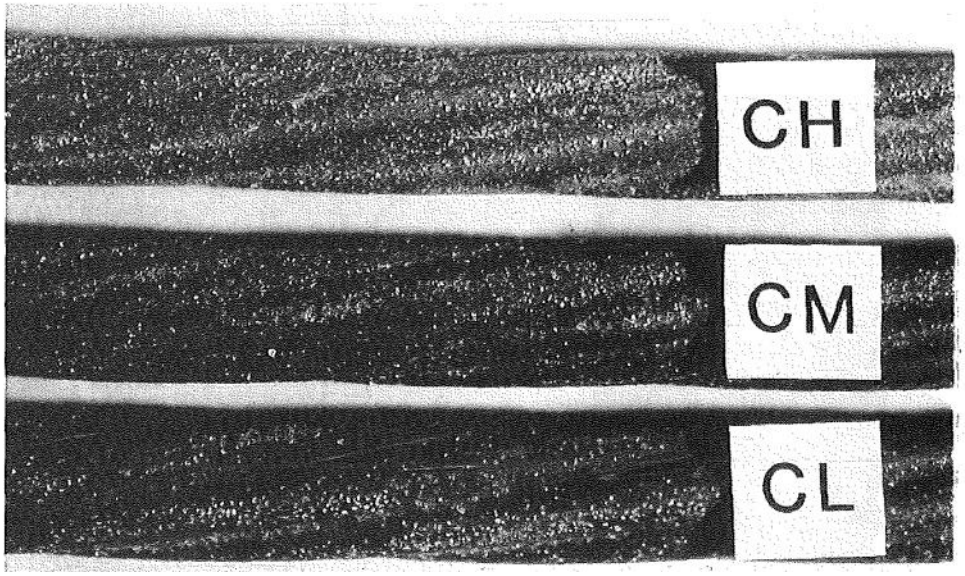

Figure 2-24. Grit densities tested by Brearly and Johnston 1990

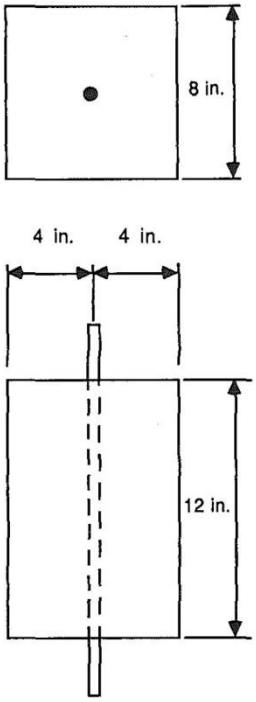

Figure 2-25. Typical pull-out test specimen (Brearly Jr. and Johnston 1990)

A test program at the University of Washington evaluated the bond performance of epoxy-coated strands to be used in the unbonded, pre-tensioned bent system. Bond characteristics of the strands were unknown and, it could not be determined what type of epoxy-coated strand had

been used by Brearly Jr. and Johnston (1990). Matthias Henry conducted a total of 65 strand bond pull-out tests, which included 3/8-in.and 1/2-in. diameter black and epoxy-coated strands. Both strand types were 270 ksi ultimate strands. The strands were embedded at various depths of 3 in., 4 in., 9 in., 12 in., and 16 in. The epoxy-coated strands used in this research were the same as used in the research of the unbonded, pre-tensioned bent system. All strands were unstressed at the time of casting. Experimental data obtained from Henry's test were analyzed by Jose Jimenez Jr. Figure 2-26 shows a typical test setup.

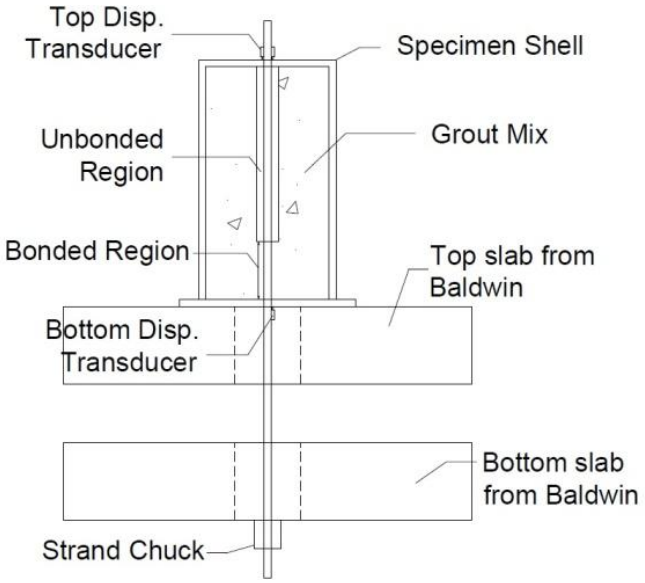

Figure 2-26. Pull-out test setup up (Jimenez Jr. 2012)

For each strand type, Jimenez (2012) looked at loads at 0.02 in. slip, at 0.1 in. slip, and at peak loads. The 0.1 in. slip was arbitrarily chosen to represent a significant prestress loss in a pre-tensioned bridge column. For a column with an unbonded prestressed height of 15 ft, the 0.1 in slip (a total of 0.2 in. because the strands slips from two ends) represents a 20%-25% prestress loss in a column that is prestressed from 135 to 160 ksi. Jimenez (2012) observed that loads in the strands at slips of 0.02 in. and 0.1 in. were on average higher in the black steel than the epoxy-coated strands. At peak loads, epoxy-coated strands had larger bond stresses than black steel. Figure 2-27 shows average bond stress versus the three load levels. Jimenez (2012) deemed the results unreliable and attributed the differences between the two types to be influenced by small number of tests conducted as well as the unknown grit density of the epoxy-coated strand.

He recommended that the differences between epoxy-coated and black strands should be considered insignificant until more tests are conducted.

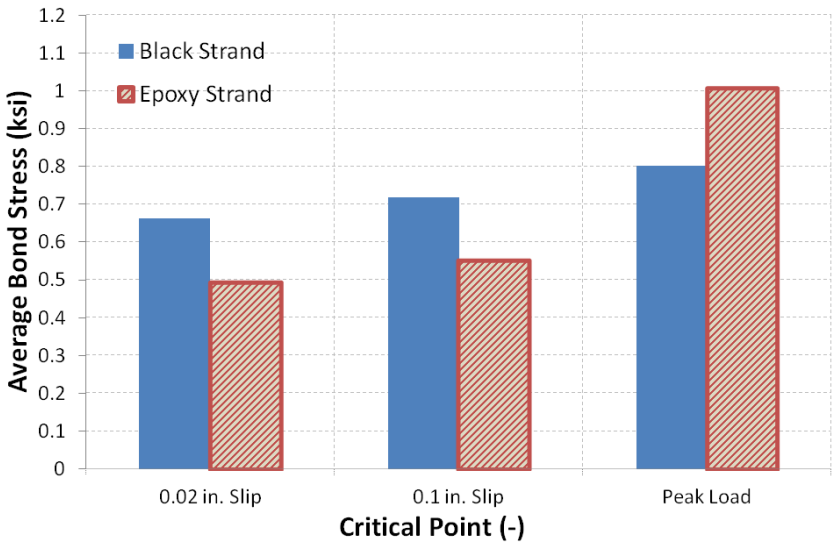

Figure 2-27. Average bond stresses at three load levels (Jimenez Jr. 2012)

2.4 Self-Centering Bridge System at University of Washington

At the University of Washington, Davis et al. (2012) tested a new unbonded pretensioned precast bridge substructure system using conventional concrete in the plastic hinge region. This system is shown in Figure 2-28.

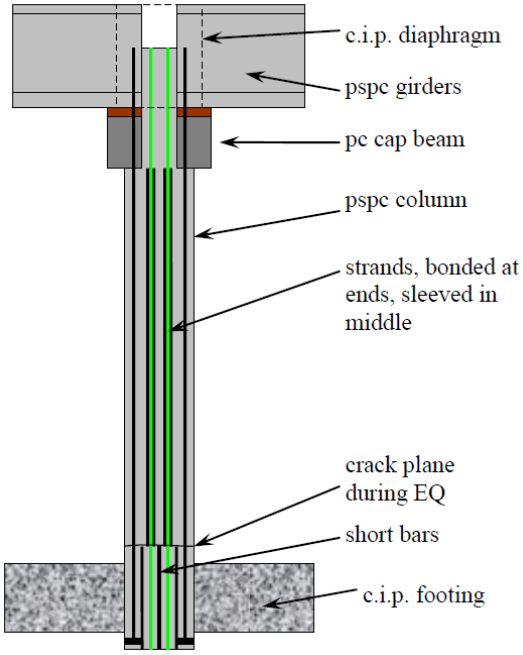

Figure 2-28. Prestressed precast column concept (Davis et al. 2012)

From the viewpoint of seismic performance, this system closely resembles the unbonded post-tensioned systems tested by Tobolski, Restrepo, Chogaen, Sakai and others. In all cases the tendon is bonded (or anchored) at the ends and unbonded over most of the column height. The unbonded tendon provides an elastic restoring force that leads to re-centering of the column while deformed bars, or other similar ductile elements, dissipate energy by yielding alternately in tension or compression.

However, the system differs radically in the way that it is fabricated and erected, and in its potential for long-term durability. The primary features that distinguish it from the post-tensioned systems are:

1. *Plant precasting and prestressing.* The column is expected to be precast and pre-tensioned in a plant. The consequence is that the difficult and critical operation of stressing is done under good QC conditions. The crew doing the site erection does not even know that the column is pre-tensioned. The assembly, using the wet socket at the bottom and the dry socket at the top, are straight forward and fast. There is no need to align the column with pre-formed ducts in the footing.
2. *No site post-tensioning* is needed. This saves an extra operation on site, as well as the time needed for any grout to set up prior to stressing. The top of the column is ready to receive the cap beam immediately. Thus the pre-tensioned system is significantly simpler and faster on site, which is a critical feature of ABC. The absence of specialist hardware (stressing anchors, stressing rams, column collars, etc.) also reduces material costs.
3. *Corrosion potential is much smaller.* Pre-tensioned strands have been used in girders for over 60 years with almost no corrosion problems, due in part to the fact that all the concrete surrounding the strands is in compression. By contrast, corrosion problems have dogged post-tensioned system for many years. (The grout "patch" over the PT anchor head is placed after the anchor is installed, and so is unstressed). Furthermore, the strands in the pre-tensioned columns are epoxy coated, and are placed near the center of the cross section, where they will have more than a foot of "cover".
4. *Construction and handling.* The system was developed from non-prestessed ABC connections with field verified constructability. These connections have been shown to reduce on-site construction time (Khaleghi et al. 2012). The system is simple to fabricate, transport and erect as the elements associated with it are linear with no protruding steel on the sides.

The new system combines unbonded prestressing strands with the wet socket connection developed by Haraldsson et al. (2013a, 2013b) and a new connection between the pre-tensioned column and the precast cap-beam (Davis et al. 2012). This connection is a hybrid of a dry socket connection and a grouted duct connection. The connection is shown in Figure 5-29. The connection has a reduced diameter extension that is grouted into a large center duct in the cap-beam. For better bond in the cap-beam's central duct, the extension is roughened with the same roughening details used in the socket connection. The strands that run through the column are

unbonded in the central part of the column and bonded in the parts of the column that are embedded in the footing and cap-beam.

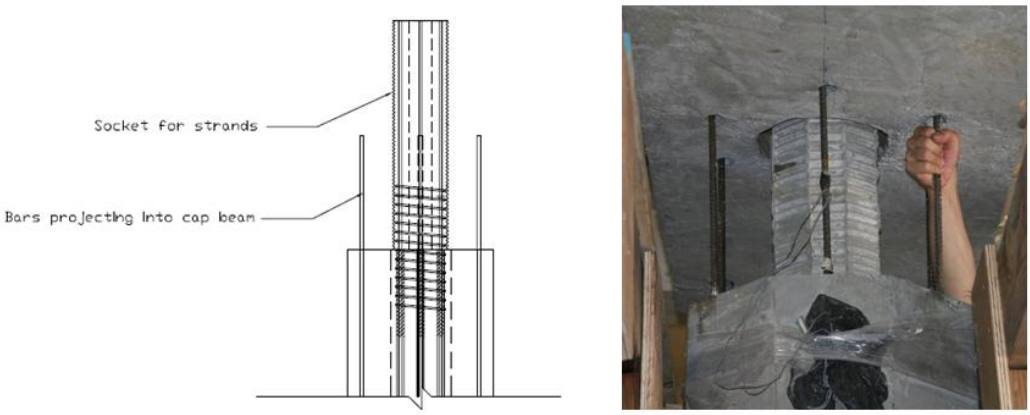

Figure 2-29. Hybrid cap-beam connection (Davis et al. 2012)

The seismic concept of the system is the same as for systems that include prestressing through post-tensioning. The strands are stressed to keep the column under compression. Once the system loaded and subsequently displaced, the column joints open up and the strands elongate and the tension force in them increase. Strains are uniformly distributed along the unbonded length. The pre-tensioning strands provide a re-centering force that "snaps" the system back to its original plumb position. Energy dissipation is provided to the system with bonded mild reinforcement that cross the interfaces between the column and the spread footing on one hand, and to the cap-beam on the other.

Davis et al. (2012) tested two 42% scale cantilever subassemblies representing the top and bottom connections. The specimens had 20-in. diameter column (representing 4-ft diameter prototype column) and 60-in. high, resulting in a span-to-depth ratio of 3.0. Both specimens hinged above the connection region and had nearly identical force-displacement hysteresis and damage progression. They showed a good re-centering capability (within 1% drift residual after being cycled to 10% drift), but spalling and bar buckling occurred at a drift ratio lower than that typically achieved in non-prestressed specimens (e.g., Pang et. al. 2008, 2010, and Haraldsson et al. 2013a, 2013b). This was attributed to the extra axial force caused by the prestressing, and is similar to the findings of Jeong et al. 2008 and Cohagen et al. 2008. Nevertheless, both pre-tensioned specimens maintained 80% of their peak lateral strength up to a drift ratio about 5%.

3 DEVELOPMENT OF THE PRE-TENSIONED BENT SYSTEM

This chapter describes the new unbonded pre-tension bent system and how it aims to improve current bridge design in three main areas:

- speed of construction
- seismic resiliency
- durability

3.1 Overview of Proposed Pre-Tensioned Bent System

The pre-tensioned system is shown in Figure 3-1. The system consists of 1) precast technology that reduces construction time, 2) unbonded pre-tensioning that minimizes residual displacements and 3) high-performance materials that extends the bridge's life–span.

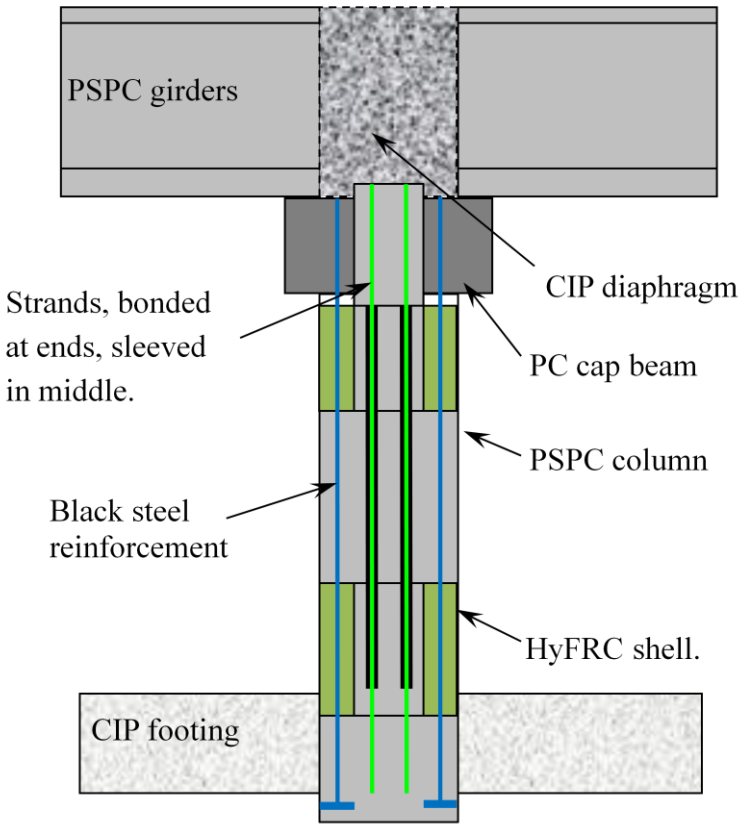

Figure 3-1. Bridge bent with unbonded pre-tensioned column

The system construction concept is to precast bridge elements off-site and assemble them rapidly on-site. To facilitate rapid construction of this system, the precast column is connected to a cast-in-place spread footing with a socket connection (Haraldsson et al. 2013a, 2013b). At the top, the column is connected to a precast cap-beam using a modified grouted "bar-in-duct" connection (Davis et al. 2012, 2013b).

To increase resiliency, the column is precast with unbonded pre-tensioning strands in the central region, and the strands' ends are bonded at the top and the bottom of the column. The strands are designed to stay elastic during an earthquake for the purpose of returning the system to its original plumb position at the end of the earthquake. Energy dissipation is provided to the system with bonded mild reinforcement that cross the interfaces between the column and the spread footing on one hand, and to the cap-beam on the other. In order to delay spalling and buckling of the longitudinal bars, plastic hinge regions are made more ductile with prefabricated shells made of Hybrid Fiber Reinforced Concrete (HyFRC) composite material (Kumar et al. 2011).

Table 3-1 summarizes the new system's design objectives and the solution strategies. The next three sections will discuss in more detail how the new system improves current bridge design in terms of faster construction, increased seismic resiliency, and enhanced durability.

Table 3-1. System design objectives and strategies

Design Objective	Strategies			
	Precast Columns and Cross-Beams	Unbonded Pre-tensioning	Socket Column-to-Footing Connection	High-Performance Materials
Objective 1: Faster Speed of Construction	Site erection much more rapid than traditional cast-in-place construction	Pre-tensioned in plant, off the critical path.	Socket connection and p.c. cap beam lead to much faster construction.	HyFRC taken off critical path by pre-casting in a commercial plant
Objective 2: Increased Seismic Resiliency	No effects on seismic performance expected.	Unbonded Pre-tensioning reduces post-earthquake displacements	Headed bars in place of hooks improve joint-shear performance.	HyFRC reduces spalling, delays bar buckling, maintains PT restoring force.
Objective 3: Enhanced Durability	Precast plants consistently deliver higher-quality components.	Extra column compression minimizes cracking	Eliminates cold joint at top of footing.	HyFRC and epoxy-coated strand increase lifetime.

3.2 Objective 1: Faster Speed of Construction

Most bridges are constructed with cast-in-place bridge bents and a superstructure that consists of precast, pre-tensioned girders (or cast-in-place box girders). The use of precast girders reduces the time needed for formwork and shoring onsite and its associated disruptions. In contrast, the use of precasting has rarely been used for the bridge substructure, especially in seismic regions. A barrier to implementation has been that connections between precast elements are typically made at the beam-column and the column-to-footing interfaces. These are the interfaces that experience the largest moment and inelastic deformation reversals under seismic loading.

The new pre-tensioned bent system is built on a technology that has already been developed for a non-prestressed system (Pang et al. 2008, 2013, Haraldsson et al. 2013a, 2013b) and implemented successfully in practice (Khaleghi et al. 2012). The concept is to precast the bridge substructure components off-site and assemble them rapidly on-site. Similarly, in the proposed system, the pre-tensioned column is likely to be precast in a commercial plant (it would be possible to precast it onsite). The fabrication sequence is that the HyFRC shells for the plastic

hinge regions are first cast separately, then placed in a form, strands are placed in the center of the column and are stressed, and finally, the rest of the column is cast. The shell casting, pre-tensioning and column casting tasks are taken off the critical path.

The use of pre-tensioning solves two main construction drawbacks of post-tensioning which is the alternative technology that has already been tried (e.g., Cohagen et al. 2008). First, it eliminates the extra steps onsite needed to post-tensioning the column, which would likely require a special subcontractor. Second, connecting the post-tensioning to the footing is a daunting challenge because access and inspection are difficult. The challenge of pre-tensioning lies in anchoring the strands. They need to be bonded at both ends of the precast column.

The pre-tensioned system incorporates the socket connection at the foundation and the modified grouted duct connection at the top. These connections have been shown to perform as well as a typical cast-in-place construction (Haraldsson et al. 2012a, 2013b, Davis et al. 2012, 2013). The concept of the socket connection is that the column is precast with an outer surface of the column that will be embedded in a cast-in-place spread footing. The region that is embedded in the spread footing contains bonded pre-tension strands. The connection differs from a conventional system in that, in the proposed system, no bars pass from the column into the foundation and therefore the vertical load is transferred by shear friction across the precast to cast-in-place interface. The column bars are terminated with mechanical anchors instead of by being bent out into the spread footing. This detail simplifies fabrication, transportation and handling, and reduces the hazard posed by protruding side bars. It also improves load transfer to the column bars. The connection offers nearly unlimited tolerances and is simple to cast. Figure 3-2 shows the roughened base that is eventually embedded in the spread footing.

The precast column contains projecting bars at the top which are grouted into ducts in the precast cap-beam. The connection is shown in figures 3-3 and 3-4. The grouted duct connection was modified from that used by Pang et al. (2008, 2010) to account for the un-bonded pre-tensioning because the strands need to be bonded within the cap-beam. The connection has a reduced diameter extension that is to be grouted into a large center duct in the cap-beam. For better bonding in the cap-beam, the section is roughened with the same roughening details used in the socket connection. Around the reduced section, mild reinforcement is distributed evenly

around (for energy dissipation) and is to be grouted into ducts that are in the cap-beam. Additionally, the reduced section provides seating for the cap-beam that relieves any need for shoring.

Figure 3-2. Socket connection column base

Figure 3-3. Reduced section of the modified “grouted-duct” top connection

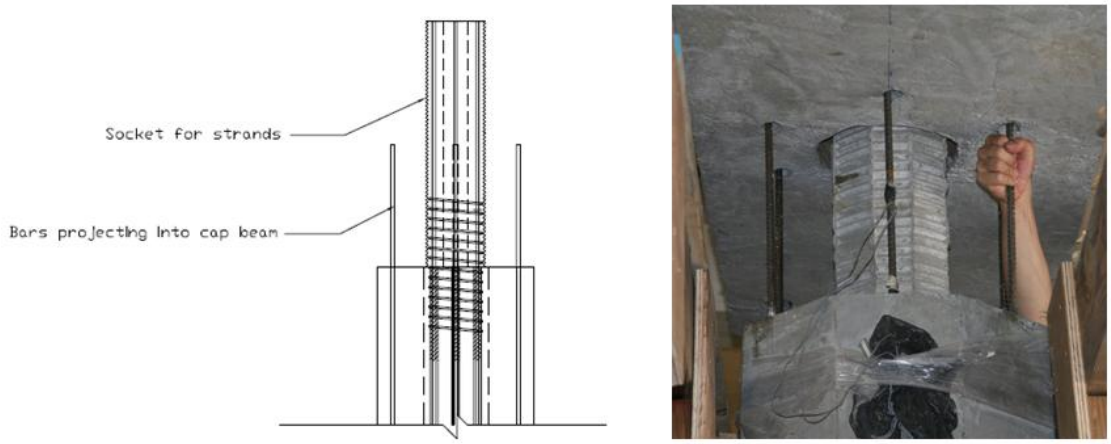

Figure 3-4. Top connection fit-up (Davis et al. 2012)

3.3 Objective 2: Increased Seismic Resiliency

Residual displacements can reduce post-earthquake bridge functionality. The residual displacement is defined as the displacement of a system the loading has been removed. If the system is loaded (and subsequently displaced) and there is no residual displacement, the system has perfectly re-centered. If the system has some displacement after being loaded, it has a residual displacement.

The new system uses unbonded pre-tensioning to provide a restoring force intended to minimize these post-earthquake displacements. The strands are unbonded over the clear height of the column, between the spread footing and the cap-beam, to distribute the strains throughout its unbonded length and bonded within the connections (for anchorage). The precast column includes mild reinforcement to provide energy dissipation to the system. Such a system is often referred to as a "hybrid" system because a yielding system is combined with an elastic system to re-center the system to its original plumb position. Idealized hysteresis loops are shown in Figure 3-5 for a bilinear elastic system, a yielding system and a hybrid system.

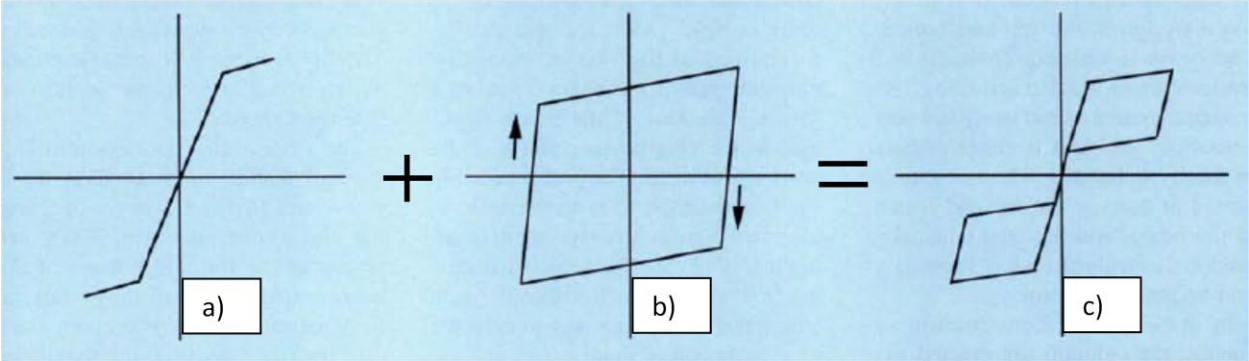

Figure 3-5. Idealized hysteresis for a) bilinear elastic system, b) yielding system, and c) hybrid systems (Stanton et al. 1997)

During earthquakes, concentration of the rotation at the ends of the columns causes high local compressive stresses and strains. These stresses become larger with the presence of the pre-tensioning and can damage the system earlier than preferred. Davis et al. (2012) conducted pseudo-static tests on an unbonded pre-tensioned column that did not include HyFRC. They observed that the columns spalled and the reinforcing bars buckled at lower drifts than observed for comparable yielding columns. A similar conclusion was drawn in an earlier study, conducted by Cohagen et al. (2008), on post-tensioned bridge columns. This early onset of damage progression can cause the system to lose the PT restoring force. To prevent losing the PT restoring force, the HyFRC shells are located in the plastic hinge regions. The HyFRC is a damage resistant composite because of its strain hardening capability in pure tension and deflection hardening capability in bending, and is thus an ideal candidate material in a region of high stresses and inelastic deformation reversals. These properties of the HyFRC are also expected to delay both spalling of the concrete and fracture of the longitudinal reinforcing bars (Kumar et al. 2011).

The connections used in the new system have been shown to perform seismically as well as traditional cast-in-place connections (Pang et al. 2008, 2010, Haraldsson et al. 2013a, 2013b, and Davis et al. 2012, 2013). These same connections were shown to be resilient with the incorporation of the unbonded pre-tensioning (Davis et al. 2012, 2013). In addition to that, strut-and-tie analysis for the socket connection indicate that the flow of forces in the connection are more direct than in traditional bent-out bar cast-in-place connection, as shown in Figure 3-6. The

socket connection is expected to have better seismic performance than traditional bent-out bar connection. In the bent-out bar connection, the diagonal strut force is transferred to the vertical bar by bond around the curved region of the bar. This force transfer can result in a joint shear crack and requires a lot of stirrups in the footing. In contrast, in the socket connection the longitudinal bars are terminated with mechanical anchors, and the load transfer can be very effectively transferred at the CCC-node.

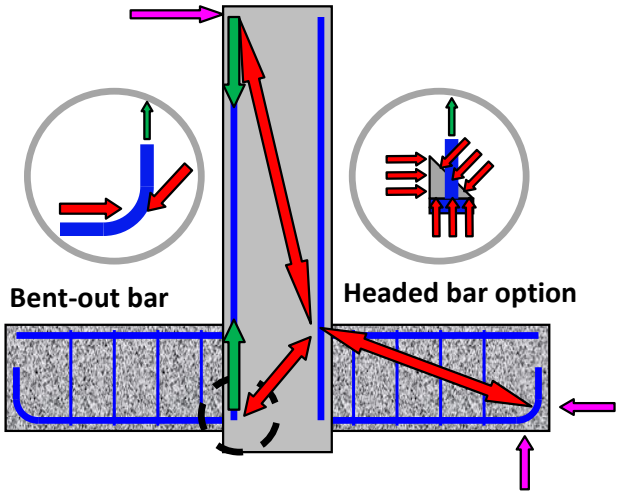

Figure 3-6. Strut-and-tie model of the socket connection (Haraldsson et al. 2012a)

3.4 Objective 3: Enhanced Durability

The durability of the proposed system is enhanced by the presence of the pre-tensioning, the HyFRC composite shells, and the epoxy-coated prestressing strands. Pre-tensioning eliminates the drawbacks associated with post-tensioning. The anchorages are particularly vulnerable to corrosion and fatigue, and if they break, the system loses all post-tensioning. In contrast to post-tension tendons, the pre-tension strands' forces are transferred to the concrete by bond only within the spread footing and the cap-beam. The strands are therefore protected throughout the bridge's life-span. The column is delivered at the construction site with tensioning already completed under well-controlled conditions in the plant.

Furthermore, the corrosion is greatly reduced because the strands are epoxy-coated and the precast column is under constant compression from the strands, which prevents ingress of moisture. The ingress of the moisture at the column-to-spread footing interface is not present in

the new system since the socket connection eliminates the cold joint that is found in traditional cast-in-place construction.

The HyFRC composite used in the shell is damage-resistant in pure tension and bending due to the presence of the steel and plastic fibers (Blunt and Ostertag, 2009a, 2009b, Trono et al. 2011). Besides having good cracking tolerances, the HyFRC shells are expected to enhance the structural integrity of system during an earthquake, and therefore aiding the system of keeping the PT restoring force provided by the pre-tension strands.

In addition to have good mechanical properties, the HyFRC has been shown to be a durable composite. The HyFRC has been used in approach bridge slabs exposed to severe environmental conditions. Extensive research on the approach slabs showed the HyFRC to have superior durability under conditions, such as frost action, corrosion, and alkali-silica reaction (Blunt and Ostertag 2008). This property can provide beneficial corrosion protection to the bridge columns' plastic hinge regions, which are the most critical regions during the earthquake.

4 QUASI-STATIC EXPERIMENTS ON SUBASSEMBLIES

In this chapter, experimental responses of quasi-static test subassemblies used for the development of the pre-tensioned bent system are presented and evaluated.

In 2008, Pang et al. (2008) tested four column-to-cap beam connections. One was a cast-in-place reference specimen and the other three specimens were precast columns with projecting column bars that were to be grouted into ducts in a precast cap-beam. Out of these three, one column had its bars fully bonded in the ducts and the other two had their bars partially debonded using two different methods. Two columns from Pang's research will be utilized in this chapter and they are the cast-in-place reference column and the precast column with bars fully bonded in the ducts. To complement these cap-beam connections, Haraldsson et al. (2013) developed a column-to-footing connection that uses a wet socket concept. A precast column with a roughened surface is embedded in a cast-in-place spread footing.

Cohagen et al. (2008), Davis et al. (2012) and Finnsson et al. (2013) all tested hybrid connections. In each hybrid system both a cap-beam and a footing connection were developed. A hybrid connection, sometimes referred to as a prestressed connection, consists of a combination of mild reinforcement for energy dissipation and unbonded prestressing, either through post-tensioning or pre-tensioning, that re-centers the column or brings the column back to its original plumb position after being displaced. Cohagen et al. (2008) tested two unbonded post-tensioned columns with different amounts of longitudinal mild reinforcement. Both Davis and Finnsson tested pre-tensioned columns; Davis tested columns with conventional concrete in the plastic hinge region and Finnsson tested a column with Hybrid Fiber Reinforced Concrete (HyFRC) in the plastic hinge region.

Here, the discussion will focus on a brief description of the test specimens, overview of the experimental program, key experimental findings and performance evaluation of the specimens. A more detailed information about the tests described in this chapter can be found in reports by Pang et al. 2008, Cohagen et al. 2008, Haraldsson et al. 2013, Davis et al. 2013, and Finnsson et al. 2013.

4.1 Description of the Test Specimens

Table 4-1 lists the specimens used in evaluating the performance of the pre-tensioned bent system using HyFRC in the plastic hinge regions. All columns tested shared similar geometric characteristics by having a 20-in. diameter (D) column with the height (L) from the foundation to the point of loading of 60 in., resulting in a span-to-depth ratio (L/D) of 3.0. This geometry represented, at 42% scale, a 48-in. diameter column. The cap-beams and the spread footings were also directly scaled down from the prototype. Specimens PreT-SF-FIB and PreT-SF-CONC differed from other specimens in terms of the span-to-depth ratio. Their span-to-depth ratio was 3.3. This was a consequence of a predetermined crack plane 6 in. above the footing surface included in Specimen PreT-SF-CONC. In all tests, the specimens were flexural critical.

Table 4-1 shows furthermore that the transverse reinforcement ratio (ρ_{spiral}) was kept the same in all specimens but they differed in terms of longitudinal mild reinforcement ratio (ρ_l). In general, prestressed connections have a lower longitudinal reinforcement ratio than non-prestressed ones because mild reinforcement is replaced by pre-tensioned strands or a post-tensioning bar. The last column in Table 4-1 reports re-centering ratios, $\lambda_{re,}$ for all the specimens. The re-centering ratio is calculated with Equation 4-1:

$$\boldsymbol{\lambda_{re}} = \frac{\boldsymbol{P_{axial}+A_p f_{po}}}{\boldsymbol{A_s f_y}} \qquad 4\text{-}1$$

where P_{axial} is the column axial load, A_p is the total area of the prestressing strands or bars, f_{po} is the initial prestressing in the strands or bars, A_s is the total area of mild reinforcement, and f_y is the yield strength of the bar (Hieber et al. 2005).

Equation 4-1 is derived by taking moment in the column cross section and assuming that all the steel has reach the yield stress. The equation quantifies the potential of the specimens to re-center to their original plumb position by taking the quotient of a re-centering moment to a resisting moment. Equation 4-1 is discussed in more detail in Section 4.5.4. Thus if a λ_{re}-value is lower than 1.0, it means the column's resisting moment is greater than its re-centering moment and the column will show little to no re-centering capabilities. The opposite is expected if the λ_{re} is larger than 1.0. In Table 4-1, the re-centering ratio is calculated by using the measured yield

stress of the mild reinforcement. In all tests, the total axial load ratio ($P_{total}/A_g f'_c$) ranged from 8.1% to 11.4%. P_{total} is the sum of the dead load and, if applicable, the initial prestressing force.

Table 4-1. UW bridge column dataset

Reference	Specimen[1]	L (in.)	L/D	ρ_l (%)	ρ_{spiral} (%)	Pre/Post tension	$\frac{P_{axial}}{A_g f'_c}$ [3] (%)	$\frac{P_{total}}{A_g f'_c}$ (%)	λ_{re}
Pang et al. 2010	CIP-CB-REF	60	3.0	1.58	0.88	None	11.2	11.2	0.81
Pang et al. 2010	PCC-CB-FB	60	3.0	1.51	0.88	None	8.1	8.1	0.91
Haraldsson et al. 2013	PCC-SF-THK1	60	3.0	1.12	0.88	None	10.1	10.1	0.73
Haraldsson et al. 2013	PCC-SF-THK2	60	3.0	1.12	0.88	None	9.2	9.2	0.73
Cohagen et al. 2008	PosT-CB-LOPT	60	3.0	1.15	0.88	1-1 3/8 in. b[4]	5	10	1.20
Cohagen et al. 2008	PosT-CB-HIPT	60	3.0	0.84	0.88	1-1 3/8 in. b	5	10	1.60
Davis et al. 2013	PreT-CB-CONC[2]	60	3.0	0.36	0.88	6-3/8 in. s	6.8	10.5	3.10
Davis et al. 2013	PreT-SF-CONC[2]	60	3.0	0.36	0.88	6-3/8 in. s	6.7	10.3	3.10
Finnsson et al. 2014	PreT-SF-FIB[2]	66	3.3	0.36	0.88	6-3/8 in. s	7.2	11.4	3.10

1. PCC/PostT/PreT := Precast/Post-Tensioned/Pre-Tensioned
   CB/SF := Cap Beam/Spread Footing
   CON/FIB := Conventional Concrete/Fiber Concrete
   REF/THK/LOPT/HIPT := Reference/Thick/Low PT/High PT
2. Octagonal column cross-section
3. P_{axial} refers to dead load applied.
4. $/s$:= bar/strands

Table 4-2 lists the measured material properties for all the specimens. In this table, the measured test day concrete strength is reported for all the columns but the concrete strength for the foundations is omitted. In all the tests, the cap-beams and the spread footings were capacity protected and therefore were not damaged during the tests.

Tension tests were performed on the longitudinal reinforcement for every test specimen. All longitudinal column steel conformed to ASTM A706 standard with a minimum specified yield stress of 60 ksi. Only in Specimen PosT-CB-LOPT, was the measured yield stress, using nominal bar dimension, less than 60 ksi. But it was only 0.33% low.

In the following subsections, the specimens will be described in more detail. Specimen drawings can be found in reports by Pang et al. 2008, Cohagen et al. 2008, Haraldsson et al. 2013, Davis et al. 2013, and Finnsson et al. 2013.

Table 4-2. UW bridge column dataset measured properties

Reference	Specimen	f'_c (psi)	f_y (ksi)	f_u (ksi)
Pang et al. 2010	CIP-CB-REF	6,830	64.2	92.1
Pang et al. 2010	PCC-CB-FB	8,340	66.2	92.5
Haraldsson et al. 2013	PCC-SF-THK1	4,995	61.6	86.1
Haraldsson et al. 2013	PCC-SF-THK2	5,496	61.6	86.1
Cohagen et al. 2008	PosT-CB-LOPT	7,020	59.8	93.7
Cohagen et al. 2008	PosT-CB-HIPT	7,420	70.6	100.7
Davis et al. 2013	PreT-CB-CONC	7,020	68.4	108.6
Davis et al. 2013	PreT-SF-CONC	7,125	68.4	108.6
Finnsson et al. 2014	PreT-SF-FIB	6,660	67.1	92.6

1. Average concrete strength on day of test.

4.1.1 Reference Cast-in-Place Column-to-Cap Beam Connection (CIP-CB-REF)

Specimen CIP-CB-REF served as a reference specimen in Pang et al.'s (2008) test program and in the subsequent research conducted at the University of Washington. The specimen was designed to conform to AASHTO LRFD Bridge Design Specifications 4th Edition (AAHSTO

2005a). It emulated a typical Washington State cast-in-place column-to-cap beam connection. The specimen was reinforced with 16 No. 5 bars ($A_s = 4.96\ in^2$), which provided a longitudinal reinforcement ratio, ρ_l, of 1.56%. The transverse reinforcement consisted of 3-gauge, 0.244-in. diameter, smooth wire conforming to ASTM A82, with the minimum specified yield strength of 80 ksi. The spiral pitch was 1.25 in., resulting in a transverse reinforcement ratio, ρ_s, of 0.88%. The column clear cover was 0.75 in. Figure 4-1 shows Specimens CIP-CB-REF's elevation.

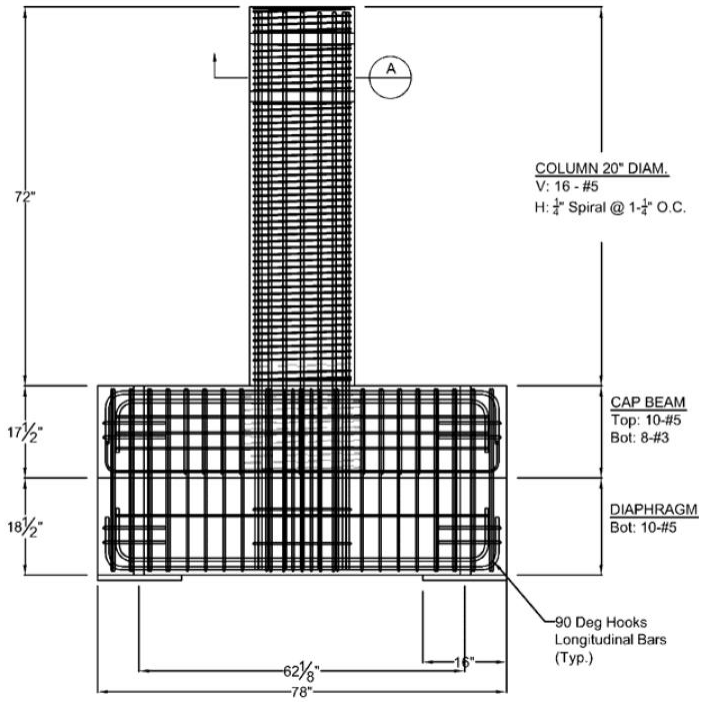

Figure 4-1. Specimen CIP-CB-REF elevation (Pang et al. 2008)

4.1.2 Precast Column-to-Cap Beam Connection (PCC-CB-FB)

Specimen PCC-CB-FB was a new connection concept, commonly referred to as the "Large-Bar Connection", that connects a precast column with projecting bars that are eventually grouted into ducts in a precast cap-beam. The concept was to use fewer but larger bars to facilitate fit up during erection on site. The specimen was reinforced with 6 No. 8 bars ($A_s = 4.74\ in^2$), which provided a longitudinal reinforcement ratio, ρ_l, of 1.51%. The column longitudinal bars were fully grouted into the precast cap-beam. The transverse reinforcement consisted of 3-gauge, 0.244-in. diameter, smooth wire conforming to ASTM A82. The spiral pitch was 1.25 in.,

resulting in a transverse reinforcement ratio, ρ_s, of 0.88%. The column clear cover was 0.75 in. Figure 4-2 shows Specimen PCC-CB-FB's elevation.

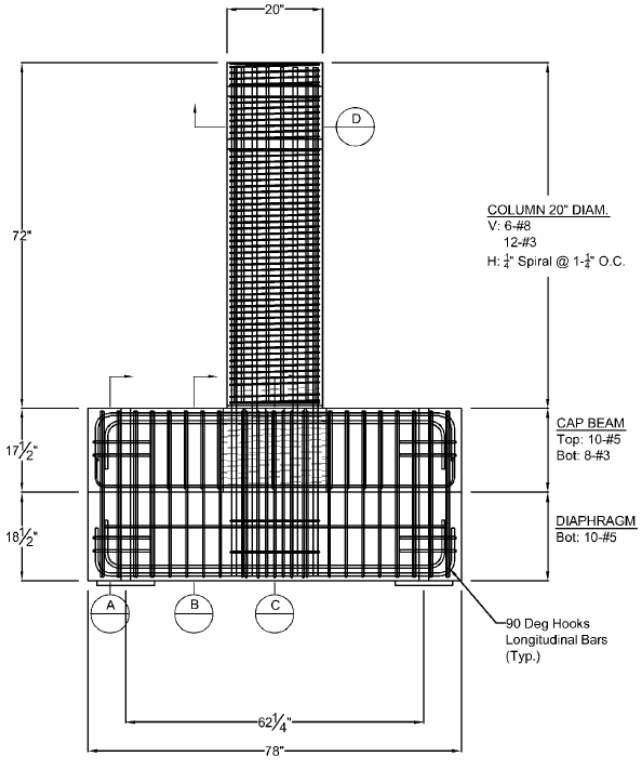

Figure 4-2. Specimen PCC-CB-FB elevation (Pang et al. 2008)

4.1.3 Precast Column-to-Footing Connections (PCC-SF-THK1 and PCC-SF-THK2)

Specimens PCC-SF-THK1 and PCC-SF-THK2 tested a new concept where a precast column is embedded in a cast-in-place spread footing. The vertical surface of the precast column is roughened where it is embedded in the spread footing. No bars cross the interface between the two, so resistance to both gravity and earthquake loads are carried by shear-friction only. The system is referred to as a "wet Socket Connection".

The two specimens were designed to confirm to AASHTO Load Resistant Factor Design Specifications (AASHTO 2009b), the AASHTO Guide Specifications (AAHSTO 2009a), the WSDOT Bridge Design Manual (WSDOT 2008), and the California DOT (Caltrans) Seismic Design Criteria (Caltrans 2006). The columns were reinforced with 8 No. 6 bars ($A_s = 3.52\ in^2$), which provided a longitudinal reinforcement ratio, ρ_l, of 1.12%. The transverse reinforcement consisted of 3-gauge, 0.244-in. diameter, smooth wire conforming to ASTM A82. The pitch of

the wire was 1.25 in., resulting in a transverse reinforcement ratio, ρ_s, of 0.88%. The column clear cover was 1.5 in. instead of 0.75 in. The reason for the difference between Haraldsson et al. (2013) and Pang et al. (2008) test programs is because Haraldsson's specimens were directly scaled from a different prototype bridge. Figure 4-3 shows PCC-SF-THK1 and PCC-SF-THK2's elevation.

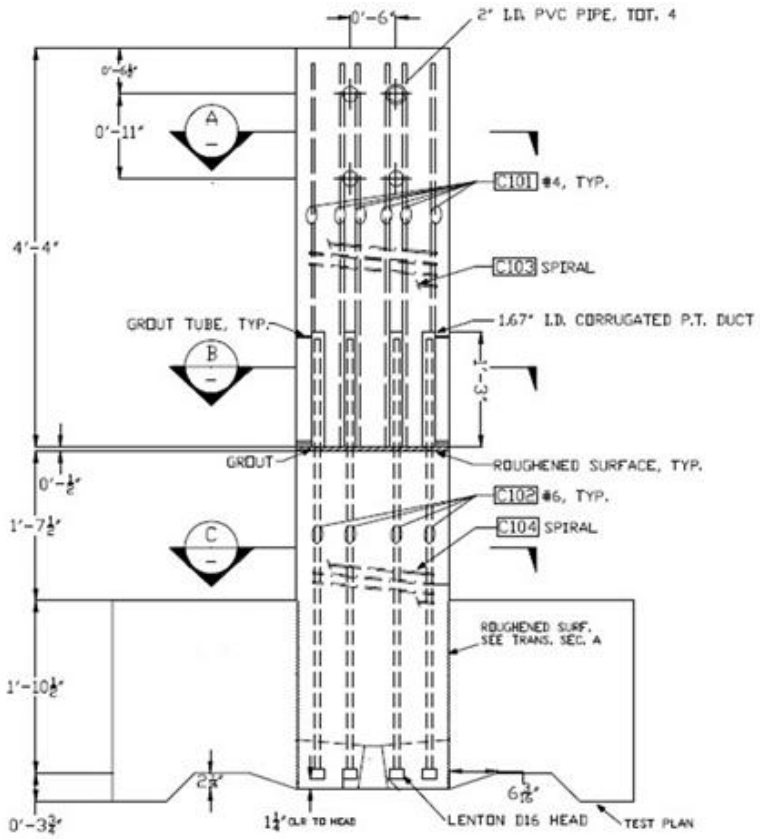

Figure 4-3. Specimens PCC-SF-THK1 and PCC-SF-THK2 elevation (Haraldsson et al. 2013)

4.1.4 Post-Tensioned Column-to-Cap Beam Connections (PosT-CB-LOPT and PosT-CB-HIPT).

Specimens PostT-CB-LOPT and PosT-CB-HIPT were hybrid connection variations of the Large-Bar connection. Each of the two specimens was both post-tensioned with a 1 3/8-in. Williams bar (PT bar), with a slightly different initial post-tension force. In this test program, the goal was to keep the axial load acting on the connection as close to 10% of $A_g f'_c$. Therefore the axial load was reduced due to the post-tensioning in the columns. This was done to facilitate comparison with the tests conducted by Pang et al. (2008).

Specimen PosT-CB-LOPT was reinforced with 6 No. 7 bars ($A_s = 3.60\ in^2$), which provided a longitudinal reinforcement ratio, ρ_l, of 1.15%. The transverse reinforcement consisted of 3-gauge, 0.244-in. diameter, smooth wire conforming to ASTM A82. The pitch of the wire was 1.25 in., resulting in a transverse reinforcement ratio, ρ_s, of 0.88%. The column clear cover was 0.75 in. Specimen PosT-CB-HIPT was identical to PosT-CB-LOPT except that it was reinforced with 6 No. 6 bars ($A_s = 2.64\ in^2$), which provided a longitudinal ratio, ρ_l, of 0.84%. At the beginning of the test, the initial prestressing force in specimens PosT-CB-LOPT and PosT-CB-HIPT was 141.3 and 140.3 kips, respectively. Figure 4-4 shows PosT-CB-LOPT and PosT-CB-HIPT's elevation.

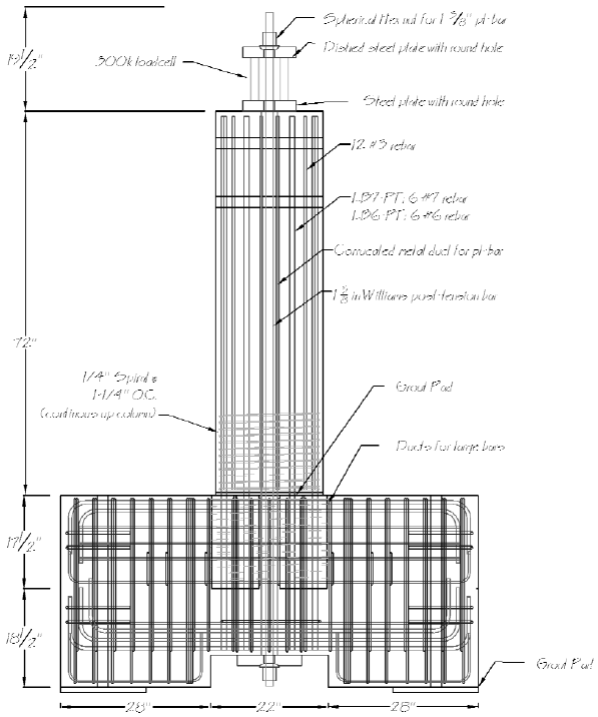

Figure 4-4. Specimens PosT-CB-LOPT and PosT-CB-HIPT elevation (Cohagen et al. 2008)

4.1.5 Unbonded Pre-Tensioned Connections (PreT-CB-CONC and PreT-SF-CONC)

Specimens PreT-CB-CONC and PreT-SF-CONC tested a new pre-tensioned bridge bent concept. The system adopted technology from previous test programs (i.e., the Large-Bar and Socket connections). Instead of using post-tensioning, which would have to be performed on a bridge construction site by a special contractor, the specimens are delivered on-site already pre-tensioned, thus eliminating the need of an extra operation and specialization on-site. The

fabrication of the pre-tensioned columns is similar to the fabrication of prestressed girders. The column is cast in a prestressing bed. However, in contrast to prestressed girders, the strands are unbonded in the clear height between the spread footing and the cap-beam, to distribute the strains in the strands and thus avoiding a strain concentration.

Specimen Pre-T-CB-CONC tested the column-to-cap beam connection. The column was reinforced with 6 No. 4 bars ($A_s = 1.20\ in^2$), which provided a longitudinal reinforcement ratio, ρ_l, of 0.36%. Transverse reinforcement ratio consisted of 3-gauge, 0.244-in. diameter, smooth wire conforming to ASTM A82. The pitch of the wire was 1.25 in, resulting in a transverse reinforcing ratio, ρ_s, of 0.88%. The column clear cover was 0.75 in. Figure 4-6 shows Specimen PreT-CB-CONC's elevation. The column was pre-tensioned with 6 3/8-in. epoxy-coated strands ($A_p = 0.51\ in^2$) that resulted in a strand ratio, ρ_p, of 0.15%. Each strand was each jacked to 15.3 kips and after accounting for stress losses, such as initial elastic and creep, each specimen was prestressed to about 84 kips. In this specimen, the column had a reduced section that the strands were bonded with the concrete and around the reduced section the mild reinforcement was distributed evenly around. Both the reduced section and the mild reinforcement were to be grouted into ducts in the precast cap-beam. This design had a construction advantage that it provided a seating for the precast cab-beam on the column during the assembly. This is shown in Figure 4-5.

Figure 4-5. PreT-CB-CONC column-to-cap beam connection (Davis et al. 2012)

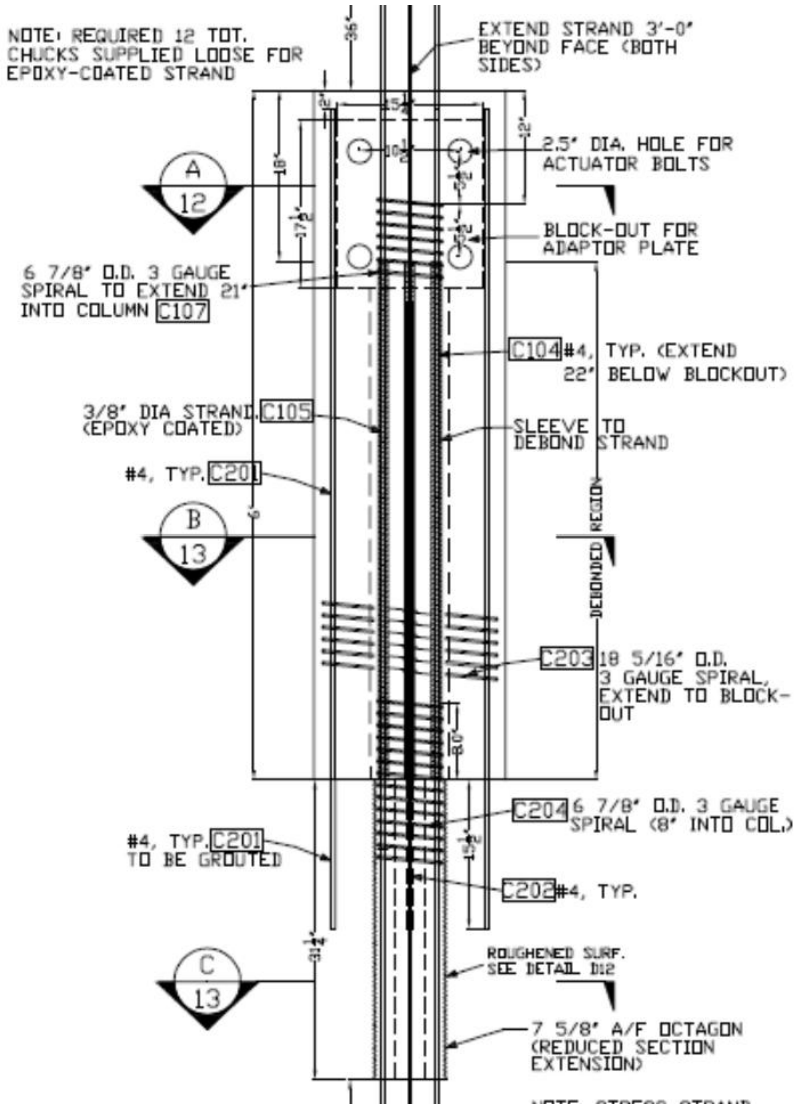

Figure 4-6. Specimen PreT-CB-CONC elevation (Davis et al. 2012)

Specimen PreT-SF-CONC tested a column-to-spread footing connection. It was reinforced and prestressed identically to the PreT-CB-CONC. No modifications were needed for the Socket Connection to include the prestressing strands. During testing of specimens PreT-CB-CONC and PreT-SF-CONC, bar buckling and fracture occurred earlier than had previously been seen in the testing of both the Large-Bar Connection and the Socket Connection. Figure 4-7 shows Specimen PreT-SF-CONC's elevation.

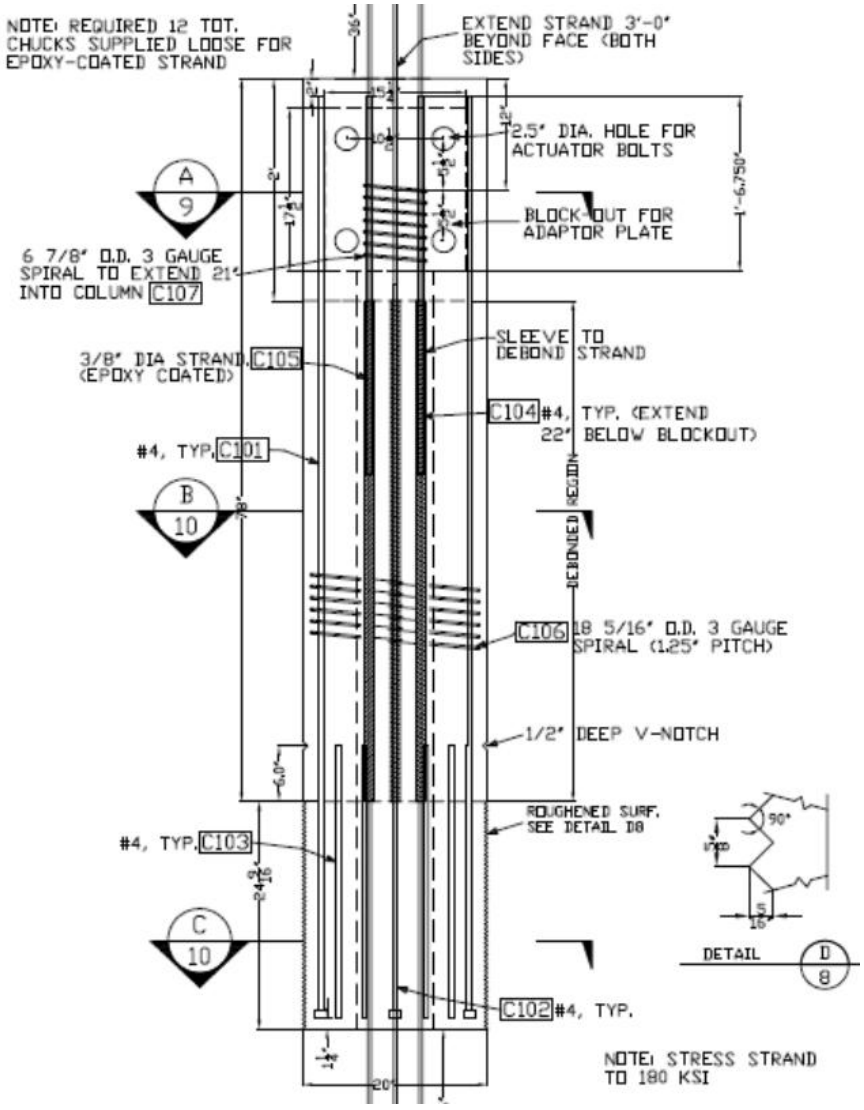

Figure 4-7. Specimen PreT-SF-CONC elevation (Davis et al. 2012)

Both of these columns were 20-in. octagons to facilitate fabrication as they were constructed in a prestressing bed. This minimal increase of the column cross-sectional area did not have any effect on the structural performance of either specimen because it was only in increase of a column cover area.

4.1.6 Unbonded Pre-Tensioned Column-to-Footing Connection with HyFRC (PreT-SF-FIB)

Specimen PreT-SF-FIB was identical to PreT-SF-CONC except it was constructed with a prefabricated shell in the plastic hinge region made of a ductile fiber reinforced concrete, as

shown in Figure 4-8. The fiber mix is called Hybrid Fiber Reinforced Concrete (HyFRC) and it is a material that was developed at UC Berkeley (Ostertag et al. 2012). It contains both steel and polymers fibers that keep the compressive strength longer and increase the tensile strength over that of regular concrete (Ostertag et al. 2013). The reason for using a shell, rather than constructing the whole column from HyFRC is that the material is both expensive and difficult to work with.

The shell extended 29-in. high and it was located in the column elevation such that 4 in. were embedded into the cast-in-place foundation. The reason for having the shell embedded into the foundation was to avoid a predefined crack at the interface between the column and the spread footing. The thickness of the shell wall was 3.6 in. so the longitudinal bars were located in the HyFRC-portion of the column cross section. Since the structural performance of the PreT-CB-CONC and PreT-SF-CONC were identical, it was deemed unnecessary to test a column-to-cap beam connection of the system using HyFRC shell in the plastic hinge region.

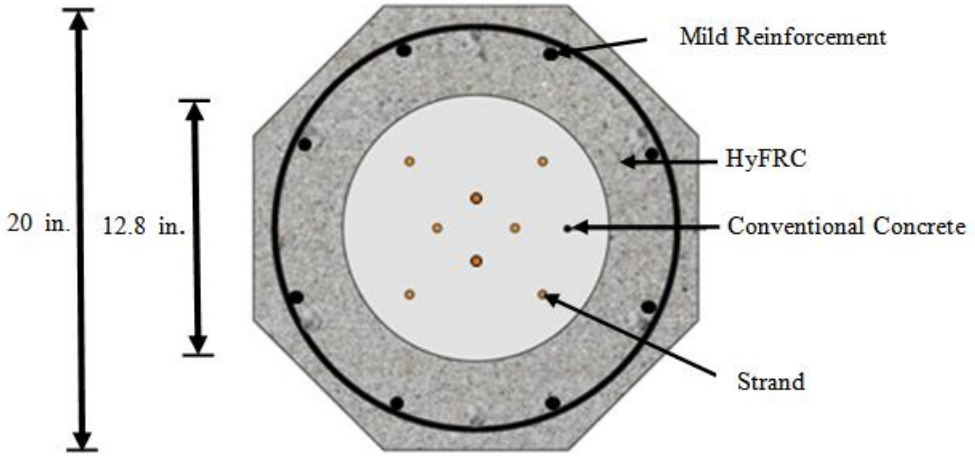

Figure 4-8. Schematic cross section of PreT-SF-FIB plastic hinge region (Finnsson et al. 2013)

4.2 Experimental Program

4.2.1 Loading Setup

Figure 4-9 shows the test-up for all the specimens. The specimens were placed inside a self-reacting frame. Horizontal loads were applied to the columns with a servo-controlled actuator with a capacity of 220 kips. The other end of the actuator was attached to a steel frame with two

vertical W20x94 beams, which were stiffened on each side with a diagonal HSS 6x6x3/8. Reactions were provided by a large concrete base on which either the cap beams or the spread footings rested to. The installation procedure for each specimen was the same. The specimen was lifted into the rig, leveled with shims and hydrostone was poured under the specimen, thus leaving specimen leveled on the reaction block. Finally, the base of the column (cap-beam or the spread footing) was post-tensioned to the block by using four 1-1/4 in. diameter William bars.

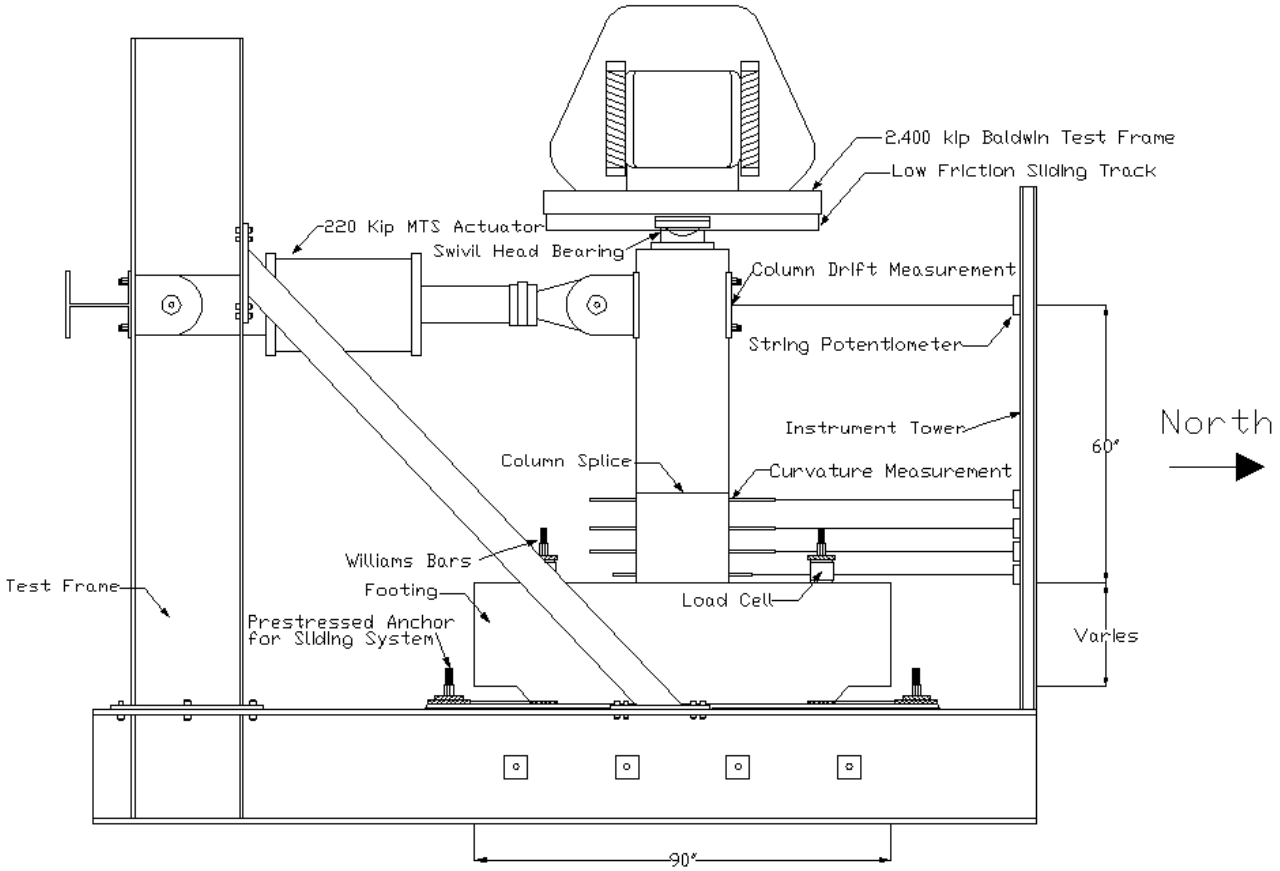

Figure 4-9. Typical test setup (Haraldsson et al. 2013)

Axial force on the column, other than the prestressing, was provided by the laboratory's 2.4-million lbs. Baldwin Universal Testing Machine. The force was transferred through a spherical bearing that slid against the Baldwin head, guided by a channel. To minimize the friction across the interface, stainless steel plates were placed in the channel and sheets of greased plythetrafluoroethyline (PTFEF) were glued to the top and the sides of the bearing.

4.2.2 Instrumentation

The responses of the specimens were monitored with load and displacement transducers on the exterior of the column and the foundation (cap-beam or spread footing), and by internal strain gauges. Where possible, locations of displacement transducers, string potentiometers, inclinometers and strain gauges were located as close as possible to the plan laid out originally by Pang et al. (2008) and modified for spread footings by Haraldsson et al. (2013). Load cells in the Baldwin Testing Machine and the MTS actuator captured the vertical and horizontal forces applied to the specimen.

Table 4-3 provides summary of instrumentation used in the test of each specimen. More detailed information can be found in Pang et al. 2008, Cohagen et al. 2008, Haraldsson et al. 2013, Davis et al. 2013 and Finnsson et al. 2013. Typically, linear potentiometers were used to capture the displacements of the specimen such as uplift (e.g., a precast column from a precast cap-beam) and to determine the rotations of the column at various heights. String potentiometers were located at various heights to determine horizontal displacements of the column relative to an independent, unloaded, instrumentation reference frame.

In all specimens, strain gauges were applied to the reinforcing, spirals and tendons where the largest strains were expected. Bars within the cap-beam and/or the spread footing were also equipped with strain gauges to determine the development of the bars.

A special motion capture system, Optotrak, was recently acquired by the University of Washington Structural Laboratory, so it was used only for the latest specimens.

Data was recorded using LabVIEW (Laboratory Virtual Instrument Engineering Workbench) from National Instruments.

Table 4-3. Summary of instrumentation used in all specimens

Specimen	MTS load cell	Baldwin load cell	Linear-potentiometer	String potentiometer	Inclino-meter	Strain gauges	Motion capture system
CIP-CB-REF	Used	Used	Used	Used	Used	Used	Not used
PCC-CB-FB	Used	Used	Used	Used	Used	Used	Not used
PCC-SF-THK1	Used	Used	Used	Used	Used	Used	Not used
PCC-SF-THK2	Used	Used	Used	Used	Used	Used	Not used
PosT-CB-LOPT	Used	Used	Used	Used	Used	Used	Not used
PosT-CB-HIPT	Used	Used	Used	Used	Used	Used	Not used
PreT-CB-CONC	Used	Used	Used	Used	Used	Used	Used
PreT-SF-CONC	Used	Used	Used	Used	Used	Used	Used
PreT-SF-FIB	Used	Used	Used	Used	Used	Used	Used

4.2.3 Test Protocol

All specimens used the same displacement history. The load history is a modification of the loading history for precast structural walls recommended by NEHRP (Building Seismic Council). The history consisted of sets of four cycles in which the peak amplitude was 1.2A, 1.4A, 1.4A, and 0.33A, respectively, where A is the peak amplitude of the previous set. The small amplitude cycle (0.33A) was intended to evaluate the residual small-displacement stiffness in the column after the set's peak amplitude. Table 4-4 lists the sets and cycles with their associated target displacements and drifts (drift is determined by dividing the target displacement by the clear height) and Figure 4-10 illustrates the displacement history. In Pang et al.'s, Haraldsson et al.'s, and Cohagen et al.'s research, the actuator moved from zero displacement to peak displacement in 20 seconds. In the other tests, the time was increased to 30 seconds from set 6 to 9 and finally to 60 seconds in set 10.

Table 4-4. Target displacement history

Set	Cycle	Drift Ratio (%)	Displ. (in.)
1	1	±0.33	±0.20
	2	±0.40	±0.24
	3	±0.40	±0.24
	4	±0.13	±0.08
2	1	±0.48	±0.29
	2	±0.58	±0.35
	3	±0.58	±0.35
	4	±0.19	±0.12
3	1	±0.69	±0.41
	2	±0.83	±0.50
	3	±0.83	±0.50
	4	±0.28	±0.17
4	1	±1.00	±0.60
	2	±1.19	±0.72
	3	±1.19	±0.72
	4	±0.40	±0.24
5	1	±1.43	±0.86
	2	±1.72	±1.03
	3	±1.72	±1.03
	4	±0.57	±0.34
6	1	±2.06	±1.24
	2	±2.48	±1.49
	3	±2.48	±1.49
	4	±0.83	±0.50
7	1	±2.97	±1.78
	2	±3.57	±2.14
	3	±3.57	±2.14
	4	±1.19	±0.71
8	1	±4.28	±2.57
	2	±5.14	±3.08
	3	±5.14	±3.08
	4	±1.71	±1.03
9	1	±6.16	±3.70
	2	±7.40	±4.44
	3	±7.40	±4.44
	4	±2.47	±1.48
10	1	±8.87	±5.32
	2	±10.65	±6.39
	3	±10.65	±6.39
	4	±3.55	±2.13

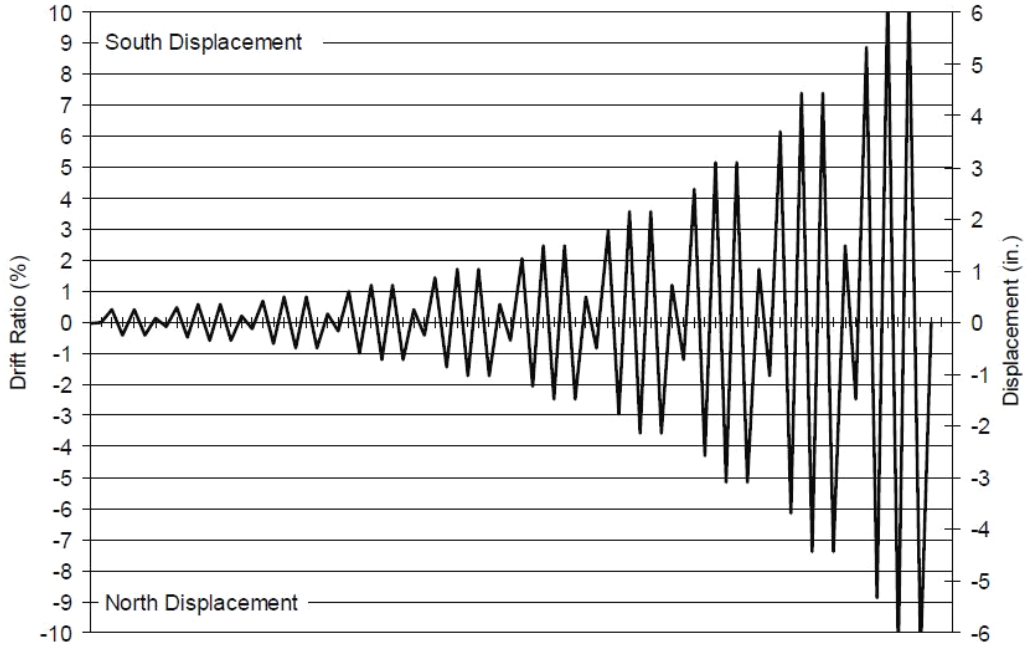

Figure 4-10. Lateral loading displacement history (Pang et al. 2008)

4.3 Damage Progression

The progression of damage throughout each test was recorded with sketches, measurements of cracks widths and extensive photography (Pang et al. 2008, Cohagen et al. 2008, Haraldsson et al. 2013, Davis et al. 2012, Finnsson et al. 2013).

4.3.1 Damage Observation

All the specimens were carefully monitored using predefined damage states, as defined by the UW/PEER Column Database (Berry and Eberhard 2004). This approach provides an easy and systemic way to compare the performances of several specimens. Table 4-5 lists and defines each of the damage state, and furthermore, provides information for all the specimens when particular damage state was reached.

For convenience, Figure 4-11 compares all the nine specimens only in terms of significant spalling (spall height is greater or equal than ¼ of column diameter), first longitudinal buckling and first bar fracture. Significant spalling did not occur below 2% column drift in any specimen and it ranged from 2.15% drift (in Specimen PCC-CB-FB) to 3.2% drift (in Specimen PreT-SF-CONC). First longitudinal buckling was reported as soon as it became visible for the naked eye.

In the non-prestressed specimens (CIP-CB-REF, PCC-CB-FB, PCC-SF-THK1 and THK2), first longitudinal bar buckling became visible after 4.6% drift. It should be noted that in the two PCC-SF-THKs columns bar buckling might have initiated earlier than what is reported. The buckling became visible later because of the thick concrete cover that was used. The standard testing practice was just to brush aside the debris and clear away spalls that required minimal force.

When the specimens are compared in terms of first longitudinal bar fracture, significant difference can be observed. All but the pre-tensioned specimens (PreTs) had their first bar fracture above 6% drift. The pre-tensioned specimens had their first bar fracture at about 4% drift. The difference between them and the others is that their longitudinal bar size was No. 4 while the closest one (PosT-CB-HIPT) had bars of size No. 6. It is also worth mentioning is that the first bar buckling in PreT-SF-FIB is observed after the first bar fracture. This peculiar line of damage progression was because of the HyFRC-fiber shell. Even though the shell was deteriorating throughout the test program, it was difficult to clean away the spalls because they were held into the column by the steel and plastic fibers in the concrete.

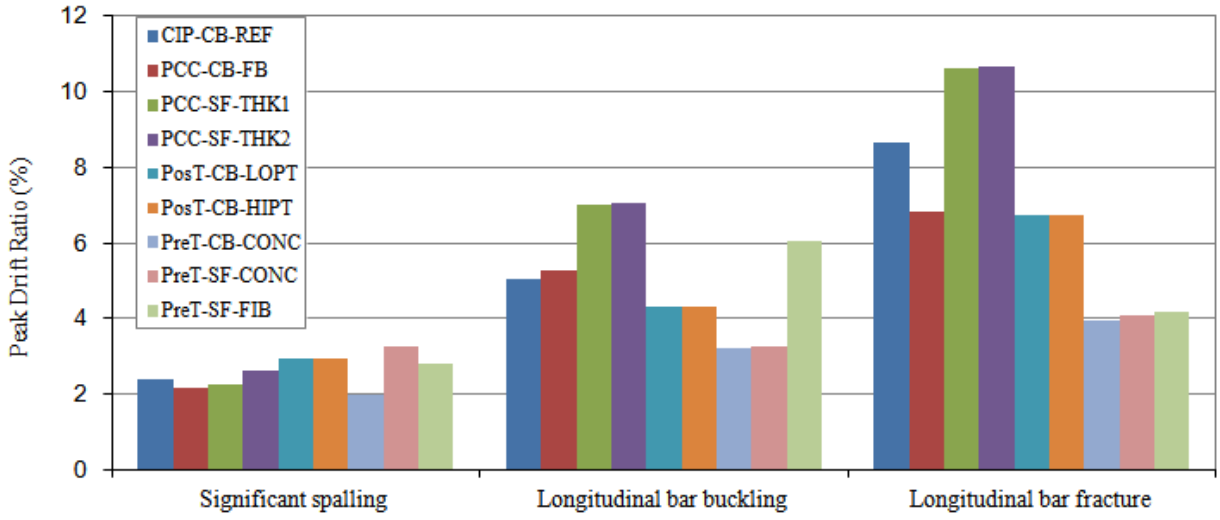

Figure 4-11. Comparison of specimens' drift ratios for selected major damage states

Table 4-5. Damage state progression for all specimens

Damage Event	CIP-CB-REF		PCC-CB-FB		PCC-SF-THK1		PCC-SF-THK2		PosT-CB-LOPT		PosT-CB-HIPT		PreT-CB-CONC		PreT-SF-CONC		PreT-SF-FIB	
	Set-Cycle	Drift (%)	Set-Cycle	Drift (%)	Set-Cycle	Drift (%)	Set-Cycle	Drift (%)	Set-Cycle	Drift (%)	Set-Cycle	Drift (%)	Set-Cycle	Drift (%)	Set-Cycle	Drift (%)	Set-Cycle	Drift (%)
First significant horizontal crack (Crack width ≥ 0.5 mm)	4-4	0.86/ -0.95	3-4	0.51/ -0.53	4-1	0.69	3-2	0.56	3-4	0.53/ -0.58	5-1	1.09/ -1.18	3-2	0.44/ -0.69	3-1	0.52/ -0.64	3-1	0.46/ -0.62
First significant diagonal crack (Diagonal crack extends 1/4 of column diameter. Crack width ≥ 0.5mm)	5-1	1.12/ -1.22	5-1	1.05/ -1.10	6-1	1.68/ -1.80	6-1	1.74	4-4	-1.43	6-4	4.17	5-2	1.2/ -1.52	6-2	2.1/ -2.3	6-2	2.24/ -2.36
First open residual crack (Residual crack width ≥ 0.25 mm)	5-4	1.45/ -1.55	5-4	1.69/ -1.76	6-1	1.68/ -1.80	4-3	0.88/ -0.95	6-1	1.80/ -1.84	6-1	1.81/ -1.90	5-1	0.96/ -1.26	4-2	0.89/ -0.98	4-1	0.73/ -0.88
First yield of longitudinal reinforcement	3-4	0.48	N/A	N/A	3-2	0.55	3-2	0.47	3-4	0.41	3-4	-0.58	1-3	-0.33	2-1	-0.28	3-1	0.46/ -0.62
First yield of transverse reinforcement	N/A	N/A	N/A	N/A	8-2	-4.63	9-1	-4.93	N/A	N/A	N/A	N/A	7-1	-2.74	7-1	-2.63	5-2	1.46/ -1.61
First spalling in footing or cap beam (Observed spalling on surface)	None	None	6-2	1.72/ -1.78	None	None	None	None	None	None	None	None	None	None	None	None	None	None
First spalling in column (Observed flaking, minor spalling)	5-4	1.44/ -1.56	6-2	1.72/- 1.78	5-1	1.07/ -1.21	5-1	1.10/ -1.19	5-4	1.41/ -1.46	6-2	1.81/ -1.85	5-1	0.96/ -1.26	5-1	1.1/ -1.2	5-2	1.46/ -1.61
Significant spalling in column (Spalled height ≥ 1/4 of column diameter)	6-4	2.35/ -2.45	6-4	2.15/ -2.20	6-2	-2.25	7-1	2.64	7-1	2.82/ -2.86	7-1	2.95/ -2.94	7-1	2.5/ -2.8	7-3	3.2/ -3.3	7-1	2.77/ -2.88
Full spalling in column (Spalling height no longer increases with increasing deformation)	7-4	3.70/ -3.72	8-4	5.42/ -5.10	9-3	7.08/ -6.90	8-1	3.98	10-1	10.07/ -3.52	8-4	-5.38	9-1	6/ -6.1	9-3	7.4/ -7.3	9-1	6.07/ -6.01
Exposure of longitudinal reinforcement (First observation of column longitudinal reinforcement)	7-4	3.70/ -3.72	7-2	2.92/ -2.85	9-1	-5.68	9-2	-6.85	7-4	3.51/ -3.52	6-4	4.17	7-2	3.1/ -.34	7-3	3.2/ -3.33	8-1	2.32/ -2.47
Buckling of longitudinal reinforcement (First observation of column longitudinal bar buckling)	8-4	4.56/ -5.52	8-4	5.42/ -5.10	9-2	7.09/ -6.88	9-3	7.19/ -6.88	8-2	4.45	6-1	-4.32	7-3	3.1/ -3.3	7-3	3.2/ -3.33	9-1	6.07/ -6.01
Large cracks in concrete core (Crack width ≥ 2.0 mm)	8-1	4.56/ -4.52	8-1	4.31/ -4.12	10-2	10.61	10-2	-9.95	None	None	None	None	N/A	N/A	9-3	7.4/ -7.3	9-1	6.07/ -6.01
Fracture of transverse reinforcement (Observation or sound)	7-4	5.60/ -5.52	9-1	6.69/ -6.24	9-2	-6.88	10-1	-8.29	8-4	-5.32	8-4	-5.38	N/A	N/A	N/A	N/A	10-1	8.90/ -8.66
Fracture of longitudinal reinforcement (Observation or sound)	9-4	8.83/ -8.44	9-2	6.81	10-2	10.61	10-2	10.65	9-1	6.74	9-1	6.75	8-1	3.8/ -4.1	8-1	4.0/ -4.2	8-1	4.14/ -4.23
Loss of axial capacity (Instability of member)	None	None	None	None	None	None	None	None	None	None	None	None	None	None	None	None	None	None

4.4 Measured Response

Figures from 4-12 to 4-20 show the normalized moment plotted against the drift ratio for all UW specimens. The measured moments are normalized by dividing by the corresponding nominal moment M_{no}using measured material properties. The M_{no} for the prestressed specimens was calculated by using the initial prestressing force. Table 4-6 reports for each specimen:

- the secant stiffness at first yield in north (negative drift value) and south (positive drift value), using the orientation of the self-reacting frame in the UW Structural Laboratory,
- the maximum moment in north and south directions, and their corresponding drift ratio,
- 80% of the maximum moment in both directions and their corresponding drift ratio, and
- M_{no} that was used to normalize them.
- The definition of drift failure used here is taken as that at which the effective lateral load drops to 80% of the maximum resistance obtained earlier in the test.

The specimens shared common features (e.g., post-tensioned columns with conventional concrete in the plastic hinge region) that resulted in a similar characteristic structural response. They can be grouped into four categories:

- **Non-prestressed.** Specimens CIP-CB-REF, PCC-CB-FB, PCC-SF-THK1, and PCC-SF-THK2 with conventional concrete.
- **Post-tensioned CONC.** Specimens PosT-CB-LOPT and PosT-CB-HIPT with conventional concrete in the plastic hinge region.
- **Pre-tensioned CONC.** Specimens PreT-CB-CONC and PreT-SF-CONC with conventional concrete in the plastic hinge region.
- **Pre-tensioned FIB.** Specimen PreT-SF-FIB with HyFRC concrete in the plastic hinge region.

Figures from 4-12 to 4-20 show that all the columns performed similarly up to about 3.0% drift. However as expected, the prestressed columns were stiffer than the non-prestressed columns. Stiffness at first yield is reported in Table 4-6. The pre-tensioned specimens were detailed to have the same strength as the non-prestressed specimens PCC-SF-THKs. Pre-tensioned specimens with conventional concrete showed greater stiffness at first yield compared

to specimens PCC-SF-THK1 and PCC-SF-THK2. However, the pre-tensioned specimen with HyFRC in the plastic hinge region showed similar stiffness as specimens PCC-SF-THKs. First yield of the longitudinal reinforcement in Specimen PreT-SF-FIB was experienced later than observed in the testing of the pre-tensioned columns with conventional concrete (Table 4-5).

Table 4-6 shows that the maximum moment in all specimens was achieved at drifts between about 1.5% and 4.0% drift. In general, the prestressed (post and pre-tensioned) columns with conventional concrete in the plastic hinge reached their maximum moment at a lower drift level than the non-prestressed specimens because the column concrete started to crush early due to the additional axial load from the prestressing. The non-prestressed columns peaked at a larger drift ratio than the prestressed columns,with conventional concrete in the plastic hinge region, or on an average at a drift ratio of 2.80%. They were less stiff than the prestressed columns so they were able to be cycled to larger drift ratios before concrete started to crush. The pre-tensioned column with fiber concrete (HyFRC) in the plastic hinge region peaked last of all specimens or at a drift ratio of 3.40%. The performance of PreT-SF-FIB was expected because the HyFRC mix is a ductile material that has been shown to keep compressive strength longer and has a higher tensile strength than conventional concrete (Ostertag et al. 2013). Table 4-5 shows that by including a HyFRC shell in the plastic hinge region the first spalling milestone was slightly delayed from what was observed in the pre-tensioned specimens with conventional concrete in the plastic hinge region (PreT-CB-CONC and PreT-SF-CONC).

As the columns were cycled more, a plastic hinge started to form and the column longitudinal bars experienced larger inelastic strains and stress reversals. According to the failure definition, the non-prestressed columns maintained strength (above 80% of the peak resistance) to an average drift of 6.81% drift. The prestressed specimens with conventional concrete in the plastic hinge region maintained on average strength to 4.80% drift. If that drift value is compared to the non-prestressed specimens' performance, it may seem low but "for many bridges, the drift ratio expected to be reached in the Design Basis Earthquake (DBE) is approximately 1.50% to 2.0%. In the Maximum Considered Earthquake (MCE), it might be 3.0% drift. At that drift ratio, the lateral resistance of each of these columns was still above 90% of its peak moment" (Davis et al. 2012). The prestressed column with HyFRC in the plastic hinge region (PreT-SF-FIB) showed superior structural performance compared to all other specimens (especially specimens

PreT-CB-CONC and PreT-SF-CONC). By including a HyFRC shell in the plastic hinge region, which includes steel and polymer fibers, the specimen maintained strength (above 80% of the peak resistance) throughout the whole test program, even though bars had fractured.

The prestressed and non-prestressed specimens displayed different hysteresis responses. By including prestressing, the overall hysteresis response becomes more pinched during unloading from a peak displacement to a zero displacement (i.e., the hysteresis crosses from a positive moment to a negative moment at a displacement closer to zero, and the other way around). The prestressing is "assisting" the specimen to return back to vertical. Referring to Table 4-1 (i.e., re-centering ratio column) and comparing the hysteresis responses, it can be observed that the hysteresis pinching gets more pronounced with an increasing re-centering ratio. This behavior can be seen by comparing PCC-SF-THKs with re-centering ratio equal to 0.73, to the pre-tensioned specimens (PreT-CB-CONC, PreT-SF-CONC, and PreT-SF-FIB) that had a re-centering ratio of 3.1.

Table 4-6. Moment and drift ratio at peak resistance and failure for all specimens

Point of Interest	Non-Prestressed								Post-Tensioned CONC[2]				Pre-Tensioned CONC				Pre-Tensioned FIB[3]	
	CIP-CB-REF		PCC-CB-FB		PCC-SF-THK1		PCC-SF-THK2		PosT-CB-LOPT		PosT-CB-HIPT		PreT-CB-CONC		PreT-SF-CONC		PreT-SF-FIB	
	North dir.	South dir.	North dir.	South dir.	North dir.	South dir.	North dir.	South dir.	North dir.	South dir.	North dir.	South dir.	North dir.	South dir.	North dir.	South dir.	North dir.	South dir.
Secant stiffness at initial yield (kip/in.)	N/A	183.6	N/A[3]	N/A[3]	108	114	116	132	N/A	170.2	140.2	N/A	180	175	225	199	128	116
Maximum column base moment (kip-in.)	-4,428	4,548	-4,806	4,830	-3,073	3,091	-3,114	3,065	-4,110	4,324	-3,809	3,919	-2,957	3,085	-2,533	2,843	-2,717	2,703
Drift ratio at maximum column moment (%)	-3.00	4.50	-3.80	3.70	-2.61	1.95	-1.45	1.38	-2.83	2.78	-1.90	4.12[1]	-2.76	1.55	-2.25	1.38	-3.45	3.35
80% of maximum column base moment (kip-in.)	-3,540	3,636	-3,846	3,864	-2,458	2,473	-2,490	2,452	3,288	3,459	-3,047	3,135	-2,366	2,468	-2,027	2,274	-2,190	2,180
Drift ratio at 80% base column moment (%)	-5.60	6.90	-5.80	6.70	-6.80	7.10	-6.90	8.70	-5.32	5.44	-4.29	4.34	-4.10	3.84	-4.94	6.10	< -9.93	> 10.39
Nominal moment, Mno (kip-in.)	3,815		3,697		2,576		2,613		3,247		3,063		2,439		2,439		2,609	
Ave. drift ratio at maximum column moment (%)	2.80								2.91				1.99				3.40	
Ave. drift ratio at 80% base column moment (%)	6.81								4.85				4.75				>10.16	

1. PosT-CB-LOPT experienced accidental “overload”.
2. PreT-SF-FIB maintained strength throughout test program.
3. Gauges damaged

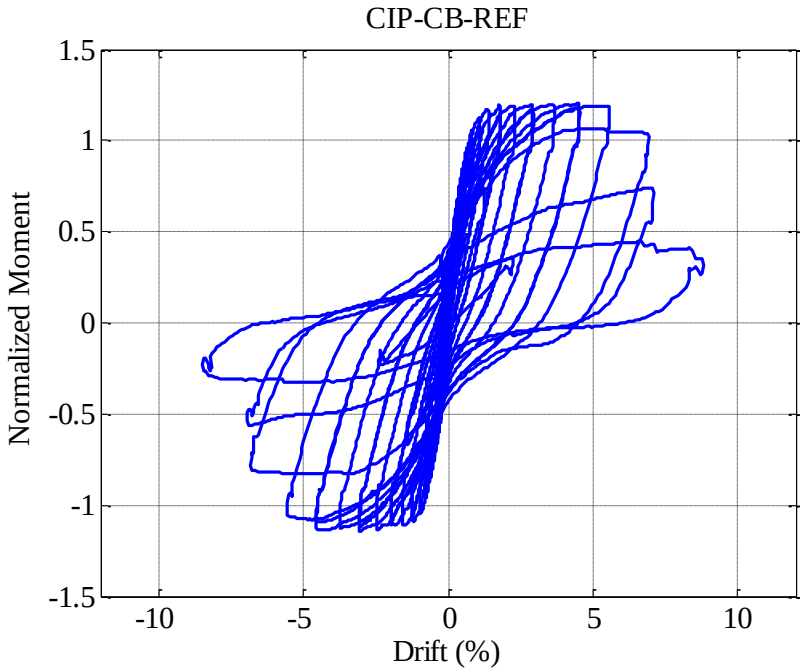

Figure 4-12. P-CB-REF normalized moment-drift response ($\boldsymbol{M_{no}}$ = 3,815 kip-in.)

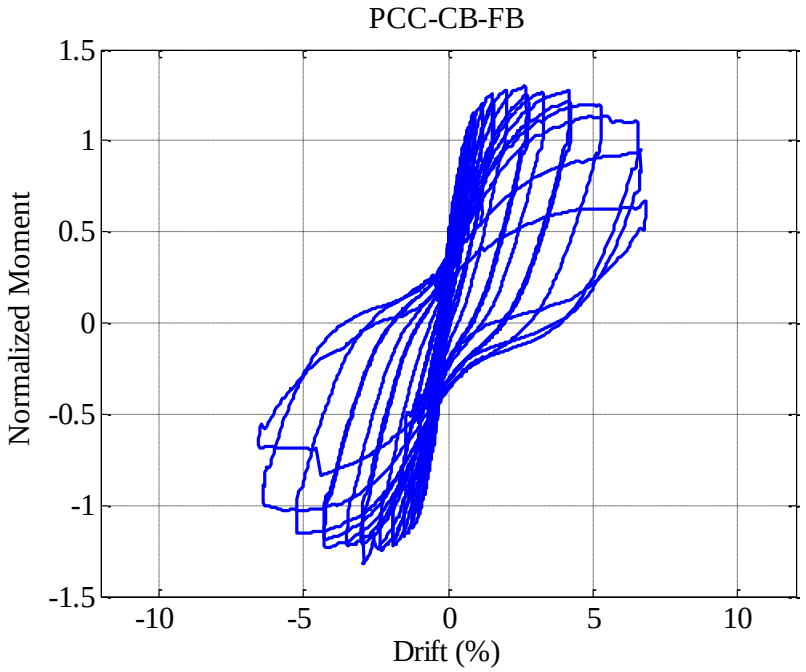

Figure 4-13. PCC-CB-FB normalized moment drift-response ($\boldsymbol{M_{no}}$ = 3,697 kip-in.)

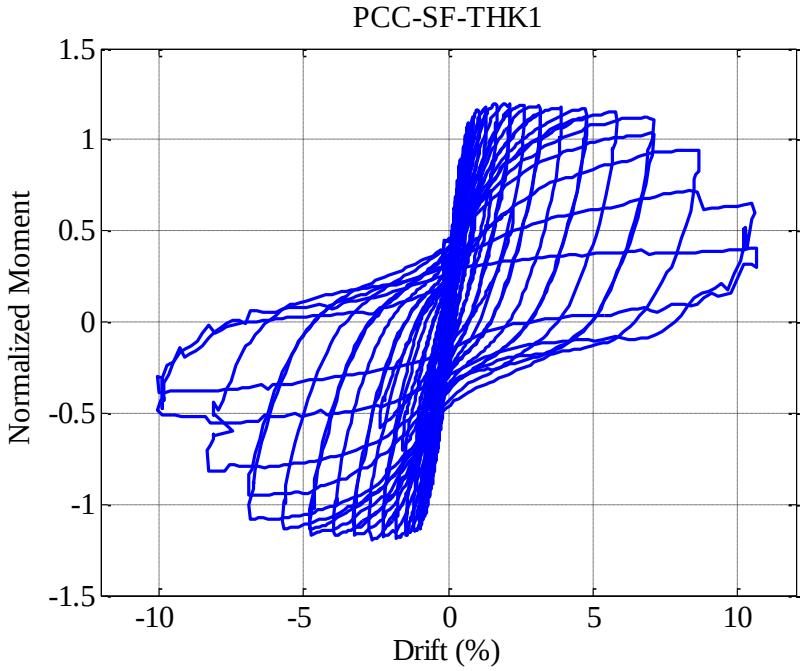

Figure 4-14. PCC-SF-THK1 normalized moment drift-response ($\boldsymbol{M_{no}}$ = 2,576 kip-in.)

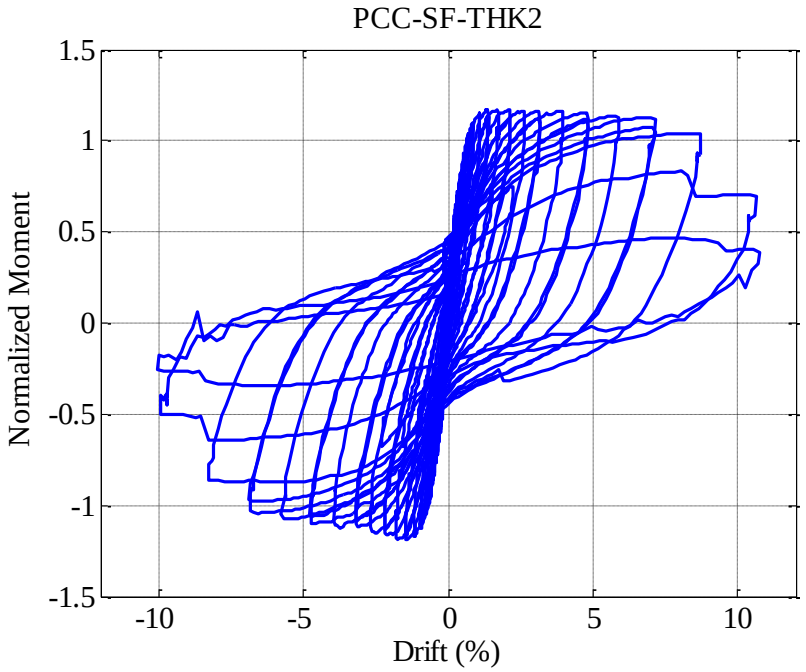

Figure 4-15. PCC-SF-THK2 normalized moment-drift response ($\boldsymbol{M_{no}}$ = 2,613 kip-in.)

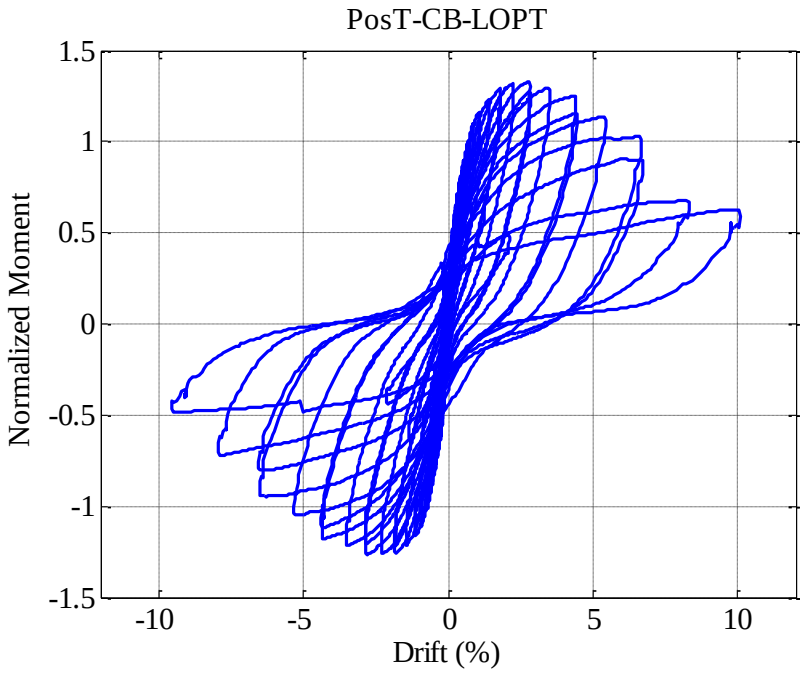

Figure 4-16. PosT-CB-LOPT normalized moment-drift response (M_{no} = 3,247 kip-in.)

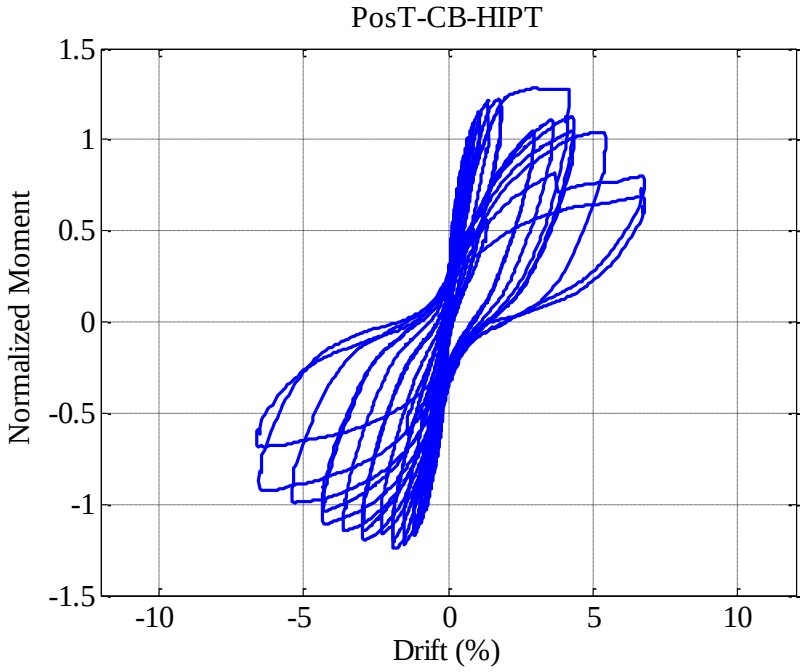

Figure 4-17. PosT-CB-HIPT normalized moment-drift response (M_{no} = 3,063 kip-in.)

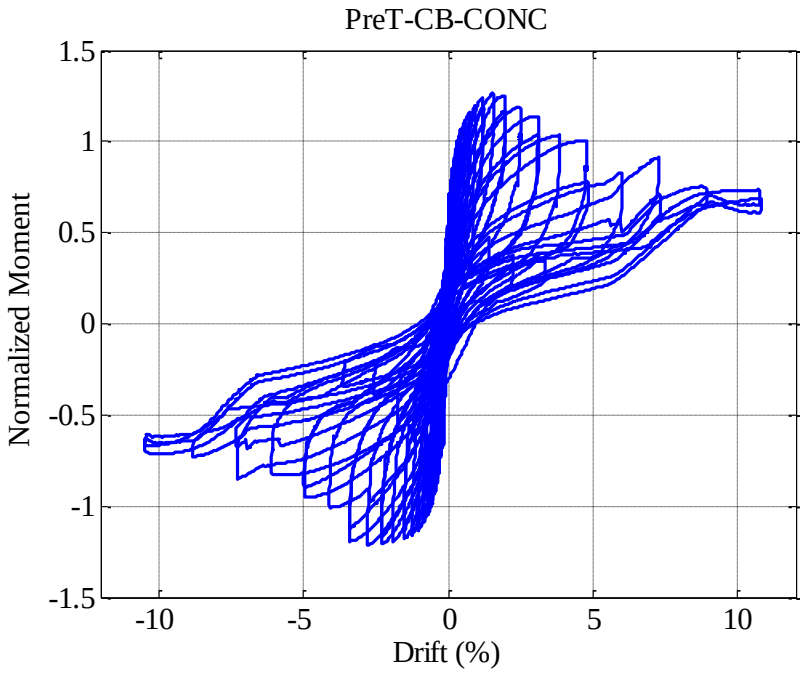

Figure 4-18. PreT-CB-CONC normalized moment-drift response (M_{no} = 2,439 kip-in.)

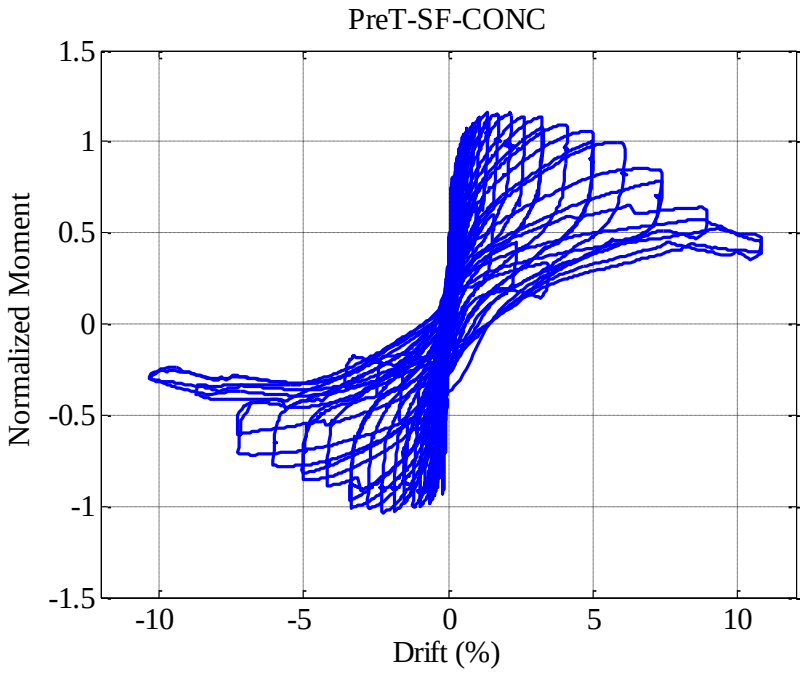

Figure 4-19. PreT-SF-CONC normalized moment-drift response (M_{no} = 2,439 kip-in.)

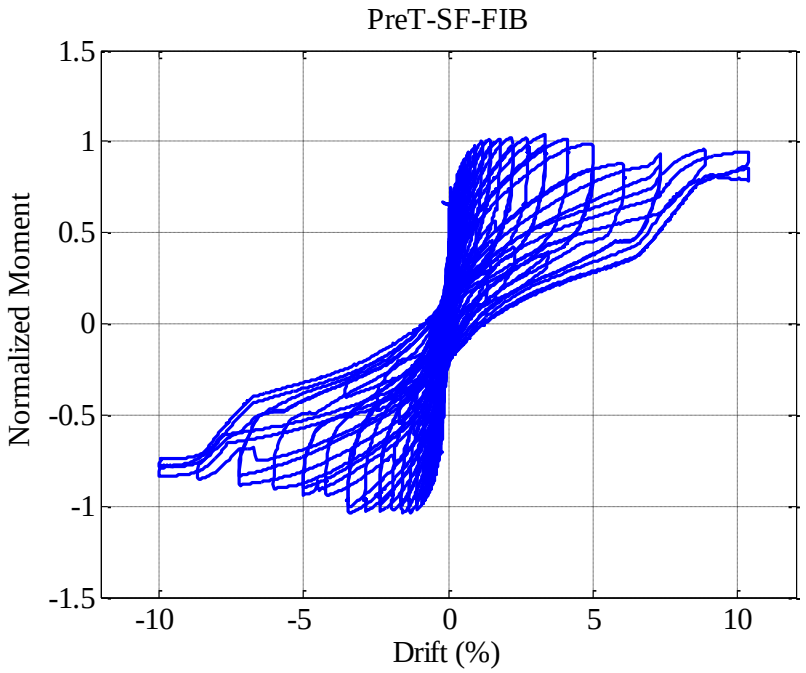

Figure 4-20. PreT-SF-FIB normalized moment-drift response ($\boldsymbol{M_{no}}$ = 2,609 kip-in.)

4.5 Evaluation of Test Results

In this section, the specimens are compared in terms of strength degradation, energy dissipation, equivalent viscous damping, and their tendency to re-center to their original plumb position, after being displaced from their original configuration.

4.5.1 Strength Degradation

Figure 4-21 compares the envelopes of all nine specimens in terms of normalized effective force versus drift ratio. The envelopes are normalized using the peak effective force in each direction separately. A positive drift ratio indicates displacement to the south. For convenience, the curves are plotted with fewer data-markers for clarity and solid thick black lines are added to show the 80% of the maximum effective force.

At the beginning of the loading history, the prestressed specimens were stiffer than non-prestressed specimens due to the prestressing force, as anticipated. All specimens reached their

peak resistance between 1.38% and 4.50% drift in the positive direction and between 1.45% and -3.80% for negative drift, as listed in Table 4-6.

Overall, the non-prestressed specimens (CIP-CB-REF, PCC-CB-FB, PCC-SF-THK1, PCC-SF-THK2) maintained strength better than both the post-tensioned and pre-tensioned columns with conventional concrete in the plastic hinge region (PosT-CB-LOPT, PosT-CB-HIPT, PreT-CB-CONC, and PreT-SF-CONC). On average in both directions, the non-prestressed specimens maintain strength above 80% peak lateral resistance beyond 6% drift. Shortly after the post- and pre-tensioned columns with conventional concrete in the plastic hinge region had reached peak lateral resistance, they began losing strength. On average, the post-tensioned specimens PosT-CB-LOPT and PosT-CB-HIPT maintained strength above 80% of the peak lateral resistance to drifts of 5.38% and 4.32%, respectively. PreT-CB-CONC and PreT-SF-CONC differed in terms of maintaining strength. PreT-SF-CONC maintained strength to about 5.0% drift while PreT-CB-CONC to about 4.0% drift.

Figure 4-22 compares the performance of pre-tensioned specimen with HyFRC shell in the plastic hinge region (Specimen PreT-SF-FIB) to the other column groups. The figure shows average drifts for when the maximum effective and the 80% of the maximum effective forces were achieved, as outlined in Section 4.4 and in Table 4-6. It can be seen that by including a HyFRC shell in the plastic hinge region the structural performance of the pre-tension system improves from just having conventional concrete. The specimen retained strength above 80% of the maximum strength throughout the test program, in which the largest drift ratio was greater than 10%.

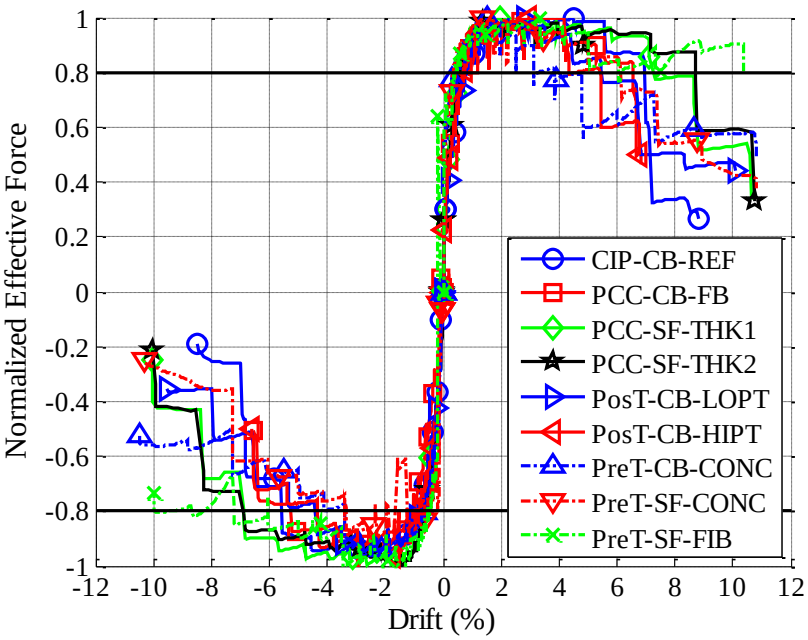

Figure 4-21. Normalized effective force-drift for all UW specimens

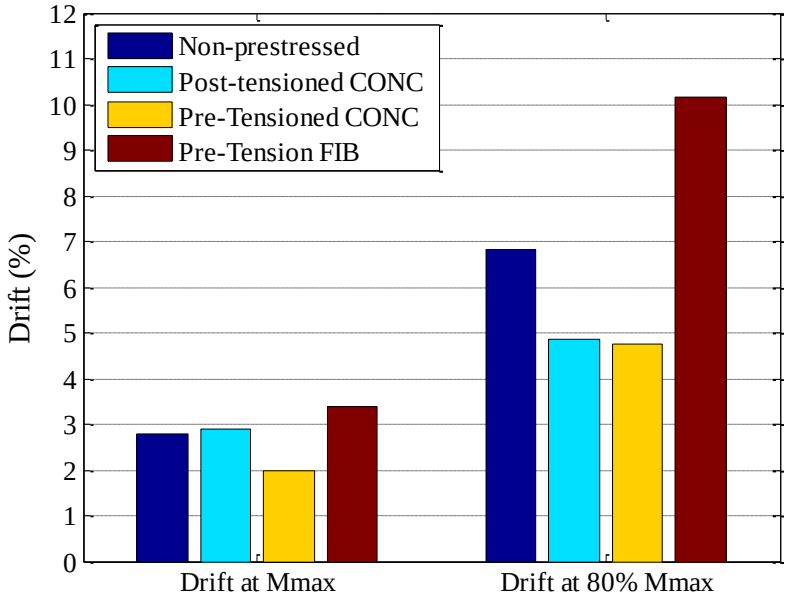

Figure 4-22. Drift comparison between four groups of column at maximum effective force and at 80% of the maximum effective force

4.5.2 Energy Dissipation

The energy dissipation is the area inside the force-displacement curve and provides a means to compare the damping potential of a particular system. It was calculated in this research by using the trapezoidal integration scheme given in Equation 4-2:

$$\boldsymbol{E_{cycle}} = \sum_{i}^{n} \frac{\boldsymbol{F_{i+1}+F_i}}{\mathbf{2}} (\boldsymbol{\Delta_{i+1} - \Delta_i}) \qquad 4\text{-}2$$

Figure 4-23 compares energy dissipated in each cycle for all specimens. For plotting purposes, instead of talking about sets and cycles on the horizontal axis, the cycles are numbered continuously from the beginning of the test. The tests consisted of sets of four cycles with the peak amplitudes of 1.2A, 1.4A, 1.4A, and 0.33A, where A is the peak amplitude of the previous cycle set. The sets are visible as "humps" in Figure 4-23. The same information is shown in Figure 4-24 but is expressed in energy dissipated versus cumulative drift. It is important to note that not all the specimens completed displacement history shown in Table 4-4, thus not all of them are plotted to cycle no. 40 (or cumulative target drift of 107%). Furthermore, the number of data-markers is reduced for clarity.

Figures 4-25 and 4-26 compare the cumulative energy dissipation versus cycle number and versus cumulative target drift for all the specimens. The figures provide essentially the same information about the energy dissipation but in cumulative format. Instead of plotting lines between data-markers for each specimen, average cumulative energy dissipation curves are shown instead for the non-prestressed specimens, the post-tensioned specimens, and the pre-tensioned specimens with concrete in the plastic hinge region. The pre-tensioned specimen with HyFRC in the plastic hinge region is shown with its own curve, as only one specimen with HyFRC was tested. At small displacements, the energy dissipation was similar for all specimens but after 20 cycles a noticeable difference can be seen between the four groups. This is attributed to different amounts of longitudinal mild reinforcement in each column.

Figure 4-27 compares the cumulative energy versus specimens' longitudinal mild reinforcement at a cumulative target drift of 56.6% (i.e., Cycle 33 in Table 4-4). The figure shows that the non-prestressed specimens dissipated the most energy. The non-prestressed

specimens were followed after by the post-tensioned specimens. Non-prestressed specimens PCC-SF-THK1 and PCC-SF-THK2 had a similar longitudinal reinforcement ratio to the post-tensioned Specimen PosT-CB-LOPT, about 1.1%. These three specimens were expected to dissipate energy similarly. However, Specimen PosT-CB-LOPT experienced first bar fracture in the preceding cycle (i.e., Cycle 32) and thus dissipated less energy afterwards than specimens PCC-SF-THK1 and PCC-SF-THK2.

The pre-tensioned specimens (PreT-CB-CONC, PreT-SF-CONC, and PreT-SF-FIB) dissipated the least energy of all, as they had the lowest mild longitudinal mild reinforcement ratio. Figure 4-25 shows that the pre-tensioned specimens dissipated energy similarly up to Cycle 25. In cycles 36 to 40, Specimen PreT-SF-FIB dissipated slightly more energy than those with conventional concrete (PreT-CB-CONC and PreT-SF-CONC). At this point in the tests, the pre-tensioned specimens with conventional concrete were almost fully spalled. In comparison, Specimen PreT-SF-FIB was rocking about one big crack that had formed earlier in the test with the cover still present. The cover was held in by the steel and the polymer fibers in the concrete mix.

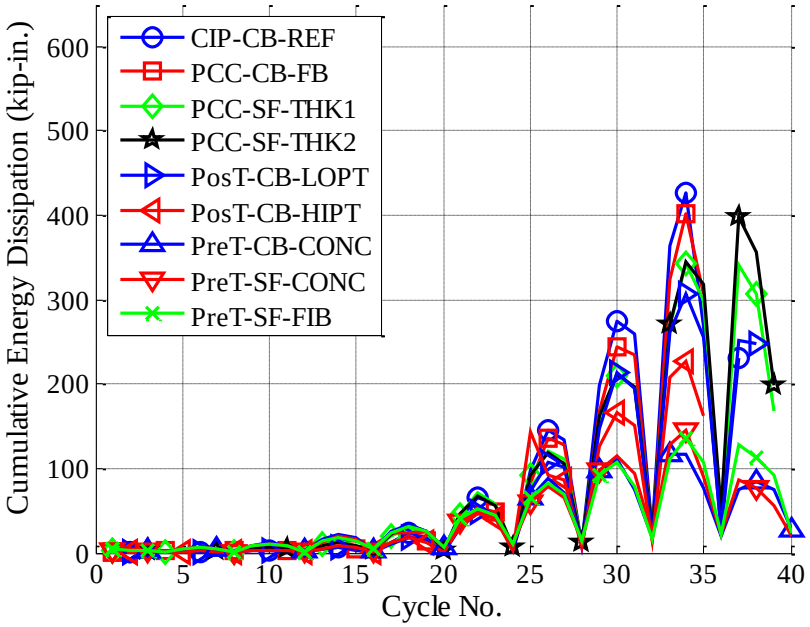

Figure 4-23. Energy dissipation-cycle number for all UW specimens

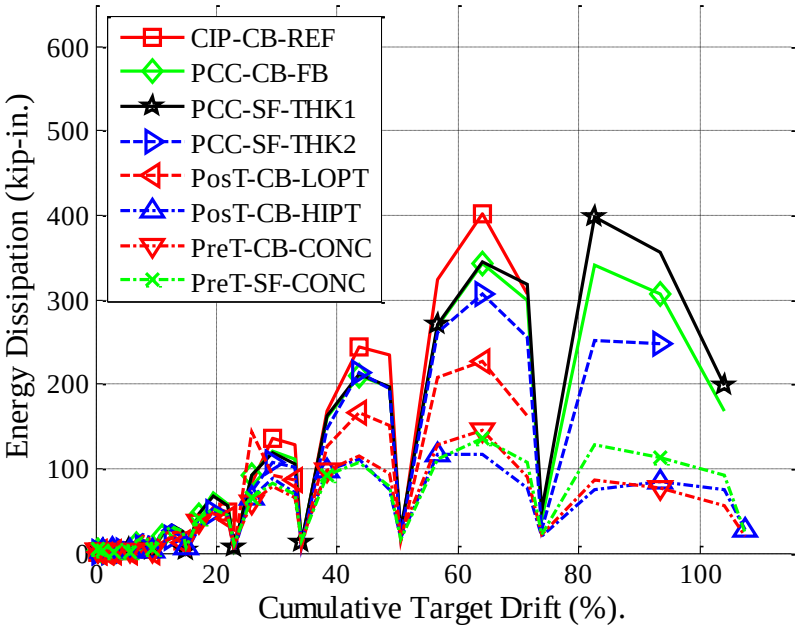

Figure 4-24. Energy dissipation-cumulative target drift for all UW specimens

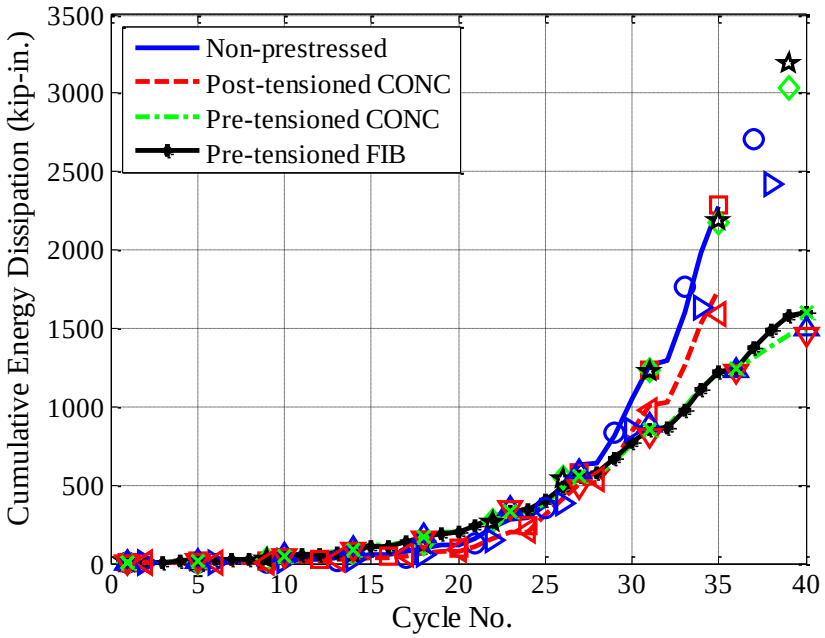

Figure 4-25. Cumulative energy dissipation-cycle no. for all UW specimens

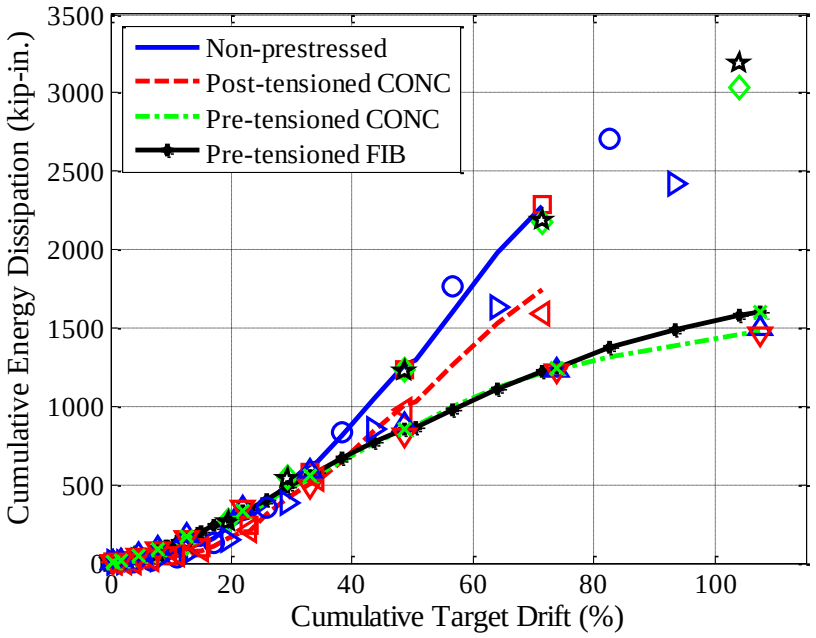

Figure 4-26. Cumulative energy dissipation-cumulative target drift for all UW specimens

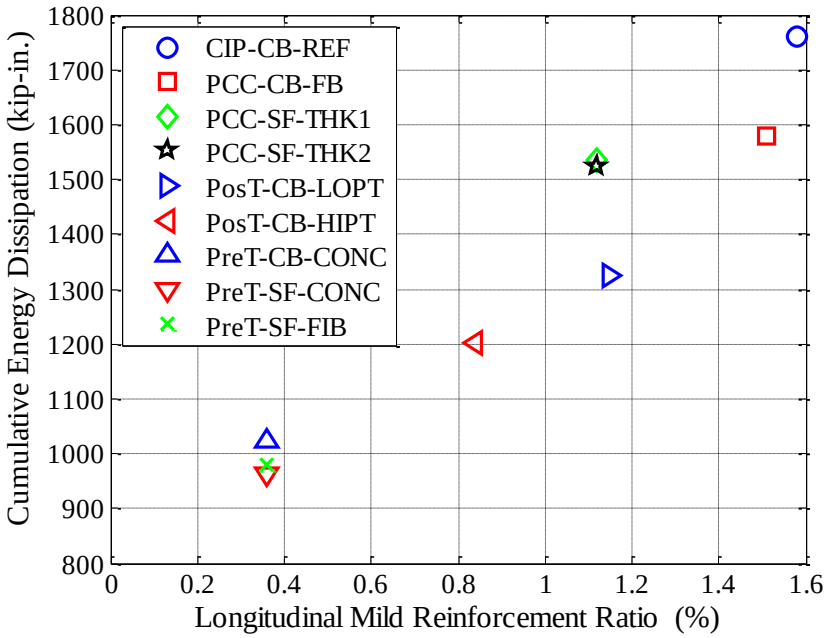

Figure 4-27. Cumulative energy dissipation-mild reinforcement ratio at cumulative target drift of 56.6% (Cycle 33) for all UW specimens

4.5.3 Equivalent Viscous Damping

Figures 4-28 and 4-29 present calculated equivalent viscous damping versus cycle number and versus drift ratio, respectively. The calculations are done only for the largest cycle in each set (cumulative cycles 2, 6, 10, 14, etc). This was done because friction correction errors, to account for the friction between the spherical bearing and the sliding channel attached to the Baldwin Universal Testing Machine, were greatest at small drifts. Throughout the test program in all specimens, the friction was relatively constant.

The equivalent damping was calculated using Equation 4-3:

$$\zeta_{eq} = \frac{2}{\pi}\left(\frac{A_{loop}}{A_{rectangle}}\right) \quad 4\text{-}3$$

where $A_{loop}$is the cycle energy and $A_{rectangle}$ is the area circumscribing the loop.

Figure 4-28 shows average equivalent damping for the versus cycle number. In the figure, four curves are shown and they represent the average equivalent damping for the three groups; non-prestressed, post-tensioned, and pre-tensioned specimens with concrete in the plastic hinge. As before, a single curve represents the pre-tensioned specimen with HyFRC. Figure 4-29 shows the same information except it is plotted against drift ratio.

All three pre-tensioned specimens (PreT-CB-CONC, PreT-SF-CONC, and PreT-SF-FIB) consistently had damping ratios in the range from 0.10 to 0.15 throughout the test program. These results from the pre-tensioned specimens are consistent with what is reported in literature. Priestly et al. (2007) report that the damping ratio in a typical hybrid connection is approximately 0.10. In contrast to the pre-tensioned specimens, all other specimens had a lower damping value below at drifts below 1%, which was unexpected. This is shown in Figure 4-29. Damping is influenced by yielding of the mild reinforcement and might explain the difference. The earlier the mild reinforcement starts to yield, the more the column should dissipate energy. In fact, Davis et al. (2012) report that as a potential explanation. Pre-tensioned specimens with conventional concrete (PreT-CB-CONC and PreT-SF-CONC) experienced first yield at lower drifts than 0.40% but in all other specimens, including the pre-tensioned specimens with HyFRC,

this milestone was achieved at higher drifts or at about 0.50%. Specimen PreT-SF-FIB is closest to other specimens but does not go at low drifts below equivalent damping of 0.10.

At large drifts, higher than 3% drift, all other specimens have a damping ratio higher than the pre-tensioned specimens (with and without HyFRC), as was expected due to the amount of mild reinforcement there was in them.

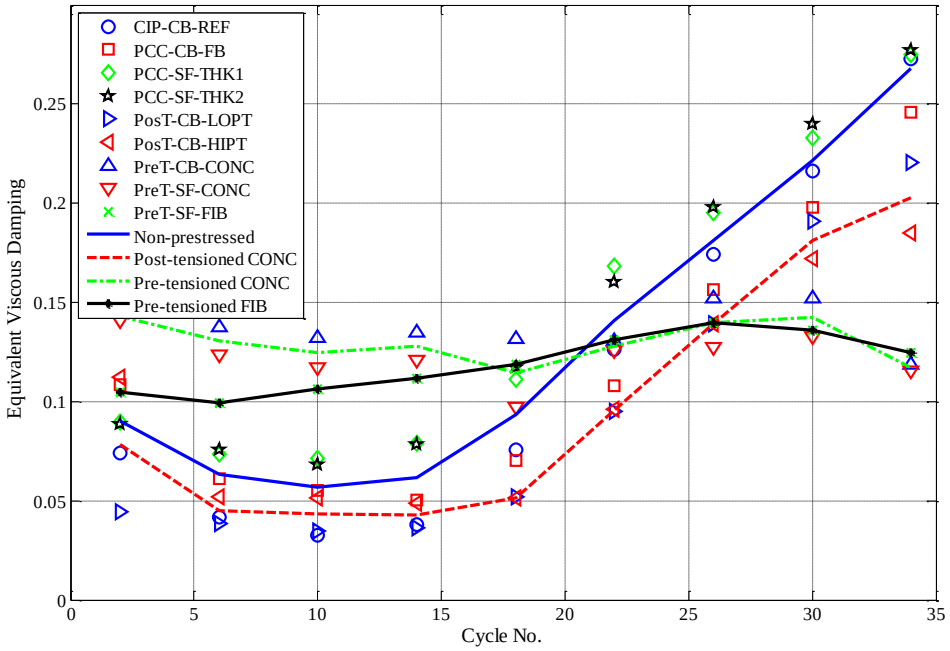

Figure 4-28. Equivilent viscous damping-cycle no. for all UW specimens

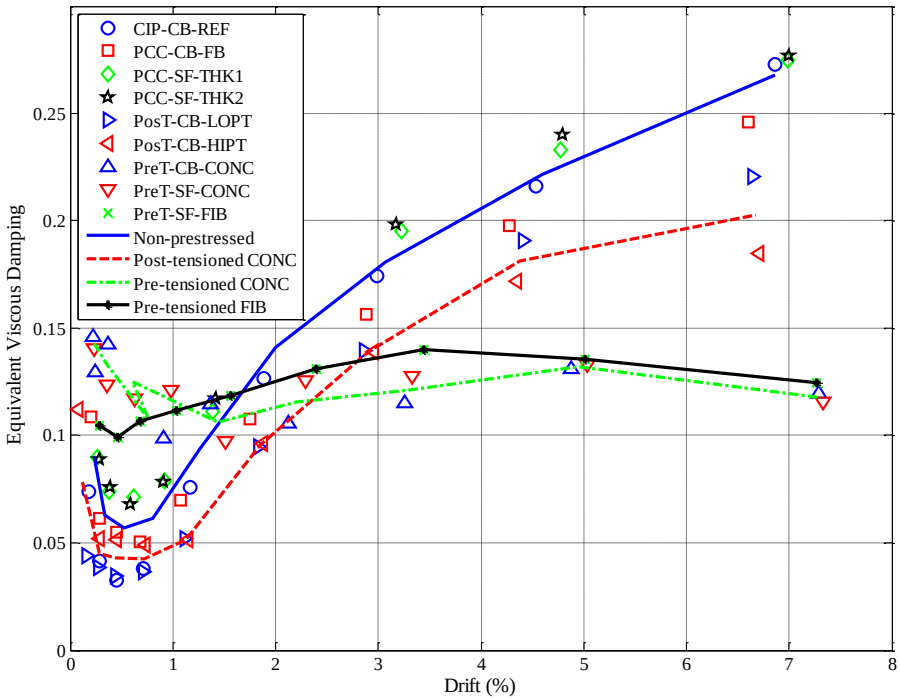

Figure 4-29. Equivalent viscous damping-drift for all UW specimens

4.5.4 Column Re-Centering

Hieber et al. (2005) developed an equation to evaluate a column's ability to re-center after being displaced from its original plumb position. The equation calculates a re-centering ratio λ_{re}, by taking a quotient of the re-centering moment to the resisting moment at the base of the column. The following discussion is taken from Cohagen et al. 2008.

Figure 4-30 shows internal and external vertical forces acting on a typical prestressed column. The re-centering ratio is derived by summing the moments acting at the base of the column. αD, where D is the column diameter and α is a scalar, is the distance from the center of the column to the centroid of the compression area. Assuming that all the mild reinforcement has yielded in the cross section, the re-centering moment and resisting moment can be calculated with equations 4-4 and 4-5, respectively:

$$\boldsymbol{M_{re-centering} = (P_{col} + A_p f_{po})\alpha D} \qquad 4\text{-}4$$

$$M_{resisting} = A_s f_y \alpha D \quad (4\text{-}5)$$

The re-centering ratio equation is obtained by combining equations 4-4 and 4-5:

$$\lambda_{re} = \frac{M_{re-centering}}{M_{resisting}} = \frac{P_{col} + A_p f_{po}}{A_s f_y} \quad (4\text{-}6)$$

where $P_{col}$is the column axial load; A_p is the total area of prestress bars (or strands); f_{po} is the initial prestress in the bar (or strands); A_s is the total area of mild reinforcement; and f_y is the yield stress of the mild reinforcement.

Equation 4-6 shows that the column should re-center if, and only if, λ_{re} is greater than 1.0. The calculated re-centering ratios for all specimens are presented in Table 4-1 and are repeated here in Table 4-8 for convenience.

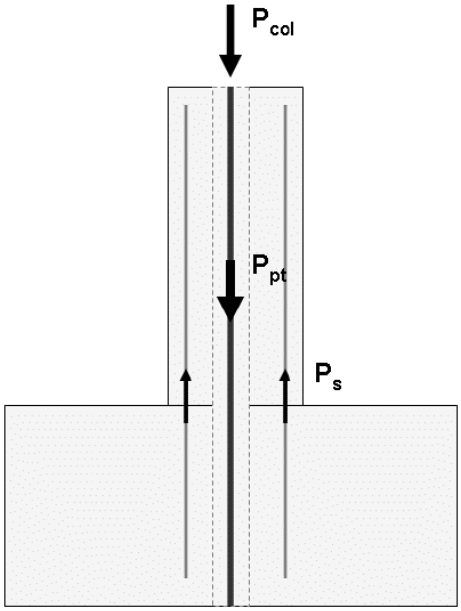

Figure 4-30. Vertical forces acting in a column cross section that includes post-tensioning bar (Cohagen et al. 2008)

Table 4-7. Re-centering ratios for all UW specimens

Reference	Specimen	λ_{re}
Pang et al. 2010	CIP-CB-REF	0.81
Pang et al. 2010	PCC-CB-FB	0.91
Haraldsson et al. 2013	PCC-SF-THK1	0.73
Haraldsson et al. 2013	PCC-SF-THK2	0.73
Cohagen et al. 2008	PosT-CB-LOPT	1.20
Cohagen et al. 2008	PosT-CB-HIPT	1.60
Davis et al. 2013	PreT-CB-CONC	3.10
Davis et al. 2013	PreT-SF-CONC	3.10
Finnsson et al. 2014	PreT-SF-FIB	3.10

The measured re-centering of these nine quasi-static tests can be evaluated using the Normalized Cross-Over Displacement (NCOD), as shown in Figure 4-31. For each test cycle, the cross-over displacement is calculated as the displacement for which the force is zero. For both positive and negative displacements, the displacements ($\Delta_{cross1}, \Delta_{cross2}$) were identified following excursions to larger displacements ($\Delta_{peak1}, \Delta_{peak2}$). The normalized cross-over displacement was then calculated with Equation 4-7:

$$\boldsymbol{NCOD} = \frac{\boldsymbol{\Delta_{cross1} - \Delta_{cross2}}}{\boldsymbol{\Delta_{peak1} - \Delta_{peak2}}} \qquad 4\text{-}7$$

NCOD can vary between 0.0 and 1.0. A low NCOD value implies that the column re-centers well. This ratios are calculated for all the test specimen for target drift ratios 2.06% (Set/Cycle 6-1), 4.28% (Set/Cycle 8-1) , and 6.16% (Set/Cycle 9-1). Figure 4-32 plots the normalized cross-over displacement versus the re-centering ratio for all specimens. Three curves are drawn into

the plot to show the three target drift ratio calculations. The trend is consistent with the concept of the re-centering ratio. The plot shows that the re-centering potential (or NCOD) goes down with increasing re-centering ratio. With increasing drift demands, both non-prestressed and post-tensioned specimens started showing residual displacements. However, the post-tensioned specimens showed better re-centering than the non-prestressed specimens. All three pre-tensioned specimens showed superior re-centering potential to the other specimens. The pre-tensioned specimens returned to a drift ratio of 1% after being displaced to a drift ratio of 10%.

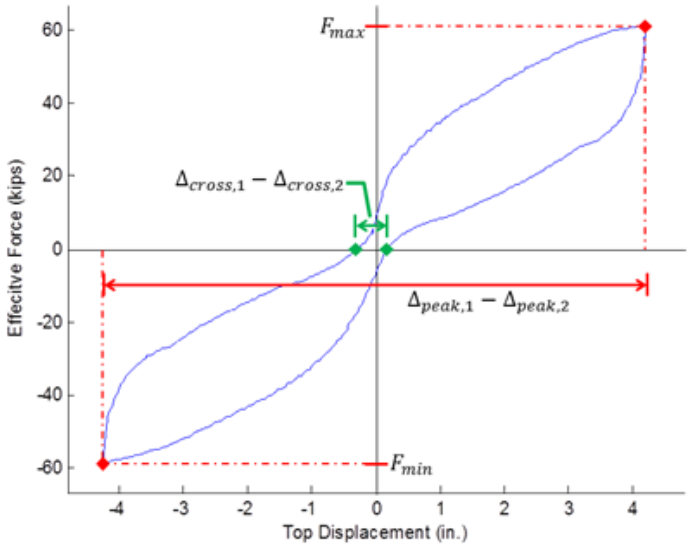

Figure 4-31. Normalized cross-over displacement definition (Kennedy 2015)

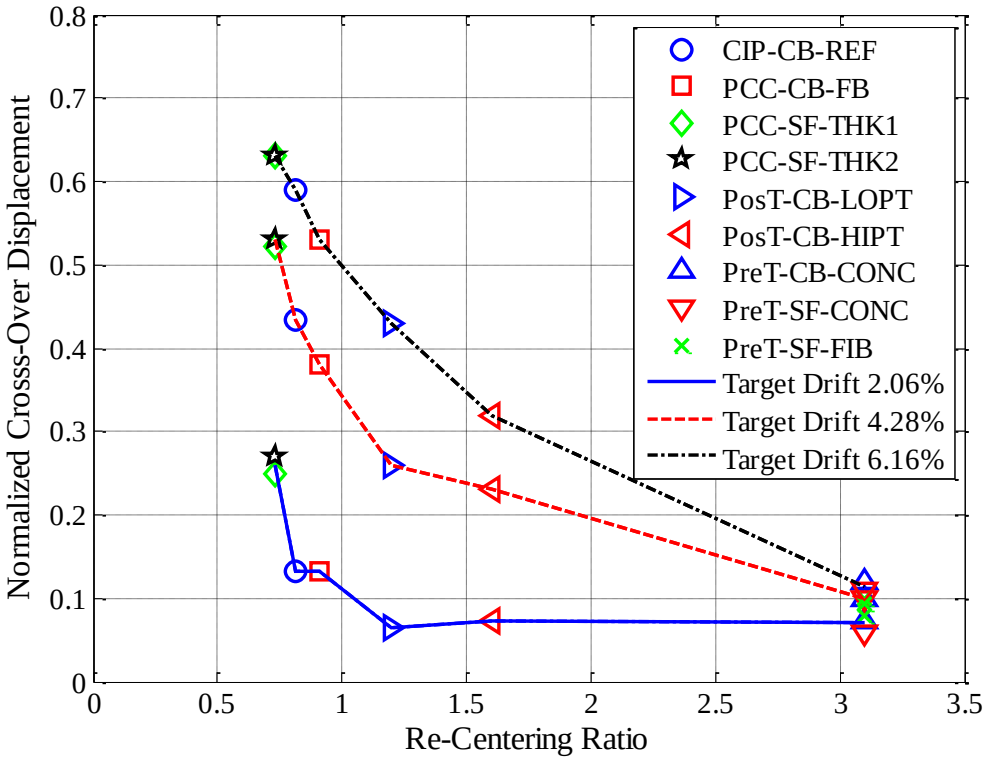

Figure 4-32. NCOD - re-centering ratio for all UW specimens for three target drifts

4.5.5 Damage Progression Models

Damage models were proposed by Berry and Eberhard (2003) to predict the onset of spalling, bar buckling, and bar fracture. The three relevant equations for spiral reinforced columns are:

Spalling: $$\frac{\Delta_{sp}^{calc}}{L}\,(\%) = 1.6\left(1-\frac{P}{A_g f'_c}\right)\left(1+\frac{L}{10D}\right) \quad 4\text{-}8$$

Bar Buckling: $$\frac{\Delta_{bb}^{calc}}{L}\,(\%) = 3.25\left(1+150\rho_{eff}\frac{d_b}{D}\right)\left(1-\frac{P}{A_g f'_c}\right)\left(1+\frac{L}{10D}\right) \quad 4\text{-}9$$

Bar Fracture: $$\frac{\Delta_{bf}^{calc}}{L}\,(\%) = 3.5\left(1+150\rho_{eff}\frac{d_b}{D}\right)\left(1-\frac{P}{A_g f'_c}\right)\left(1+\frac{L}{10D}\right) \quad 4\text{-}10$$

where P is the axial load applied, L is the distance to the point of contraflexure (here 60 in.), D is the column depth (here 20 in.), A_g is the column gross-sectional area, d_b is the longitudinal

reinforcement diameter, f'_c is the concrete compressive strength, $\omega_s = \rho_s f_{ys} / f'_c$ where ρ_s is the transverse volumetric ratio, and f_{ys} is the transverse reinforcement yield strength.

The empirical equations 4-8 to 4-10 were not developed for prestressed columns so the prestressing force was added to the reported dead load applied to the specimen. The results from their models are compared, using measured material properties, with the observed behaviors from the tests in Table 4-5. In Table 4-8, the prestressing force added to the dead load was taken to be the initial prestressing load

Table 4-8. Comparison of damage model predictions and observed occurrences

Specimen	Drift ratio at onset of spalling (%)			Drift ratio at onset of bar buckling (%)			Drift ratio at onset of bar fracture (%)		
	Pred.	Obs.	Obs./Pred.	Pred.	Obs.	Obs./Pred.	Pred.	Obs.	Obs./Pred.
CIP-CB-REF	1.85	2.35	1.27	4.18	5.52	1.32	4.50	6.80	1.51
PCC-CB-FB	1.91	2.15	1.13	4.46	5.10	1.14	4.81	4.60	0.96
PCC-SF-THK1	1.87	1.07	0.57	6.03	7.09	1.18	6.50	10.61	1.63
PCC-SF-THK2	1.89	1.10	0.58	5.89	7.19	1.22	6.34	10.65	1.68
PosT-CB-LOPT	1.82	1.81	1.00	5.17	4.32	0.84	5.57	6.75	1.21
PosT-CB-HIPT	1.82	1.41	1.29	4.97	4.45	0.90	5.35	6.74	1.26
PreT-CB-CONC	1.86	1.11	0.77	5.00	3.20	0.64	5.43	3.95	0.73
PreT-SF-CONC	1.86	1.15	0.62	5.00	3.25	0.65	5.43	4.10	0.76
PreT-SF-FIB	1.90	1.46	0.77	4.99	6.01	1.20	5.38	4.14	0.77
Mean	1.86	1.51	0.81	5.08	5.12	1.01	5.48	6.48	1.18

Table 4-8 shows considerable variations between predicted and observed response. At onset of spalling, Equation 4-8 under-predicts on average first spalling by 19%. Equations 4-9 and 4-10 over-predict on average 1% and 18%, respectively. In general, the empirical equations under-predict pre-tensioned specimens but do reasonable predictions for the post-tensioned specimens. Davis et al. investigated this phenomenon extensively and they concluded that the “diameter and

amount of bonded longitudinal reinforcement may have stronger influence on the damage states than the [damage] state equations show." (Davis et al. 2012).

4.6 Summary

In this chapter, the structural performance of the pre-tensioned bent system with HyFRC was evaluated and compared with eight other test subassemblies; non-prestressed specimens from the parent precast bent system, post-tensioned specimens, and pre-tensioned specimens using conventional concrete in the plastic hinge region. The specimens were evaluated in terms of strength degradation, energy dissipation, viscous damping, and re-centering potential. The following was observed:

- The pre-tensioned specimen with HyFRC in the plastic hinge region had similar loading envelopes and strength as previously tested non-prestressed and pre-tensioned specimens with conventional concrete. The specimen maintained strength throughout the test program, in which the largest peak drift ratio reached was over a drift ratio of 10%. On average, the non-prestressed specimens, post-tensioned specimens, and pre-tensioned specimens with conventional concrete in the plastic hinge maintained strength to about 7%, 4.85%, and 4.75%, respectively.
- The unloading curves of all pre-tensioned specimens indicate that the pre-tensioned system is likely to re-center and have small residual displacements. At a target drift of 6.16%, the normalized cross-over displacement ratio for non-prestressed specimens PCC-SF-THKs and the pre-tensioned specimens were 0.63 and 0.11, respectively. Furthermore, all three pre-tensioned specimens returned to about 1% drift from vertical after being displaced horizontally to a 10% drift.
- All prestressed specimens dissipated less energy than the non-prestressed specimens. The pre-tensioned specimens had the lowest reinforcement ratio of all specimens. Thus, the pre-tensioned specimens dissipated the least of all. At a drift ratio of 4.5%, the average equivalent viscous damping of all pre-tensioned specimens was about 13% while this

ratio was 22% for the non-prestressed specimens and 18% for the post-tensioned specimens.

- By including a HyFRC shell in the plastic hinge region in the pre-tension system, spalling was delayed compared to what was observed in the testing of the pre-tensioned specimens with conventional concrete. However, the HyFRC shell did not delay first bar fracture in comparison with the pre-tensioned specimens with conventional concrete. All pre-tensioned specimens experienced first bar fracture at a drift ratio of about 4.0%. This damage state occurred at a lower drift ratio than in the test program of the non-prestressed specimens.

5 NUMERICAL MODELING STRATEGIES FOR QUASI-STATIC RC TESTS

5.1 Introduction

In recent years, both researchers and practicing engineers have focused their attention on Performance-Based Earthquake Engineering (PBEE). In addition to addressing collapse prevention and life safety issues, as is done in current building codes (e.g., International Building Code, IBC), PBEE attempts to evaluate the probabilities of reaching various damage levels and to use those probabilities for design (Berry and Eberhard 2004). In general, PBEE is a methodology that "implies design, evaluation, and construction of engineered facilities whose performance under common and extreme loads responds to the diverse needs of and objectives of owner-users and society" (Krawinkler 2000). The goal of the PBEE methodology is to design various types of structures, such as bridges, so that they meet predefined levels of acceptable post-earthquake performance. The methodology consists of four main steps (Porter 2003):

1. *Hazard analysis*. In hazard analysis, the seismic environment (e.g., nearby faults and site distances) around the structure is considered and a suite of candidate earthquake ground motions is identified.
2. *Structural analysis*. In structural analysis, the performance of the structure is analyzed with computer models using candidate earthquakes from the hazard analysis. This step is addressed using nonlinear time-history analysis.
3. *Damage analysis*. In damage analysis, results (e.g., column drift ratio or column rotation) from structural analysis are used as input into a set of fragility functions, which are developed from experimental results. A fragility function models the probability of various levels of physical damage, such as first column spalling, first bar buckling, and first bar fracture in a bridge concrete column.
4. *Loss analysis*. In loss analysis, the performance of the structure (e.g., at Design Level Earthquake, or at Maximum Credible Earthquake) is evaluated using results from the

damage analysis. Typical decision variables include number of injuries or fatalities, repair duration, and economic loss.

More information about PBEE can be found in Porter (2003), Moehle and Deierlein (2004) and Lee and Billington (2009).

Bridges are particularly vulnerable to earthquakes. After extreme earthquake ground shaking, bridges might be left in a displaced condition and thus unusable and hazardous. Bridge columns might be left with spalling of the cover concrete, as well as buckling or even fracture of the longitudinal reinforcement. In extreme cases, the bridge might collapse. Columns are vulnerable elements in bridges, because if a column experiences structural failure the impact on the bridge as a whole can be catastrophic. Bridges are therefore an ideal structural type to be addressed with PBEE.

In this chapter, a fiber-based model was developed to model reinforced concrete (RC) columns, in which cyclic, nonlinear constitutive laws were used to represent the responses of the concrete and steel fibers in the cross-section. A lumped-plasticity strategy for integration was investigated and adopted. The lumped-plasticity column model was developed following the recommendations of Berry and Eberhard (2007). The model's constitutive laws were calibrated against results from a set of RC column tests available within the UW-PEER Column Database (Berry et al. 2013). The performance of the column model calibration described here is evaluated in Chapter 9 against a set of shake-table tests of RC cantilever columns.

5.2 Finite Element Model

The analytical platform Open System for Earthquake Engineering Simulation (OpenSees v. 2.4.1 2013) was used for this work. This programming environment is attractive, because it is capable of modeling cyclic and bi-directional loading, and variable axial loads.

At the global system level, OpenSees is a displacement-based finite element analysis platform in which the global unknowns are the displacements and rotations at the joints. At the element level, concrete columns can be modeled with either a force-based element (FBE) or a displacement-based element (DBE). Both element formulations are displacement driven, in that

the elements are given current nodal displacements and they return nodal forces and an element stiffness matrix. Globally, compatibility is ensured automatically by the displacement formulation, and iteration is used to find a solution state that satisfies equilibrium at the nodes.

Figure 5-1 shows the calculation process for a time step using force-based elements. All quantities are incremental and are added to the values from the previous time step once all the iterations are complete. Most of the steps are identical to those used with displacement based elements.

First, the element stiffness matrices are constructed. For force-based elements, the process involves some additional complications, which are discussed below. The global stiffness matrix is assembled from the element stiffnesses. Next the load vector for that iteration on global displacements is built from the external loads and the residual unbalanced loads from the previous iteration. The global (nodal) displacements are found from the loads and the global stiffness matrix, and the element deformations are obtained from them. The linearized element forces, Δq_{linear}^{ele}, are given by the element stiffness matrix multiplied by the element deformations. The true element forces, Δq_{true}^{ele}, are then found from the element deformations. Once again, this step is more complicated when force-based elements are used. The unbalanced element forces are given by the difference between the linearized and true values, and these are summed at each node to give the global unbalanced forces. If the latter are small enough to satisfy the convergence criterion, the iteration stops and the calculations proceed to the next step.

The complications introduced by the use of force-based elements occur in building the element stiffness matrices and in computing the true element forces corresponding to a given set of element deformations. For the latter (i.e., process B in Figure 5-1), a second level of iteration is needed, and it occurs at the element level, in order to find a set of forces that lead to deformations that match the desired ones. In the beam-column element, that means iteratively guessing the end moments and axial load and computing the corresponding displacements. However, in a general force-based element, this means that, at each integration point, the curvature corresponding to the local moment must be found, and those curvatures are then numerically integrated (using a quadrature scheme) along the member to give the end

deformations. If the element is fiber-based, as is the often the case for reinforced concrete, this involves a third level of iteration at the integration point level, because curvatures are needed from given moments, but moments can only be computed from curvatures.

The element stiffness matrix is formed using similar nested iteration cycles. It is obtained by inverting the flexibility matrix, which expresses end deformations in terms of end forces. But for any given force (or moment) field, the local curvatures corresponding to local moments at the integration points can only be found iteratively. While the operations of establishing the element flexibility matrix and find the true element forces are shown in the flow chart as separate items, they are in practice achieved within a single call to the element routine.

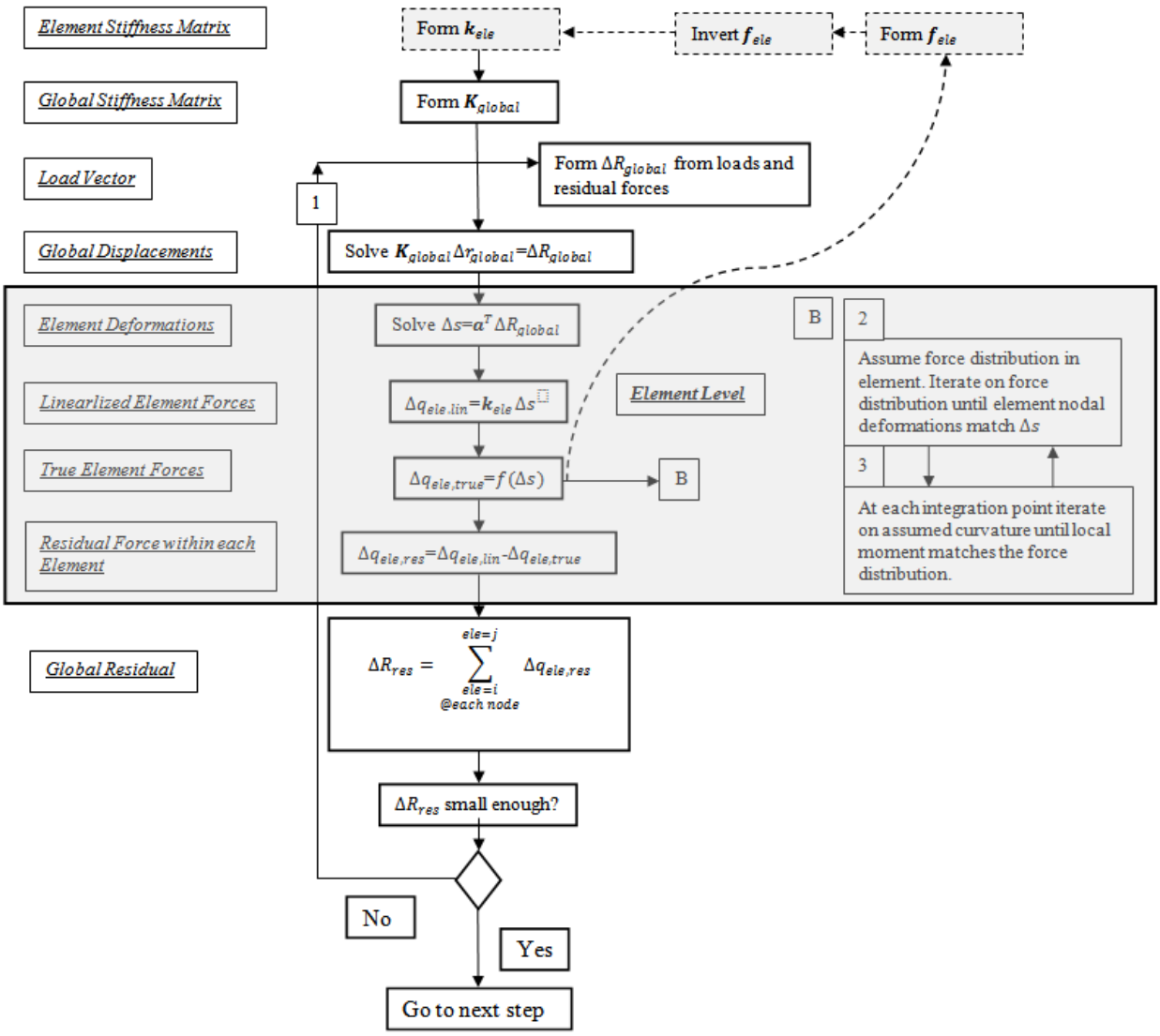

Figure 5-1. Calculation process for a time step using force-based elements

The displacement-based element follows a standard implementation of a typical finite element method (FEM) element. The section deformations are interpolated from an approximate displacement field. To achieve the same level of modeling accuracy of a typical concrete column using these two element formulations, the column needs to be discretized differently. The column can be modeled with a single forced-based element whereas it needs to be discretized with many displacement-based elements. In a displacement-based element, a constant axial strain

and a linear curvature are enforced along the element, thus more displacement-based elements are needed to represent the nonlinear curvature response along the concrete column.

Compared to displacement-based elements, force-based elements require additional levels of iteration, but only one element is needed to simulate a column. They offer computational efficiency if the additional iteration comes at less computational cost than that associated with the additional global degrees-of-freedom needed to achieve the same level of accuracy with displacement-based elements. Because the iteration is carried out on small (element) matrices, this is generally the case, and force-based elements prove to be more efficient. This is particularly true if the convergence tolerance at each cycle of the innermost iteration loops is not too stringent.

Two types of force-based elements are available in OpenSees: a distributed-plasticity fiber beam-column element, and a lumped-plasticity fiber beam-column element. The distributed-plasticity element displacement response is obtained by weighted integration of the section responses (Taucher et al. 1991). However, the drawback of the distributed-plasticity column element is that it is susceptible to strain localization that yields inaccurate predictions at the local and global levels in a degrading member (Coleman and Spacone 2001). Berry and Eberhard (2007) investigated this issue. They showed that the local and global response of the element was sensitive to the number of integration points assigned to the element. Inelastic strains become localized in the first integration point in the plastic hinge region and they do not spread up to other integration points. As more integration points are assigned to the element, the strain in the first integration point increases, and the force-deformation response degrades faster.

Figure 5-2 shows a schematic representation of the lumped-plasticity force-based element developed by Scott and Fenves (2006). In this element, the inelastic response is concentrated within two plastic hinges, one at each end. The user defines the plastic hinge lengths and their associated fiber sections, and the properties of the linear elastic portion (i.e., Young's modulus, section moment of inertia, and area). This element employs a modified Gauss-Radau integration scheme with four integration points used for the entire element: one in each of the plastic hinges and two within the elastic interior of the element. Inelastic action occurs only with a plastic hinge

length at each end of the element. The curvature distribution is linear in the linear elastic part of the column and constant within each plastic hinge.

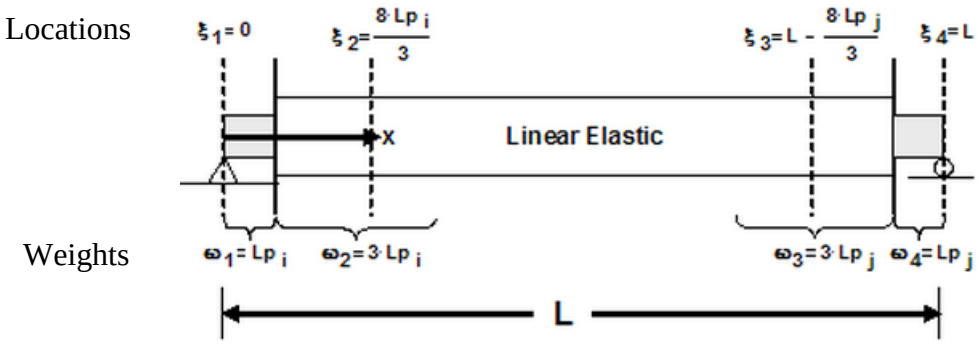

Figure 5-2. Lumped-plasticity (beamWithHinges) element (OpenSees Manual 2014)

5.2.1 Modeling Strategy

In this research, the lumped-plasticity modeling strategy was implemented following modeling recommendations developed by Berry and Eberhard (2007), and Berry et al. (2008). The following description is adapted from their work.

Figure 5-3 shows a cantilever column subjected to a lateral load. The figure also shows the moment and the associated curvature distributions, and the idealized curvature distribution that is the basis of the lumped-plasticity models.

Figure 5-3(d) shows the idealized curvature distribution in a cantilever column associated with a lumped-plasticity element with the use of a plastic hinge only at the base of the column. The element retains the standard four integration points but, because only the base suffers inelastic response, there is no plastic hinge at the top, and the uppermost quadrature point, which would fall within the top plastic hinge in a fixed-fixed column, now lies in the elastic region. Given this element formulation, one inelastic quadrature point is located at $x = 0$ and the other three elastic quadrature points are located at $x = 8/3L_p$, $4L_p + 1/2(L - 4L_p)(1 - 1/\sqrt{3})$, and $4L_p + 1/2(L - 4L_p)(1 + 1/\sqrt{3})$. For these four quadrature points, quadrature weights are $L_p, 3L_p, 1/2\,(L - 4L_p)$, and $1/2\,(L - 4L_p)$, respectively. The quadrature points are shown schematically in Figure 5-3(e). The curvature φ_{base} in Figure 5-3(d) is *constant* over plastic

hinge, L_p. and is calculated with moment-curvature analysis. The curvature is linear above the plastic hinge.

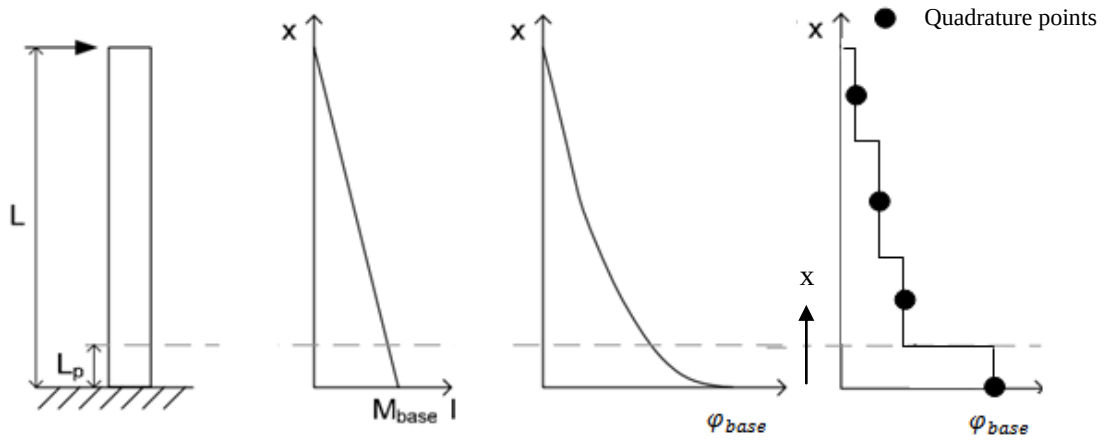

(a) Idealized Column

(b) Moment Distribution

(c) Actual Curvature Distribution

(d) Curvature Distribution for Lumped-Plasticity Element

Figure 5-3. Moment and curvature distributions in plastic-hinge models (Berry and Eberhard 2007)

The lumped-plasticity fiber beam-column element is implemented in OpenSees with the beamWithHinges command. Using this command, the user is required to define a fiber section, plastic-hinge length, and user specification of the effective "elastic stiffness" of the interior element. This stiffness is used at the two interior quadrature points if two hinges are defined and at three quadrature points if one hinge is defined (Figure 5-3(d)).

Berry and Eberhard (2007) developed a column model using the beamWithHinges command and calibrated it to a set of 37 reinforced concrete bridge columns available in the UW-PEER column database (Berry et al. 2013). All columns were cantilever columns. They provide recommendations on how to calculate the plastic hinge length and estimating the effective stiffness (EI_{eff}) such that the model has a correct stiffness at first yield. This research utilizes their recommendations.

The plastic hinge length (Berry and Eberhard 2007) was calculated with Equation 5-1:

$$\boldsymbol{L_p = 0.05L + 0.1\frac{f_y d_b}{\sqrt{f'_c}} \leq \frac{L}{4}} \quad \text{5-1}$$

where L is the height of the column, and f_y, d_b, and f'_c are the measured yield stress, bar diameter of the tension reinforcement, and the concrete compression strength, respectively.

For a cantilever column, the yield displacement is typically calculated with Equation 5-2:

$$\Delta_y^{calc} = \frac{M_y L^2}{3(EI)_{eff}} \quad \text{5-2}$$

where L is the height of the column, $M_y$is the moment at first yield, and $(EI)_{eff}$ is the effective stiffness of the cross section which can be calibrated to reproduce a measured Δ_y. This effective stiffness is often taken as the secant stiffness, $(EI)_{sec}$ to the yield moment in a moment-curvature plot. Using the secant stiffness provides a reasonable estimate of the displacement due to bending at first yield but it does not take into account shear deformation and bar slip. To approximate these other sources of deformation, Berry and Eberhard (2007) introduced a stiffness modification ratio α_{sec} for use with $(EI)_{sec}$. Equation 5-3 is Equation 5-2 rewritten with the secant stiffness and the stiffness medication ratio:

$$\boldsymbol{\Delta_y^{calc}} = \frac{1}{\alpha_{sec}} \frac{M_y L^2}{3(EI)_{sec}} \quad \text{5-3}$$

The stiffness modification ratio was calibrated to experimental data in terms of span-to-depth, axial load ratio, longitudinal reinforcement ratio, and bond slip. Equation 5-4 was the result of their study.

$$\boldsymbol{\alpha_{sec} = 0.35 + 0.1\frac{L}{D} \leq 1.0} \quad \text{5-4}$$

where L is the height of the column, and D is the diameter of the column cross section.

Implementing this stiffness modification ratio is a challenge as the beamWithHinges command does not take this scalar as an input. However, as mentioned above, the element takes as inputs Young's modulus and the section moment of inertia. The following describes how they overcame this challenge.

For the lumped-plasticity element formulation, the cantilever column tip displacement at first yield can be calculated with Equation 5-5. This equation has two terms; contributions from curvatures in the elastic portion of the column and in the plastic hinge. Equation 5-2 can be broken into two components that reflect those responses.

$$\Delta_y^{OpenSees} = \frac{M_y}{(\boldsymbol{EI})_{\boldsymbol{sec}}}\left(\frac{\boldsymbol{L^2}}{\boldsymbol{3}} - \boldsymbol{LL_p}\right) + \varphi_y LL_p \qquad 5\text{-}5$$

where M_y is the yield moment, and φ_y is the curvature at first yield in the element plastic hinge. The inelastic portion, $\boldsymbol{\varphi_y LL_p}$, is driven by moment-curvature analysis and is not readily subject to modification. Thus only the elastic portion can be modified, and that is done with a factor $\widehat{\alpha_{sec}}$.

Equation 5-6 shows Equation 5-5 with a new modification factor $\widehat{\alpha_{sec}}$:

$$\Delta_y^{OpenSees} = \frac{M_y}{\widehat{\alpha_{sec}}(EI)_{sec}}\left(\frac{\boldsymbol{L^2}}{\boldsymbol{3}} - \boldsymbol{LL_p}\right) + \varphi_y LL_p \qquad 5\text{-}6$$

By equating equations 5-3 and 5-6 and substituting the identities $\frac{M_y}{(\boldsymbol{EI})_{\boldsymbol{sec}}} = \boldsymbol{\varphi_y}$, Equation 5-7 is derived to calculate $\widehat{\alpha_{sec}}$ for the lumped-plasticity element. The equation takes as an inputs three known variables, and they are the height of the column, plastic hinge length and the stiffness modification ratio α_{sec}.

$$\widehat{\boldsymbol{\alpha_{sec}}} = \frac{\boldsymbol{\alpha_{sec}(L-L_p)}}{\boldsymbol{L-3\alpha_{sec}L_p}} \qquad 5\text{-}7$$

The procedure to use Berry and Eberhard's recommendations for beamWithHinges is as follows:

- First, a moment-curvature analysis is performed on the fiber section associated with the plastic hinge to determine the secant stiffness $(EI)_{sec}$. The plastic hinge length, L_p**,** and the stiffness modification, α_{sec}, are calculated with equations 5-1 and 5-4, respectively.
- Once these variables are determined, the secant stiffness obtained from the moment-curvature analysis is then modified specifically for beamWithHinges command using Equation 5-7. The $\widehat{\alpha_{sec}}$-factor is applied to the product $(EI)_{sec}$.

Note that this approach was calibrated to provide the correct stiffness at yield, but it was not calibrated to provide the correct stiffness before cracking. The derivation is explained in more detail in Berry and Eberhard (2007) and Berry et al. (2008).

5.2.2 Constitutive Models

The lumped-plasticity model was calibrated by optimizing the model parameters in both the new concrete constitutive model (Concrete08), which was developed as part of this research, and two steel constitutive models (i.e., Steel02 and ReinforcingSteel). These constitutive models are discussed in the following subsections.

5.2.2.1 Concrete Constitutive Model Concrete08

A new uniaxial concrete material model Concrete08 was developed for OpenSees as part of this research. The model is based on an existing uniaxial concrete model, called *Concrete04* in OpenSees, developed at the University of Washington by Berry and Mitra (Berry and Eberhard 2007). Concrete04 includes Popovic's curve (Popovics 1973) in compression and a linear-stress strain response in tension up to the cracking strength f_t. The tension strength decreases exponentially beyond the cracking strain, ε_t. Concrete08 shares these properties with Concrete04, and the mathematics are shown later in this section. In the current implementation of Concrete04, the material has a tensile capacity only if the strain value is tensile ($\varepsilon \geq 0.0$). Examples of envelopes and cyclic responses for the compression and the tensile responses are shown in figures 5-4 and 5-5, respectively. Figure 5-4(a) shows the compression envelope for both unconfined concrete and confined concrete.

The cyclic response of Concrete04 in compression was defined by using a modification (Mazzoni et al. 2006) of a model proposed by Karsan and Jirsa (1969). To account for cracks that do not perfectly close when unloading from tension to compression, Berry (Berry and Eberhard 2007) modified Concrete04 to allow early reloading in compression, as proposed by Stanton and McNiven (1979). The concept is that tension cracks get partially filled with small particles of rubble and/or shear deformations may result in misaligned cracks. Lee and Billington (2010) developed a similar model with their constitutive model *Concrete01SITC (Stuff-In-The-*

Cracks). Their model is a Kent-Scott-Park concrete material model with unloading/reloading according to Karsan and Jirsa (1969) with no tensile strength. Further discussion about Concrete04 and the modification of Concrete04 can be found in Berry and Eberhard (2007).

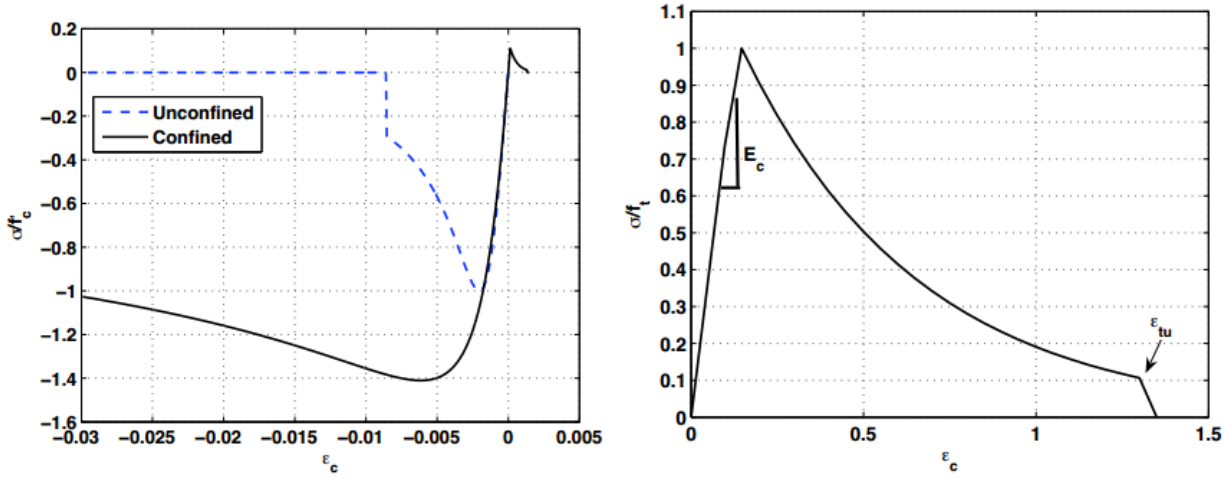

(a) Monotonic Response Normalized by Cylinder Strength

(b) Tensile Response Detail Normalized by Tensile Strength

Figure 5-4. Concrete04 envelopes in compression and tension (Berry and Eberhard 2007)

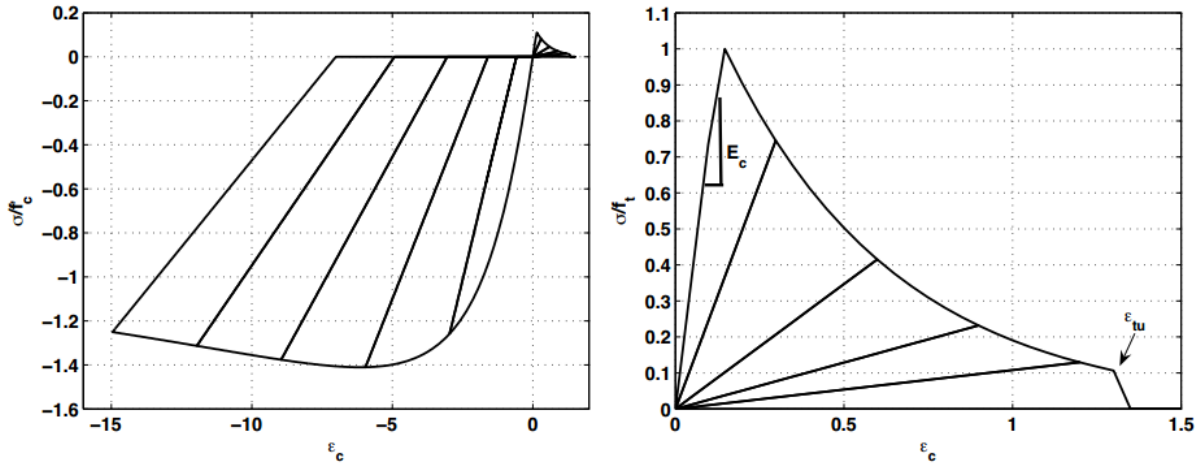

(a) Response in Compression and Tension

(b) Response in Tension

Figure 5-5. Concrete04 cyclic responses in compression and tension (Berry and Eberhard 2007)

An example of a stress-strain response of the new material is shown in Figure 5-6. Concrete08 differs from Berry and Eberhard's modified Concrete04 in three ways:

- The material may resist tension even if the strain is not positive. If the tension capacity of the concrete has not been exceeded before, the material can load in tension immediately after unloading from compression. An example of this is shown in Figure 5-6 (Point C).
- If the early reloading compression mode is activated, the concrete can start reloading in compression from the tension region ($\varepsilon \geq 0.0$). This is shown in Figure 5-6, as well (Point D).
- The early reloading rules are modified from those proposed originally by Stanton and McNiven (1979).

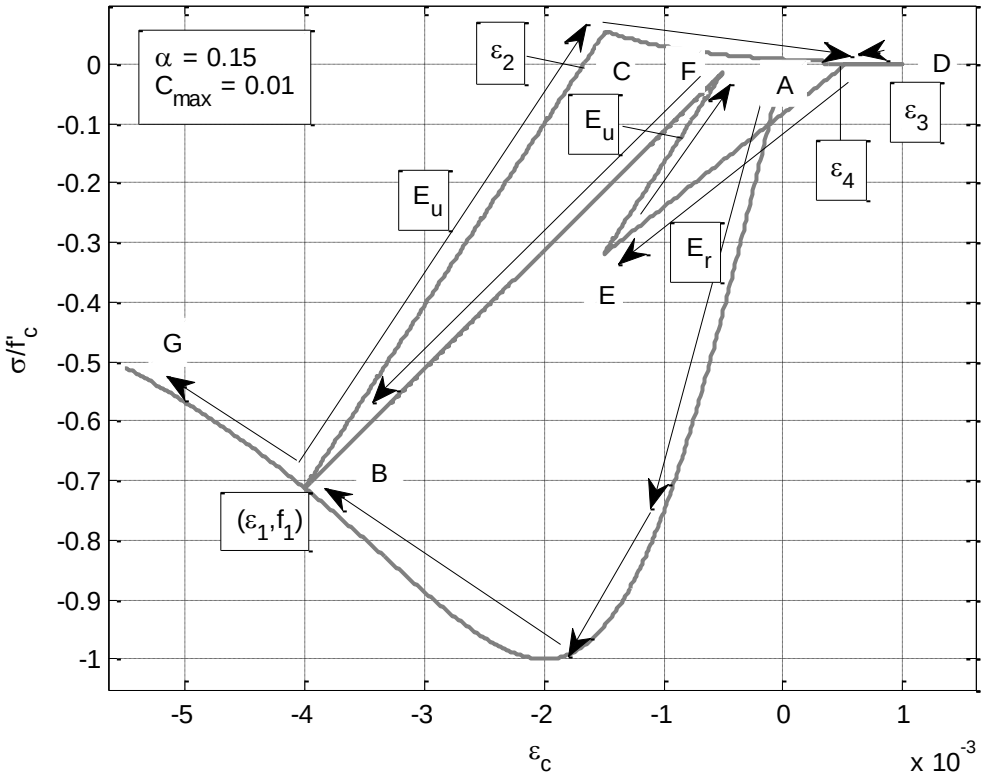

Figure 5-6. Stress-strain behavior of Concrete08 model

Referring to Figure 5-6, the following rules explain the material behavior mathematically.

1. The monotonic stress-strain curve in compression also serves as the envelope and is defined by Popovics' curve:

$$\boldsymbol{\sigma(\varepsilon) = f'c * \eta * \frac{r_2}{r_2 - 1 + \eta^{r_2}}\ ,\ \varepsilon_{cu} \leq \varepsilon \leq 0} \qquad 5\text{-}8$$

where $\boldsymbol{\varepsilon_{cu}}$ is the concrete crushing strain; $\boldsymbol{r_2 = 400}$ if $\boldsymbol{E_{sec} \geq E_c}$ (default if the user accidentally assigns a very small $\boldsymbol{E_c}$) or $\boldsymbol{r_2 = E_c/(E_c - E_{sec})}$; $\boldsymbol{E_c}$ is the initial stiffness provided by the user, $\boldsymbol{E_{sec}}$ is the secant stiffness defined as $\boldsymbol{f'c/\varepsilon'_c}$, $\boldsymbol{\eta = \varepsilon/\varepsilon'_c}$, $\boldsymbol{\varepsilon}$ is the strain at any load, and $\boldsymbol{\varepsilon'_c}$ is the concrete strain at maximum strength. If the initial stiffness, $\boldsymbol{E_c}$, is defined as $\boldsymbol{57,000\sqrt{f'_c}}$ (in psi), the compression curve will be identical to that proposed by Mander et al. (1988). In the model, $\boldsymbol{f'c}$, $\boldsymbol{\varepsilon'_u}$, and $\boldsymbol{\varepsilon_{cu}}$ are input as negative values.

2. The stress-strain curve in tension is linear to the cracking strength, f_t. Beyond the cracking strain, the tensile strength decreases exponentially to a strain ε_{tu} . Furthermore, the tensile strength property is not fixed at the origin $[(\varepsilon, \sigma) = (0.0)]$, as mentioned above. The stress-strain curve in tension is defined as:

$$\boldsymbol{\sigma(\varepsilon)} = \begin{cases} \boldsymbol{E_u * \varepsilon}\ , & \boldsymbol{\varepsilon \leq \varepsilon_t} \\ \boldsymbol{f_{tn} * \beta^{\frac{(\varepsilon - \varepsilon_t)}{(\epsilon_{tu} - \varepsilon_t)}}}\ , & \boldsymbol{\varepsilon_t < \varepsilon \leq \varepsilon_{tu}} \\ \boldsymbol{0.0}\ , & \boldsymbol{\varepsilon > \varepsilon_{tu}} \end{cases} \qquad 5\text{-}9$$

where $\varepsilon = \varepsilon_3 - \varepsilon_2$; ε_2 is the strain at which the stress becomes zero on unloading and the strain where tensile response starts if the tensile capacity has not been exceeded; ε_3 is the maximum strain reached during the unload cycle; $\varepsilon_t = f_t/E_c$; β is taken as 1/10; E_u is the unloading stiffness from compression, and $f_{tn} = f_t * E_u/E_c$

3. The unloading and reloading responses are governed by strains ε_1, $\varepsilon_2, \varepsilon_3$ and ε_4, and stiffnesses E_u and E_r. $\varepsilon_1$and f_1 are the strain and stress at which the unloading curve departs from the envelope curve; ε_2 is the strain at which the stress becomes zero on unloading and the strain where tensile response starts if the tensile capacity has not been exceeded; ε_3 is the maximum strain reached during the unload-reload cycle; and ε_4 is the strain at which reloading in compression starts. E_u is the unloading stiffness defined by the Karsan and Jirsa model; E_r is the reloading stiffness, which is a line that goes from the reloading strain ε_4 to (ε_1, f_1). In Concrete08, crack opening and closure are assumed

to occur at zero stress. If perfect crack closure is assumed, the concrete starts to reload in compression at the strain ε_2. If imperfect crack closure is incorporated, however, the reloading in compression starts at the strain ε_4. The reloading strain ε_4 is calculated for two different cases:

$$\boldsymbol{\varepsilon_4 = \varepsilon_2 + \left(\frac{(\varepsilon_3 - \varepsilon_2)}{C_{max}}\right)^{\frac{1}{\alpha}-1} * (\varepsilon_3 - \varepsilon_2), \quad (\varepsilon_3 - \varepsilon_2) \leq C_{max} \ (Case\ 1)} \qquad 5\text{-}10$$

$$\boldsymbol{\varepsilon_4 = \varepsilon_2 + C_{max}\ , \quad (\varepsilon_3 - \varepsilon_2) > C_{max} \ (Case\ 2)} \qquad 5\text{-}11$$

In these equations, C_{max} represents a limiting strain, and so is dimensionless. For Case 1, the strain difference, $(\varepsilon_3 - \varepsilon_2)$, has not exceeded C_{max} and the imperfect crack closure can be adjusted by varying the α factor between 0.0 and 1.0. The physical reasoning for Case 1 is that at lower level of column deformations cracks widths are small so only small particles can be trapped in between the cracks. In Case 2, the strain difference exceeds C_{max} and thus C_{max} is added to ε_2. For Case 2, column deformations are large enough that concrete has, perhaps, started to spall off and shear deformations are severe enough to cause fully misaligned cracks in the column core. Two special values of α are worth mentioning. First, if $\alpha = 1$, the model assumes that concrete cracks do not close. Second, if $\alpha \to 0$, the model assumes that cracks partially close until strain difference $(\varepsilon_3 - \varepsilon_2)$ gets greater than C_{max}.

The command for Concrete08 in OpenSees and the source code of the constitutive material are given in Appendix D.

This research used model parameters proposed by Mander et al. (1998) for both for the confined and the unconfined concrete. The following two equations were proposed by Mander et al. for maximum compressive stress of confined concrete (f'_{cc}) and its corresponding compressive strain (ε'_{cc}).

$$\boldsymbol{f'_{cc} = f'_c\left(2.254\sqrt{1 + 7.94\frac{f_{pl}}{f'_c}} - 2\frac{f_{pl}}{f'_c} - 1.254\right)} \qquad 5\text{-}12$$

$$\boldsymbol{\varepsilon'_{cc} = 0.002\left(1 + 5\left(\frac{f'_{cc}}{f'_c} - 1\right)\right)} \qquad 5\text{-}13$$

where

$$\boldsymbol{f_{pl} = \frac{1}{2}\rho_{sc} f_{yt} k_e} \quad \text{5-14}$$

$$\boldsymbol{k_e = 1 - \frac{\frac{s'}{2d_c}}{1-\rho_{lc}}} \quad \text{5-15}$$

$$\boldsymbol{s' = s - d_{trans}} \quad \text{5-16}$$

$$\boldsymbol{\rho_{sc} = 4\left(\frac{A_t}{d_c s}\right)} \quad \text{5-17}$$

Here, f'_c is the concrete compressive strength, f_{pl} is the effective lateral confining stress on the concrete, d_c is the diameter of the core, ρ_{sc} is the volume of transverse confining steel to the volume of confined concrete ratio, k_e is the confinement effectiveness coefficient, ρ_{lc} is the ratio of the area of longitudinal steel to the area of core of section, A_t, d_{trans}, s and f_{yt} are the area , wire diameter, spacing and yield stress of the spiral reinforcement.

The concrete was assumed to have strength in tension up to f_t at $\varepsilon_t = \frac{f_t}{E_c}$. The maximum tensile stress was calculated with the following equation from ACI 318-11:

$$\boldsymbol{f_t = 7.5\lambda\sqrt{f'_c}} \quad \text{5-18}$$

here f'_c is in psi, and λ was 1.0 for normal-weight concrete.

Similarly, the initial stiffness, E_c, of the concrete was calculated with the following equation from ACI 318-11:

$$\boldsymbol{E_c = 57,000\sqrt{f'_c}} \quad \text{5-19}$$

where f'_c is in psi.

Tables 5-1 and 5-2 list the range of input values in Concrete08 used in the calibration of the column model for Steel02 and ReinforcingSteel, respectively. In the concrete constitutive model, α values ranged from 0.01 to 1.0. C_{max} ranged from 0.0 to 0.15.

Table 5-1. Concrete08 calibration parameter values with Steel02

Constitutive Model	Model Parameter	Calibration Parameter Values				
Concrete08	α	0.01	0.33	0.50	1.00	-
	C_{max}	0.000	0.005	0.050	0.100	0.150

Table 5-2. Concrete08 calibration parameter values with ReinforcingSteel

Constitutive Model	Model Parameter	Calibration Parameter Values							
Concrete08	α	0.01	0.33	0.50	1.00	-	-	-	-
	C_{max}	0.000	0.005	0.010	0.050	0.100	0.150	-	-

5.2.2.2 Steel Constitutive Model Steel02

Steel02 is a constitutive model for reinforcing steel based on the work of Menegotto and Pinto (1973) available in OpenSees. The monotonic response of this material is shown in Figure 5-7.

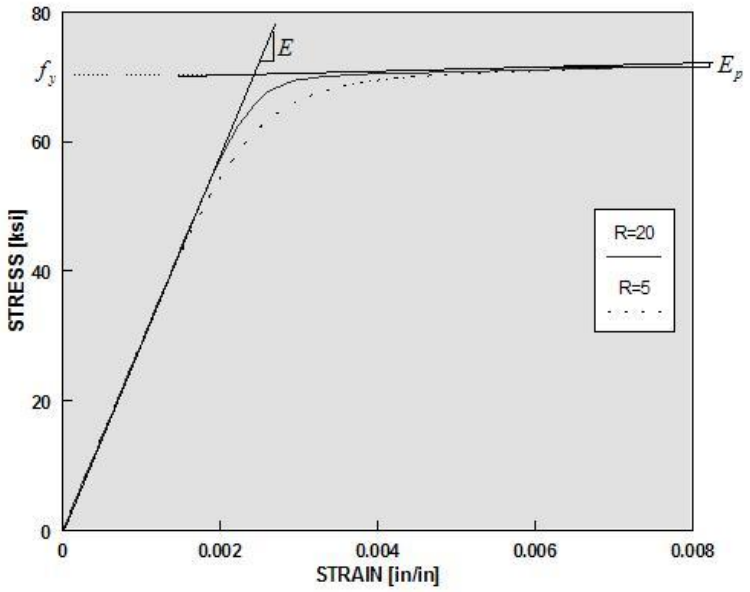

Figure 5-7. Steel02 monotonic response (OpenSees Manual 2013)

The model's backbone curve is bilinear with a rounded transition between the two straight line segments. The post-yield stiffness, E_p, is a fraction, b, of the initial elastic stiffness, E. The curve is defined by Equation 5-20:

$$\boldsymbol{\sigma^* = b\varepsilon^* + \frac{(1-b)\varepsilon^*}{(1+\varepsilon^*)^{1/R}}} \quad \text{5-20}$$

where b is the hardening ratio and the R is the parameter that defines the curvature of the transition curve.

In the current implementation of Steel02 in OpenSees, the parameter R varies with the accumulated plastic strain as

$$\boldsymbol{R(\xi) = R_0\left(1 - \frac{cR_1\xi}{cR_2+\xi}\right)} \quad \text{5-21}$$

where ξ is a plastic strain variable, cR_1 controls the final value of $R(\xi)$ and cR_2 controls how fast the exponent $R(\xi)$ degrades.

The model takes into account the Bauschinger effect as the steel is cycled. The drawback of the model is that is does not include a yield plateau, bar buckling, and bar fracture (Berry and Eberhard 2007). This model was included in this research, because it is commonly used in practice. The OpenSees library includes a fatigue model object that can be used to wrap around an existing constitutive model, but this wrapper was not included in this research.

Parameters optimized in the steel model were the Bauschinger effect parameters R_0, cR_1 and cR_2 (i.e., transition curve) and the steel hardening ratio, b.

The formulation in Equation 5-21 is inconvenient for optimization, because, as discovered in trial optimization runs, the final value of $R(\xi)$ is one of the most important parameters, yet it is a function of both R_0 and cR_1, as opposed to being a function of a single variable. Optimization is most effective if the parameters of the system control distinct features of the model. Therefore the parameters in the model were mapped onto a modified set, given by R_{inf}, the final value of $R(\xi)$, and ξ_{50}, the value of ξ when the R value had degraded half way from its initial value R_0, to its final value R_{inf}. Those two new variables are defined by equations 5-22 and 5-23.

$$\boldsymbol{R_{inf} = R_0(1 - cR_1)} \quad 5\text{-}22$$

$$\boldsymbol{\xi_{50} = cR_2} \quad 5\text{-}23$$

These equations can be verified by making the appropriate substitutions in Equation 5-21.

Equation 5-21 can then be rewritten as follows:

$$\boldsymbol{R(\xi) = R_{inf}\left(\frac{\alpha + {\xi}/{\xi_{50}}}{1 + {\xi}/{\xi_{50}}}\right)} \quad 5\text{-}24$$

where $\alpha = {R_0}/{R_{inf}}$; ξ is a plastic strain variable (as before); and ξ_{50} controls how fast $R(\xi)$ degrades.

$R(\xi_{50})$ is calculated using Equation 5-25:

$$\boldsymbol{R(\xi_{50}) = R_{50} = \frac{R_0 + R_{inf}}{2}} \quad 5\text{-}25$$

Table 5-3 lists the input values in Steel02 used in the calibration of the model with Concrete08 (Steel02 does not take R_{inf} as an input). R_0 ranged from 10.0 to 18.5, cR_1 ranged from 0.80 to 0.94, and ξ_{50} was kept fixed at 0.15. The selections of R_0 and cR_1resulted in R_{inf} values ranging from 0.60 to 3.70, calculated with Equation 5-22. The hardening ratio was kept in the range of typical measured hardening ratios (between 1.0-2.0%).

Table 5-3. Steel02 calibration parameter values with Concrete08

Constitutive Model	Model Parameter	Calibration Parameter Values				
Steel02	R_0	10.0	12.0	14.0	16.0	18.5
	cR_1	0.80	0.90	0.92	0.94	-
	ξ_{50}	0.15	-	-	-	-
	b	0.0100	0.0125	0.0150	0.0175	-

The combination of these eighty Steel02 parameters (Table 5-3) with the twenty Concrete08 parameters (Table 5-1) resulted in 1600 combinations of parameters for each column.

In this research, the elastic stiffness of the reinforcement, E, was taken to be 29,000 ksi. Further information about the Steel02 constitutive model can be found in Filippou et al. (1983).

5.2.2.3 Steel Constitutive Model ReinforcingSteel

ReinforcingSteel is a steel constitutive model developed by Mohle and Kunnath (2006) "that can be used to account for isotropic hardening, diminishing yield plateau, Bauschinger effect, degrading strength and stiffness due to bar buckling, and degrading strength and stiffness due to cycling" (Berry and Eberhard 2007). The bar buckling can be modeled with the method proposed by Gomes and Appleton (1997), or the one by Dhakal and Maekawa (2002). The Coffin and Manson fatigue model (Coffin 1954, 1971 and Manson 1965) is used to calculate the degradation of strength and stiffness due to cycling of the steel. In this research, the isotropic hardening and bar buckling options were not used since, they appear to have errors in the code implementation of the steel model (Kashani 2014).

According to the Coffin and Manson law, the reinforcing bar is assumed to fracture once the cumulative damage variable D reaches a value of 1.0, in which D is defined as:

$$\boldsymbol{D = \sum \left({\varepsilon_p}/{C_f} \right)^{1/\alpha}} \quad \text{5-26}$$

where ε_p is the half-cycle plastic strain defined as

$$\boldsymbol{\varepsilon_p = \varepsilon_t - {\sigma_t}/{E}} \quad \text{5-27}$$

where ε_t and σ_t are the total change in half-cycle strain and stress; C_f is a ductility constant that controls the number of cycles to bar fracture, and α is a damage strain range constant. In this research, the value of $\alpha = 0.506$ was used, as recommended by Mohle and Kunnath (2006).

ReinforcingSteel also accounts for a loss in strength due to cumulative damage. The degradation parameter Φ_{SR} is defined as follows:

$$\phi_{SR} = \sum \left({}^{\varepsilon_p}/_{C_d} \right)^{1/\alpha} \qquad 5\text{-}28$$

where C_d is a strength reduction constant that controls the amount of strength degradation per cycle. The degradation parameter is directly multiplied to the basic stress calculated in the reinforcement. The effects of C_f and C_d on the steel are shown in Figure 5-8. Berry and Eberhard (2007) describe this model in more detail.

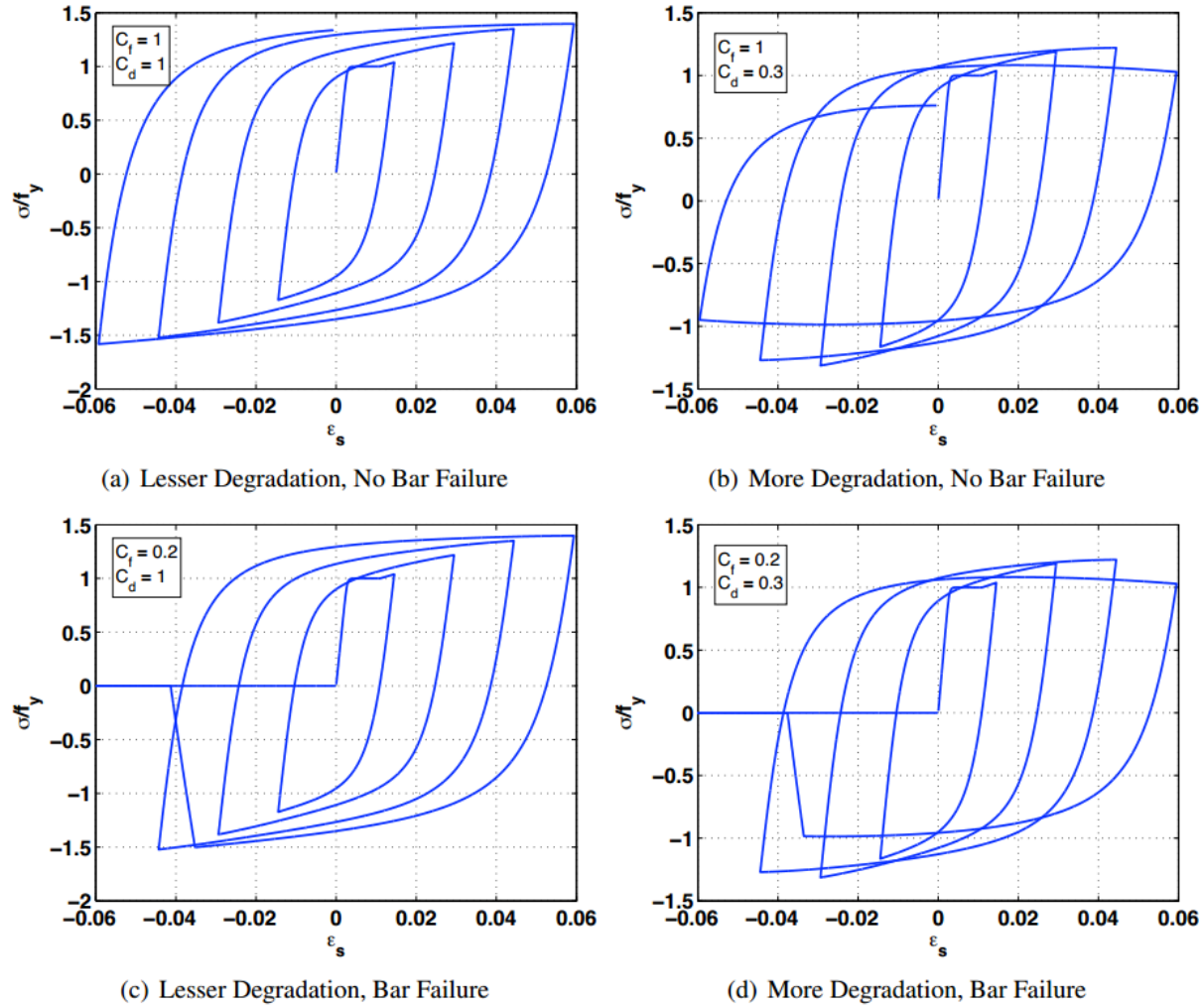

(a) Lesser Degradation, No Bar Failure

(b) More Degradation, No Bar Failure

(c) Lesser Degradation, Bar Failure

(d) More Degradation, Bar Failure

Figure 5-8. Effect of C_f and C_d on cyclic response of steel (Berry and Eberhard 2007)

Table 5-4 lists the input values in ReinforcingSteel used in the calibration of the model with Concrete08. The ductility constant, C_f, in ReinforcingSteel varied between 0.20 and 0.34 with a step size of 0.02. The strength reduction constant, C_d, varied from 0.37 and 0.52 with a step size of 0.02 as well. The ranges of both values in the ReinforcingSteel were chosen to be near the optimal values identified in a previous study by Berry and Eberhard (2007).

Table 5-4. ReinforcingSteel calibration parameter values with Concrete08

Constitutive Model	Model Parameter	Calibration Parameter Values							
ReinforcingSteel	C_f	0.20	0.22	0.24	0.26	0.28	0.30	0.32	0.34
	C_d	0.37	0.39	0.41	0.43	0.45	0.47	0.50	0.52

The optimization procedure with ReinforcingSteel differed from the optimization with Steel02. First, the columns for which the drift ratio at bar fracture was known were identified and a ductility constant C_f of ReinforcingSteel was obtained using the following procedure. It is similar to the one described by Berry and Eberhard (2007), but with slight modifications.

1. A subset of 18 columns from Table 5-5 was identified that has drift ratios reported at first bar fracture.
2. The subset was cycled with different combination of C_f with $C_d = 1000$. A large C_d value leads to a small strength reduction in each cycle. Strains were recorded at the rebar located at the extreme tension and compression in each column. C_f input values tried are listed in Table 5-4.
3. For each C_f value, a damage index was calculated for each column at the displacement corresponding to observed bar fracture. A mean value of all 18 columns was calculated. The half-cycle plastic strain was calculated using the Rainflow-Counting Method (Matsuishi and Endo 1968).
4. This procedure was repeated with different C_f until the mean value of the damage indices at the onset of bar fracture was ~1.0. A 5.0% tolerance was allowed to keep the C_f value at two decimal places, for simplicity purposes.

After the optimal C_f was obtained, 30 columns were analyzed by varying the concrete parameters, α and C_{max}, and the strength reduction factor in the steel model, C_d. The optimum concrete parameters and strength reduction factor were obtained by minimizing the objective function described in Section 5.4. The strength reduction factor is an average number for all the columns considered in this study. The factor was not calibrated specifically like C_f because no information is available about the strength degradation of those bars in confined concrete.

The elastic stiffness of the reinforcement, E_s, was taken as 29,000 ksi.

5.3 Bridge Column Database

The column model described in Section 5.2 was calibrated to a set of quasi-statically tested columns available in the UW-PEER column database (Berry et al. 2013). The database is readily accessible through the World Wide Web (http://www.ce.washington.edu/~peera1/). The database documents column geometry, material properties, and reinforcement details for spiral reinforced columns, rectangular columns, and retrofitted columns. Furthermore, it provides force-displacement histories and lists observed displacements at the onset of various damage states.

Spiral reinforced concrete columns were the focus of the calibration of the column model. The database was screened for columns that were representative of modern bridge column construction. The following screening criteria are the same as used by Berry and Eberhard (2007). Six columns tested by Kunnath et al. 1997 did satisfy the screening criteria but were not included in this study. Their experimental responses were not suitable for displacement cross-over and force cross-over studies (see Section 5.4).

- $P/A_g f'_c \leq 0.30$
- $\omega_s \geq 0.05$
- $\rho_l \leq 0.04$
- $s/d_b \leq 6.0$
- $cover/D \leq 0.10$
- Quasi-statically tested

where P is the axial load $A_g$is the gross cross-sectional area, f'_c is the concrete compressive strength, $\rho_s$is the transverse reinforcement ratio, ω_s is the reinforcement index, ρ_l is the longitudinal reinforcement ratio, s is the spacing of the spiral reinforcement, d_b is the diameter of the longitudinal reinforcement, $cover$ is the distance from the column face to the edge of the transverse reinforcement, and D is the diameter of the column.

Table 5-5 lists 34 columns that satisfied these screening criteria. All had a circular cross-section, except for seven that were octagonal. Table 5-5 also lists the drift ratios at onset of bar fracture, Δ_{bf}/L.

Table 5-5. Bridge column dataset

Reference	Specimen	Cross-Section[1]	L (in.)	L/D	$P/A_g f'_c$ (%)	ρ_l (%)	ρ_{eff} (%)	S/d_b	Δ_{bf}/L (%)
Munro et al. 1976	No. 1	O	107.5	5.5	0.0	2.60	13.0	1.85	N/A
Ang et al. 1981	No. 1	O	63	4.0	20.0	2.40	9.0	2.50	3.75
Potangaroa et al. 1979	No. 1	O	47.2	2.0	23.0	2.40	8.0	3.13	N/A
Wong et al. 1990	No. 1	C	31.5	2.0	19.0	3.20	11.0	3.75	N/A
Stone and Cheok 1989	Flexure	C	359.8	6.0	7.0	2.00	9.0	2.07	5.89
Stone and Cheok 1989	Shear	C	179.9	3.0	7.0	2.00	19.0	1.26	5.89
Stone and Cheok 1989	No. N1	C	29.5	3.0	10.0	2.00	26.0	1.27	10.29
Stone and Cheok 1989	No. N2	C	29.5	3.0	21.0	2.00	27.0	1.27	7.45
Stone and Cheok 1989	No. N3	C	59.1	6.0	10.0	2.00	13.0	2.07	6.83
Stone and Cheok 1989	No. N4	C	29.5	3.0	10.0	2.00	26.0	1.27	7.11
Stone and Cheok 1989	No. N5	C	29.5	3.0	20.0	2.00	26.0	1.27	6.44
Stone and Cheok 1989	No. N6	C	59.1	6.0	10.0	2.00	14.0	2.07	6.72
Kunnath et al. 1997	No. A2	C	54.0	4.5	9.0	2.00	14.0	2.00	N/A
Kunnath et al. 1997	No. A3	C	54.0	4.5	9.0	2.00	14.0	2.00	N/A
Hose et al. 1997	No. SRPH1	C	144.1	6.0	15.0	2.70	9.0	2.56	8.74
Vu et al. 1998	No. NH3	C	35.8	2.0	15.0	2.40	13.0	3.78	N/A
Kowalsky et al. 1999	No. FL3	C	143.9	8.0	30.0	3.60	12.0	4.79	9.08
Lehman and Moehle 2000	No. 415	C	96.0	4.0	7.0	1.50	14.0	2.00	7.30
Lehman and Moehle 2000	No. 815	C	192.0	8.0	7.0	1.50	14.0	2.00	9.12
Lehman and Moehle 2000	No. 1015	C	240.0	10.0	7.0	1.50	14.0	2.00	10.42
Lehman and Moehle 2000	No. 407	C	96.0	4.0	7.0	0.80	14.0	2.00	5.21
Lehman and Moehle 2000	No. 430	C	96.0	4.0	7.0	3.00	14.0	2.00	N/A
Lehman and Moehle 2000	No. 328	C	72.0	3.0	9.0	2.70	16.0	1.33	7.22
Lehman and Moehle 2000	No. 828	C	192.0	8.0	9.0	2.70	16.0	1.33	N/A
Lehman and Moehle 2000	No. 1028	C	240.0	10.0	9.0	2.70	16.0	1.33	N/A
Henry and Mahin 1999	No. 415p	C	96.0	4.0	12.0	1.50	12.0	2.00	5.54
Henry and Mahin 1999	No. 415s	C	96.0	4.0	6.0	1.50	6.0	4.00	N/A
Moyer and Kowalsky 2001	No. 1	O	96.0	5.3	4.0	2.00	12.0	4.00	7.66
Moyer and Kowalsky 2001	No. 2	O	96.0	5.3	4.0	2.00	11.0	4.00	10.27
Moyer and Kowalsky 2001	No. 3	O	96.0	5.3	4.0	2.00	12.0	4.00	N/A
Moyer and Kowalsky 2001	No. 4	O	96.0	5.3	4.0	2.00	11.0	4.00	N/A
Pang et al. 2008	CIP-CB-REF	C	60.0	3.0	11.2	1.58	8.3	2.00	6.80
Haraldsson et al. 2013	PCC-SF-THK1	C	60.0	3.0	10.1	1.12	10.9	1.67	10.61
Haraldsson et al. 2013	PCC-SF-THK2	C	60.0	3.0	9.2	1.12	9.9	1.67	10.65

Note: C = Circular, O = Octagonal.

5.4 Strategy for Optimizing the Column Model

5.4.1 Measures of Accuracy

In order to optimize the fit between measured and predicted column global response to cyclic loading, an objective cost function was developed. This function consisted of the weighted sum of three error measures, namely a Cyclic Force error, a Cross-over Force error and a Cross-over Displacement error. These error measures are discussed below.

Global Force Error (E_{force}). The global force error is defined as

$$\boldsymbol{E_{force}} = \sqrt{\frac{\sum_{i=1}^{n}\left(\boldsymbol{F_{meas}^{i} - F_{calc}^{i}}\right)^{2}}{\boldsymbol{max}\,(\boldsymbol{abs}(\boldsymbol{F_{meas}}))^{2}\boldsymbol{n}}} \qquad 5\text{-}29$$

where F_{meas} and F_{calc} are the measured and calculated effective forces at a particular displacement; n is the number of data points in the history per column.

Displacement Cross-Over Error (E_{DCO}). The displacement cross-over error is defined as

$$\boldsymbol{E}_{\boldsymbol{DCO}} = \sqrt{\frac{\sum_{i=1}^{n}\left(\boldsymbol{DCO_{meas}^{i} - DCO_{calc}^{i}}\right)\boldsymbol{2}}{\boldsymbol{max}\,(\boldsymbol{abs}(\boldsymbol{DCO_{meas}}))^{2}\boldsymbol{n}}} \qquad 5\text{-}30$$

where DCO_{meas} and $DCO_{calc}$are the measured and calculated cross-over displacements, respectively. For each test cycle, the displacement cross-over was calculated as the displacement for which the force was zero; n is the number of displacement cross-overs per column.

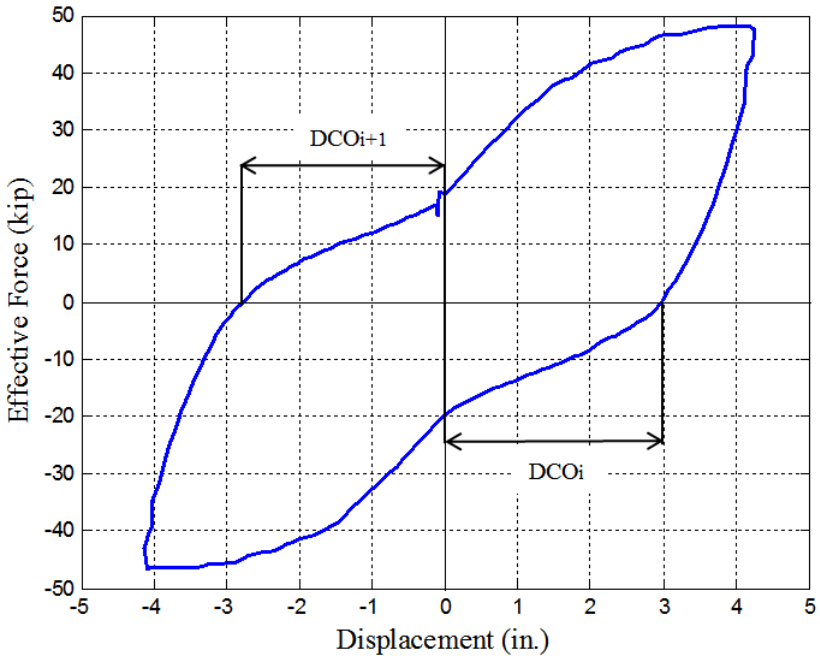

Figure 5-9. Definition of displacement cross-over displacement (DCO) error

Force Cross-Over Error (E_{FCO}). The force cross-over error is defined as

$$\boldsymbol{E_{\mathrm{FCO}}} = \sqrt{\frac{\sum_{i=1}^{n}(\boldsymbol{FCO_{meas}^{i} - FCO_{calc}^{i}})\boldsymbol{2}}{\boldsymbol{max\,(abs(FCO))^{2}n}}} \qquad 5\text{-}31$$

where FCO_{meas} and FCO_{calc} are the measured and calculated force cross-over, respectively. For each test cycle, the force cross-over was calculated as the force at which the displacement was zero; n is the number of force cross-overs per column.

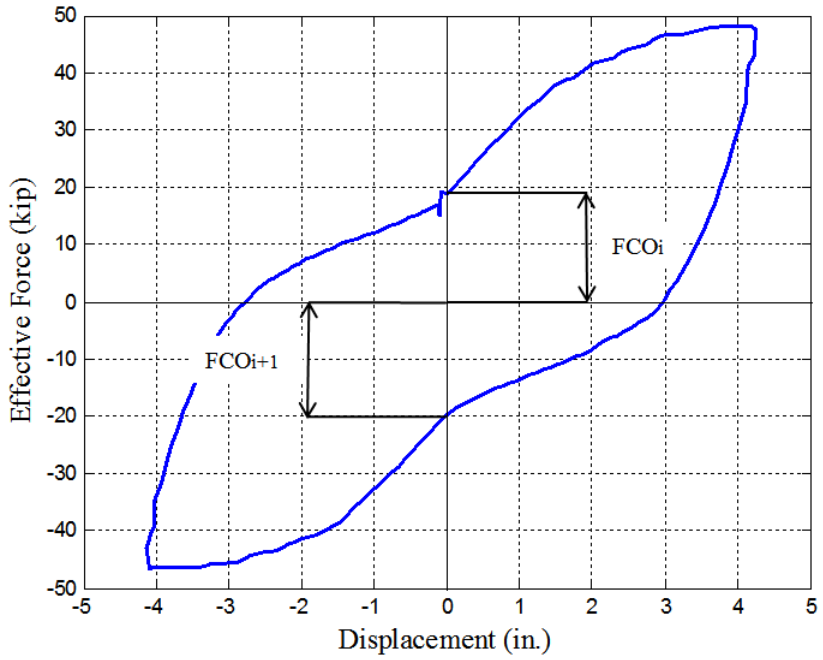

Figure 5-10. Definition of force cross-over (FCO) error

The error parameters used here differed from the ones used by Berry and Eberhard (2007). They used error measurements that calculated pushover error, stiffness ratio error, moment error, and degradation error. In this research, besides calculating the global force error, it was of special interest was to capture more accurately the column's response at low levels of excitation that might follow a large displacement excursion. For the purpose of this research, the low level response error was quantified by the "Displacement Cross-Over Error". The columns' hysteretic response at zero displacement was also deemed important. Lee and Billington (2010) concluded that a pinching in the hysteretic behavior of the concrete material in the range of zero horizontal column displacement causes the model to fail to capture residual displacements during dynamic analysis. For the purpose of capturing accurately the column's response at zero displacement, the "Force Cross-Over Error" was defined.

5.4.2 Objective Function

The objective function was a combination of the three error parameters:

$$\boldsymbol{E_{total}^{mean\ per\ run}} = \frac{\mathbf{1}}{\mathbf{3}}\frac{\sum_{i=1}^{n_{col}} \boldsymbol{E_{force}}}{\boldsymbol{n_{col}}} + \frac{\boldsymbol{\alpha_1}}{\mathbf{3}}\frac{\sum_{i=1}^{n_{col}} \boldsymbol{E_{DCO}}}{\boldsymbol{n_{col}}} + \frac{\boldsymbol{\alpha_2}}{\mathbf{3}}\frac{\sum_{i=1}^{n_{col}} \boldsymbol{E_{FCO}}}{\boldsymbol{n_{col}}} \quad 5\text{-}32$$

where

$$\boldsymbol{\alpha_1} = \frac{\boldsymbol{min_{all\ runs}}\left(\frac{1}{\boldsymbol{n_{col}}}\sum_{i=1}^{n_{col}} \boldsymbol{E_{force}}\right)}{\boldsymbol{min_{all\ runs}}\left(\frac{1}{\boldsymbol{n_{col}}}\sum_{i=1}^{n_{col}} \boldsymbol{E_{DCO}}\right)} \quad 5\text{-}33$$

$$\boldsymbol{\alpha_2} = \frac{\boldsymbol{min_{all\ runs}}\left(\frac{1}{\boldsymbol{n_{col}}}\sum_{i=1}^{n_{col}} \boldsymbol{E_{force}}\right)}{\boldsymbol{min_{all\ runs}}\left(\frac{1}{\boldsymbol{n_{col}}}\sum_{i=1}^{n_{col}} \boldsymbol{E_{FCO}}\right)} \quad 5\text{-}34$$

Here, n_{col} represents is the number of columns being simulated in each run and α_1 and α_2 ensure that the three error terms are of similar magnitude in the objective function. These parameters (α_1 and α_2) are defined by dividing the minimum mean E_{force} value from all runs by the minimum mean E_{DCO} value and the minimum mean E_{FCO} value from all runs, respectively.

The optimal column model with the new concrete model and the two steel models are evaluated in the next section.

5.5 Column Model Evaluation

The column model was optimized by changing discretely the input parameters in both the concrete and steel constitutive materials, as described in Section 5.2.2. The search for the best combination was performed for two scenarios.

- First, the simulations were conducted up to the point at which the effective lateral load resistance drops below 80% of the maximum resistance obtained earlier in the column's test history (hereinafter referred to as 80% run). The model was optimized first up to 80% of the maximum effective force, so that the models could be evaluated before significant degradation occurred, a degradation that is not represented in Steel02.

- Second, the simulations were conducted for the entire test history program for each test (hereinafter referred to as full-run). This scenario took into account the ability of the models to simulate degradation.

In some columns, (e.g., Specimen No. 4 by Moyer and Kowalsky 2001), the strength never dropped below 80% of its peak value, in which case the two scenarios were identical.

5.5.1 Concrete08 with Steel02

Table 5-6 summarizes the best combinations for both the 80% and full runs.

Table 5-6. Optimal constitutive model parameters for both 80%-run and full run

Optimization	Concrete08			Steel02				$mean\ E_{total}$ (%)
	α	C_{max}	R_0	cR_1	R_{inf}	ξ_{50}	b	
80%-run	~0.00	0.150	12.0	0.90	1.20	0.15	0.0125	8.93
Full run	1.00	0.005	16.0	0.94	0.96	0.15	0.0100	13.28

The steel constitutive parameter R_{inf} (derived from the Bauschinger effect parameters R_0 and cR_1) controlled the accuracy of the simulations more than did the early reloading features of the concrete model. For all combinations of concrete parameters, the minimum total error, E_{total}, was obtained at specific fixed values of R_{inf}. For the 80% run and the full run the R_{inf} values were 1.20 and 0.96, respectively.

Figure 5-11 shows a typical surface plot of mean E_{total} against R_{inf} and hardening ratio, b, for the 80%-runs and with the early concrete parameters fixed at α = 0.0, and C_{max} = 0.0 (in this case, the Concrete08 constitutive model defaults to Concrete04). The figure shows that the two variables, R_{inf} and b, essentially decouple and that the minimum occurs at $R_{inf} \approx 1.20$ for all b, and that the error is not sensitive to b. If R_{inf} is set equal to 1.0, Equation 5-20 simplifies to:

$$\boldsymbol{\sigma}^* = \left(\frac{\mathbf{1}+\boldsymbol{b}\boldsymbol{\varepsilon}^*}{\mathbf{1}+\boldsymbol{\varepsilon}^*}\right)\boldsymbol{\varepsilon}^* \qquad 5\text{-}35$$

For the 80% runs, the column displacements were moderate, so the steel strains were also moderate, in which case ε^* was not large and the value of b made little difference to the

predicted stress. On the other hand, the parameter R degraded fast enough that, in most cases, it parameter had its final value during most of the cyclic load history. R_{inf} thus influenced the total error more than did R_0.

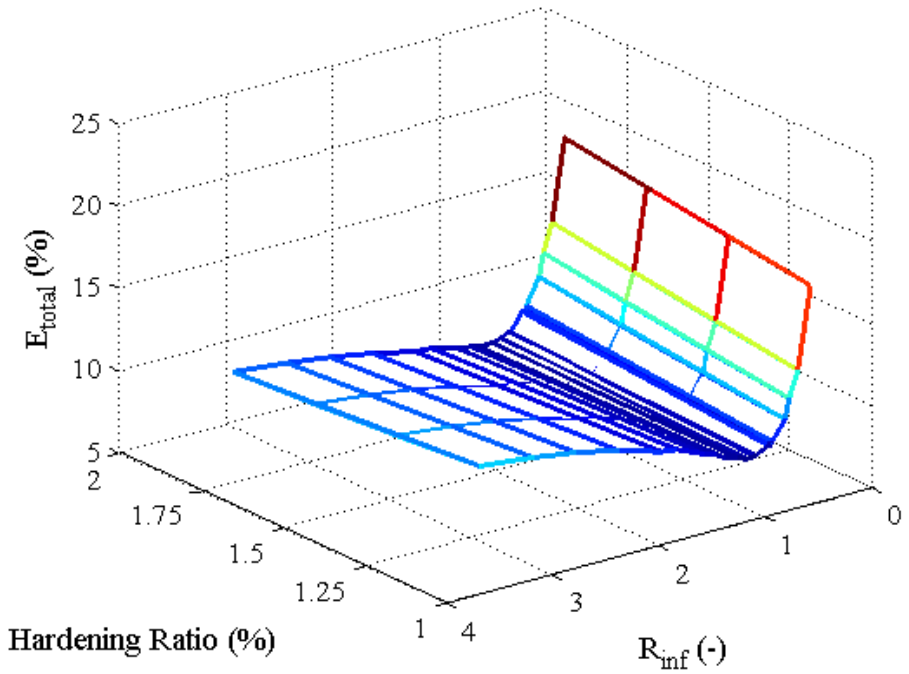

Figure 5-11. Typical surface plot of total error against $\boldsymbol{R_{inf}}$ and hardening ratio for 80%-run

Tables 5-7 and 5-8 show cyclic response statistics of the column model for both the 80% run and the full run using Concrete08 and Steel02. The tables compare cyclic statistics between three combination sets of input values for both Concrete08 and Steel02. The first column in both tables show the results using optimized values from Table 5-6, then the next column shows a so-called "Modified Optimization". In that column, α and C_{max} are set equal to 0.0 (i.e., model defaults to Concrete04), the hardening ratio, b, equal to 1.0%, and using same Bauschinger effect steel input values from Table 5-6. For comparison, the last column (i.e., Berry and Eberhard 2007) in both tables show the statistics using the recommended steel values to represent the transition curve (i.e., $R_{inf} = 1.39$, and $\xi_{50} = 0.15$) reported in the OpenSees manual (OpenSees Manual 2013) with a hardening ratio of 1.0% and without early concrete reloading.

Table 5-7. Cyclic response statistics for 80%-run using Concrete08 and Steel02

	Optimization (Table 5-6)			Modified Optimization			Berry and Eberhard (2007)		
	E_{cyclic}	$E_{cross\,\Delta}$	$E_{cross\,F}$	E_{cyclic}	$E_{cross\,\Delta}$	$E_{cross\,F}$	E_{cyclic}	$E_{cross\,\Delta}$	$E_{cross\,F}$
Mean (%)	8.97	5.89	16.53	8.87	6.04	16.53	9.20	6.59	17.13
Min (%)	4.94	1.77	7.19	5.25	2.21	7.11	5.58	1.81	6.33
Max (%)	16.05	43.14	29.95	15.51	45.14	29.98	15.04	46.74	38.21

Table 5-8. Cyclic response statistics for full run using Concrete08 and Steel02

	Optimization (Table 5-6)			Modified Optimization			Berry and Eberhard (2007)		
	E_{cyclic}	$E_{cross\,\Delta}$	$E_{cross\,F}$	E_{cyclic}	$E_{cross\,\Delta}$	$E_{cross\,F}$	E_{cyclic}	$E_{cross\,\Delta}$	$E_{cross\,F}$
Mean (%)	13.08	9.24	19.82	13.07	9.07	20.74	13.25	9.98	20.97
Min (%)	6.24	2.53	6.64	5.28	2.42	8.38	5.58	2.55	6.29
Max (%)	33.97	48.82	42.26	33.39	42.84	42.66	35.84	46.74	52.58

By setting α and C_{max} equal to 0.0, and the hardening ratio, b, equal to 1.0%, using the same R_{inf} values from Table 5-6, the mean total errors, E_{total}, for 80%-run and full-run did not increase significantly. They were 8.93% and 13.40%, respectively. In both runs, using the recommended values for the steel model and the concrete model with no early reloading, the error differences were higher, indicating that the steel model influenced the column model more than did the new concrete constitutive model. The errors were larger at the full-run than at the 80%-run, as expected. Even though the model did reasonably well for the full-run, it is not recommended for degrading systems.

Since R_{inf} was an important parameter for the overall simulation for both the 80%-run and the full-run, the model was run again up to 2% drift ratio by keeping R_{inf} values fixed at 1.0 and 1.2, for various R_0 using 32 columns, to determine an appropriate ξ_{50}. This was performed to accurately predict how fast the exponent $R(\xi)$ degrades in Equation 5-24. Columns No. 3 and 5 tested by Moyer and Kowalsky (2001) were not included because they did not have either force- or displacement cross-overs under 2% drift. Figures 5-12 and 5-13 show E_{total} versus ξ_{50} for

various R_{50} using a mild reinforcement hardening ratio of 1.0% and no early concrete reloading. Tables 5-7 and 5-8 show that the difference between simulations using a hardening ratio of 1.0% without early concrete reloading and 1.25% hardening ratio with early concrete reloading was minimal. Figures 5-12 and 5-13 show expected trends. When R_0 is very small (e.g., $R_0 = 8.0$), the total simulation error gets gradually smaller as ξ_{50} as increases. This is because ξ_{50} delays the already low R from converging to R_{inf}. As R_0 gets larger, two different trends can be observed. First, a large R_0 needs to degrade faster to R_{inf}, and this requires a low ξ_{50} value. This indicates that the sharp steel transition curve corner in the early cycles is causing a significant part of the error. Second, for a large ξ_{50} the error increases with a larger R_0, as expected.

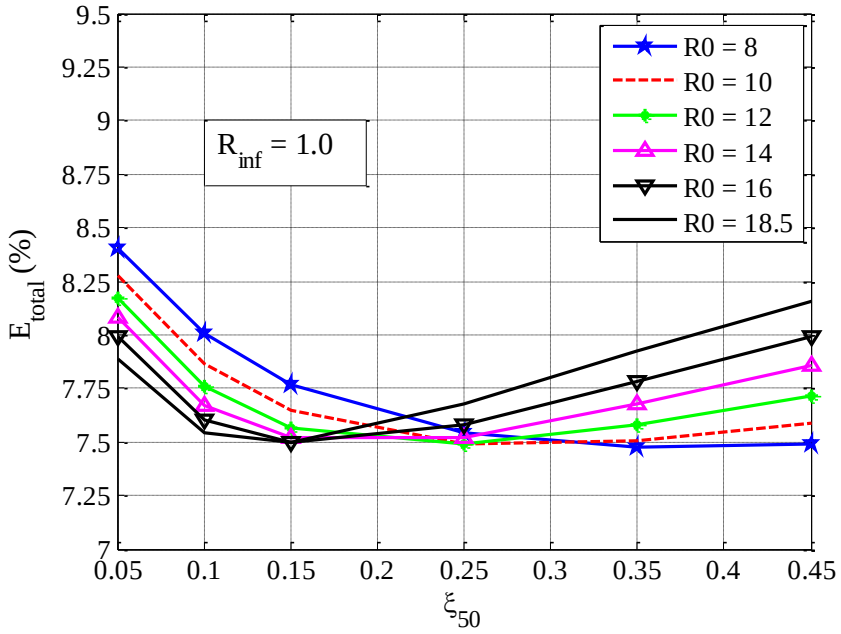

Figure 5-12. $\boldsymbol{E_{total}\ vs.\ \xi_{50}}$ for various $\boldsymbol{R_0}$ with $\boldsymbol{R_{inf} = 1.0}$ and $\boldsymbol{b}$ = 1.0%

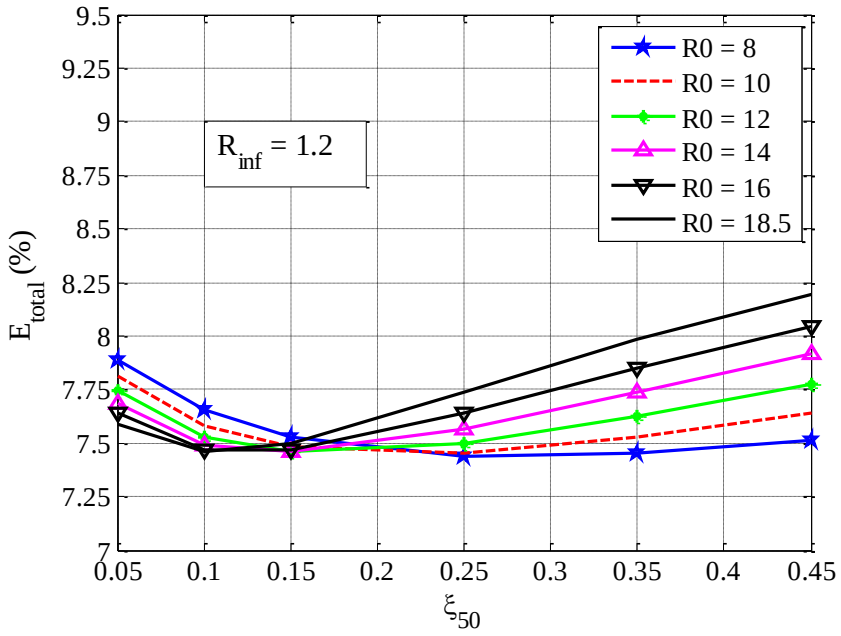

Figure 5-13. $\boldsymbol{E_{total}\ vs.\ \xi_{50}}$ for various $\boldsymbol{R_0}$ with$\boldsymbol{R_{inf} = 1.2}$ and $\boldsymbol{b}$, 1.0%

In general when a user is simulating an RC column quasi-statically, he or she first determines the extent of his simulation. Then the user decides on both R_0 and R_{inf}. Since the current implementation of Steel02 does not take R_{inf} as an input, cR_1 is derived by rearranging Equation 5-24 and ξ_{50} is obtained from either Figure 5-12 or 5-13. For example if he decides to simulate an RC column up to 80% of the peak effective force (R_{inf} = 1.0) using R_0 equal to 18.5, Equation 5-24 yields cR_1 to be 0.946 and Figure 5-12 ξ_{50} to be 0.15.

Figures 5-14 and 5-15 compare the measured and calculated force-deformation responses for eight columns in the dataset, from Table 5-5, using the optimized values from Table 5-6. These columns were tested by Lehman and Moehle (2000) and represent a good range of RC bridge columns in terms of span-to-depth (L/D), longitudinal reinforcement (ρ_l), and axial force ($P/A_g f'_c$).

Figure 5-14 shows that the column behavior was accurately captured up to 80% of the maximum effective force. It should be noted that the drift at which the strength first falls to 80% of the peak is larger in more slender columns. This occurs because the elastic deformations

represent a larger proportion of the total than is the case in stockier columns. At the full run, the simulation of the columns became less accurate and failed to capture the column softening. This lower accuracy is shown in Figure 5-15.

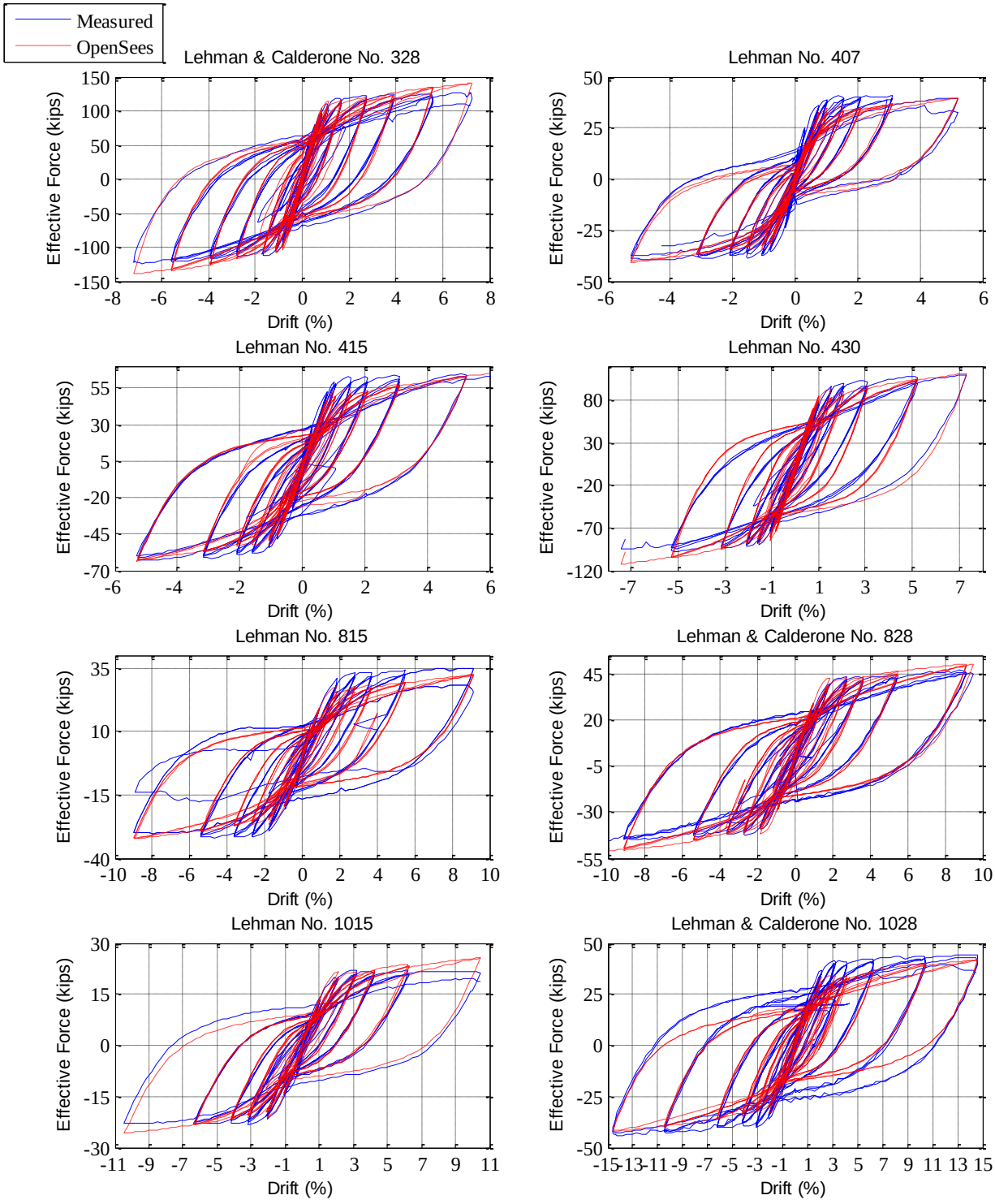

Figure 5-14. Effective force-drift responses for Lehman, Calderone, and Moehle dataset for 80% run using Concrete08 with Steel02

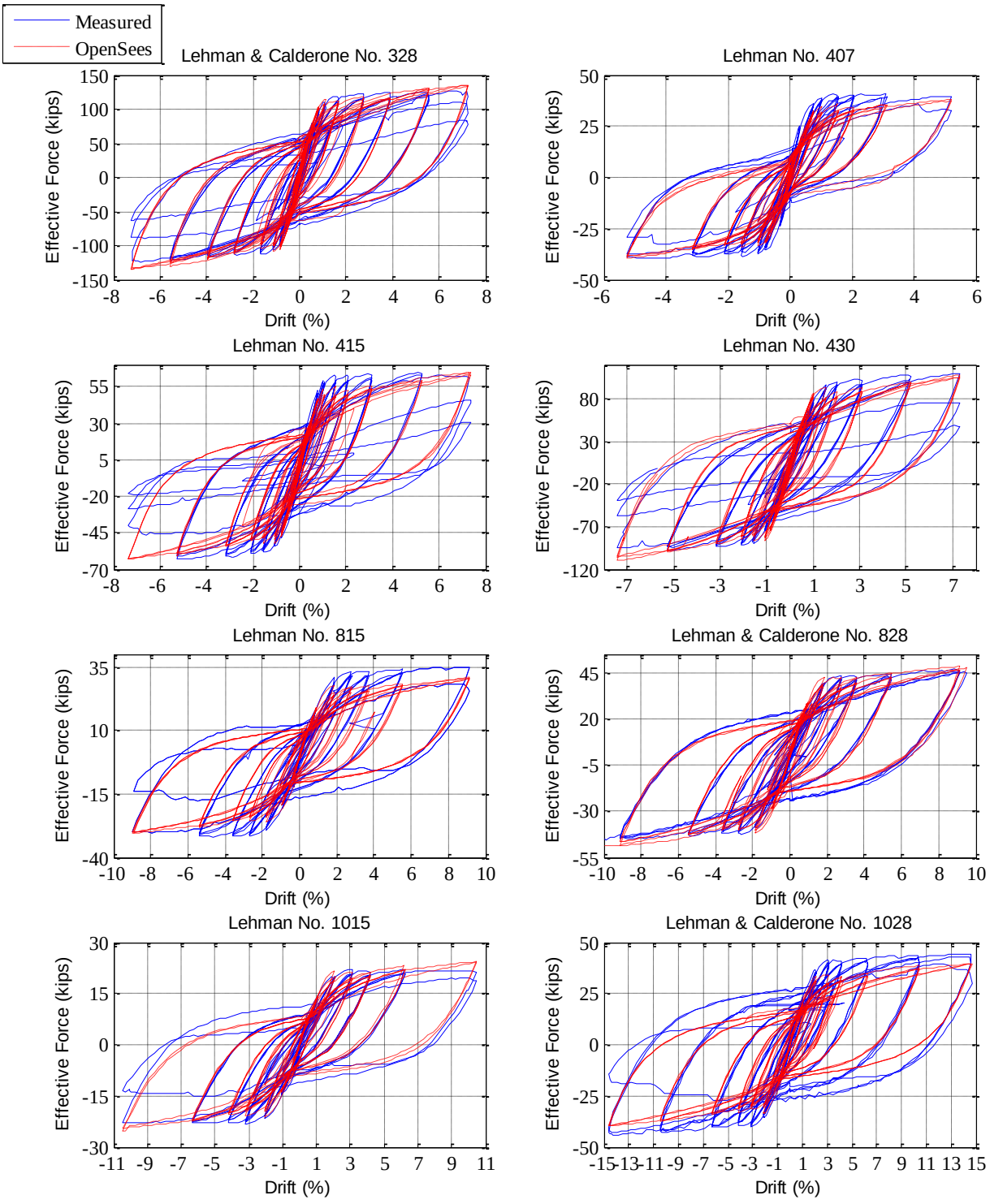

Figure 5-15. Effective force-drift responses for Lehman, Calderone, and Moehle dataset for full-run using Concrete08 with Steel02.

5.5.2 Concrete08 with ReinforcingSteel

In optimizing the combination of Concrete08 and ReinforcingSteel, the parameters optimized were the fatigue parameters, C_f and C_d, in the steel constitutive model and the early reloading parameters in Concrete08 (i.e., α and C_{max}). A total of 30 columns were considered. Four columns were omitted from this study due to convergence problems (N1 by Stone and Cheok 1989, FL3 by Kowalsky et al. 1999, A2 by Kunnath et al. 1997, and No. 2 Moyer and Kowalsky 2001).

As described in Section 5.2.2.3, the ductility constant, C_f, was determined first. The procedure outlined there resulted in an optimal C_f value of 0.28. This value differs slightly from the 0.26 obtained by Berry and Eberhard (2007). The column model was then run by varying the concrete parameters in Concrete08 and the strength reduction parameter, C_d, in ReinforcingSteel. Table 5-9 lists the best results with C_f fixed to a value of 0.28.

Table 5-9. Optimal constitutive model parameters for 80%-run and full run with $\boldsymbol{C_f = 0.28}$

Optimization	Concrete08		ReinforcingSteel		$mean\ E_{total}$ (%)
	α	C_{max}	C_f	C_d	
80%-run	~0.00	0.100	0.28	0.41	9.40
Full-run	~0.00	0.100	0.28	0.39	10.31

Tables 5-10 and 5-11 compare the cyclic response statistics of both the 80%-run and the full for three combinations of input parameters. The first set of parameters was selected from Table 5-9, and the second set of parameters assumed that the concrete model would default to Concrete04. The third column shows the simulation statistics recommended by Berry and Eberhard (2007), in which the calibrated ductility constant, C_f, and strength reduction constant, C_d, are equal to 0.26 and 0.45, respectively.

Both tables show that the best result is obtained with the optimized parameters from Table 5-9, as expected. The simulation accuracy was slightly decreased by removing the early reloading component from Concrete08. For the Modified Optimization, the mean total error, E_{total} in Equation 5-32, for the 80%-run and the full-run increased to 9.77% and 11.93%,

respectively. Similarly, the simulation accuracy was the least of the three using steel parameters obtained by Berry and Eberhard (2007), and Concrete08 with no early reloading.

Table 5-10. Cyclic response statistics for 80%-run using Concrete08 and ReinforcingSteel

	Optimization (Table 5-9)			Modified Optimization			Berry and Eberhard (2007)		
	E_{cyclic}	$E_{cross\,\Delta}$	$E_{cross\,F}$	E_{cyclic}	$E_{cross\,\Delta}$	$E_{cross\,F}$	E_{cyclic}	$E_{cross\,\Delta}$	$E_{cross\,F}$
Mean (%)	9.79	6.25	18.29	9.96	6.48	19.46	10.55	6.63	20.25
Min (%)	5.91	1.76	6.41	5.91	1.76	5.40	5.72	1.74	6.32
Max (%)	20.98	44.06	32.25	22.64	44.06	32.25	23.32	43.38	33.22

Table 5-11. Cyclic response statistics for full run using Concrete08 and ReinforcingSteel

	Optimization (Table 5-9)			Modified Optimization			Berry and Eberhard (2007)		
	E_{cyclic}	$E_{cross\,\Delta}$	$E_{cross\,F}$	E_{cyclic}	$E_{cross\,\Delta}$	$E_{cross\,F}$	E_{cyclic}	$E_{cross\,\Delta}$	$E_{cross\,F}$
Mean (%)	10.20	7.63	19.50	10.45	11.15	20.73	10.91	11.21	21.53
Min (%)	5.80	2.00	6.90	6.05	2.02	4.83	5.71	2.02	6.32
Max (%)	19.26	43.66	40.73	23.17	44.42	34.41	23.39	43.38	36.00

Figures 5-16 and 5-17 compare the measured and calculated force-deformation responses for the eight columns in the dataset tested by Lehman and Moehle (2000) using the optimized values from Table 5-9. Figure 5-16 shows that model captured reasonably well the column behavior up to 80% of the maximum effective force. Simulation of Lehman & Calderone 1028 was good up to 10% drift but failed to simulate well the cycles at 14% drift. For the full-run, the effect of the degradation in the steel model was evident.

A comparison of tables 5-7 and 5-10 shows that the simulation of the RC columns was slightly more accurate for 80%-run with Steel02 constitutive model using values from Table 5-6, with or without the early reloading effect in the concrete, than the ReinforcingSteel model. Even if the column data is reduced from 34 columns to 30, the mean total errors were still smaller using Steel02. The mean error for the model using the steel values in Table 5-6 without early concrete reloading was 7.37%. For the full-run simulation, it is more appropriate to use the ReinforcingSteel constitutive model as it takes into account degradation of the steel.

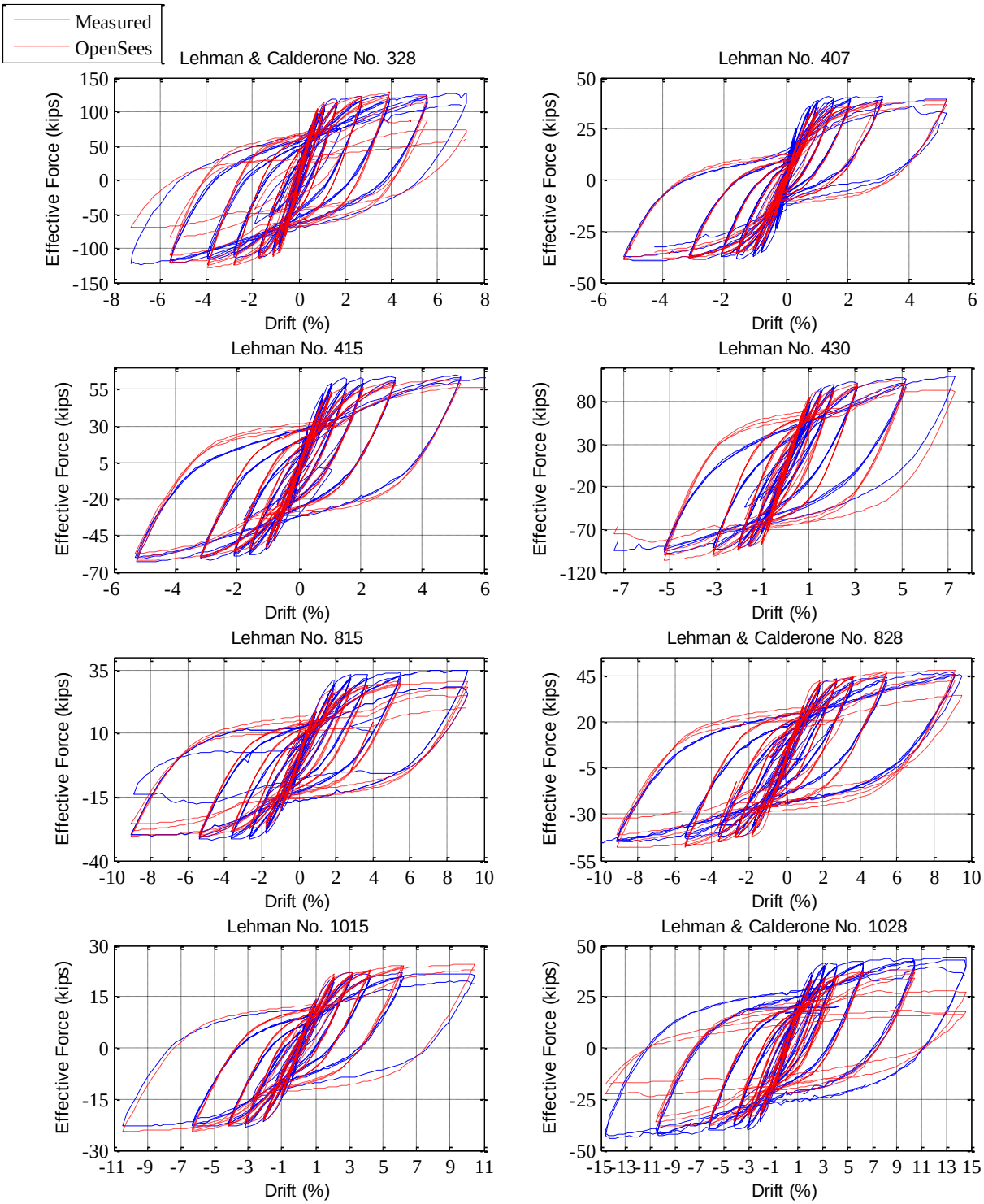

Figure 5-16. Effective force-drift responses for Lehman, Calderone, and Moehle dataset for 80%-run using Concrete08 with ReinforcingSteel

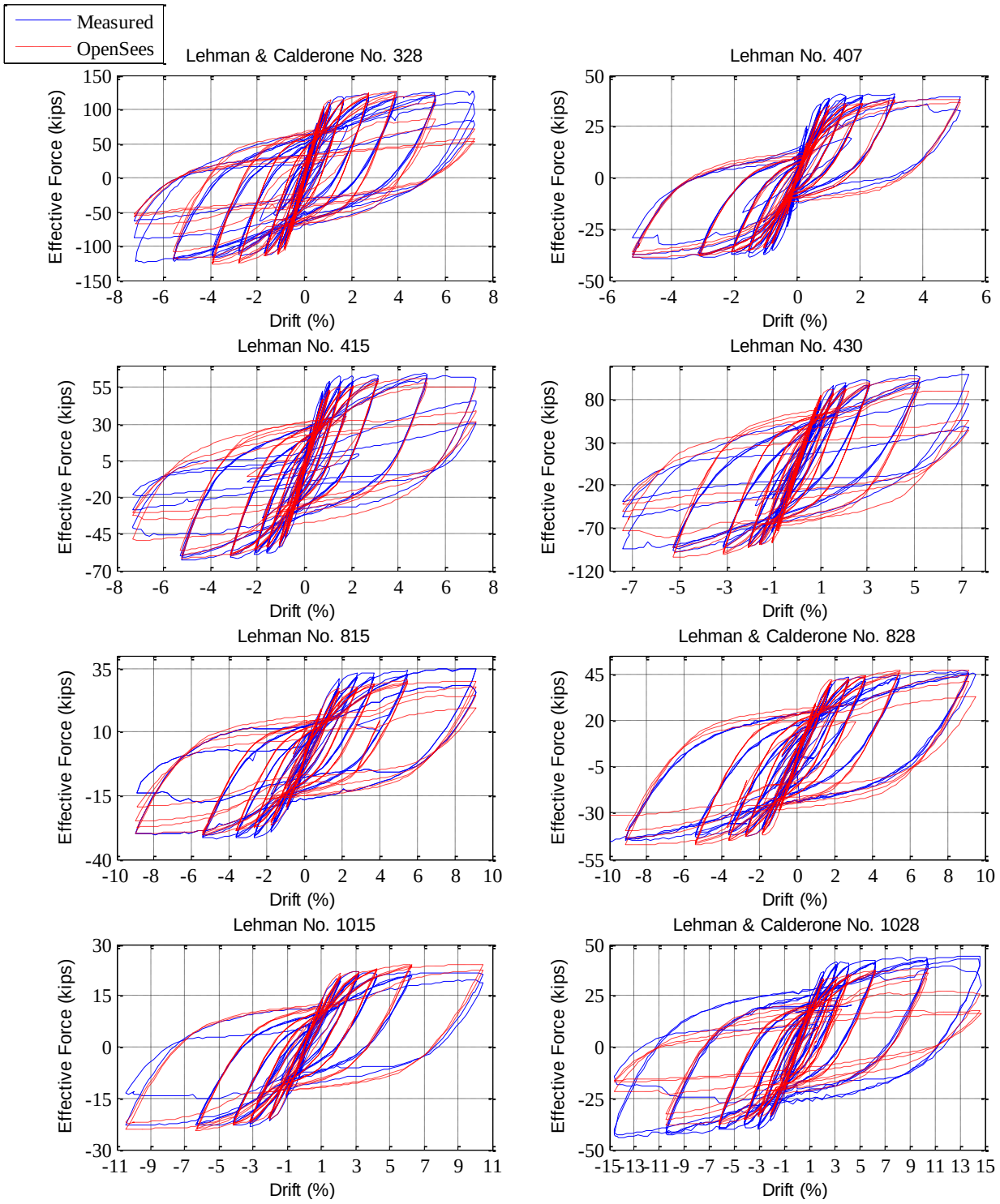

Figure 5-17. Effective force-drift responses for Lehman, Calderone, and Moehle dataset for full run using Concrete08 with ReinforcingSteel

5.6 Summary

In this chapter, a lumped-plasticity column model was implemented in OpenSees following recommendations provided by Berry and Eberhard (2007). The simulation strategy was optimized for the Concrete08 concrete constitutive model, which was recently developed, and for two steel constitutive models; Giuffre-Menegotto-Pinto's (Steel02) model, and Mohle and Kunnath's (ReinforcingSteel) model.

Commonly used concrete models assume perfect crack closure and do not take into account the fact that tension cracks get partially filled with small particles of concrete and that shear deformations may result in misaligned cracks, both of which result in early re-loading. The new concrete model allows the concrete to reload before the cracks are fully closed.

The simulation strategy was optimized to capture as accurately as possible the force-displacment response of RC columns. The variables that were free to change during the optimization were the parameters in the constitutive models. The lumped-plasticity model was calibrated twice, since the two steel models are fundamentally different. Steel02 does not model cyclic degradation whereas ReinforcingSteel does. Thus first, the model was optimized up to the first point where the effective lateral load resistance drops below 80% of the maximum resistance obtained earlier in the test history (referred to as 80%-run), and then throughout the entire test history program for each test (referred to as full-run). The following was observed in this study:

- The steel constitutive modeling influences the global behavior more than does the concrete. This observation applies to both the 80%- and full-runs.
- Suppressing the early reloading option in the concrete constitutive model caused only a minimal decrease in accuracy
- On average, for the 80%-run, Steel02 simulated the column data set better than did ReinforcingSteel. For these limited displacements, the columns did not show significant softening. At large deformations and increased cycling (i.e., full-run), ReinforcingSteel simulated the data set better, as expected, because it takes into degradation of the steel

but Steel02 does not. Recommendations for steel parameter inputs for Steel02 and ReinforcingSteel are provided in sections 5.5.1 and 5.5.2.

6 SINGLE-COLUMN SHAKE-TABLE TEST PROGRAM

This chapter contains a description of shaking table tests on two single-column subassemblies that were used for the development of the pre-tensioned bent system.

6.1 Introduction

In 2011, the Pacific Earthquake Engineering Research Center (PEER) initiated a research program to investigate new resilient columns designed to re-center to their original plumb position after being displaced during an earthquake. Four cantilever column-to-footing specimens were designed, constructed, and tested dynamically on the shaking table at the Richmond Field Station Earthquake Simulation Laboratory of the University of California (UC) at Berkeley. The test program was a collaboration between UC Berkeley, UC San Diego, and University of Washington.

Three of the specimens were examples of a new technology, in which unbonded prestressing is used to re-center the column after the ground motion stops. The fourth column served as a non-prestressed reference specimen, detailed according to current standards and practice (Schoettler et al. 2013). The three new designs consisted of:

- an unbonded post-tensioned rocking column with Hybrid Fiber Reinforced Concrete (HyFRC) in the plastic hinge region (from UC Berkeley, Trono et al. 2013),
- an unbonded post-tensioned rocking dual-shell column (from UC San Diego, Guerrini and Restrepo 2013), and
- a precast, unbonded pre-tensioned column (from the University of Washington).

The two rocking columns were designed to rock as rigid bodies about their bases, while the pre-tensioned column was intended to deform in a continuous curve like a conventional column. Out of all three new column designs, the unbonded, pre-tensioned column resembled most closely the reference column. The main difference was that it included unbonded pre-tensioned strands, for re-centering purposes, and a plastic hinge region that was made of a Hybrid Fiber-Reinforced Concrete (HyFRC) shell, filled with conventional concrete, to reduce spalling.

In June 2012, shake table tests were performed on the prestressed columns to evaluate their seismic performance, and in particular their ability to re-center to their original plumb position. The reference column was tested in December 2012. Here, the discussion will focus on a description of the reference and unbonded, pre-tensioned columns and the experimental program. Key experimental findings and a performance evaluation of the two specimens will be presented in chapters 7 and 8, respectively. More detailed information about the reference specimen described in this chapter can be found in Schoettler et al. 2013.

6.2 Description of the Test Specimens

Table 6-1 lists the properties of the reference specimen and the pre-tensioned column. Both were 16-in. diameter (D) cantilever columns with height (L) from the foundation to center-of-mass (COM) of 96 in., resulting in a span-to-depth ratio (L/D) of 6.0. This geometry represented, at 33% scale, a 48-in. diameter single column bent, 24 ft high. All specimens in the test program had a 60-in. x 60-in. x 20-in. cast-in-place spread footing designed to remain elastic throughout test program. Any damage in the footing would have jeopardized the primary objective of the research which was to investigate the columns' re-centering capability.

Table 6-1 shows that the transverse reinforcement ratio (ρ_{spiral}) was kept same the same in both specimens but they differed in terms of column longitudinal mild reinforcement ratio (ρ_l). The axial load ratio ($P_{axial}/A_g f'_c$) from the mass blocks differed between specimens since the concrete strength in the reference was considerable lower than in the pre-tensioned specimen (Table 6-2), but the total axial load ratio ($P_{total}/A_g f'_c$) differed slightly because the unbonded pre-tensioned specimen included prestressing strands. The last column shows the calculated re-centering ratio (λ_{re}) both shaking table test, using Equation 4-1 in Chapter 4, using measured material properties. The re-centering ratio of the pre-tensioned specimen was calculated using effective concrete strength from the conventional concrete in the core and the HyFRC in the shell.

Table 6-1. Shake-table bridge column dataset

Reference	Specimen[1]	L (in.)	L/D	ρ_l (%)	ρ_{spiral} (%)	Pre-tension	$\frac{P_{axial}}{A_g f'_c}$ [4] (%)	$\frac{P_{total}}{A_g f'_c}$ (%)	λ_{re}
Schoettler et al. 2013	CIP-SF-REF-SHK	96	6.0	1.59	0.88	None	7.89	7.89	0.26
Haraldsson	PreT-SF-FIB-SHK[2]	96	6.0	0.75	0.88	8-3/8 in. s[3]	3.33	9.92	1.39

1. CIP /PreT := Cast-in-Place /Pre-Tensioned
   SF := Spread Footing
   FIB := Fiber Concrete
   REF/SHK:= Reference/Shake
2. Octagonal column cross-section
3. s := strands
4. P_{axial} refers to dead load applied

Table 6-2 lists the measured material properties for both specimens.

Table 6-2. Shake table bridge column dataset measured properties

Reference	Specimen	$f'_{c,col}$[1] (psi)	$f'_{c,HyFR}$1 (psi)	$f_{t,HyFR}$[1] (psi)	$f'_{c,fot}$[1] (psi)	$f_{y,l}$ (ksi)	$f_{u,l}$ (ksi)	$f_{y,s}$ (ksi)	$f_{u,s}$ (ksi)
Schoettler et al. 2013	CIP-SF-REF-SHK	3,278	None	None	5,032	63	94.4	79.0	93.9
Haraldsson	PreT-SF-FIB-SHK[2]	7,209	8,065	1,068	4,860	68	99.1	64.0	94.6

1. Average concrete strength on day of test

Footing and column concrete design strength, $f'_{c,col}$, for both columns was specified to be 4.0 ksi. Specimen CIP-SF-REF-SHK did reach the design strength for the footing but did not reach the design strength for the column. Consequently, the observed stiffness and estimated yield displacement were larger than expected (Schoettler et al. 2013). For Specimen PreT-SF-FIB-SHK, both the column, $f'_{c,col}$ and $f'_{c,HyFRC}$, and the footing exceeded the minimum specified strength of 4 ksi. The tensile strength HyFRC, $f_{t,HyFRC}$, was noticeably higher than in typical conventional concrete. The split breaks were similar to what is typically seen in fiber mixtures; the samples began to crush locally under the loading plate and subsequently formed tension cracks, but nevertheless continued to show resistance.

Tension tests were performed on the longitudinal reinforcement for both specimens. All longitudinal reinforcement conformed to ASTM A706 with a minimum specified yield stress of 60 ksi. The A706 longitudinal bars exceeded their minimum specified yield stress, $f_{y,l}$, of 60 ksi. In fact, the bars in Specimen PreT-SF-FIB-SHK reached 68 ksi, which is the expected value that AASHTO Guide Specifications recommends to be used for design. In both specimens, the ultimate tensile stress, $f_{u,l}$, was above 90 ksi. The spiral strength of Specimen PreT-SF-FIB-SHK was measured to be 64 ksi, $f_{y,l}$, (yield strain was taken to be 0.35% to be consistent with earlier spiral tests at the University of Washington) which is less than the specified strength of 70 ksi for ASTM A82. This low value is attributed to the fact that the spiral was coiled up and needed to be straightened out before tensile testing. Schoettler et al. 2013 report the yield stress of Specimen CIP-SF-REF-SHK was 79.0 ksi, using a 0.20% strain method.

In the following subsections, the specimens will be described in more detail. Specimen drawings can be found in Appendix A.

6.2.1 Reference Cast-in-Place Column (CIP-SF-REF-SHK)

The prototype column for the test program was detailed according to the AASHTO Load Resistant Factor Design (2012), AASHTO Guide Specifications for LRFD Seismic Design (2011), and Caltrans Seismic Design Criteria (2006).

The prototype design had a 48-in. diameter column and was reinforced longitudinally with 18 No. 11 bars, resulting in a longitudinal reinforcement ratio, ρ_l, of 1.6%. This value was chosen to represent a typical Caltrans design. The column was transversely reinforced with a No. 5 spiral at 3.25 in. pitch, resulting in a transverse reinforcement ratio, ρ_s, of 0.88%. The column clear cover to the spiral was 2.25 in. The height from the top of the foundation to the center of gravity in the superstructure was assumed to be 24 ft.

Specimen CIP-SF-REF-SHK was a 33.3% scale cantilever model of the prototype column, resulting in a 16-in. diameter column 0.75-in. clear cover. The test specimen's aspect ratio was kept at 6.0 to match the prototype column geometry. This aspect ratio also matched previous shake table test programs (i.e., Jeong et al. 2008 and Hachem et al. 2003). To keep the same

longitudinal reinforcement ratio as in the prototype, Specimen CIP-SF-REF-SHK was reinforced with 16 No. 4 longitudinal bars. The spiral in the test specimen was made from 4-gauge (0.225-in. diameter) A82 smooth wire at a pitch of 1.25 in., to keep the transverse reinforcement ratio the same as in the prototype column. Wire was used because A706 reinforcement is not produced in a size smaller than No. 3.

The concrete design strength was 4 ksi in both the footing and the column. Figure 6-1 shows Specimen CIP-SF-REF-SHK's.

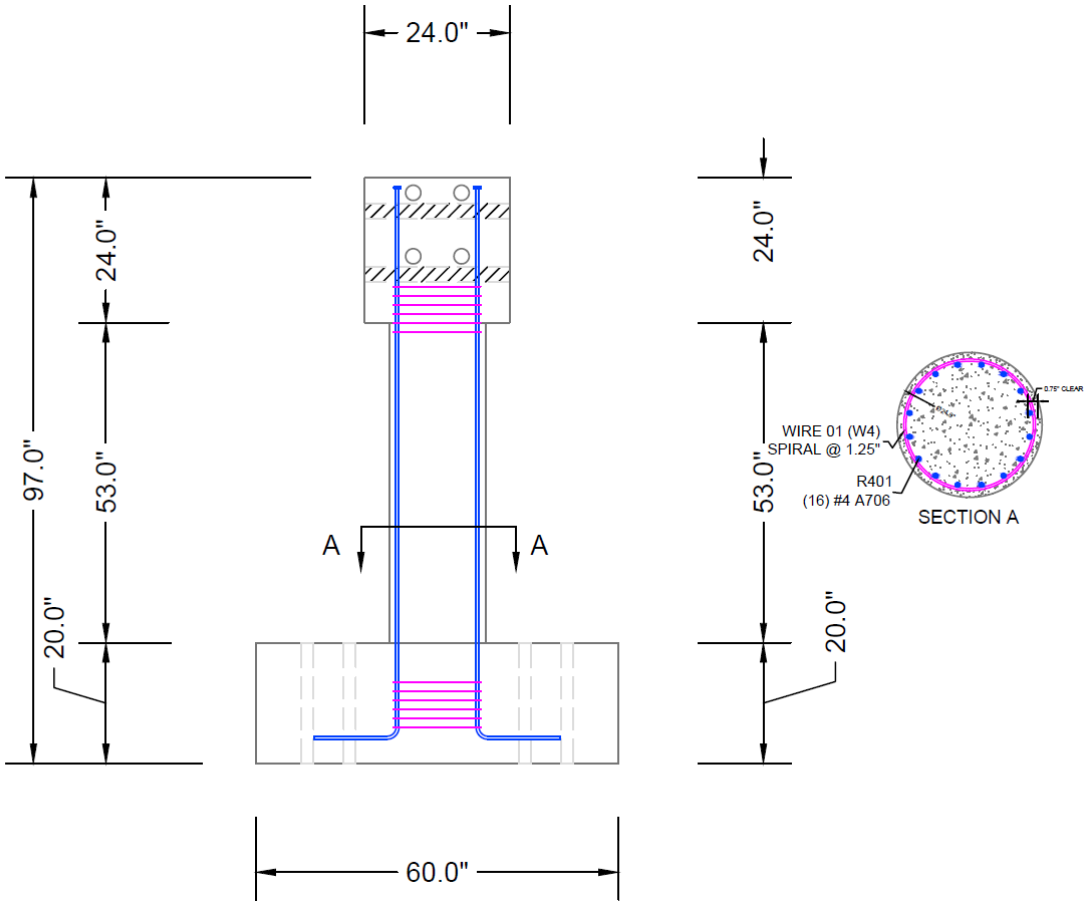

Figure 6-1. Specimen CIP-SF-REF-SHK elevation

6.2.2 Unbonded Pre-Tensioned Column with HyFRC (PreT-SF-FIB-SHK)

Specimen PreT-SF-FIB-SHK was designed to have the same moment strength as the reference column and to re-center by means of unbounded pre-tensioning. The configuration of the

reinforcement was similar to that used by Davis et al. (2012) and Finnsson et al. (2013). The design concept was to select an optimal amount of mild reinforcement to pre-tension steel to increase the column re-centering capability. The pre-tension strands are sleeved in the clear height of the column (to distribute the strains) and bonded in the footing and the cap-beam. In contrast to the reference column (Specimen CIP-SF-REF-SHK), Specimen PreT-SF-FIB-SHK column cross section was made as an octagon (16 in. across flats, $A_g = 212.1\ in^2$) instead of circular to facilitate fabrication of the column.

To achieve both the moment strength and re-centering, the ratio of contribution to the column flexural strength of the mild reinforcement and unbonded pre-tensioned strands were chosen to be 40% and 60%, respectively. To match the moment-curvature analysis of the reference specimen, the final design was eight No. 4 bars ($A_s = 1.6\ in^2$, $\rho_l = 0.75\%$) and eight 3/8-in. diameter strands ($A_p = 0.68\ in^2$, $\rho_p = 0.32\%$). Epoxy-coated prestressing strands were used to improve bond and minimize corrosion. The transverse column reinforcement was identical to that of the reference specimen, or A82 4-gauge spiral at 1.25-in. pitch (ρ_s = 0.88%). Figure 6-2 shows Specimen PreT-SF-FIB-SHK's elevation.

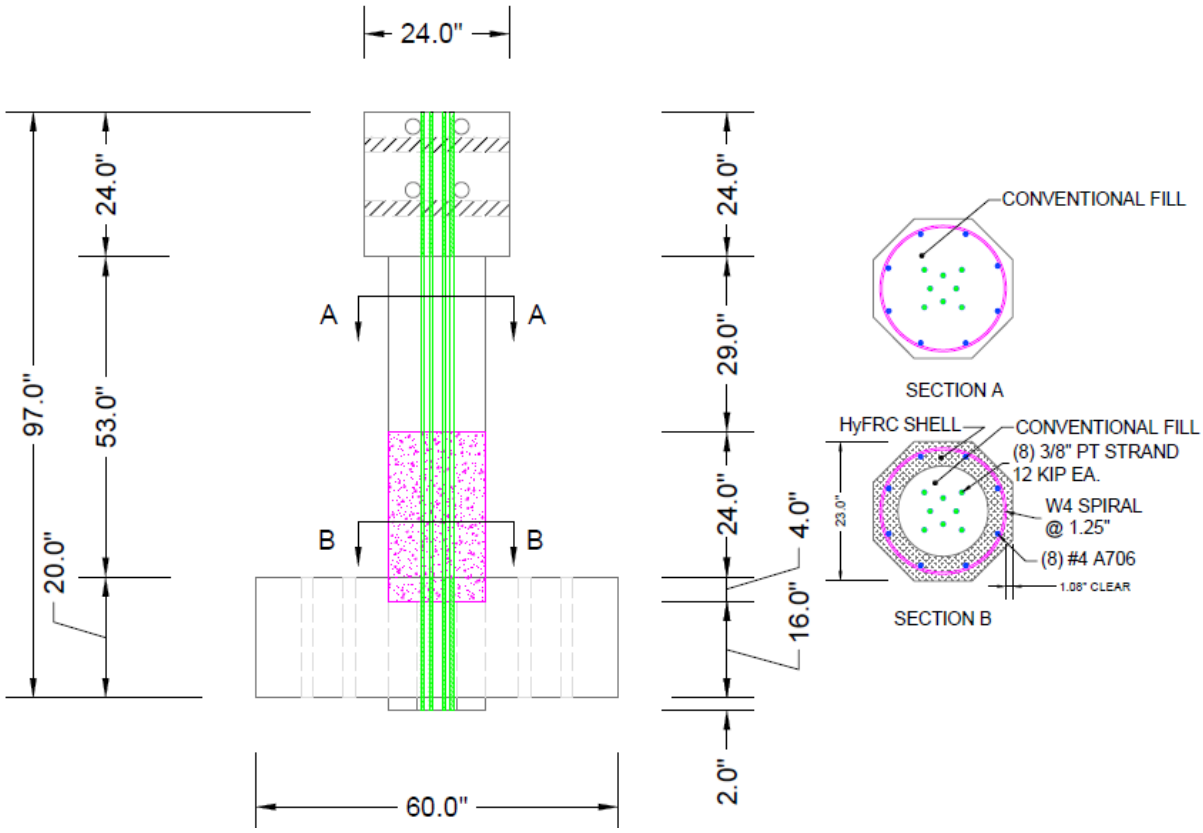

Figure 6-2. Specimen PreT-SF-FIB-SHK elevation

Besides having prestressed strands, the specimen differed from the reference specimen by also including a shell in the plastic hinge region, as shown schematically in Figure 6-3. The shell was made of Hybrid Fiber Reinforced Concrete (HyFRC) that has been shown to provide better damage resistance and seismic performance (Kumar et al. 2011) than that of conventional concrete. The height of the shell was 28 in. with a wall thickness of 2.8 in. The shell extended 4 in. into the spread footing to avoid the cold joint opening at the column-to-footing interface, therefore leaving 24 in. (or $1.5Dc$) extending up the column. To increase bond between the HyFRC shell and the regular concrete, the inside of the shell was spirally roughened with a 3/16-in. diameter wire at 1.5-in. pitch. The concrete design strength was 4 ksi in both the footing and the column (both conventional concrete and HyFRC).

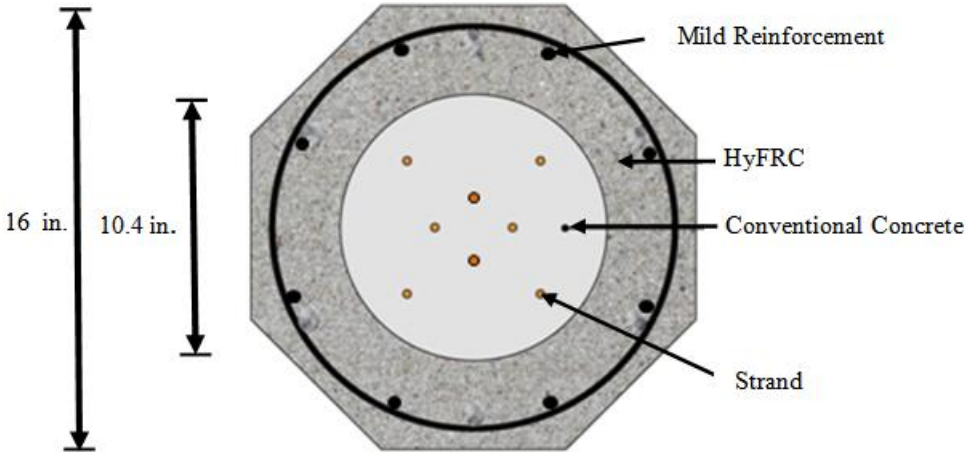

Figure 6-3. Schematic section of plastic hinge region (Finnsson et al. 2012)

The column was designed to have the strands remain elastic up to 3.0% drift. The strands were placed in the column core and jacked up to a stress of 162 ksi, which resulted in a computed effective stress of 141.7 ksi in the column after initial and long-term losses (assuming a nominal initial concrete strength of 5,000 psi with a nominal modulus of 4,000 ksi). A shrinkage strain of 300 micro-strain (or 8.6 ksi prestress loss) and a creep loss of 7.8 ksi (twice the initial elastic loss) were assumed. The total force in the column after stress transfer was 97 kips, which resulted in a compressive stress in the concrete of 457 psi.

The precast column was connected to the spread footing by a wet socket connection, as described by Haraldsson et al. 2013. The base of the column that was embedded in the cast-in-place spread footing was roughened using a saw-tooth detail, using one third of the prototype dimensions recommended by Haraldsson et al. (0.71 in. amplitude at 1.41 in. spacing). The part of the shell that extended into the foundation was not roughened with the saw-tooth detail but rather with a retarder with a sandblast finish. This was done to allow the shell not to be completely locked down in the foundation.

6.2.2.1 Construction of Unbonded Pre-Tensioned Column with HyFRC (PreT-SF-FIB-SHK)

The column was fabricated entirely in the Structural Laboratory at the University of Washington. First, the precast Hybrid Fiber Reinforced Concrete (HyFRC) shell was constructed for the column plastic hinge region. To begin with, the column cage was tied only for the shell portion of the column and then placed in the shell form, as shown in Figure 6-4. Before the cage was installed, threaded couplers for curvature rods were attached inside the form. A Sonotube was subsequently placed inside the shell form to create a void for the prestressing strands. It had steel wire wrapped around it, secured by duct tape, to form a roughened surface that would permit bond to the core concrete that was cast later.

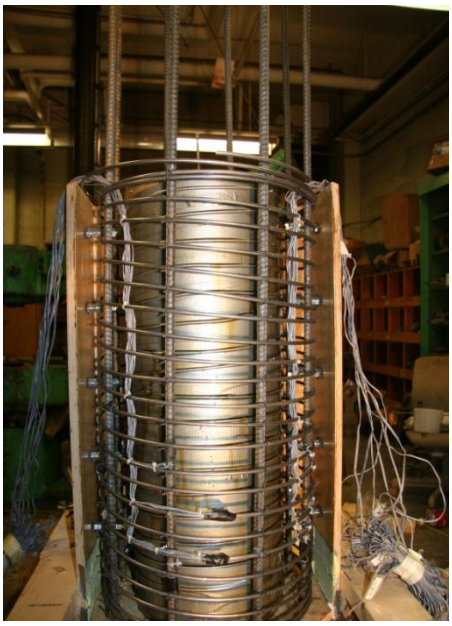

Figure 6-4. HyFRC shell form before closing

The HyFRC was mixed in a drum mixer in three batches. The first two batches were mixed together in a wheelbarrow to avoid any discontinuity between the two first batches that constituted the majority of the HyFRC shell. The third batch finished filling the shell form and was used for concrete test cylinders. Internal vibration was almost impossible because the shell wall was narrow and contained a lot of steel, so the HyFRC mix was vibrated externally by

placing the vibrator sideways on the shell formwork. A detailed description HyFRC mixing procedure can be found in a report by Finnsson et al. 2013.

Once the HyFRC shell had cured, the reinforcing cage was completed by adding the spiral outside the shell, and it was then placed in a custom-built horizontal octagonal wood form lying inside a prestressing rig (figures 6-5 and 6-6). The roughened surface at the base of the precast column was formed by nailing wood strips inside the octagonal form. The prestressing rig was fabricated specifically for this project (see Figure 6-7). The strands were led through the column and stressed. Figure 6-8 shows a strand being jacked to a stress of 162 ksi. The column was cast with a Type III cement concrete mix (designed to reach strength of 6,000 psi in 7 days) to allow for early release of the strands. The concrete was cast from one end of the column to prevent air to be trapped in the shell. Figure 6-9 shows the pre-tensioned column ready to be cast.

After releasing the strands, the precast column was shipped to the University of California at Berkeley where the spread footing formwork was constructed and the footing cage was tied, as shown in Figure 6-10. The column was lifted, positioned in the spread footing, and braced, as shown in Figures 6-11 and 6-12. The positioning of the column took approximately 15 minutes.

Figure 6-5. Specimen PreT-SF-FIB-SHK before installation in prestressing rig

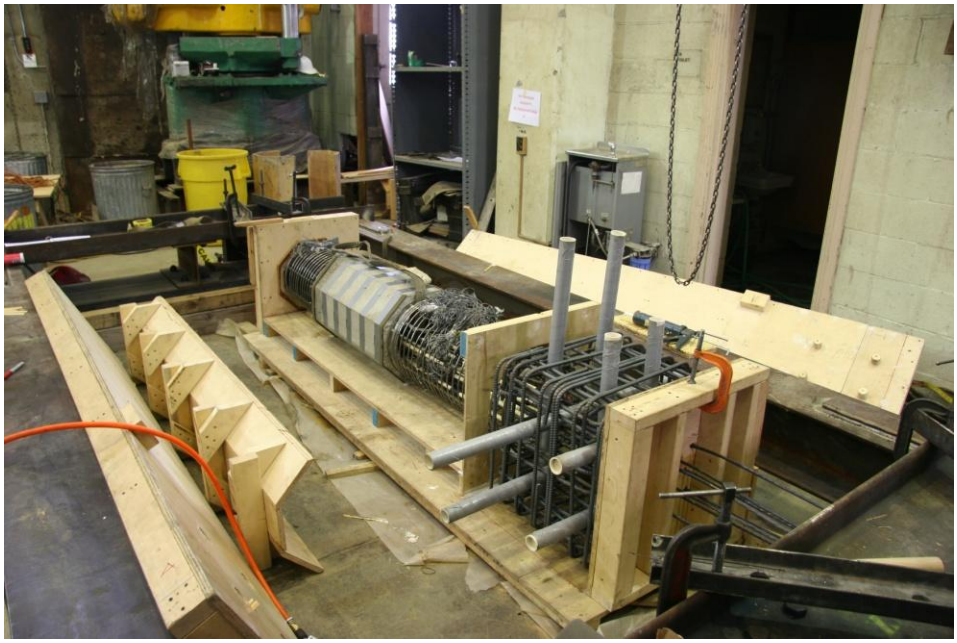

Figure 6-6. Specimen PreT-SF-FIB-SHK column installed in prestressing rig

Figure 6-7. Prestressing rig fabricated for Specimen PreT-SF-FIB-SHK

Figure 6-8. Stressing of the column strands

Figure 6-9. Specimen PreT-SF-FIB-SHK ready to be cast

Figure 6-10. Spread footing ready for installment of Specimen PreT-SF-FIB-SHK

Figure 6-11. Specimen PreT-SF-FIB-SHK being lowered into the foundation

Figure 6-12. Specimen PreT-SF-FIB-SHK braced and ready for casting of the foundation

6.3 Shake-Table Setup and Global Coordinate System

Figure 6-13 shows the test setup for both specimens CIP-SF-REF-SHK and PreT-SF-FIB-SHK. The table is 20 ft x 20 ft and is controlled in all six degrees-of-freedom. The table limits are:

- Horizontal displacement in each principal direction (north-south, east-west) is ± 5 in. Vertical displacement is ± 2 in.
- All axis velocity is 30 in./s with an unloaded table
- All axis acceleration is 3g with an unloaded table

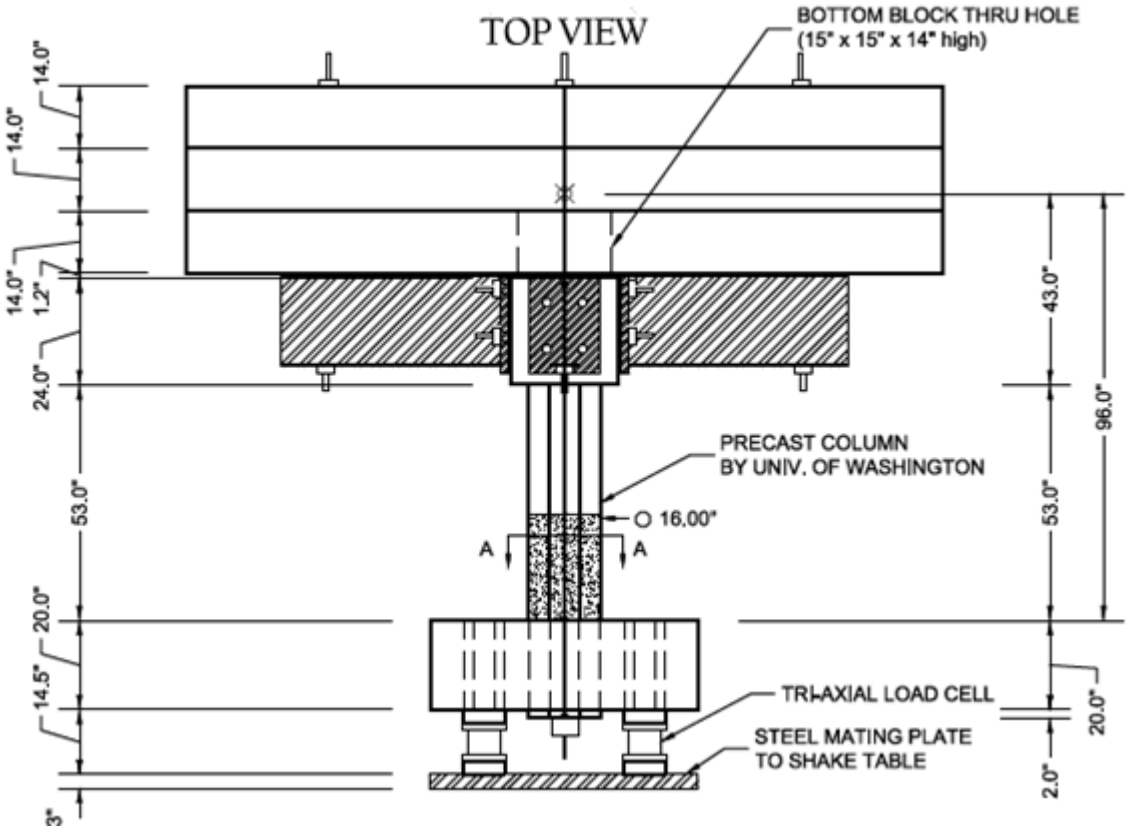

Figure 6-13. Test setup

The specimen was placed on the shake table, leveled with shims and attached to the underlying tri-axial load cells with hydrostone. The load cells were located at the four corners of the spread footing. The spread footing was post-tensioned to the top of the tri-axial load cells with four 7/8-in. diameter threaded roads that were threaded through plastic tubes in the footing. The bottom parts of the load cells were post-tensioned to a 3.25-in. thick 8 ft x 8 ft steel plate with 4 four 7/8-in. diameter threaded rods. The steel plate itself was post-tensioned to the shake table with nine 1-in. diameter Williams bars.

On top of the column were three mass blocks (each 120 in. x 120 in. x 14 in.) that provided a total of approximately 54 kips dead load in total. The blocks are hollow at the center to provide access to pre-tensioned strands or a post-tensioned tendon. To support the mass blocks on top of the column, steel brackets were post-tensioned to the load stub. Hydrostone was placed between the lowest mass block and the steel brackets to ensure direct contact between the two

before the blocks were post-tensioned down. Figure 6-14 shows Specimen PreT-SF-FIB-SHK ready for test.

A right hand global coordinate system was used, with its origin at the center of the 8 ft x 8 ft steel plate. The positive x-axis was aligned northwards. Figure 6-15 shows the designated global coordinate system.

Figure 6-14. Specimen PreT-SF-FIB-SHK ready for testing

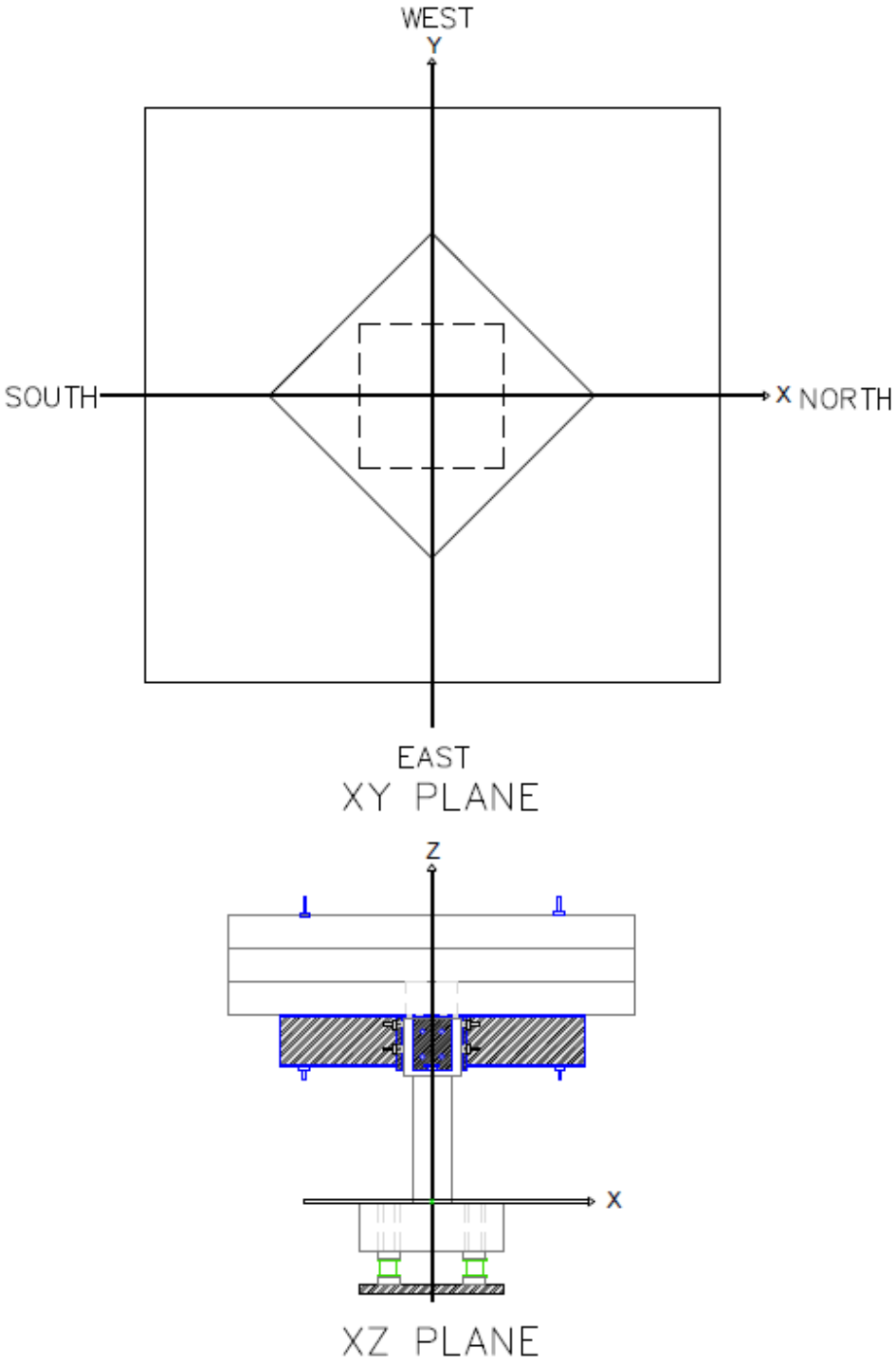

Figure 6-15. Global coordinate system

6.4 Instrumentation

The responses of the specimens were monitored with tri-axial load cells, external displacement transducers, acceleration sensors, and internal strain gauges (approximately 160 sensors in each specimen). The strain gauges were applied to selected spiral turns in the column and to selected column flexural bars. No strain gauges were included in the foundation because it was designed to stay elastic throughout the test.

The specimens were placed on top of four tri-axial load cells in order to capture the axial load, the shear force, and the moment during shaking. Eight custom-made, uni-axial, strand load cells were also placed on the prestressing strands at the bottom of Specimen PreT-SF-FIB-SHK column to monitor any potential strand slip during the test. It was deemed unnecessary to monitor the strands at the top both because the embedment length was 24 in., compared with 20 in. at the bottom, and because the steel brackets (supporting the mass blocks) were post-tensioned into the column load stub, thus providing additional confinement around the strands, which was expected to improve the bond of the strands. Accelerometers were attached to the foundation, the column, and on to the mass block. One pair was glued on each vertical face of the foundation. The accelerometers were oriented to measure the horizontal accelerations in the North-South (x-direction) and East-West (y-direction), and the vertical acceleration (z-direction). Sixteen accelerometers were attached to the column itself at two different vertical locations (26.5 in., and 48 in. above the foundation) on all four principal column sides (north, south, west, and east faces) in the both horizontal directions and vertically. Finally, eight accelerometers were placed on the mass block, located in pairs at the north, south (vertical acceleration, east-west acceleration), east, and west (vertical acceleration, north-south acceleration) corners of the mass block. For redundancy, two accelerometers were located at the top center. They measured the vertical acceleration and the acceleration in the east-west direction.

A total of 30 linear potentiometers were mounted on the column to capture local behavior of the specimen. Figure 6-16 shows their locations. Potentiometers (No. 1 to 28) captured relative rotations of the column at specific heights. The curvature rods were located at heights 1.5 in., 5.5 in., 10.5 in., 15.5-in., 20.5 in, 25.5 in., and 51.5 in. above the column-to-footing interface. The

top pairs were located 1.5 in. under the load stub. Column shear slip was monitored 2 in. above the foundation in the west (No. 29) and north direction (No. 30).

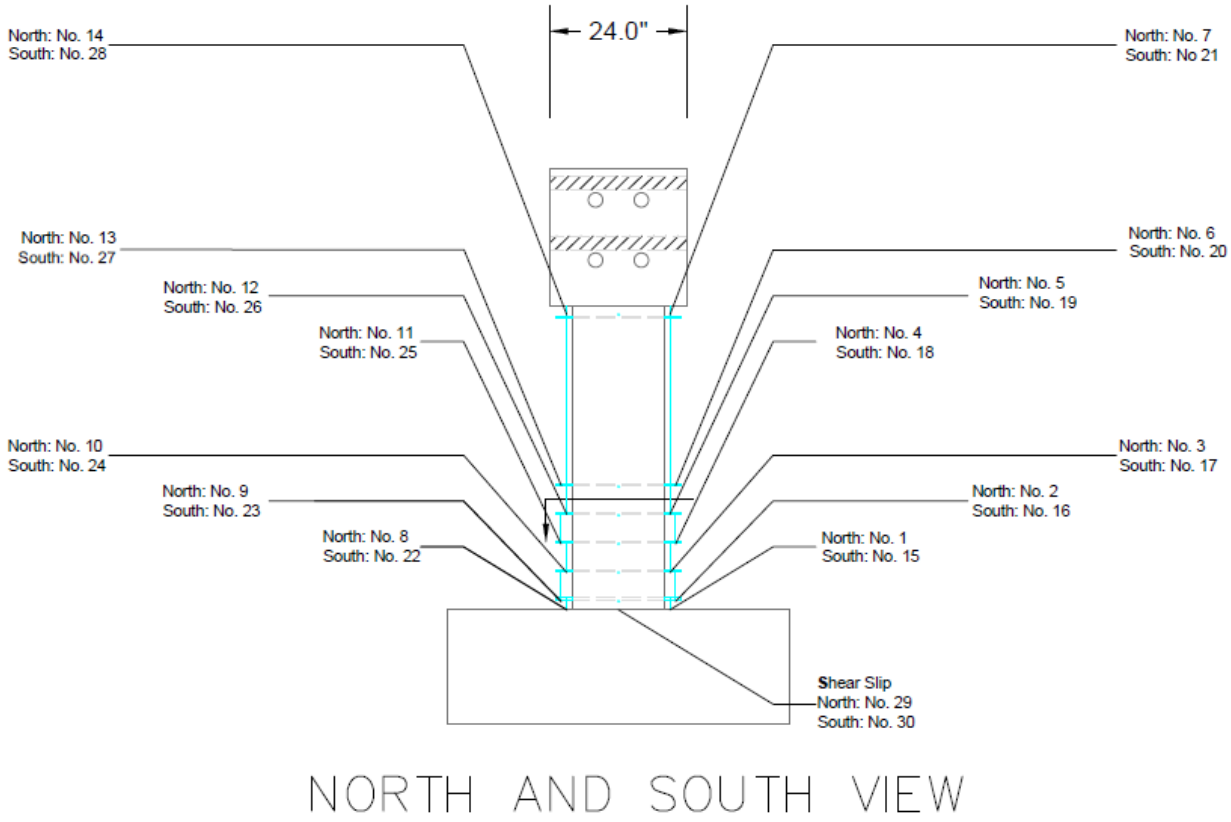

Figure 6-16. Location of potentiometers

Displacement of the column during the test was monitored with string potentiometers attached to targets on the foundation and on the mass block. A total of 9 string pots monitored three targets (i.e., a total of 3 string pots per target to resolve three components of displacement) on the foundation, while 12 string pots monitored 4 targets on the mass blocks.

Figure 6-17 shows the location of the strain gauges. All strain gauges were supplied by Texas Instruments. The type of strain gauges varied among the columns and the types used are summarized in Table 6-3. Because of stock availability, four different types of strain gauges were used in Specimen PreT-SF-FIB-SHK.

Table 6-3. Strain gauge types used in test specimens

Specimen	Longitudinal Bars	Spiral	Prestressing Strands
CIP-SF-REF-SHK	YFLA-5-5L	YFLA-5-5L	None
PreT-SF-FIB-SHK	FLA-6-115LT/ YFLA-5-5L/ FLA-6-11-5L	FLA-6-115LT/ YFLA-5-5L	FLA-6-11-5LT

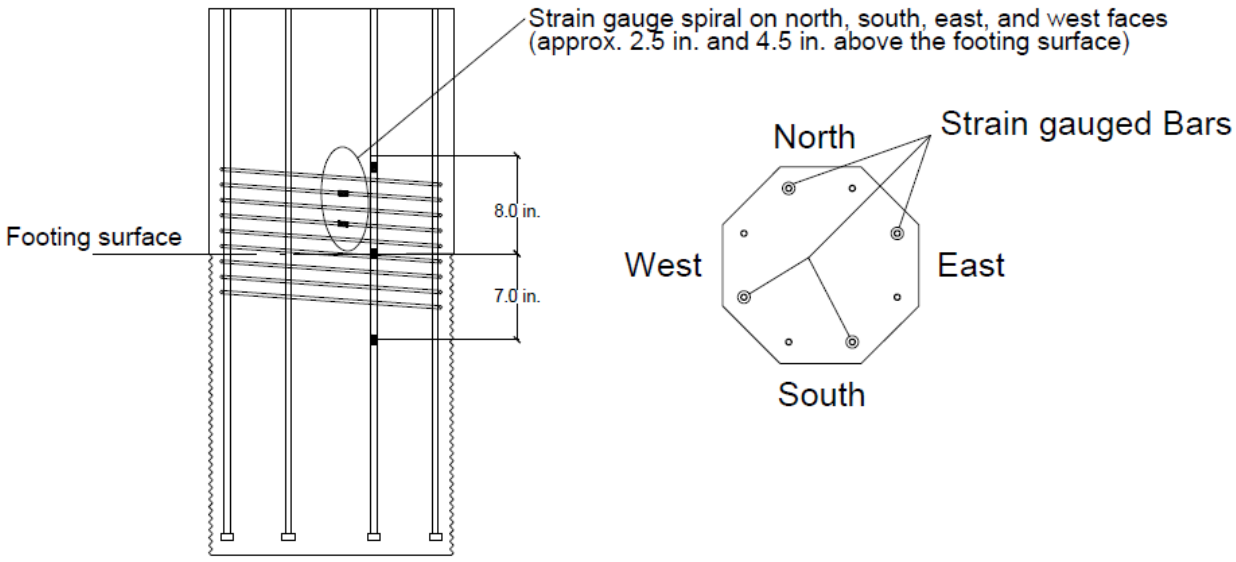

Figure 6-17. Location of strain gauges

Specimen PreT-SF-FIB-SHK used the same strain gage pattern as Specimen CIP-SF-REF-SHK, but had sixteen additional gages, mounted in pairs, to monitor the eight prestressing strands in the unbonded region. In both specimens, strain gauges were applied to four longitudinal bars at three locations: 7 in. below the column-to-footing interface, at the interface, and 8 in. above the interface. The longitudinal bars were located on the principal sides of the columns (north, south, east, and west). Similarly, the column spiral was gauged with a total of 16 strain gauges in pairs at two locations, approximately 2.25 in. and 4.5 in. above the column to footing interface.

During each earthquake test, data were recorded with a sampling rate of 0.005 seconds (200 Hz) using LabVIEW (Laboratory Virtual Instrument Engineering Workbench) from National Instruments.

6.5 Ground Motions

Caltrans (2010) specifies that a conventional concrete column should reach a ductility demand of up to 4.0 during design level event that corresponds to a 975-year return period. Based around this concept, the test protocol consisted of a set of simulated earthquakes intended to displace the reference column, Specimen CIP-SF-REF-SKH, to specified target drift ratios that, at the same time, corresponded to specific ductility ratios. The targeted ductility ratios were <1.0, 2.0, 4.0, 6.0, and 8.0. The first yield displacement of Specimen CIP-SF-REF-SKH was determined analytically to be 1.0 in. (Schoettler et al. 2013). The column height to the center of mass was 96 in, so this displacement corresponds to approximately 1% drift ratio.

The next two subsections describe the process of selecting candidate ground motions.

6.5.1 Ground Motion Processing

All tri-axial ground motions were selected to:

- Impose similar targeted displacement demands on all four test specimens over a period ranging from 0.4 to 0.7 seconds at a specimen scale.
- Contain velocity pulses, and
- Represent a strike-slip fault mechanism.

The candidate ground motion selection process was performed in five main steps.

1. Target displacement demands were obtained from a dynamic elastic analysis of Specimen CIP-SF-REF-SHK. Ductility ratios of 2.0, 4.0, 6.0, and 8.0 were based on Specimen CIP-SF-REF-SHK's calculated yield displacement.
2. Once the target displacements were obtained, they were converted into a target acceleration spectrum.

3. The PEER strong motion databases (2000 and 2012beta) were used to scan for motions that matched the target acceleration spectrum. In this research, the target accelerations were multiplied by a factor of 1.17 to account for the 5% damped values searchable in the PEER database. It was presumed that this increase correlates to the lower damping (1% to 2%) inherent in bridge columns.
4. Acceleration time histories of potential ground motions were downloaded and bidirectional response spectra were created. Special priority was given to records that produced smooth spectra over the anticipated period range.

Finally, the last step (which consisted of smaller steps), the candidate records were processed for compatibility with the shake table capacities. First, the time history of the records was scaled by a factor of $\sqrt{1/3}$, to be consistent with the 33.3% geometric scale factor. Then, the acceleration histories were double integrated to create displacement time histories, and they were then band-pass filtered between 0.1-25 Hz. The shake table's displacements limits were checked (+/- 4.0 in. horizontal, and +/- 1.5 vertical). If records exceeded the limit, they were high-pass filtered at an incrementally larger cutoff frequency until they were within acceptable displacement limits of the shake table. Any abrupt jolts were eliminated by incorporating a one-second long taper into and out of the excitation with a cosine function. The ground motions were then spliced with 3 seconds of leading zeros and 15 seconds of trailing zeros and then resampled at 100 Hz. The table velocity limits were checked by taking a 4th-order central difference approximation of the 1st-derivative from the displacement histories. It was re-used for the acceleration time histories created for shake table input signal and the analytical models of the five test specimens. Schoettler et al. (2013) describes this process in more detail.

6.5.2 Ground Motion Final Selection

Preprocessed candidate ground motions were used as input on a bare shake table where accelerations were recorded in horizontal North-South (x-direction), East-West (y-direction), and Vertical directions (z-direction) (see Figure 6-18). The recorded accelerations were then used as an input in a nonlinear time-history OpenSees analysis of Specimen CIP-SF-REF-SHK for a

final selection. Table 6-4 shows the target reference column drift values and the corresponding displacement ductility demands.

Table 6-4. Target drift and ductility demand for Specimen CIP-SF-REF-SKH

Test	Drift Ratio (%)	Ductility Demand (-)
Earthquake 1	< 0.47	1.0
Earthquake 2	2.1	2.0
Earthquake 3	2.1	2.0
Earthquake 4	4.2	4.0
Earthquake 5	4.2	4.0
Earthquake 6	6.3	6.0
Earthquake 7	8.4	8.0
Earthquake 8	10.5	10.0

The selected earthquakes that matched the targeted drift values for Specimen CIP-SF-REF-SHK were sent to the other participants in the test program for verification. Table 6-5 summarizes the earthquakes chosen for the test program and their associated table peak ground accelerations (PGAs). For comparison, bracketed numbers show the input signal PGA peaks.

Table 6-5. Test program ground motions

Test	EQ. Name	Magnitude (M_w)	Station	Acceleration Scale Factor	Table N-S[1] PGA (g)	Table E-W[2] PGA (g)	Table Vert.[3] PGA (g)
Earthquake 1	Coalinga, 1983	5.0	46T07 Harris Ranch	2.50	0.35 (0.15)	0.28 (0.08)	0.13 (0.06)
Earthquake 2	Imperial Valley, 1979	6.5	EC Meloland Overpass FF	0.80	0.36 (0.22)	0.32 (0.12)	0.09 (0.07)
Earthquake 3	Morgan Hill, 1984	6.2	Coyote Lake Dam (SW Abutment)	0.70	0.64 (0.44)	0.67 (0.47)	0.15 (0.26)
Earthquake 4	Northridge, 1994	6.7	Rinaldi Receiving Station	0.56	0.53 (0.76)	0.31 (0.90)	0.29 (0.36)
Earthquake 5	Northridge, 1994	6.7	Sylmar, Olive View Med FF	-0.80	0.66 (0.38)	0.70 (0.26)	0.16 (0.18)
Earthquake 6	Northridge, 1994	6.7	Rinaldi Receiving Station	0.90	1.39 (0.58)	0.56 (0.49)	0.60 (0.61)
Earthquake 7	Kobe, Japan, 1995	6.9	Takatori	0.77	0.58 (0.70)	0.54 (0.57)	0.09 (0.38)
Earthquake 8	Kobe, Japan, 1995	6.9	Takatori	-0.90	0.66 (0.58)	0.61 (0.74)	0.11 (0.44)

1. x-direction (see Figure 6-15)
2. y-direction
3. z-direction

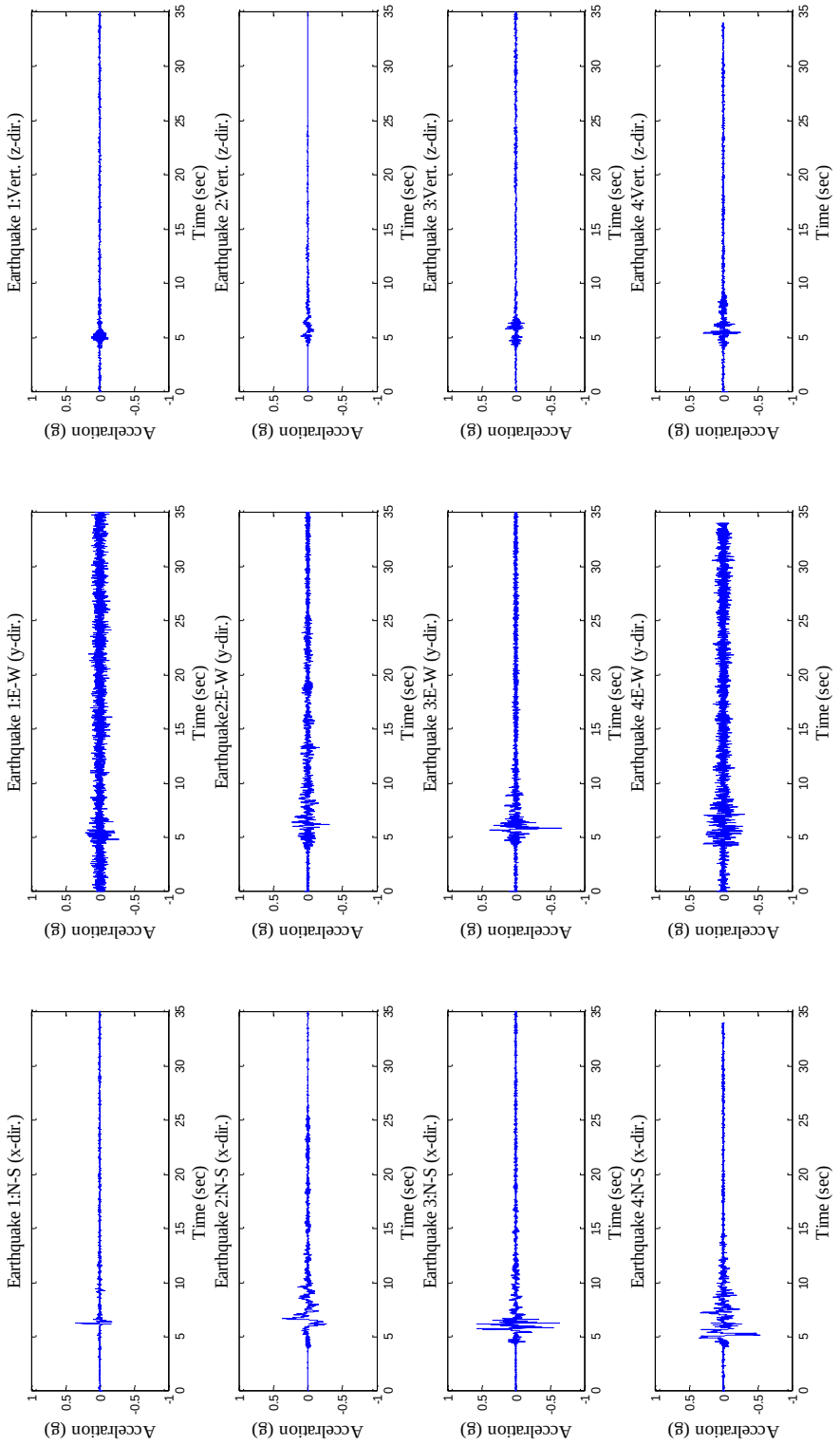

Figure 6-18. Table feedback ground motion accelerations

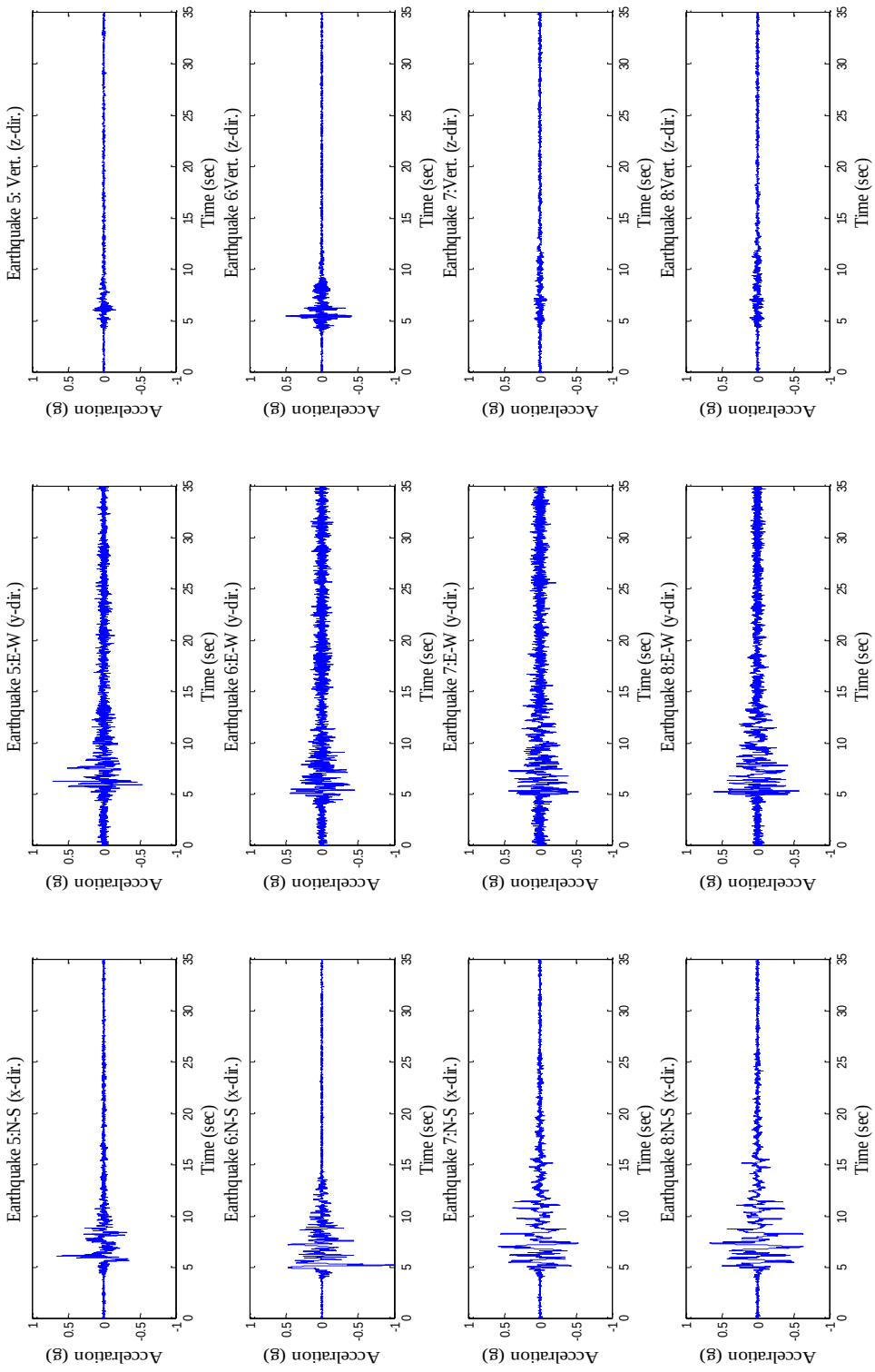

Figure 6-18. Table feedback ground motion accelerations (cont.)

6.5.3 White Noise Tests

After each earthquake record, two low-amplitude white noise records were created to excite the column separately in x and y directions with the intent of detecting the changes in the specimen's natural period and damping due to accumulated damage. The natural period can be obtained from Fourier spectrum of the response and the damping can be estimated from using a power spectral density estimate.

6.6 Test Protocol

The testing protocol for both specimens CIP-SF-REF-SHK and PreT-SF-FIB-SHK was identical. First, free-vibration tests were performed in the two principal directions (North-South, and East-West), then the eight ground motions were applied, in order of ascending severity. Free-vibration tests were only conducted in the North-South (x-direction) for Specimen CIP-SF-REF-SHK. The following two subsections discuss the testing protocol in more detail.

6.6.1 Free-Vibration Tests

The free-vibration tests were performed in North-South (x-direction) and South-West (y-direction) to investigate the dynamic properties of the undamaged column. The testing procedure was as follows: first, a reference frame was set up with two linear potentiometers located at the top and at the bottom of the column. A cable, inclined at about 16 degrees to the horizontal, was hooked up to the steel bracket carrying the mass block and was led to a fixed anchor on the laboratory floor. At the center of the cable system was an assembly that consisted of a machined bolt, a "come-along", and a load cell. The cable system was loaded up to 2 kips then the machined bolt was cut with a bolt cutter. Figure 6-19 shows a free-vibration test being conducted in the North-South direction.

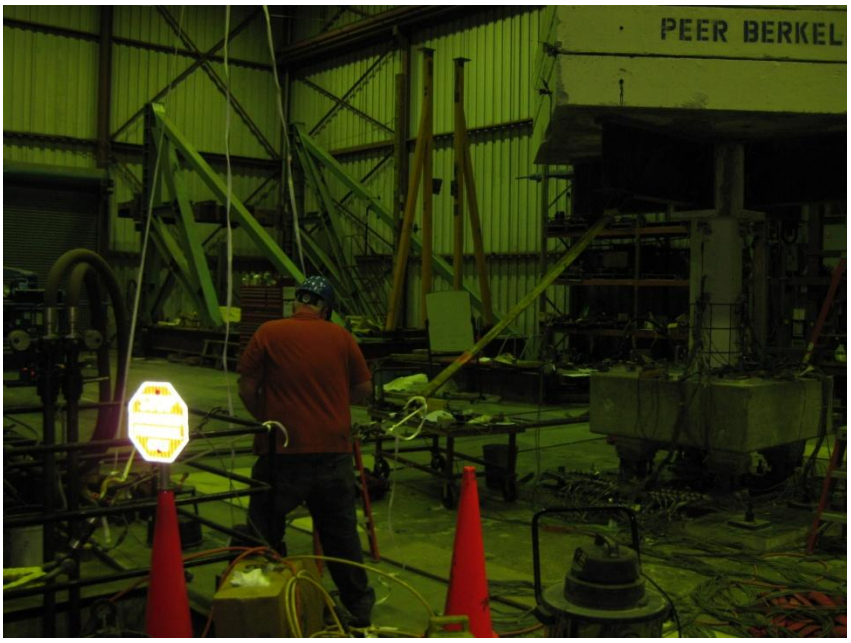

Figure 6-19. Cable being cut in a free-vibration test

6.6.2 Shake-Table Tests

The shake table tests followed the free-vibration test. The official test schedule consisted of eight tri-axial ground motions and two white noise records. Before each earthquake test, the low-amplitude white noise tests were performed to verify the change of natural period and damping ratio due to the damage from the last earthquake loading. The earthquake test records were arranged such that the intensity level increased in five levels. Level 1 was intended to displace the column well under the first yield displacement of Specimen CIP-SF-REF-SHK. Levels 2.0, 3.0, 4.0, 5.0 and 6.0 were intended to displace the column 2.1% ($\mu_\Delta = 2.0$), 4.2% ($\mu_\Delta = 4.0$), 6.3% ($\mu_\Delta = 6.0$), 8.4% ($\mu_\Delta = 8.0$), and 10.5% drift ($\mu_\Delta = 10.0$), respectively.

7 SINGLE-COLUMN SHAKE-TABLE TEST RESULTS

In this chapter, the responses of specimens CIP-SF-CIP-SHK and PreT-SF-FIB-SHK are compared. Global measures of response include accelerations recorded at the center-of-mass (COM) during each earthquake test, column-drift response, moment-drift response, and effective force displacement. Local measures include column curvature, column axial strains.

As listed in Table 6-4, the test program consisted of a total of eight tri-axial ground motions. Specimen CIP-SF-REF-SHK was subjected to only seven ground motions because the column started to show significant residual displacement, whereas the PreT-SF-FIB-SHK completed the test program. Specimen PreT-SF-FIB-SHK was also subjected to an additional test, in which a Design-Level earthquake was repeated (Earthquake 5 in Table 6-5).

It should be noted that the polarity of the vertical component of each ground motion in Specimen CIP-SF-REF was accidentally reversed compared to the ones used in Specimen PreT-SF-FIB-SHK. In general, the effect of vertical ground motion is ignored, because bridge columns have easily enough axial capacity to resist the extra vertical forces generated from that component of motion. Various researchers have studied numerically the effect of vertical ground motion. Button et al. (1999) performed analysis on several bridges using ground motions with and without the vertical ground motion component. The ground motions represented a 6.5 magnitude event with different fault distances (5 km and 20 km) and site conditions (rock and soil). They performed a linear time history analysis on three bridges and a nonlinear time history analysis on one bridge. Their analysis showed that horizontal displacements were not affected by including the vertical component. Hachem et al. (2002) performed similar study on a single reinforced concrete column using both near-fault and far-field earthquakes at different intensities. They concluded similarly that the vertical component did not influence the horizontal response of a column system. Overall, it is not expected that the reversed polarity of the ground motion's vertical component in this research to dramatically change the global behavior (i.e., horizontal column displacements). However, the reversed vertical polarity has the possibility to alter the local behavior such as column such as cross-sectional moment and strains.

The focus of this chapter will be on earthquakes no. 1, 4, and 7. They represented ground motions that displaced the columns to below first yield (Earthquake 1), to the design level (Earthquake 4), and 2 times the design level (Earthquake 7). Figures will show the responses of the columns in the principal directions North-South (x-direction) and East-West (y-direction). Information about the other earthquake tests can be found in Appendix C.

7.1 Observed Damage

Before the specimens were subjected to any ground motions, they were subjected to pull-back tests in the principal direction North-South. In addition, Specimen PreT-SF-FIB-SHK was subjected to a pull-back test in the East-West direction. The columns were inspected after each test and no cracks were found. Figure 7-1 shows Specimen PreT-SF-FIB-SHK before testing.

During the shake table testing, the table was not always set down between ground motions, which prevented access to the column for inspection. ("Setting down" refers to release of the air pressure that supports the weight of the table and specimens during the motion. While the air pressure is activated, safety rules prevent access to the table). After the first three ground motions, hairline cracks (<0.04 in.) were observed in the bottom 16 in. of the columns, or 1.0 column diameter. Residual drift was not visually observed in either column. Analysis of the data recorded showed that the residual drifts for specimens CIP-SF-REF-SHK and PreT-SF-FIB-SHK measured 0.37% and 0.12%, respectively after the first three motions.

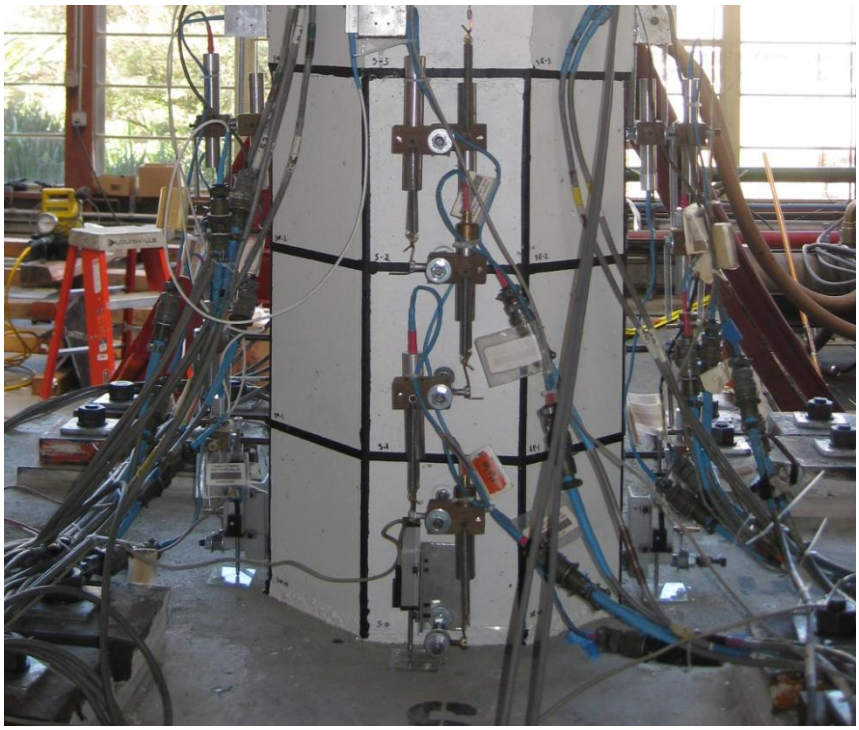

Figure 7-1. Specimen PreT-SF-FIB-SHK at the start of the test program

Figure 7-2 shows the two columns after the first design level earthquake (Earthquake 4: Northridge-Rinaldi 1994, 4.2% target drift, μ_Δ = 4.0). Both columns were observed to re-center back to their original plumb position; residual drifts were 0.31% for Specimen CIP-SF-REF-SHK and 0.07% for Specimen PreT-SF-FIB-SHK. Cracks propagated around the columns but in Specimen PreT-SF-FIB-SHK very little cracking occurred higher than 16 in. above the column-to-footing interface. In Specimen PreT-SF-FIB-SHK, the largest residual crack measured 0.03 in., approximately 8 in. above the interface on the southeast side of the column. First spalling (minor spalling) was observed in both columns after Earthquake 4. No separation between the column and the spread footing was noticed in Specimen PreT-SF-FIB-SHK.

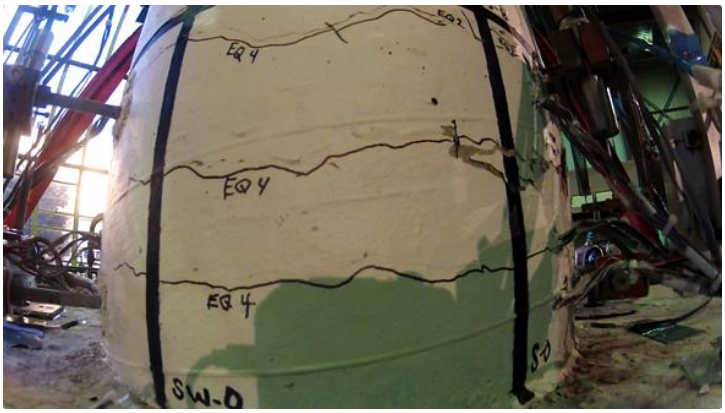

a) Specimen CIP-SF-REF-SHK column base (Schoettler et al. 2013)

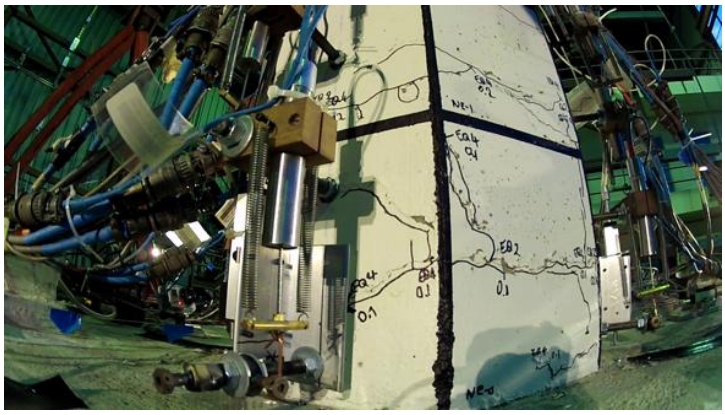

b) Specimen PreT-SF-FIB-SHK column base

Figure 7-2. Column base after first design level earthquake (Earthquake 4: Northridge-Rinaldi 1994)

In Earthquake 5: Northridge-Sylmar 1994 (4.2% target drift, μ_Δ = 4.0), new spalling occurred 4 in. above the interface in Specimen PreT-SF-FIB-SHK. The spall was located on the whole north side of the column (north, northwest, northeast faces). A level placed on the column showed that it was still re-centering to its original position, confirming the visual observation. In contrast, Specimen CIP-SF-REF-SHK showed 0.82% residual drift.

Cracking and spalling became more pronounced in both columns after Earthquake 6: Northridge-Rinaldi 1994 (6.3% target drift, μ_Δ = 6.0). In Specimen PreT-SF-FIB-SHK, a very visible dominant crack appeared 4 in. above the column-to-footing interface. The crack was seen opening and closing during the whole test program. The column continued to be essentially

plumb (measured 0.21% drift) when it was at rest. The measured residual drift for specimen CIP-SF-REF-SHK was much larger, at 1.57%.

In Earthquake 7: Kobe, Japan-Takatori 1995 (8.3% target drift, μ_Δ = 8.0), both columns were displaced more than the targeted 8.3% drift. The measured peak drifts for specimens CIP-SF-REF-SHK and PreT-SF-FIB-SHK were 10.68% and 9.52%, respectively. Concrete spalling in Specimen CIP-SF-REF-SHK was deep and it exposed the transverse reinforcement. Although not shown in Figure 7-3, "the area of spalling covered half of the column circumference to a height of 24 in. or 1.5 column diameters" (Schoettler et al. 2013). Specimen CIP-SF-REF-SHK showed significant residual displacement or about 6.70% drift. The retained its flexural capacity but testing was terminated. The large residual displacement suggested that collapse would occur during Earthquake 8 with the attendant possibility of equipment damage. Post-inspection revealed that some longitudinal bars had buckled but no bars or spiral had fractured.

In Specimen PreT-SF-FIB-SHK, a hairline crack in the cold joint between the HyFRC shell and the conventional concrete (located 24 in. above the column-to-footing interface) was noticed for the first time. Specimen PreT-SF-FIB-SHK appeared plumb after the test (measured 0.21% drift). Figure 7-3 shows the two columns after Earthquake 7.

Earthquake 8: Kobe, Japan-Takatori (10.4% target drift, μ_Δ = 10.0) was the last record in the test program. During the shake, two fracture sounds were heard in Specimen PreT-SF-FIB-SHK. A spiral fracture became visible through spalling crack on the north face of the column approximately 6 in. above the interface, but the spalls was held together by the steel fibers in the HyFRC. The other fractured spiral or longitudinal bar could not be located. Bar buckling was observed 8 in. above the interface on the northeast face of the column. Residual drift was apparent. Figure 7-4 compares selected damage states observed for the two specimens during the test program. Drift values presented are the largest measured peak drifts in any direction.

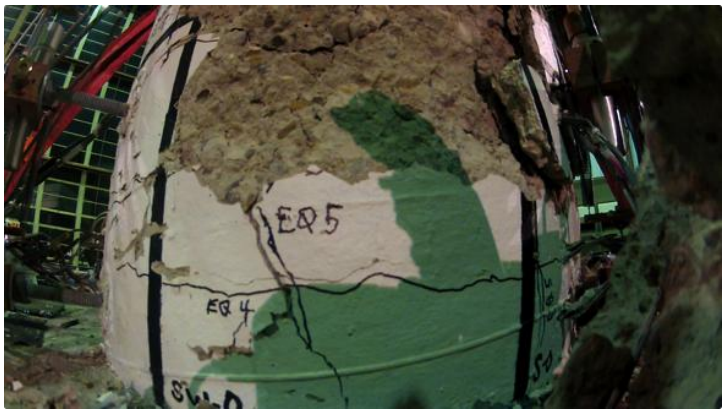

a) Specimen CIP-SF-REF-SHK column base (Schoettler et al. 2013)

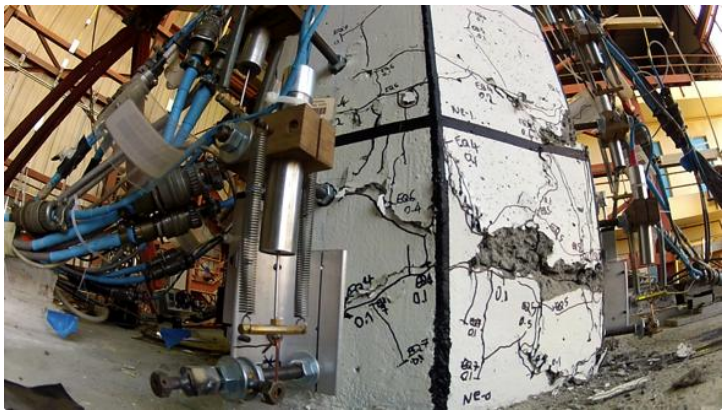

b) Specimen PreT-SF-FIB-SHK column base

Figure 7-3. Column base after Earthquake no. 7 (Kobe, Japan-Takatori 1995)

Because no longitudinal bar fracture had been detected in Specimen PreT-SF-FIB-SHK, Earthquake 5 was re-run. Two more fracture sounds were heard and after them the column was seen to have a residual lean towards the north. Post-test inspection of the column revealed that four out of eight longitudinal bars fractured (two on the north side, two on the south side) and the rest had buckled. This is consistent with the fact that all the ground motions were stronger in the North-South direction than in the East-West direction.

All longitudinal bar fractures were located 4 to 8 in. above the interface. During the test program, the column rocked about cracks located in this height. The spiral was only fractured in one place (on the northwest side) and was associated with bar buckling there. The plastic hinge length was measured to be 9 in. long on all sides except the west side, which was 4 in. The

plastic hinge length was taken from the measure from column-to-footing interface to a piece of cover concrete that was not spalling. Figure 7-5 shows Specimen PreT-SF-FIB-SHK after the test program.

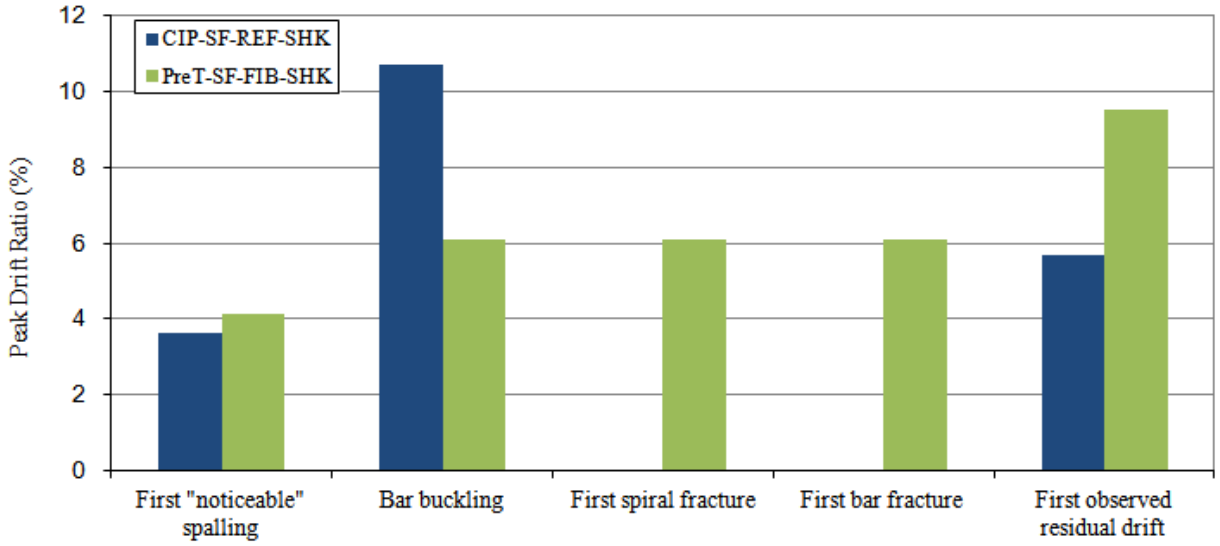

Figure 7-4. Comparison of specimens' peak drift ratios for selected major damage states. Note: testing of Specimen CIP-SF-REF-SHK was stopped before the bars buckled or the spiral fractured.

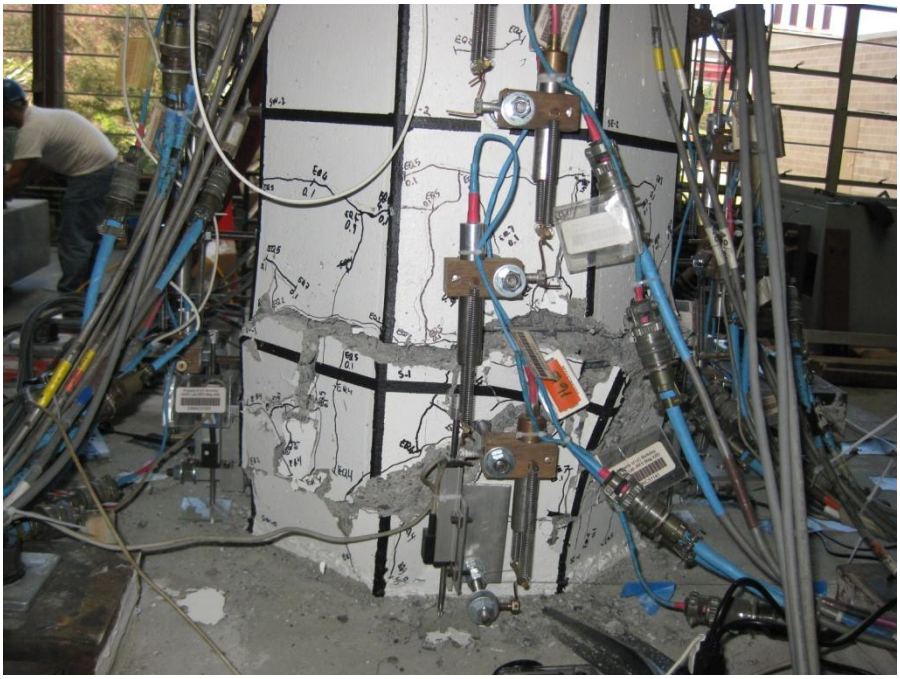

Figure 7-5. Specimen PreT-SF-FIB-SHK at the end of the test program

7.2 Natural Period, Initial Stiffness and Damping Properties

Before the shake table test program started, the specimens were tested in free-vibration to determine their initial periods, initial stiffnesses and damping values. The specimens were pulled back as is described in Section 6.6 with a force ranging from 1.5-1.8 kips. The displacement of the column was monitored with a linear potentiometer that was attached to a reference frame on the foundation. Two free-vibration tests were conducted in each principal directions North-South. Additional tests were conducted in East-West for Specimen PreT-SF-FIB-SHK. Table 7-1 summarizes the results obtained from both specimens. Initial stiffnesses presented in Table 7-1 are the ratio of effective stiffness, EI_{eff}, to the gross-section stiffness, EI_{gross}.

Table 7-1. Damped Period, initial stiffness and damping for specimens CIP-SF-REF-SHK and PreT-SF-FIB-SHK

Specimen	Damped Period (s)		Initial Stiffness (-)		Initial Damping (%)	
	North-South	East-West	North-South	East-West	North-South	East-West
CIP-SF-REF-SHK[1]	0.53	N/A	0.66	N/A	0.15	N/A
PreT-SF-FIB-SHK[2]	0.38	0.38	0.77	0.77	0.63	0.76

1. $EI_{gross} = 10{,}367{,}629\ kip\text{-}in^2$
2. $EI_{gross} = 17{,}139{,}302\ kip\text{-}in^2$

Specimen PreT-SF-FIB-SHK had a lower initial period and higher stiffness compared to Specimen CIP-SF-REF-SHK. This was an expected consequence of pre-tensioning. Specimen CIP-SF-REF-SHK showed lower initial damping by factor of almost four. This peculiar result (i.e., less damping in the reference column) is attributed to the fact that the initial yield displacement was higher than expected because of very low column concrete strength in Specimen CIP-SF-REF-SHK (Table 6-2).

1.3 Recorded Accelerations

Accelerations were recorded with accelerometers mounted on top of the foundation, on the column itself, and on the mass blocks. Accelerations were monitored in the principal directions (North-South [x-dir.], East-West [y-dir.], and vertically [z-dir.]). Table 7-2 summarizes the peak accelerations measured on top of the foundation for each earthquake test.

Table 7-2. Measured foundation peak acceleration for specimens CIP-SF-REF-SHK and PreT-SF-FIB-SHK

Test	EQ. Name	Magnitude	Station	Accel. Scale Factor	Peak Acceleration (g)					
					Specimen CIP-SF-REF-SHK			Specimen PreT-SF-FIB-SHK		
					N-S[1]	E-W[2]	Vert.[3]	N-S[1]	E-W[2]	Vert.[3]
Earthquake 1	Coalinga, 1983	5.0	46T07 Harris Ranch	2.50	0.37	0.11	0.09	0.29	0.04	0.16
Earthquake 2	Imperial Valley, 1979	6.5	EC Meloland Overpass FF	0.80	0.38	0.08	0.09	0.35	0.23	0.11
Earthquake 3	Morgan Hill, 1984	6.2	Coyote Lake Dam (SW Abutment)	0.70	0.88	0.25	0.36	0.85	0.58	0.22
Earthquake 4	Northridge, 1994	6.7	Rinaldi Receiving Station	0.56	0.64	0.34	0.26	0.59	0.29	0.41
Earthquake 5	Northridge, 1994	6.7	Sylmar, Olive View Med FF	-0.80	0.90	0.59	0.13	0.79	0.56	0.18
Earthquake 6	Northridge, 1994	6.7	Rinaldi Receiving Station	0.90	1.31	0.53	0.62	1.12	0.37	0.95
Earthquake 7	Kobe, Japan, 1995	6.9	Takatori	0.77	0.72	0.78	0.34	0.60	0.57	0.12
Earthquake 8	Kobe, Japan, 1995	6.9	Takatori	-0.90	N/A	N/A	N/A	0.73	0.74	0.15
Earthquake 9	Northridge, 1994	6.7	Sylmar, Olive View Med FF	-0.80	N/A	N/A	N/A	0.83	0.53	0.20

1. x-direction
2. y-direction
3. z-direction

Figures 7-6 through 7-8 compare the peak accelerations measured on top of the foundation in both specimens. Acceleration data in both specimens were band-pass between 0.25 and 25Hz (Schoettler et al. 2013). The acceleration responses were similar in North-South (x-direction) but differed in East-West (y-direction).

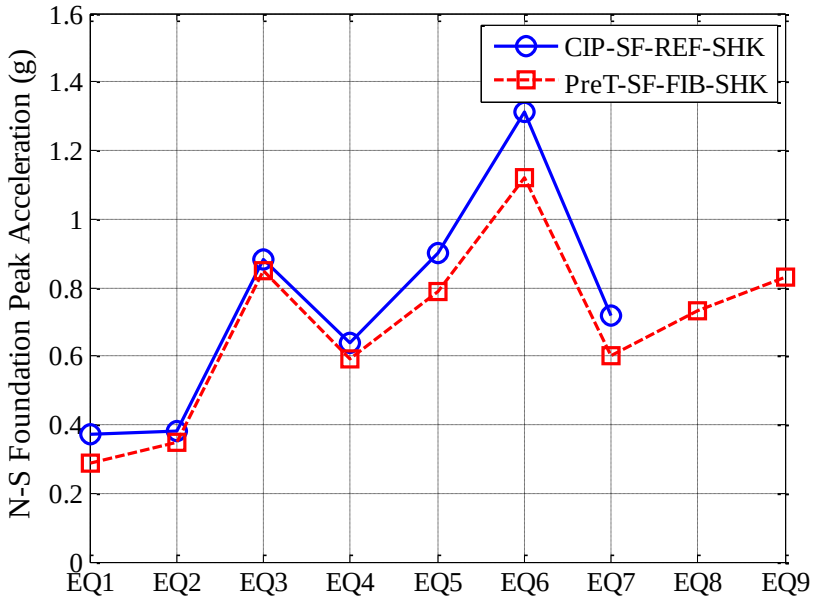

Figure 7-6. Peak North-South acceleration measured on top of foundation for specimens CIP-SF-REF-SHK and PreT-SF-FIB-SHK

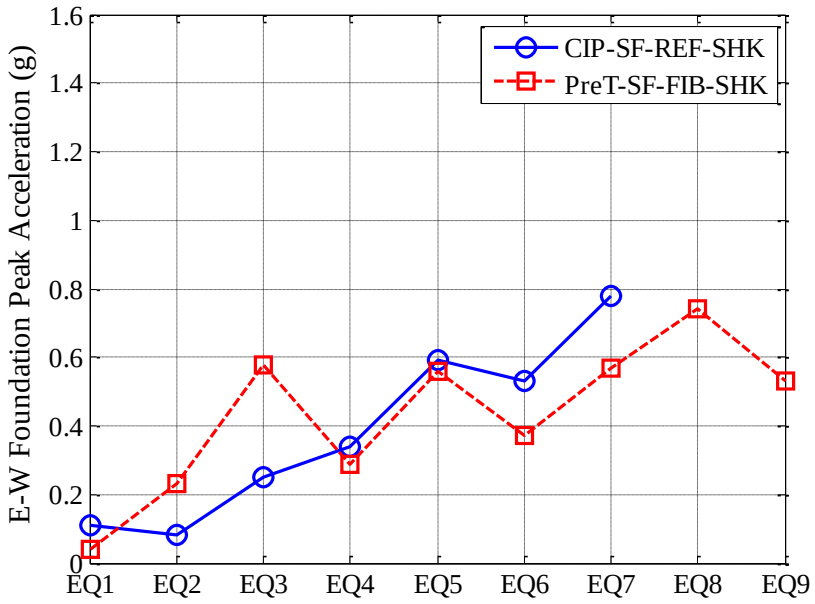

Figure 7-7. Peak East-West acceleration measured on top of foundation for specimens CIP-SF-REF-SHK and PreT-SF-FIB-SHK

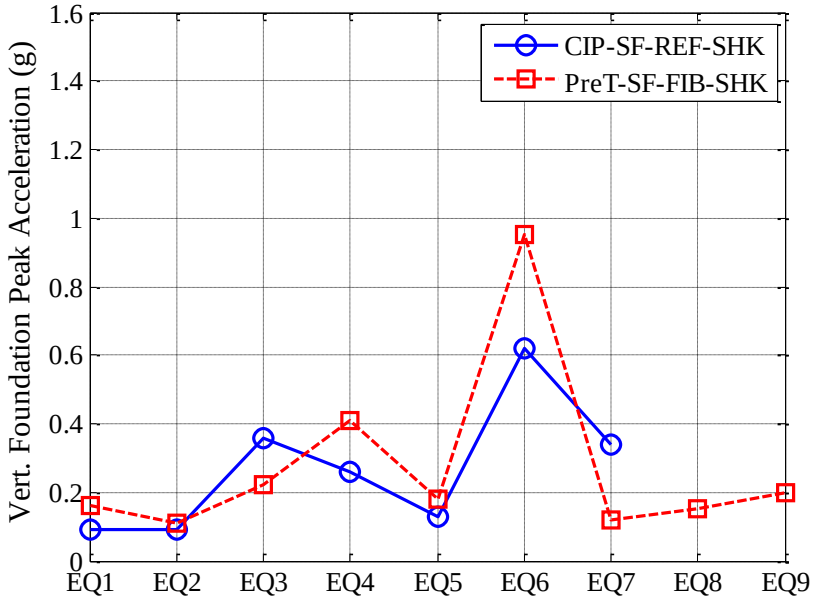

Figure 7-8. Peak vertical acceleration measured on top of foundation for specimens CIP-SF-REF-SHK and PreT-SF-FIB-SHK

Table 7-3 summarizes the measured mass block peak accelerations at the center-of-mass (COM) for both specimens. Figures 7-9 through 7-11 compare the mass block peak accelerations in both specimens. The North-South measured peak accelerations were nearly identical but the East-West ones differed; after Earthquake 4, Specimen CIP-SF-REF-SHK experienced more East-West acceleration than did Specimen PreT-SF-FIB-SHK.

Table 7-3. Measured mass block (at COM) peak acceleration for specimens CIP-SF-REF-SHK and PreT-SF-FIB-SHK

Test	EQ. Name	Magnitude	Station	Accel. Scale Factor	Peak Acceleration (g)					
					Specimen CIP-SF-REF-SHK			Specimen PreT-SF-FIB-SHK		
					N-S[1]	E-W[2]	Vert.[3]	N-S[1]	E-W[2]	Vert.[3]
Earthquake 1	Coalinga, 1983	5.0	46T07 Harris Ranch	2.50	0.13	0.11	0.12	0.19	0.03	0.25
Earthquake 2	Imperial Valley, 1979	6.5	EC Meloland Overpass FF	0.80	0.33	0.17	0.11	0.32	0.22	0.18
Earthquake 3	Morgan Hill, 1984	6.2	Coyote Lake Dam (SW Abutment)	0.70	0.50	0.21	0.37	0.42	0.32	0.62
Earthquake 4	Northridge, 1994	6.7	Rinaldi Receiving Station	0.56	0.35	0.38	0.37	0.39	0.24	0.53
Earthquake 5	Northridge, 1994	6.7	Sylmar, Olive View Med FF	-0.80	0.44	0.29	0.19	0.43	0.23	0.50
Earthquake 6	Northridge, 1994	6.7	Rinaldi Receiving Station	0.90	0.35	0.46	0.75	0.38	0.32	0.85
Earthquake 7	Kobe, Japan, 1995	6.9	Takatori	0.77	0.36	0.51	0.40	0.32	0.26	0.45
Earthquake 8	Kobe, Japan, 1995	6.9	Takatori	-0.90	N/A	N/A	N/A	0.26	0.39	0.53
Earthquake 9	Northridge, 1994	6.7	Sylmar, Olive View Med FF	-0.80	N/A	N/A	N/A	0.30	0.14	0.56

1. x-direction
2. y-direction
3. z-direction

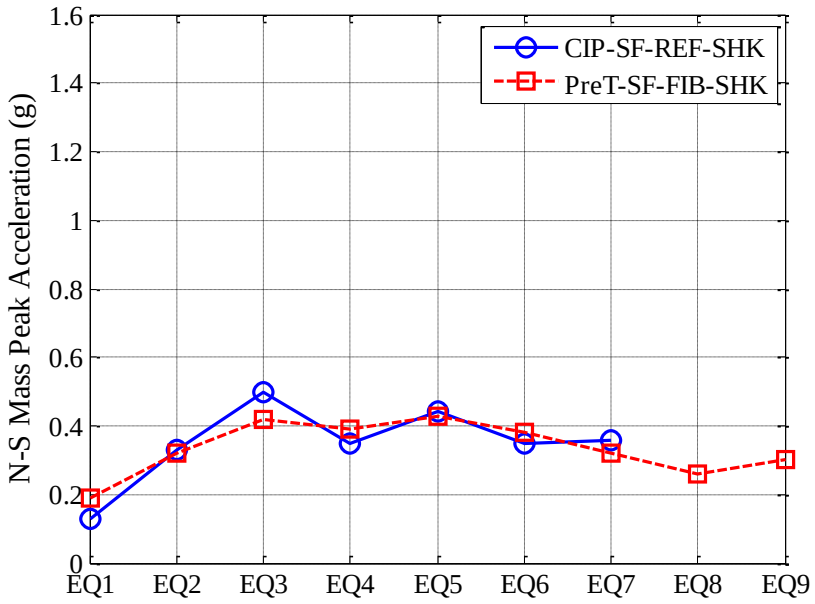

Figure 7-9. Peak North-South acceleration measured at center-of-mass (COM) for specimens CIP-SF-REF-SHK and PreT-SF-FIB-SHK

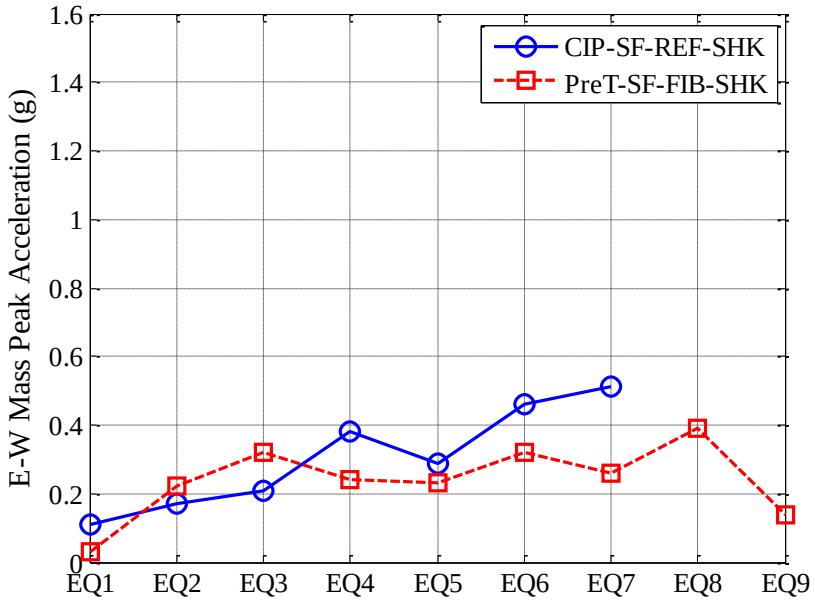

Figure 7-10. Peak East-West acceleration measured at center-of-mass (COM) for specimens CIP-SF-REF-SHK and PreT-SF-FIB-SHK

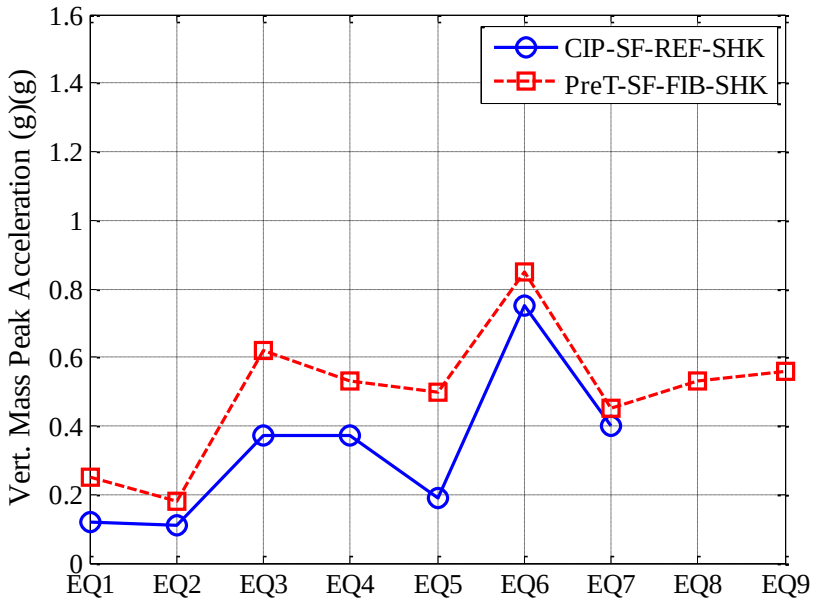

Figure 7-11. Peak vertical acceleration measured at center-of-mass (COM) for specimens CIP-SF-REF-SHK and PreT-SF-FIB-SHK

7.3 Column Drift-Time Response

Table 7-4 lists both the absolute measured peak drift and residual drift ratios for both specimens. These values were obtained by taking the vector sum of the displacements at each time step, and finding the maximum over time of those sums. Additionally, Table 7-4 shows in parenthesis the ductility demand on Specimen CIP-SF-REF-SHK. This ductility demand is lower than the targeted ones listed in Table 6-4 and was a result of the low concrete strength (i.e., lower stiffness) in Specimen CIP-SF-REF-SHK's column (Schoettler et al. 2013). Figure 7-12 shows the same information in a bar chart. The measured peak drift ratios for both specimens are similar in all tests except Earthquake 2 and Earthquake 7. As shown in Figure 7-12, Specimen PreT-SF-FIB-SHK re-centered much better than Specimen CIP-SF-REF-SHK and therefore achieved that design goal. For example, Specimen PreT-SF-FIB-SHK re-centered to a drift ratio of only 0.21% after experiencing a peak drift ratio of 5.49%. Thus it continued to re-center after the design drift ratio for re-centering (3.0%) and the drift ratio at yield of the prestressing steel (3.48%), and in that sense exceeded expectations. In comparison, at a comparable peak drift ratio

of 5.67%, Specimen CIP-SF-REF-SHK had a residual drift ratio of 0.83%, which is nearing the practical limit for reparability.

During testing of Specimen PreT-SF-FIB-SHK, all of the strand load cells worked throughout the test with the exception of the one. Post-test analysis of the strand load cell data (section 6.4) indicate that one strand slipped during Earthquake 5. It was the NW-load cell and it showed a load increase of about 1 kip.

Table 7-4. Peak and residual drift response (in any direction) results for specimens CIP-SF-REF-SHK and PreT-SF-FIB-SHK

EQ No.	CIP-SF-REF-SHK Target Drift Ratio (%)	CIP-SF-REF-SHK Peak Drift Ratio (%)	CIP-SF-REF-SHK Residual Drift Ratio (%)	PreT-SF-FIB-SHK Peak Drift Ratio (%)	PreT-SF-FIB-SHK Residual Drift Ratio (%)
1	< 0.47	0.44	0.00	0.43	0.01
2	2.1 (1.6)	3.48	0.36	1.79	0.08
3	2.1 (1.6)	1.49	0.37	2.16	0.12
4	4.2 (3.2)	3.65	0.30	4.15	0.07
5	4.2 (3.2)	5.67	0.86	5.49	0.21
6	6.3 (4.8)	6.02	1.57	5.69	0.21
7	8.4 (6.4)	10.68	6.72	9.52	1.28
8	10.5 (8.0)	N/A	N/A	7.48	1.80
9	N/A	N/A	N/A	10.50	5.39

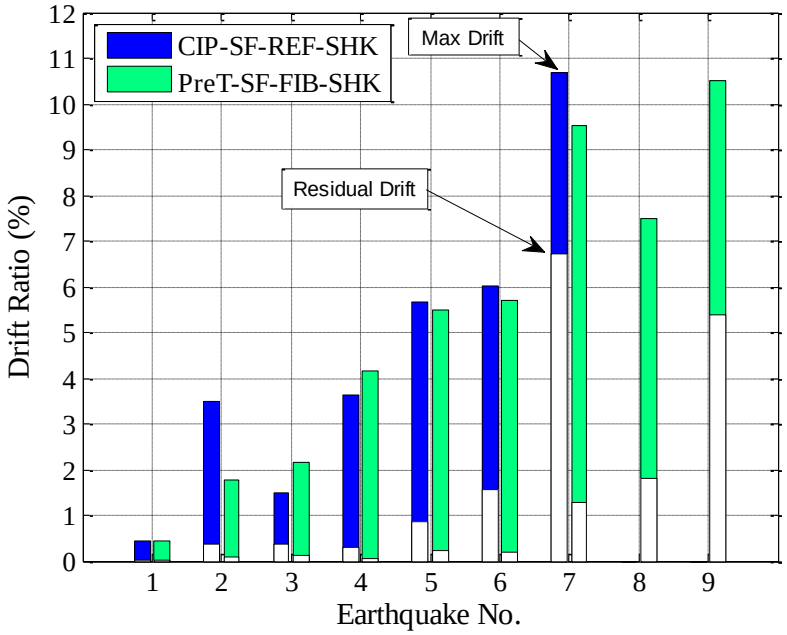

Figure 7-12. Peak and residual drift (in any direction) comparison between specimens CIP-SF-REF-SHK and PreT-SF-FIB-SHK

Figures 7-13 to 7-18 compares the two specimens in terms of drift versus time in both principal directions (North-South and East-West) for three earthquake tests: Earthquake 1 (below first yield), Earthquake 4 (Design Level), and Earthquake 7 (2 x Design Level). The excitation intensity was more severe in North-South direction than in East-West and thus the displacement demands were greater in North-South. A period difference between the specimens is apparent in all figures. Specimen PreT-SF-FIB-SHK had shorter periods than Specimen CIP-SF-REF-SHK throughout the test program. This behavior was expected since Specimen PreT-SF-FIB-SKK was pre-tensioned.

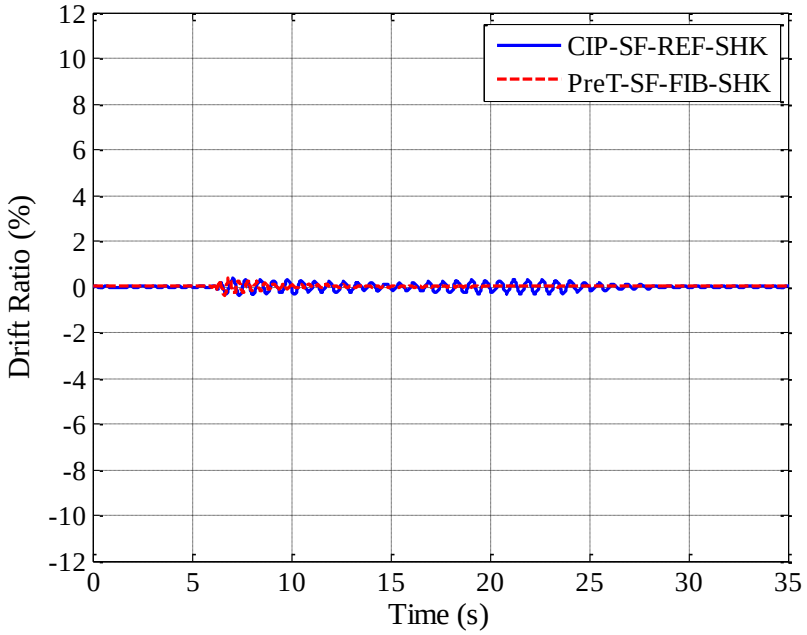

Figure 7-13. North-South drift ratio vs time. Earthquake 1 (below first yield)

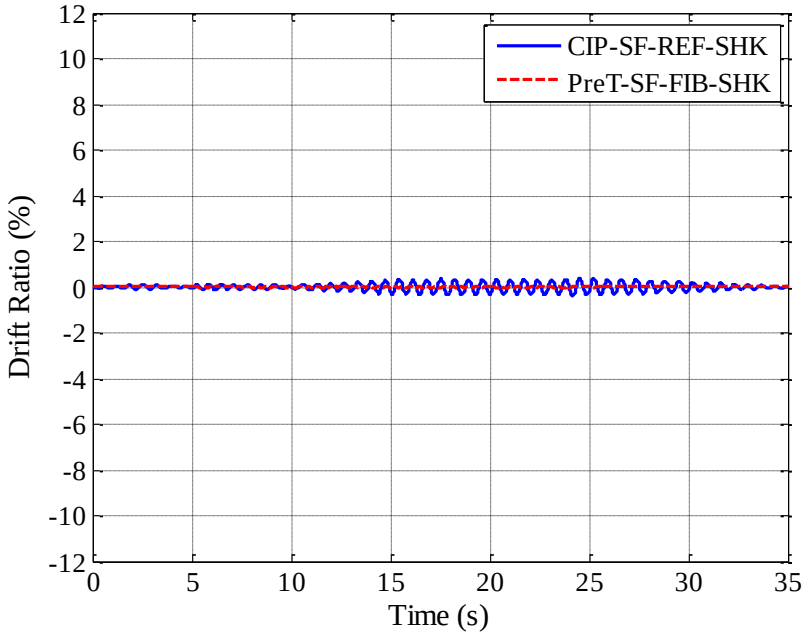

Figure 7-14. East-West drift ratio vs time. Earthquake 1 (below first yield)

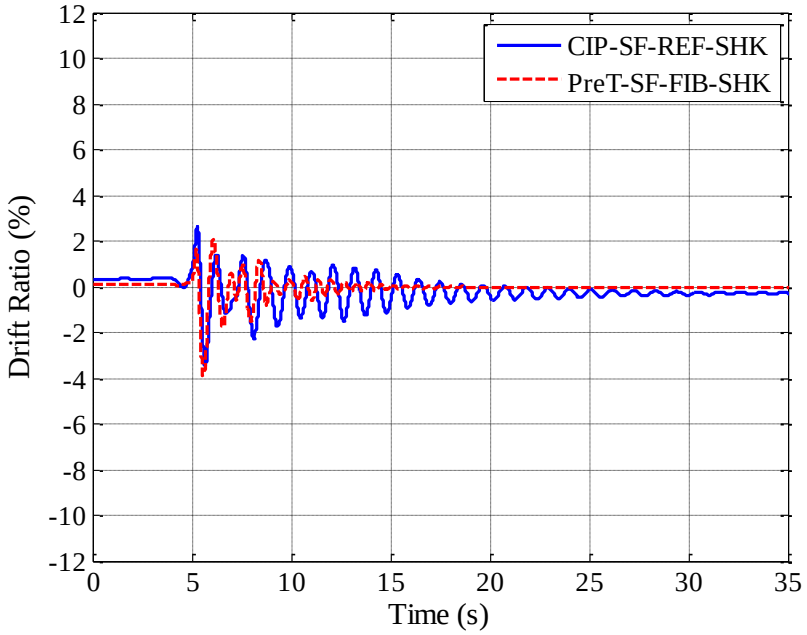

Figure 7-15. North-South drift ratio vs time. Earthquake 4 (Design Level)

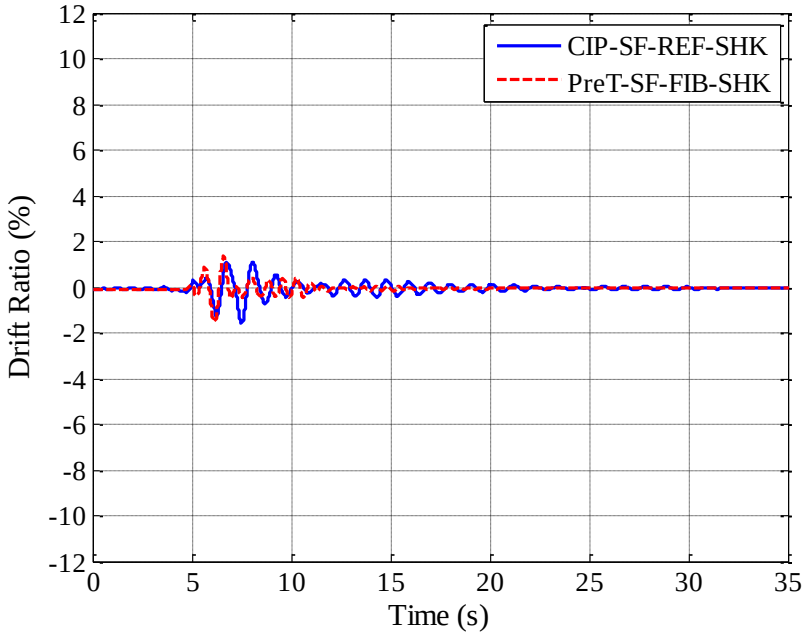

Figure 7-16. East-West drift ratio vs time. Earthquake 4 (Design Level)

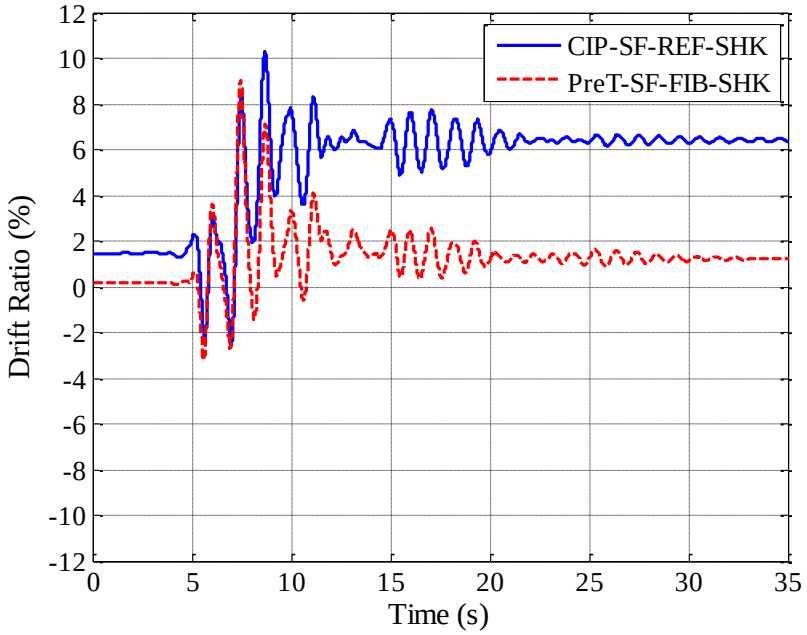

Figure 7-17. North-South drift ratio vs time. Earthquake 7 (2 x Design Level)

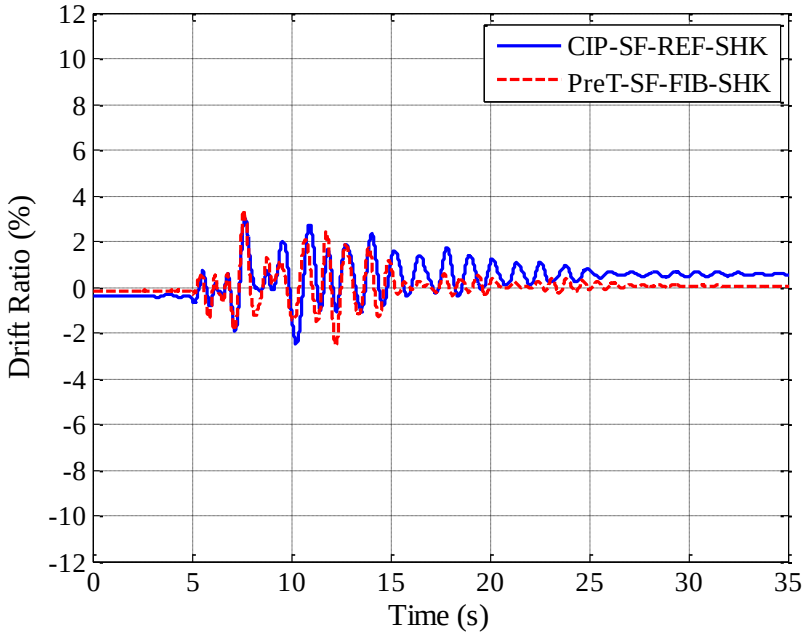

Figure 7-18. East-West drift ratio vs time. Earthquake 7 (2 x Design Level)

7.4 Moment-Drift Response

The column moment was calculated using two methods. First, moment was calculated by using the load cell measurements underneath the foundation and then by using inertial forces. Both approaches yielded almost identical results. Table 7-5 lists the peak calculated moments using inertial forces in both principal directions for both specimens for all earthquakes. The bracketed numbers in the table are the corresponding drift ratios at which peak moment was obtained.

Figures 7-19 through 7-24 show the moment vs. drift ratio responses of both specimens subjected to earthquake 1,4 and 6. At the beginning of the test program, Specimen PreT-SF-FIB-SHK was noticeably stiffer than Specimen CIP-SF-REF-SHK due to the pre-tensioning. As both columns were subjected to more earthquakes, Specimen PreT-SF-FIB-SHK showed more pinched response than Specimen CIP-SF-REF-SHK, indicating the self-centering capability and lower damping of Specimen PreT-SF-FIB-SHK.

Table 7-5. Maximum moment in North-South and East-West for specimens CIP-SF-REF-SHK and PreT-SF-FIB-SHK

EQ No.	CIP-SF-REF-SHK North-South Maximum Moment (kip-in.)		CIP-SF-REF-SHK East-West Maximum Moment (kip-in.)		PreT-SF-FIB-SHK North-South Maximum Moment (kip-in.)		PreT-SF-FIB-SHK East-West Maximum Moment (kip-in.)	
	Max	Min	Max	Min	Max	Min	Max	Min
1	584.2 (0.34%)	-613.7 (-0.38%)	530.9 (0.37%)	-544.6 (-0.40%)	1098.0 (0.42%)	-1086.0 (-0.40%)	153.5 (0.06%)	-156.6 (-0.05%)
2	1,860 (3.12%)	-1,504 (-1.30%)	956 (1.16%)	-977.7 (-1.21%)	1,696 (1.70%)	-1,206 (-0.60%)	1,205 (0.64%)	-1,068 (-0.59%)
3	1,433 (1.45%)	-1,037 (-0.11%)	306.6 (0.25%)	-397.2 (-0.18%)	1,805 (1.81%)	-1,304 (-1.03%)	1,459 (1.20%)	-2,087 (-2.09%)
4	1,546 (2.21%)	-1,929 (-3.22%)	1,066 (1.01%)	-1,145 (-1.67%)	1,595 (2.05%)	-2,289 (-3.48%)	1,396 (1.40%)	-1,235 (-1.58%)
5	2,026 (5.05%)	-1,732 (-2.89%)	1,173 (1.65%)	-1,142 (-1.57%)	2,161 (5.21%)	-2,010 (-3.70%)	1,283 (1.92%)	-1,185 (-1.78%)
6	2,024 (5.96%)	-1,663 (-2.04%)	1,323 (1.92%)	-1,509 (-3.07%)	1,780 (3.42%)	-2,499 (-5.42%)	1,290 (1.25%)	-1,395 (-2.27%)
7	2,074 (10.66%)	-1,749 (-2.66%)	1,281 (2.84%)	-1,320 (-2.38%)	2,245 (9.15%)	-1,672 (-3.32%)	1,344 (3.44%)	-1,467 (-2.68%)
8	N/A	N/A	N/A	N/A	1,559 (6.38%)	-1,762 (-3.79%)	1,392 (3.23%)	-1,523 (-3.62%)
9	N/A	N/A	N/A	N/A	1,304 (10.11%)	-1,276 (-2.03%)	526.7 (0.72%)	-621.6 (-1.96%)

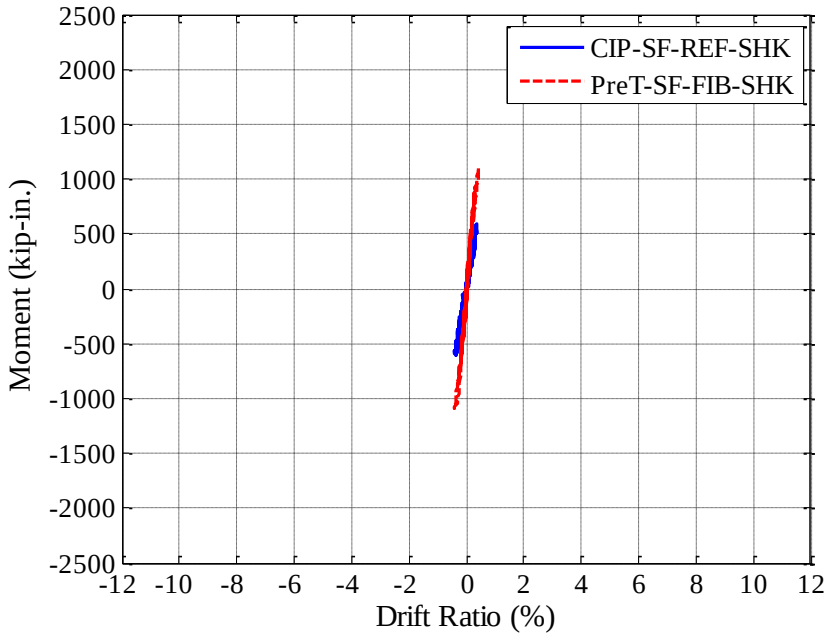

Figure 7-19. North-South moment vs drift ratio. Earthquake 1 (below first yield)

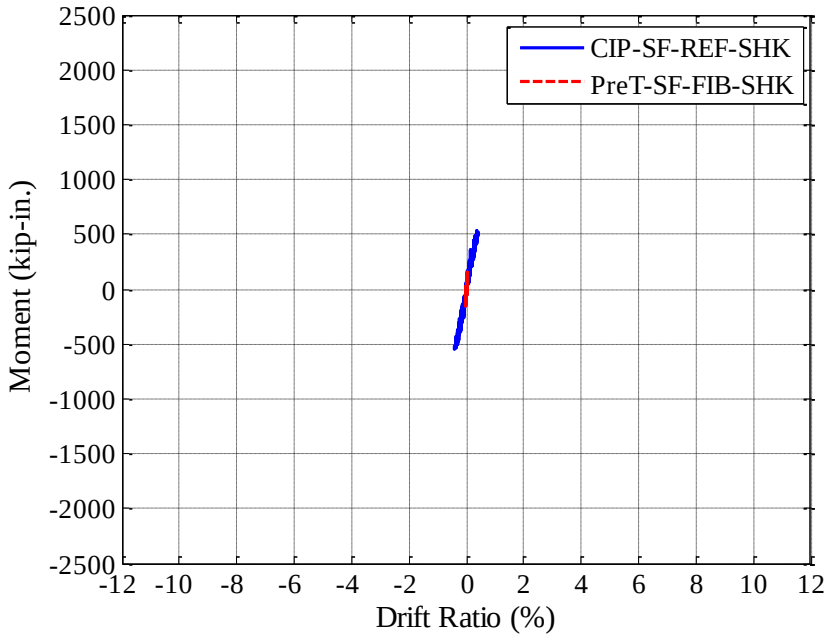

Figure 7-20. East-West moment vs drift ratio. Earthquake 1 (below first yield)

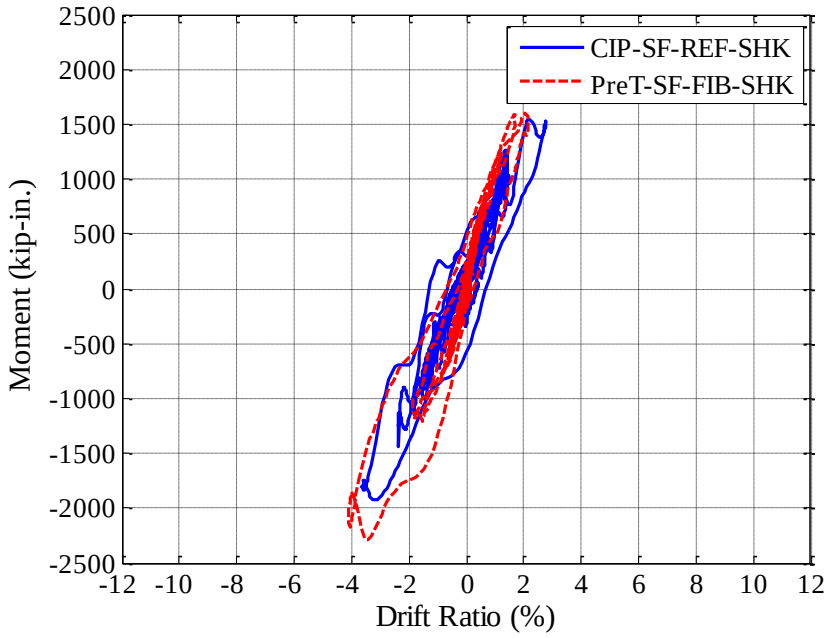

Figure 7-21. North-South moment vs drift ratio. Earthquake 4 (Design Level)

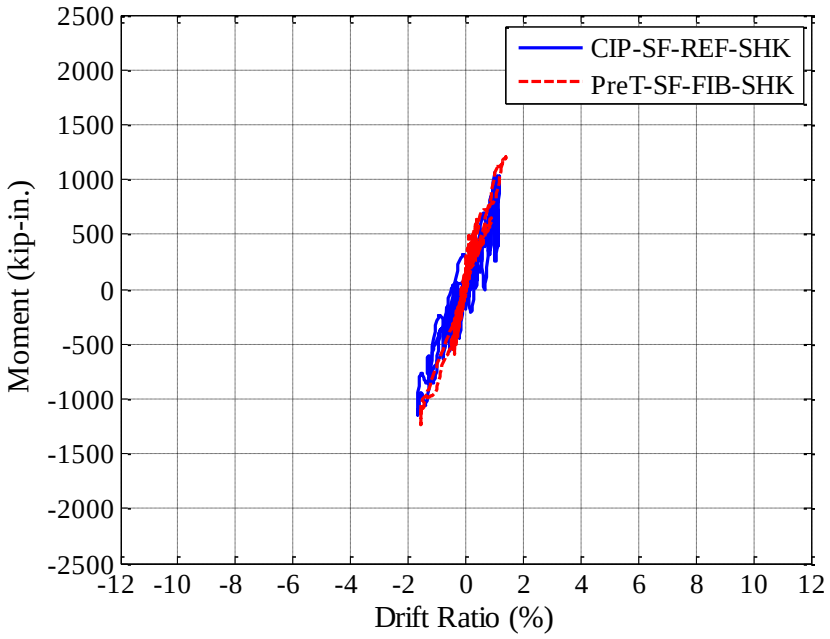

Figure 7-22. East-West moment vs drift ratio. Earthquake 4 (Design Level)

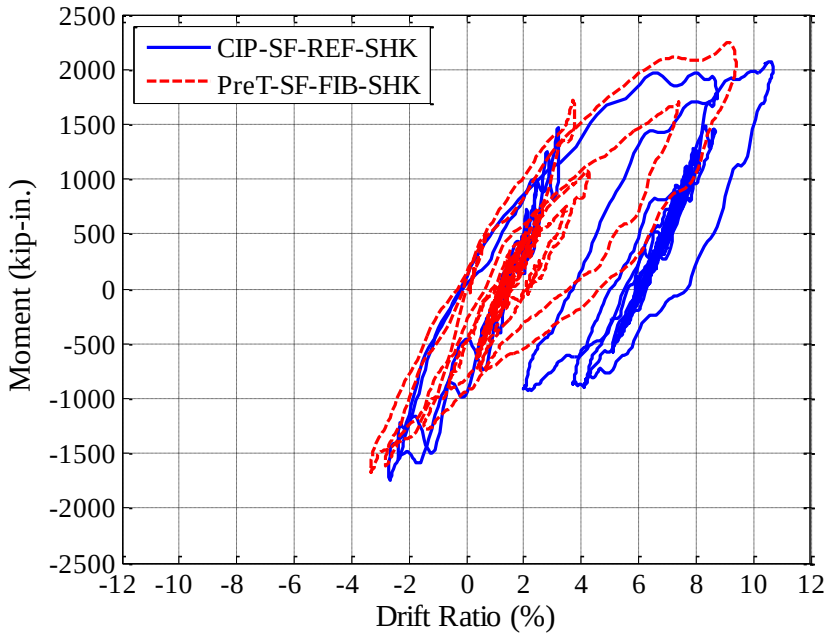

Figure 7-23. North-South moment vs drift ratio. Earthquake 7 (2 x Design Level)

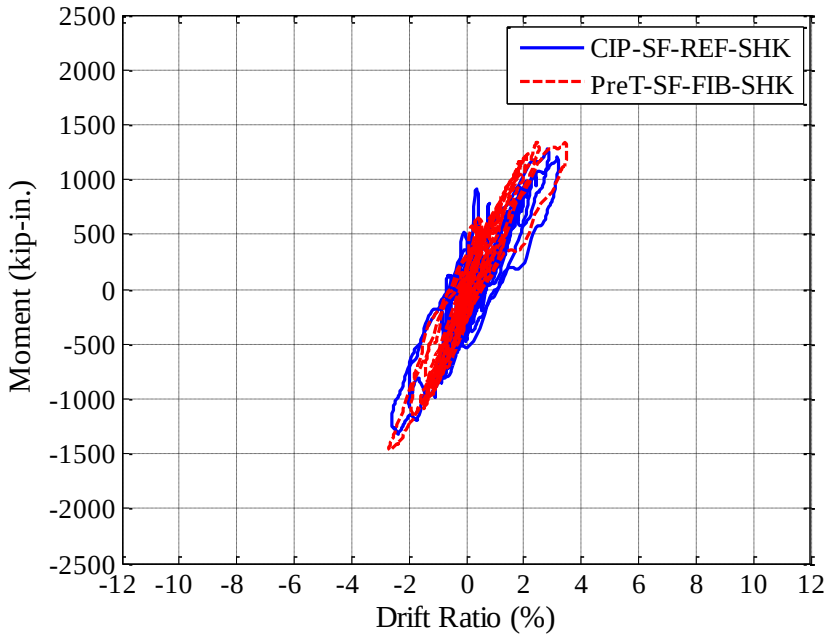

Figure 7-24. East-West moment vs drift ratio. Earthquake 7 (2 x Design Level)

7.5 Effective Force-Displacement Response

Table 7-6 lists the peak effective forces measured and their associated displacements in the two principal directions for both specimens. They are calculated by dividing the moment at the base of the column by the height from the top of the spread footing to the Center-of-Mass (COM). Figures 7-25 through 7-30 show similar plots to figures 7-19 through 7-24 except they are expressed in terms of effective force and displacement.

Table 7-6. Maximum effective force in North-South and East-West for specimens CIP-SF-REF-SHK and PreT-SF-FIB-SHK

EQ No.	CIP-SF-REF-SHK North-South Effective Force (kip)		CIP-SF-REF-SHK East-West Effective Force (kip)		PreT-SF-FIB-SHK North-South Effective Force (kip)		PreT-SF-FIB-SHK East-West Effective Force (kip)	
	Max	Min	Max	Min	Max	Min	Max	Min
1	6.1 (0.33 in.)	-6.4 (-0.36 in.)	5.5 (0.36in.)	-5.7 (-0.38 in.)	11.4 (0.40 in.)	-11.3 (-0.38 in.)	1.6 (0.06 in.)	-1.6 (-0.05 in.)
2	19.4 (3.00 in.)	-15.7 (-1.25 in.)	10.0 (1.11 in.)	-10.2 (-1.16 in.)	17.7 (1.63 in.)	-12.6 (-0.58 in.)	12.6 (0.61 in.)	-11.1 (-0.57 in.)
3	14.9 (1.39 in.)	-10.8 (-0.11 in.)	3.2 (0.24in.)	-4.1 (-0.17 in.)	18.8 (1.74 in.)	-13.6 (-0.99 in.)	15.2 (1.15 in.)	-21.7 (-2.01 in.)
4	16.1 (2.12 in.)	-20.1 (-3.09 in.)	11.1 (0.97 in.)	-11.9 (-1.60 in.)	16.6 (1.97 in.)	-23.8 (-3.34 in.)	14.5 (1.34 in.)	-12.9 (-1.52 in.)
5	21.1 (4.85 in.)	-18.0 (-2.77 in.)	12.2 (1.58 in.)	-11.9 (-1.51 in.)	22.5 (5.00 in.)	-20.9 (-3.55 in.)	13.4 (1.84 in.)	-12.3 (-1.71 in.)
6	21.1 (5.72 in.)	-17.3 (-1.96 in.)	20.0 (1.84 in.)	-15.7 (-2.95 in.)	18.5 (3.28 in.)	-26.0 (-5.20 in.)	13.4 (1.20 in.)	-14.5 (-2.18 in.)
i7	21.6 (10.23 in.)	-18.2 (-2.55 in.)	13.3 (2.73in.)	-13.8 (-2.28 in.)	23.4 (8.78 in.)	-17.4 (-3.19 in.)	14.0 (3.30 in.)	-15.3 (-2.57 in.)
8	N/A	N/A	N/A	N/A	16.2 (6.12 in.)	-18.4 (-3.64 in.)	14.5 (3.10 in.)	-15.9 (-3.48 in.)
9	N/A	N/A	N/A	N/A	13.6 (9.71 in.)	-13.3 (-1.95 in.)	5.5 (0.72 in.)	-6.5 (-1.88 in.)

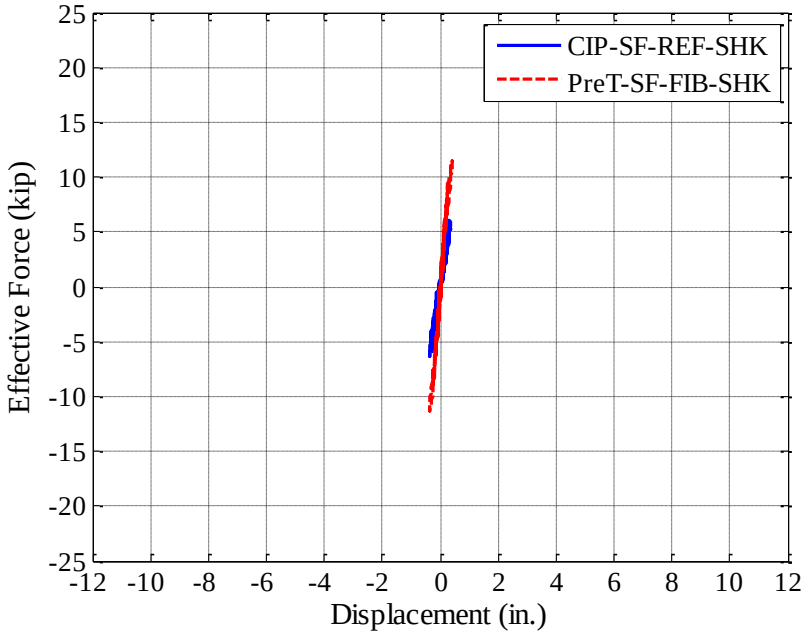

Figure 7-25. North-South moment vs drift ratio. Earthquake 1 (below first yield)

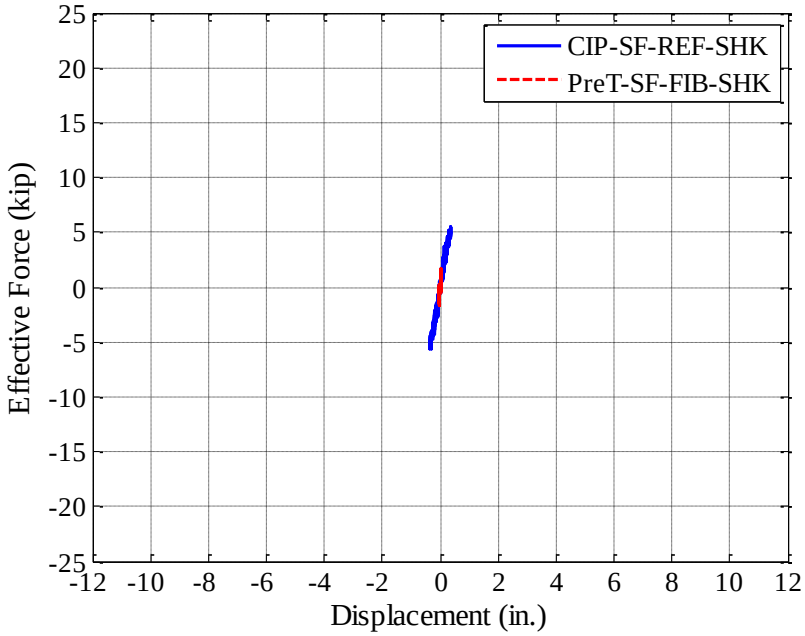

Figure 7-26. East-West moment vs drift ratio. Earthquake 1 (below first yield)

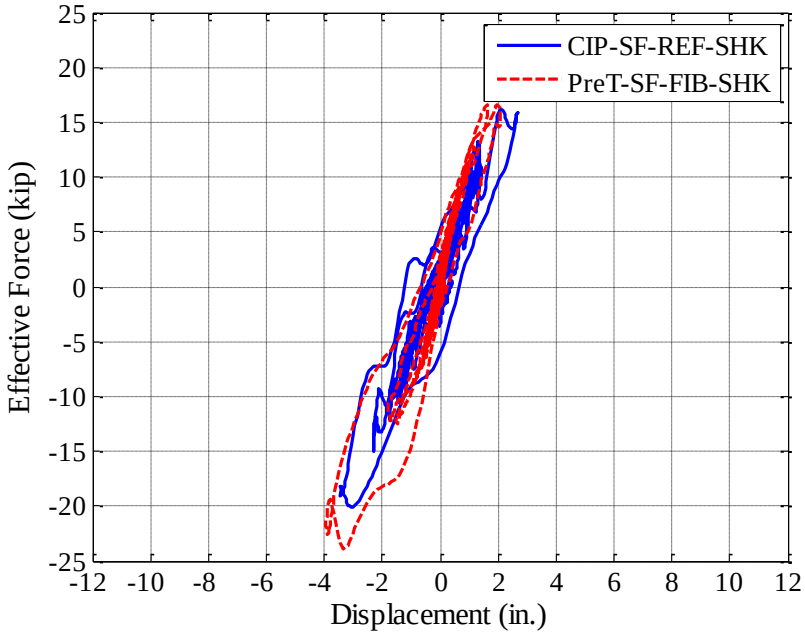

Figure 7-27. North-South moment vs drift ratio. Earthquake 4 (Design Level)

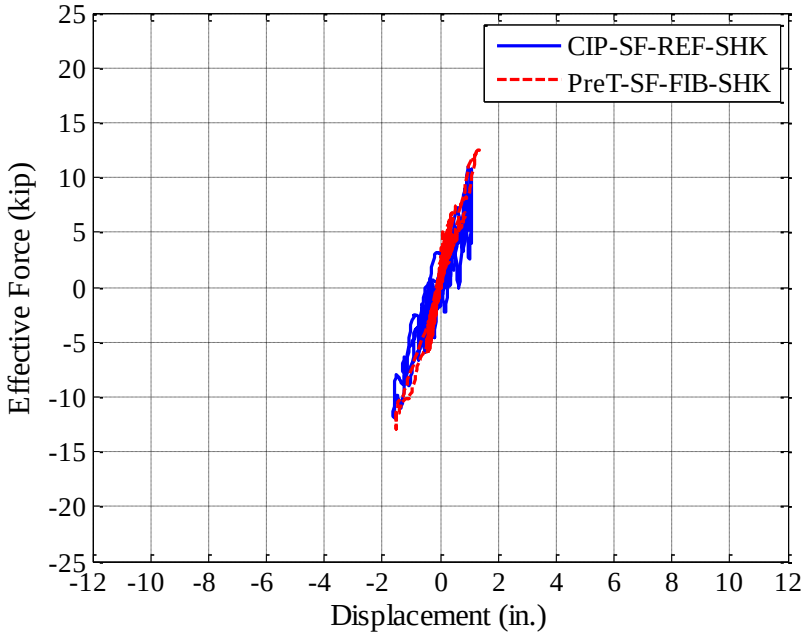

Figure 7-28. East-West moment vs drift ratio. Earthquake 4 (Design Level)

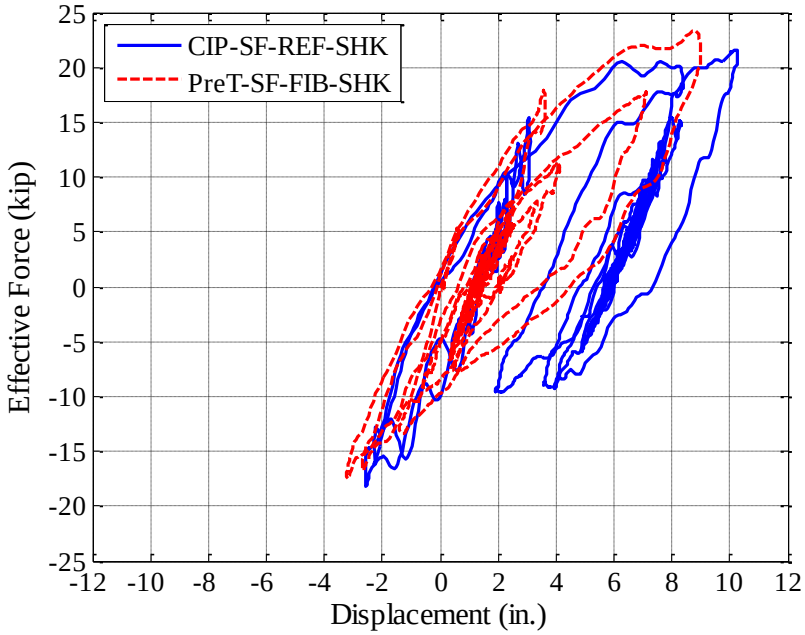

Figure 7-29. North-South moment vs drift ratio. Earthquake 7 (2 x Design Level)

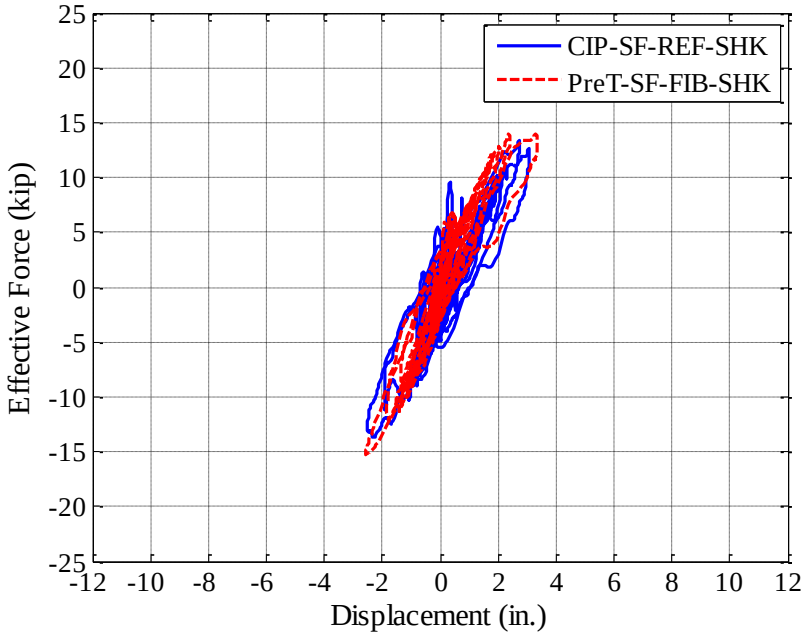

Figure 7-30. East-West moment vs drift ratio. Earthquake 7 (2 x Design Level)

7.5.1 Distribution of Column Curvature

Column curvatures were determined at various heights in both North-South and East-West directions. These curvatures were obtained from relative vertical displacements between the ends of threaded rods embedded horizontally in the column about 1.5, 5.5, 11.5, 16.5, 21.5, 26.5, and 52 inches above the footing surface. The average curvature within a column segment between rods is plotted at the midpoint of the segment.

Figures 7-31 through 7-36 show the average max-min peak curvature for both specimens in the principal directions (i.e., North-South and East-West). In the figures, positive curvature indicates that the column displaced in the positive direction (see sign convention in Figure 6-15) and vice a versa. The global coordinate system is discussed in Chapter 6.

Figures 7-31 and 7-32 show the curvature responses of specimens CIP-SF-REF-SHK and PreT-SF-FIB-SHK in Earthquake 1. Both columns were displaced below 0.40% drift ratio so a minor curvature was measured. Once the columns were subjected to design level earthquake (figures 7-33 and 7-34) and 2 x design level earthquake (figures 7-35 and 7-36), the deformation was concentrated at the base in both columns, as expected. The curvature distributions between the two specimens are different. In Specimen CIP-SF-REF-SHK, curvature was evenly distributed over the plastic hinge. In contrast, the curvature in Specimen PreT-SF-FIB-SHK is more concentrated where the shell cracked for the first time. It was noticed that the column rocked mainly about the same cracks in both directions. At heights more than one column diameter above the base, the column rocked as a rigid body and exhibited essentially no curvature.

Figures 7-37 through 7-42 show the residual curvatures in both columns after the tests. Consistently, Specimen CIP-SF-REF-SHK shows more residual curvature than Specimen PreT-SF-FIB-SHK. This shows that the pre-tensioning strands were re-centering Specimen PreT-SF-FIB-SHK back to vertical.

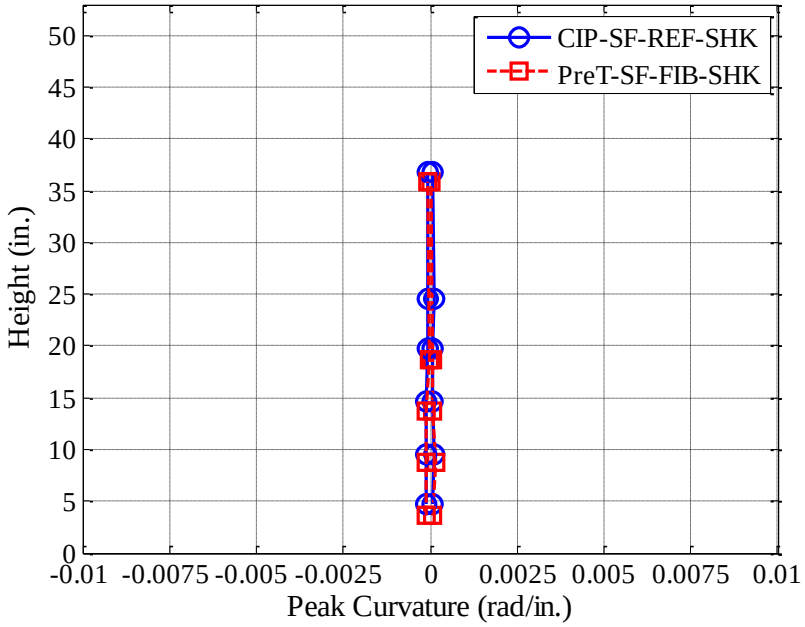

Figure 7-31. North-South peak column curvature. Earthquake 1 (below first yield)

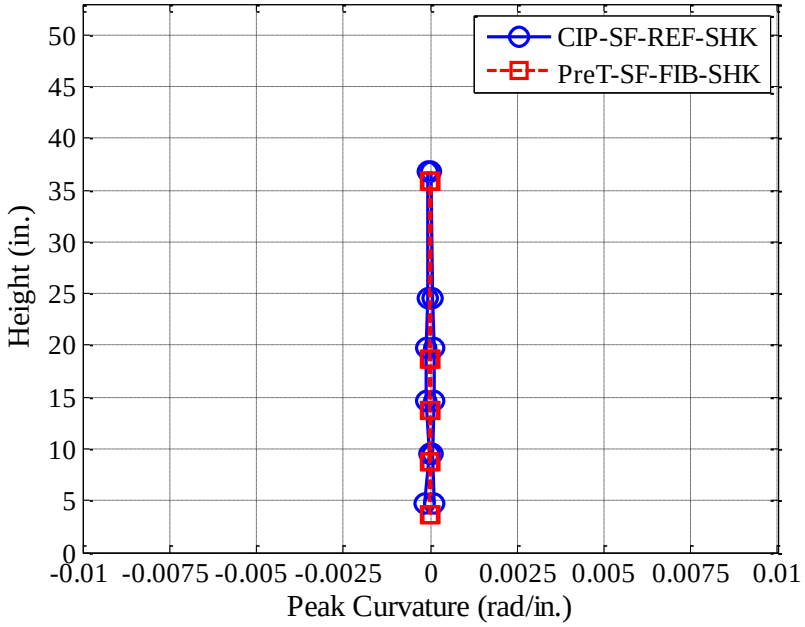

Figure 7-32. East-West average peak column curvature. Earthquake 1 (below first yield)

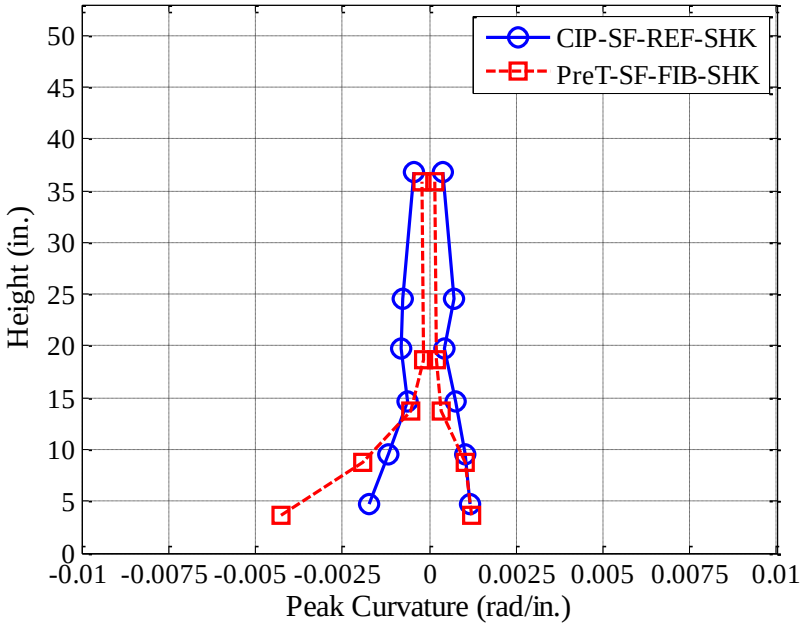

Figure 7-33. North-South average peak column curvature. Earthquake 4 (Design Level)

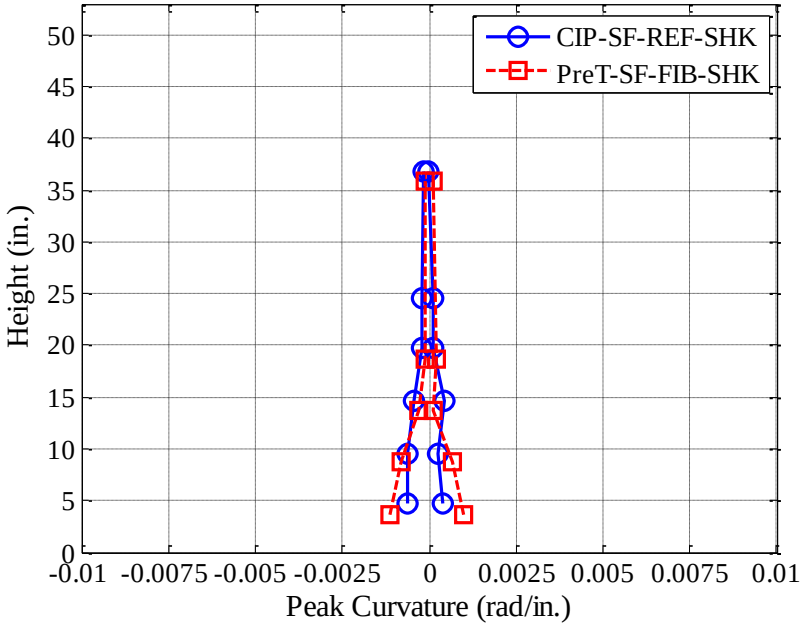

Figure 7-34. East-West average peak column curvature. Earthquake 4 (Design Level)

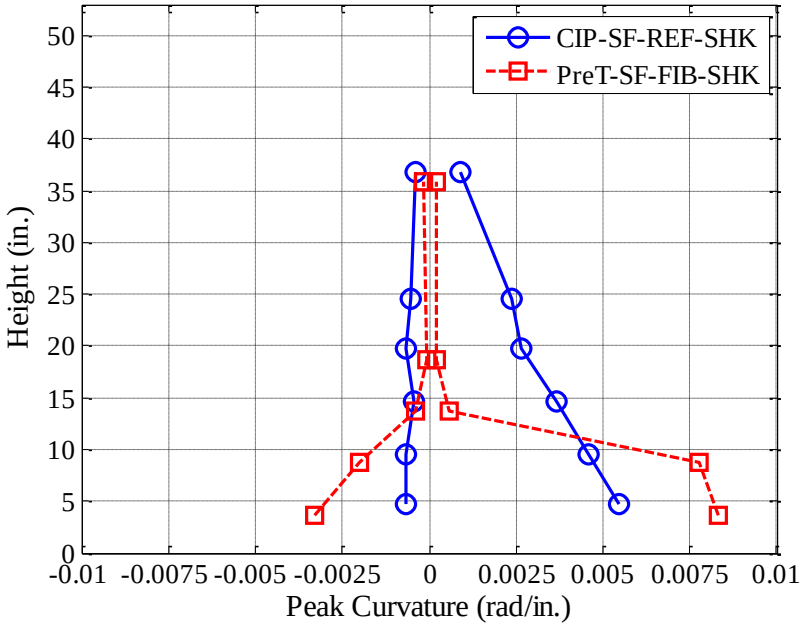

Figure 7-35. North-South average peak column curvature. Earthquake 7 (2 x Design Level)

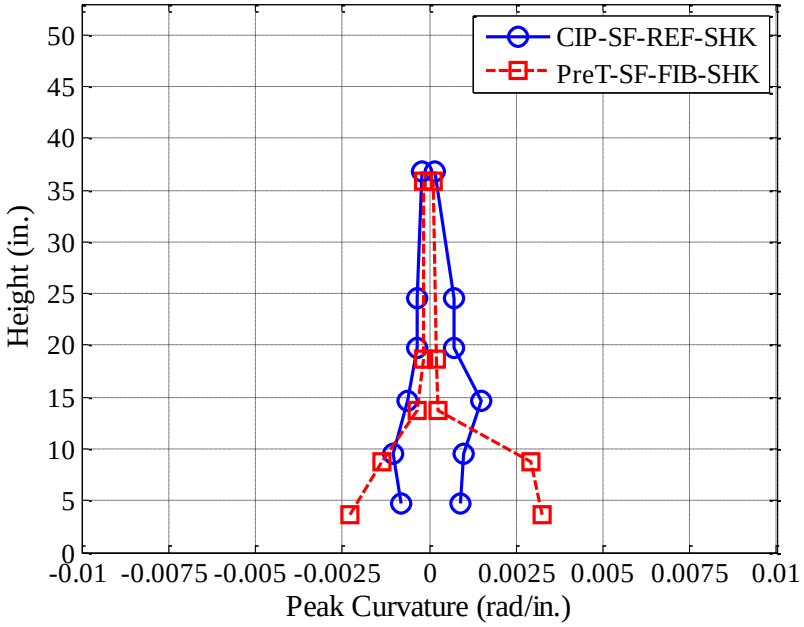

Figure 7-36. East-West average peak column curvature. Earthquake 7 (2 x Design Level)

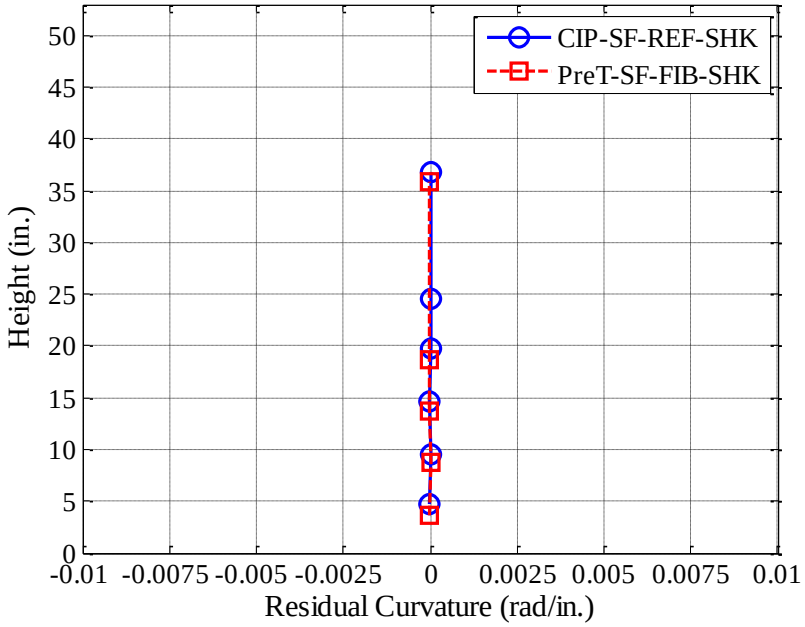

Figure 7-37. North-West average residual column curvature. Earthquake 1 (below first yield)

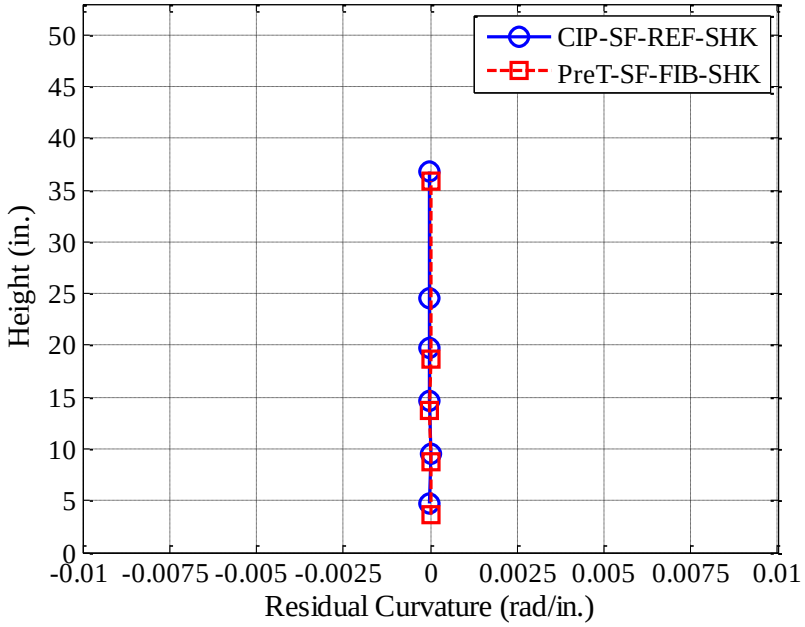

Figure 7-38. East-West average residual column curvature. Earthquake 1 (below first yield)

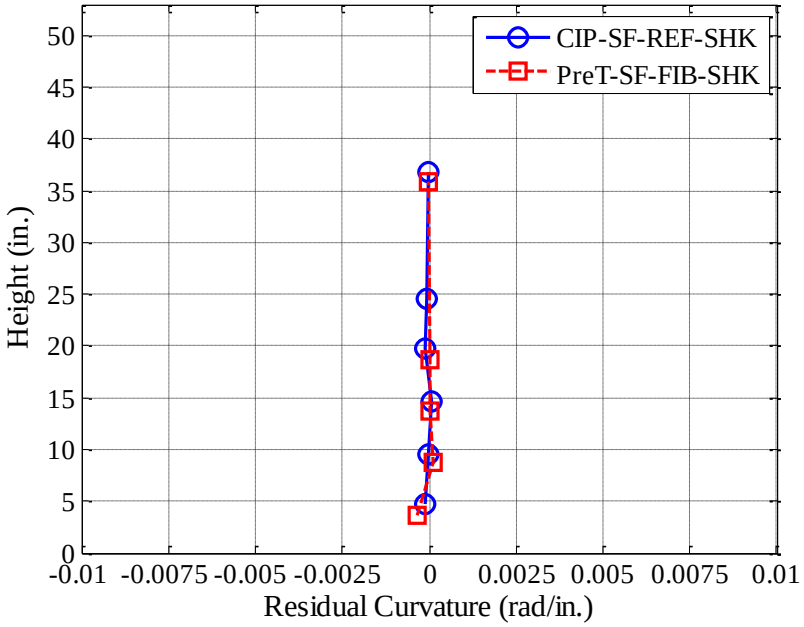

Figure 7-39. North-South average residual column curvature. Earthquake 4 (Design Level)

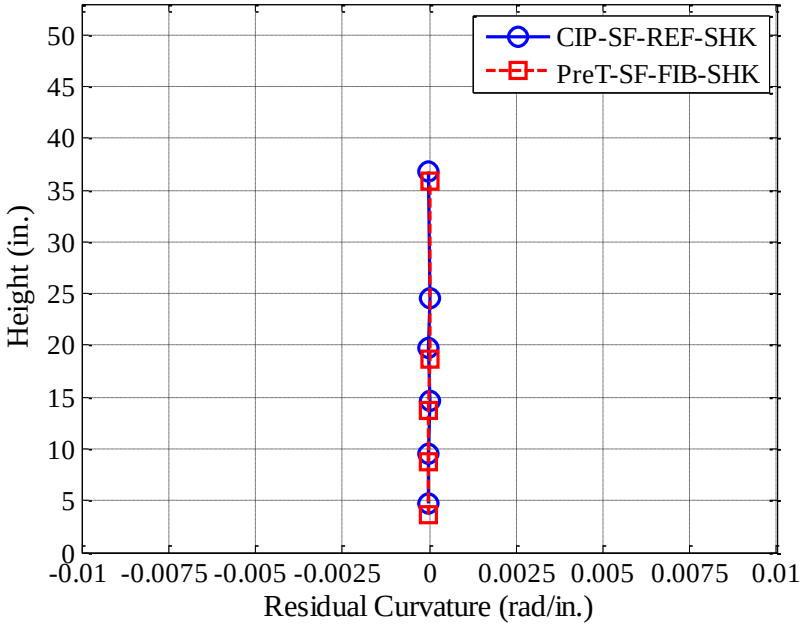

Figure 7-40. East-West average residual column curvature. Earthquake 4 (Design Level)

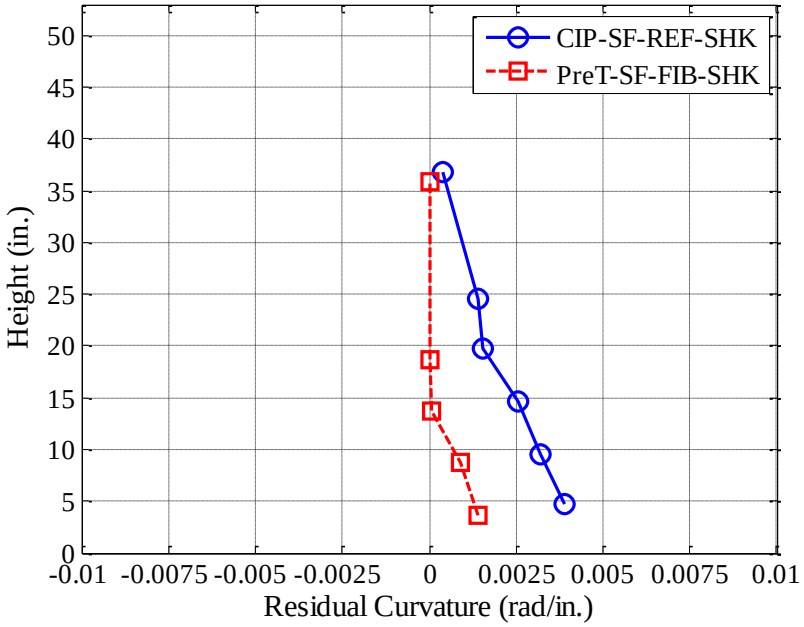

Figure 7-41. North-South average residual column curvature. Earthquake 7 (2 x Design Level)

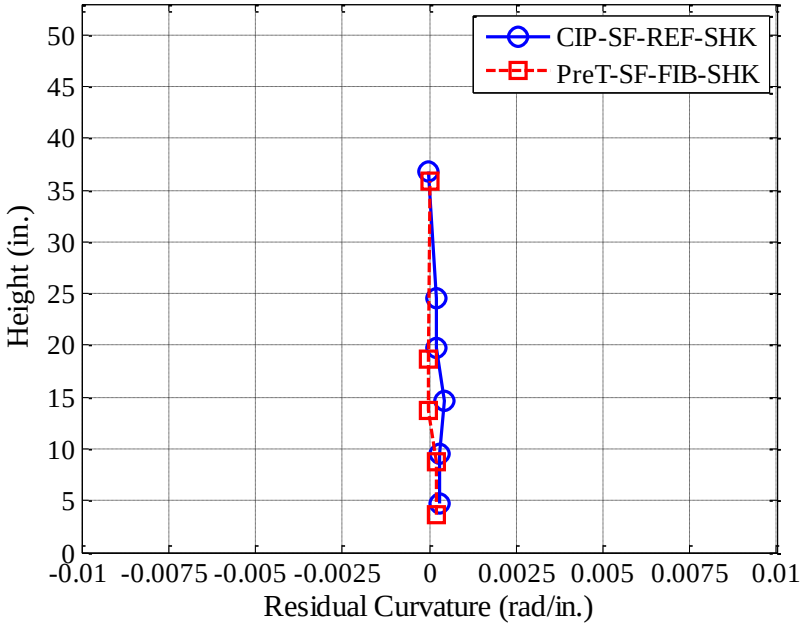

Figure 7-42. East-West average residual column curvature. Earthquake 7 (2 x Design Level)

7.6 Axial Column Strains

Axial column strains were determined by the same relative displacements between the ends of threaded rods embedded horizontally in the column about 1.5, 5.5, 11.5, 16.5, 21.5, 26.5, and 52 inches about the footing surface. In figures 7-43 through 7-45, the average strain is presented in North-South and East-West directions. Tension strain is positive. Figures 7-44 and 7-45 reveal that the axial strains in Specimen PreT-SF-FIB-SHK were concentrated in the crack plane that at which the column rocked.

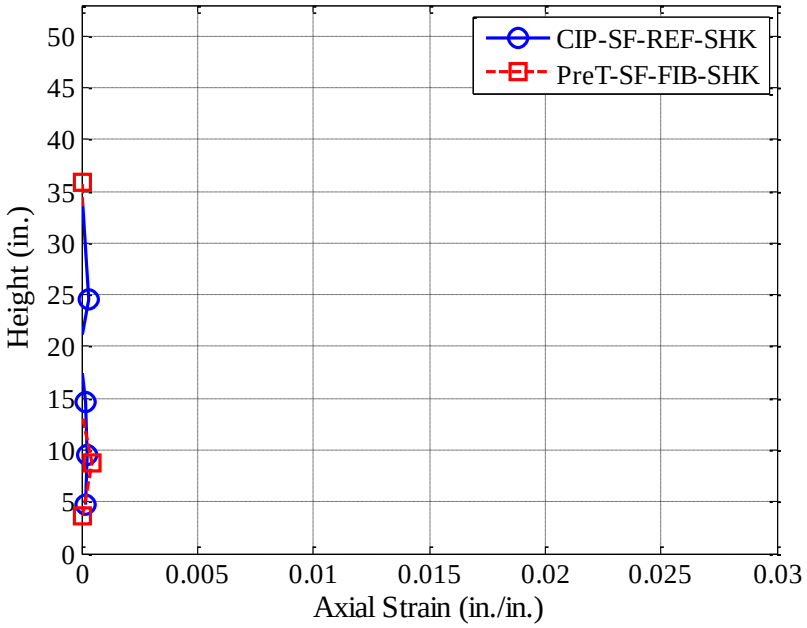

Figure 7-43. Average column axial strains at peak displacement (in any direction). Earthquake 1 (below first yield)

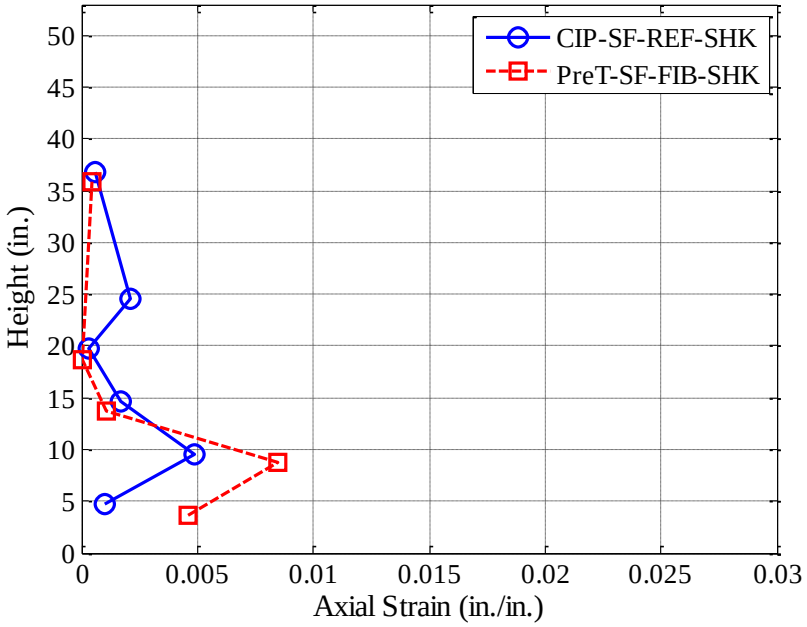

Figure 7-44. Average column axial strains at peak displacement (in any direction). Earthquake 4 (Design Level)

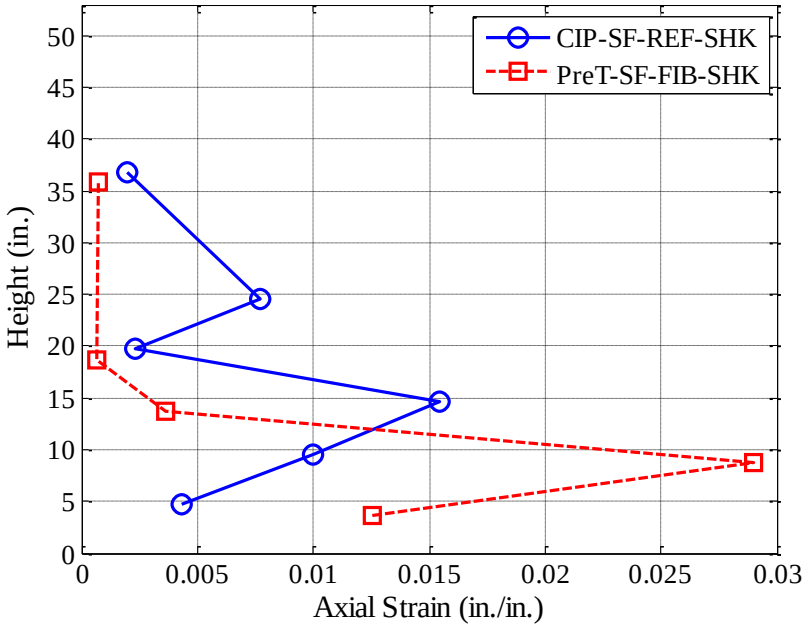

Figure 7-45. Average column axial strains at peak displacement (in any direction). Earthquake 7 (2 x Design Level)

8 Evaluation of Single-Column Test Results

In this chapter, the two shake-table specimens are compared in terms of column period elongation, stiffness, damping, and their tendency to re-center to their original plumb position after being subjected to earthquake ground motions.

8.1 Column Period

Before the shake table tests were conducted on Specimens CIP-SF-REF-SHK and PreT-SF-REF-SHK, the columns were tested in free-vibration to determine the systems' initial periods, stiffnesses and damping coefficients. The specimens were pulled back with a force ranging from 1.5-1.8 kips, as described in Chapter 6. The displacements of the columns were monitored with a linear string potentiometer that was attached to a reference pole. Both specimens were tested in the North-South direction, and only Specimen PreT-SF-FIB-SHK was tested in the East-West direction. The two pull-back tests on Specimen PreT-SF-FIB-SHK yielded same results, as expected. Between shake table tests, the column properties were evaluated using low-amplitude white noise excitation, rather than pull-back tests, in the interests of saving time.

The first period, T_1, of each column was obtained using two methods.

- Taking the Fourier Spectrum of the column's white noise test response, and
- By using the free-vibration of the column after each earthquake test. The period was determined by counting zero crossings of successive cycles and taking the average. The column free-vibration was assumed to start when shake-table hydraulics stopped.

Table 8-1 lists the first period obtained using both the Fourier Spectrum and free-vibration approach. The two methods were quite consistent.

Table 8-1. First period, T_1, estimated with two methods.

EQ No.	First Period (s)							
	Specimen CIP-SF-REF-SHK				Specimen PreT-SF-FIB-SHK			
	Fourier Spectrum		Free-Vibration		Fourier Spectrum		Free-Vibration	
	North-South	East-West	North-South	East-West	North-South	East-West	North-South	East-West
1	0.661	0.717	0.683	0.701	0.413	0.414	0.402	0.403
2	1.011	0.900	0.998	0.994	0.454	0.437	0.440	0.433
3	0.996	1.002	0.986	0.980	0.454	0.475	0.471	0.470
4	1.018	1.018	1.086	1.084	0.552	0.503	0.575	0.561
5	1.146	1.111	1.105	1.015	0.621	0.523	0.640	0.535
6	1.118	1.126	1.129	1.078	0.648	0.544	0.744	0.739
7	1.126	1.118	1.014	1.045	0.910	0.691	1.010	0.798
8	N/A	N/A	N/A	N/A	1.354	0.845	1.380	0.902
9	N/A	N/A	N/A	N/A	1.672	0.895	1.583	0.857

Note that in general the free-vibration duration was typically shorter in Specimen PreT-SF-FIB-SHK than in Specimen CIP-SF-REF-SHK because the former showed typically more damping than the latter. A possible explanation is that the achieved displacement ductility of Specimen CIP-SF-REF-SHK was lower than in Specimen PreT-SF-FIB-SHK because of lower column stiffness, which was a consequence of lower concrete strength. Furthermore, Specimen CIP-SF-REF-SHK endured almost double the target peak drift in Earthquake 2 than Specimen PreT-SF-FIB-SHK, resulting in significant yielding of the column mild reinforcement.

The period of the second mode, T_2, was difficult to determine with Fourier Spectrum and is therefore omitted here.

Figures 8-1 and 8-2 show the first period, determined from free-vibration, for both specimens in each principal direction (North-South and East-West). In these figures, data points represent periods measured just after each particular test (e.g., EQ2 means “just after EQ2”).

- Throughout the test program, both specimens experienced period elongation in both directions as the columns accumulated more damage.
- Specimen PreT-SF-FIB-SHK consistently had shorter period than Specimen CIP-SF-REF-SHK due to additional stiffness provided by the pre-tensioned strands. Initial period difference was about 40% (the initial period for specimens CIP-SF-REF-SHK and PreT-SF-FIB-SHK were 0.53 and 0.38 seconds, respectively).
- During Earthquake 2, Specimen CIP-SF-REF-SHK was displaced nearly double the target drift ratio (see Table 6-4) that resulted in a period increase from about 0.70 seconds to 1.0. After that test, the period ranged between 1.0 and 1.13 seconds. No column longitudinal bars or spiral fractured during testing of Specimen CIP-SF-REF-SHK.
- In contrast to Specimen CIP-SF-REF-SHK, PreT-SF-FIB-SHK's period gradually increased throughout the test program. As a result of pre-tensioning strands being designed to remain elastic up to 3.0% drift, the period increase was minimal up to Earthquake 4. In Earthquake 8, two longitudinal bars fractured that resulted in a significant period increase from 1.0s to 1.4s in North-South direction.
- For both columns, the period in East-West direction was lower than in North-South direction. The difference is more extreme in Specimen PreT-SF-FIB-SHK. This is consistent to the fact that the ground motions and the resulting damage were more severe in North-South direction.

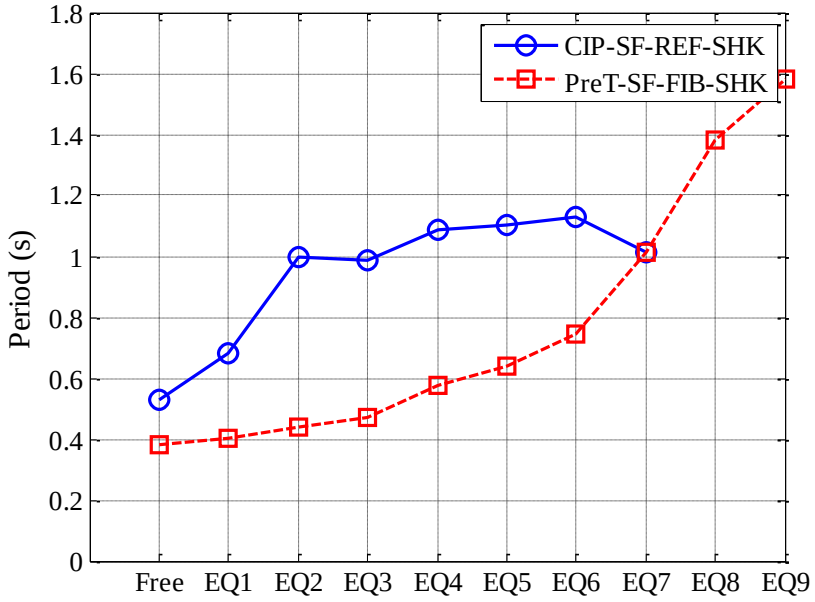

Figure 8-1. North-South variation of measured period

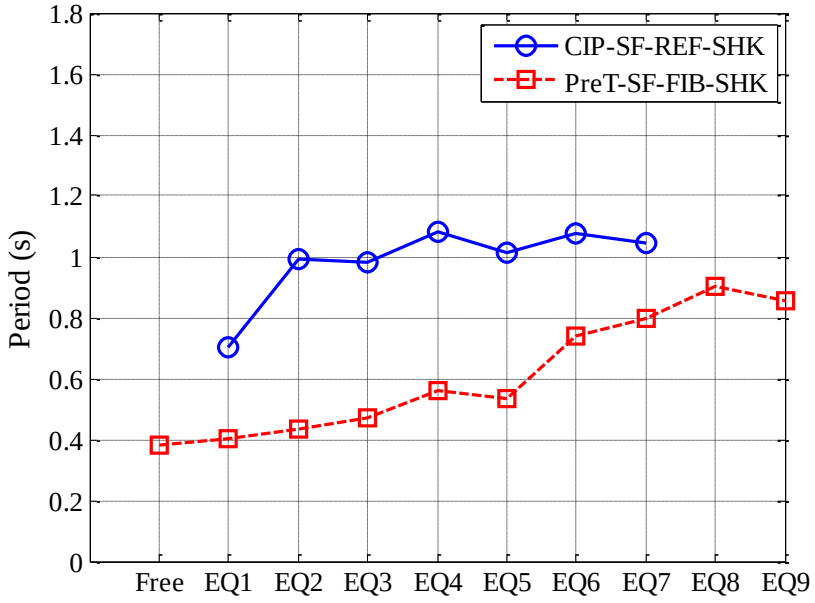

Figure 8-2. East-West variation of measured period for specimens

8.2 Column Stiffness

The dynamic properties of specimens CIP-SF-REF-SHK and PreT-SF-FIB-SHK were with idealized with two versions of a Two-Degree-of-Freedom (2DOF) system with a rigid end zone. They differed in terms of the length of the rigid end zone. As described in Chapter 6, the cantilever specimens had steel brackets post-tensioned into the load stub that supported the mass blocks. Figure 8-3 shows the two system idealizations.

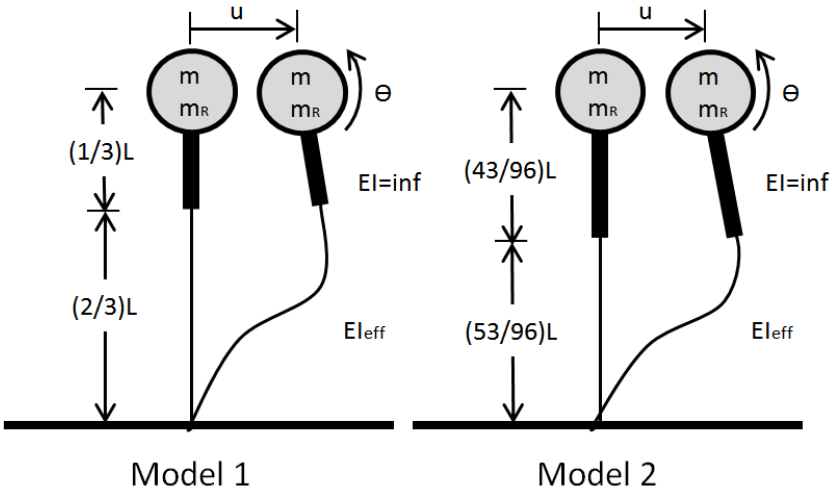

Figure 8-3. 2DOF idealizations with rigid end zone

In Model 1, the rigid end zone length was taken as one-third of the height from the top of the spread footing to the center-of-mass (COM), or 32 in, whereas in Model 2 the length was increased to 43 in. to include the entire height of the load stub. Out of the two idealizations, Model 2 is considered to be the more accurate one since the load stub was large and well reinforced.

The effective stiffness, EI_{eff}, was determined by solving Equation 8-1:

$$det[k - \omega_n^2 m] = 0 \qquad 8\text{-}1$$

where k is the stiffness matrix and m is the mass matrix that includes the mass ($m = 0.135\ kip \cdot kip \cdot \frac{s^2}{in}$.) and the mass moment of inertia of the blocks ($m_r = 181\ kip - in. - s^2$)m.

The matrices for the two models are defined as following:

- Model 1

$$k = \begin{bmatrix} \frac{40.5EI_{eff}}{L^3} & \frac{27EI_{eff}}{L^2} \\ \frac{27EI_{eff}}{L^2} & \frac{19.5EI_{eff}}{L} \end{bmatrix}$$

$$m = \begin{bmatrix} m & 0 \\ 0 & m_r \end{bmatrix}$$

- Model 2

$$k = \begin{bmatrix} \frac{71.328EI_{eff}}{L^3} & \frac{51.638EI_{eff}}{L^2} \\ \frac{51.638EI_{eff}}{L^2} & \frac{39.195EI_{eff}}{L} \end{bmatrix}$$

$$m = \begin{bmatrix} m & 0 \\ 0 & m_r \end{bmatrix}$$

Since the natural circular frequency of vibration, ω_1, is known, the effective stiffness of the system, EI_{eff}, can be extracted from Equation 8-1. Table 8-2 reports the concrete modulus of elasticity for specimens CIP-SF-REF-SHK and PreT-SF-FIB-SHK.

Table 8-2. Concrete modulus for specimens CIP-SF-REF-SHK and PreT-SF-FIB-SHK

Reference	Specimen	$E_{c,col}$ (ksi)
Schoettler et al. 2013	CIP-SF-REF-SHK[1]	3,274
Haraldsson	PreT-SF-FIB-SHK[2]	4,750

1. Estimated with ACI Equation
2. Material test on HyFRC

For periods ranging from 0.2s to 2.0s, figures 8-4 and 8-5 plot the effective stiffness-to-gross stiffness ratio curves for each specimen using the two models. The curves are plotted as period versus EI_{eff}/EI_{gross}. For comparison, a curve from a single-degree-of-freedom system is

included in both plots. In the SDOF system, the height is taken as the height from the foundation surface to the center-of-mass (COM), or 96 in.

Figure 8-5 shows a peculiar result for Specimen PreT-SF-FIB-SHK. For a fundamental period of 0.38 seconds measured in the pull-back tests, all models underestimate the effective stiffness (i.e., EI_{eff}/EI_{gross} is less than 1.0). For following reasons, one would expect this ratio to be closer to 1.0 due to the pre-tensioning.

- Pullback tests never induced high enough moment to cause decompression and no cracks were detected before the specimen was allowed to go into free-vibration. The same applied for Specimen CIP-SF-REF-SHK.
- No defects were detected in the HyFRC shell after it was cast. Both outer and inner surface of the shell indicated good consolidation of the HyFRC.
- The HyFRC shell extended 4 in. into the foundation with roughened outer surface. There were no signs throughout the test program that the shell was lifting up from the foundation.

For EI_{eff}/EI_{gross} equal to 1.0, 2DOF models predict the natural period to be in the range from 0.33 to 0.34 seconds. A possible reason for a higher measured natural period is that the specimen was sitting on load cells with packer plates and grout which introduced additional flexibility.

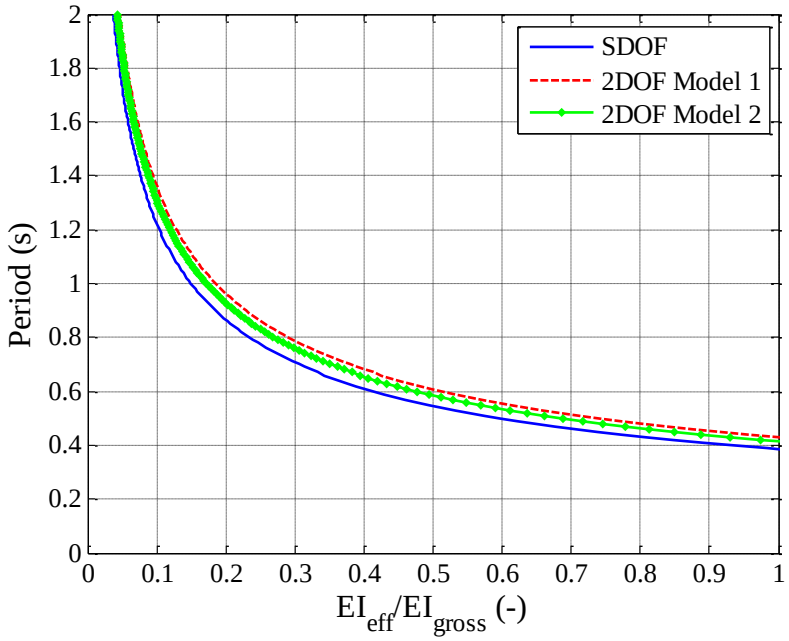

Figure 8-4. Period-EIeff/EIgross comparison for Specimen CIP-SF-REF-SHK

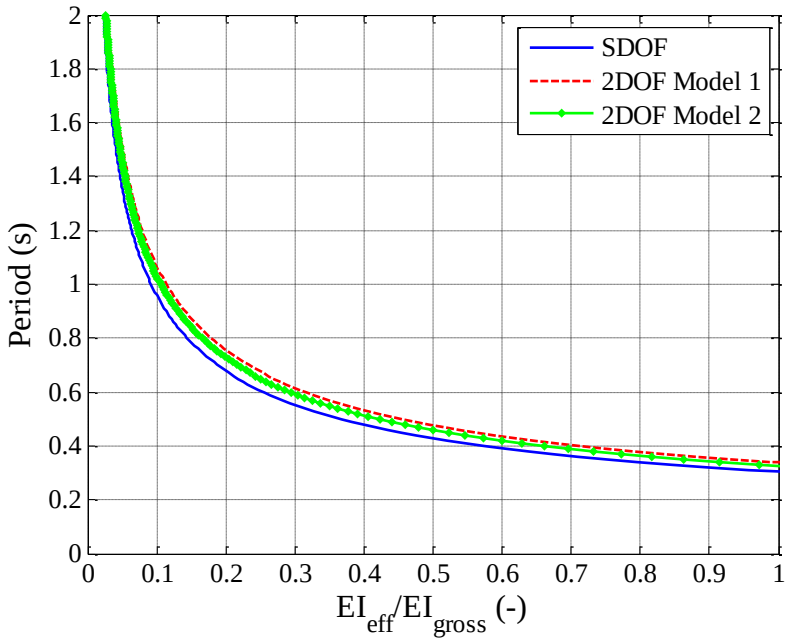

Figure 8-5. Period-EIeff/EIgross comparison for Specimen PreT-SF-FIB-SHK

Figures 8-6 and 8-7 compare the effective stiffness-to-gross stiffness ratios of the two specimens in both principal directions, respectively, throughout the test program using both models. In these figures, each data point is an estimation of the ratio using the period obtained at that particular test.

- Both models show that the pre-tensioned Specimen PreT-SF-FIB-SHK was stiffer than Specimen CIP-SF-REF-SHK, as expected.
- The effective stiffness of Specimen CIP-SF-REF-SHK goes down significantly after Earthquake 2 due to yielding of the mild reinforcement. Specimen CIP-SF-REF-SHK experienced was nearly the double the target displacement.
- In contrast to Specimen CIP-SF-REF-SHK, PreT-SF-FIB-SHK's effective stiffness goes gradually down as the strands start to yield and the specimen loses prestressing. In North-South direction, the stiffness goes well below 0.10 in earthquakes 8 and 9 for both Model 1 and 2. This was not unexpected since two bars fractured in Earthquake 8 and in the subsequent earthquake additional two more fractured.

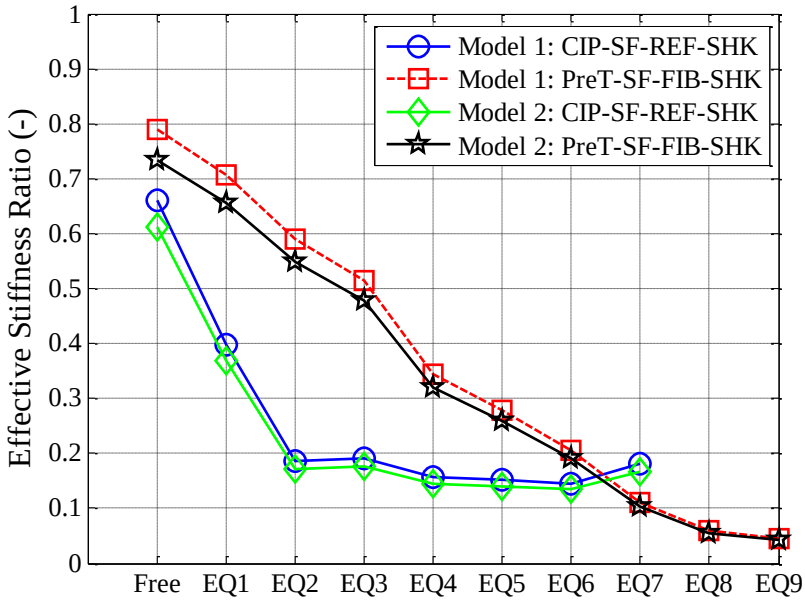

Figure 8-6. North-South variation of effective stiffness for specimens CIP-SF-REF-SHK and PreT-SF-FIB-SHK

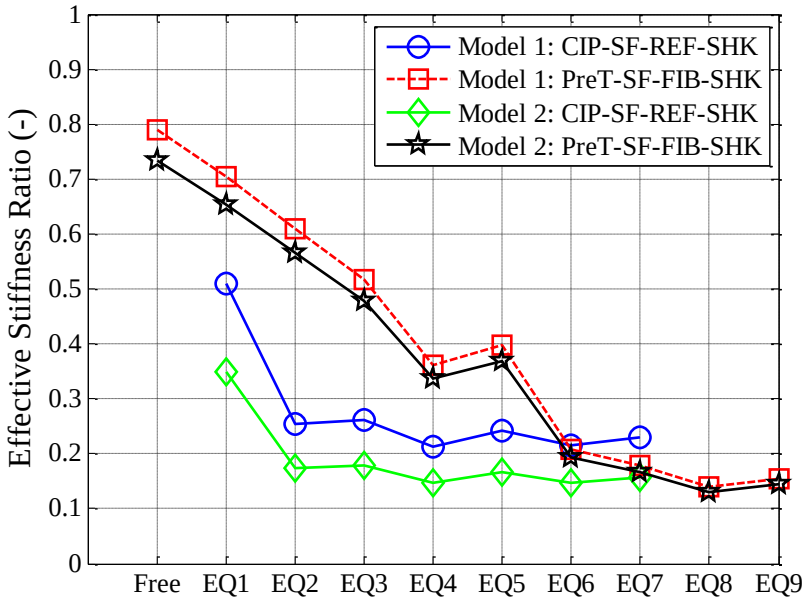

Figure 8-7. Variation of effective stiffness of specimens CIP-SF-REF-SHK and PreT-SF-FIB-SHK

ACI 318-08 Section 10.10.4.1 provides recommendations on how to determine the effective stiffness for concrete members to calculate lateral deflections. For columns, the following recommendations are given:

- Using $0.7E_cI_g$, or alternatively
- $\boldsymbol{E_cI = \left(0.8 + 25\frac{A_{st}}{A_g}\right)\left(1 - \frac{M_u}{P_u h} - 0.5\frac{P_u}{P_0}\right)I_g \leq 0.875E_cI_g}$

where E_c is the concrete modulus of elasticity calculated as $57{,}000\sqrt{f'c}$, I_g is the gross moment of inertia, A_{st} is the area of steel, A_g is the gross section area, h is the height of the column, P_u and M_u are axial and moment under consideration, respectively, and P_u is nominal axial strength.

Figure 8-10 compares ACI recommendations to the results obtained for Specimen CIP-SF-REF-SHK in North-South direction. The curves from Model 1 and Model 2 are the same ones used in Figure 8-8. As inputs for P_u and M_u, measured values from each earthquake test was used. Comparing the two models to ACI the following can be observed:

- In the pullback test, Model 1 and Model 2 predict similarly the effective stiffness as ACI's simple $0.7E_cI_g$ assumption.
- At a low level of shaking below first yield (EQ1), ACI overestimates the effective stiffness. Both Model 1 and 2 show stiffness reduction.
- In subsequent earthquakes, the difference between ACI and the two models gets more pronounced. Both ACI' allowed recommendations show that the effective stiffness is about $0.7E_cI_g$. In comparison, both models show at this point the effective stiffness is about $0.15E_cI_g$. Other researchers have observed similar stiffness reduction in their tests on RC columns (e.g., Hachem et al. 2002).

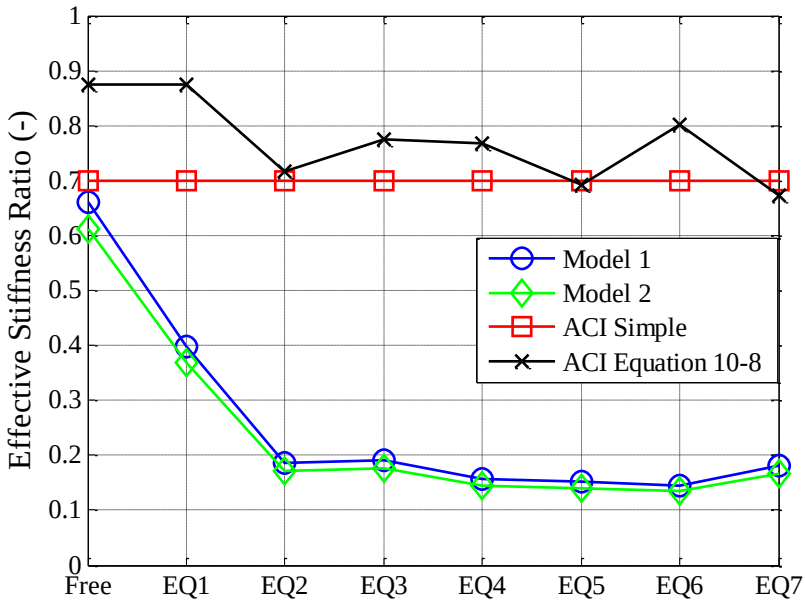

Figure 8-8. Comparison of effective stiffness for Specimen CIP-SF-REF-SHK in North-South direction

8.3 Column Viscous Damping

As described in Section 8.1, the column viscous damping can ideally be approximated by using power spectral density estimate through the use of the half-power method. This method did not yield consistent results and in later earthquake tests showed that the columns had little or no damping. As the test program progressed, the columns were displaced far enough such that the white noise did not excite the columns enough to make them go beyond their new elastic range (steel has yielded and thus has permanent deformation), resulting in no damping. Instead of using the power spectral density approach, the free-vibration decay of the columns after each earthquake was used instead. As before, the column free-vibration was assumed to start when shake-table hydraulics stopped.

The free vibration is bounded by envelopes defined by equations 8-2 and 8-3 (Chopra 2005):

$$u(t) = u_0 + \rho_{top} e^{-\zeta \omega_n t} \quad 8\text{-}2$$

$$u(t) = u_0 - \rho_{bottom} e^{-\zeta \omega_n t} \quad 8\text{-}3$$

where ξ is the damping ratio to be determined, ω_n is the natural frequency of vibration, ρ_{top} and ρ_{bottom} are the magnitudes of top and bottom decay curves at the start of the free vibration (i.e., $t = 0$), and u_0 is the displacement which free vibration is occurring about.

Most structural applications are considered low damping ratio such that first period, T_n, can be approximated to be equal to the damped period of vibration, T_d.

By taking the logarithms of equations 8-2 and 8-3, equations 8-4 and 8-5 can be solved with linear regression to obtain the damping ratio, ξ. This is an iterative procedure to find the u_0 where both equations yield the same damping ratio. This method is described in more detail by Dodd and Cooke (1992) and Hachem et al. (2002).

$$\ln(u(t) - u_0) = -\xi \omega_n t + \ln(\rho_{top}) \quad 8\text{-}4$$

$$\ln\big(u_0 - u(t)\big) = -\xi \omega_n t + \ln(\rho_{bottom}) \quad 8\text{-}5$$

Figures 8-9 and 8-10 compare the damping between the two specimens. In general, Specimen PreT-SF-FIB-SHK shows more damping than Specimen CIP-SF-REF-SHK. This was not an expected behavior since the mild reinforcement in Specimen PreT-SF-FIB-SHK was half of what was used in Specimen CIP-SF-REF-SHK. Possible explanations for this behavior are:

- The stiffness of Specimen CIP-SF-REF-SHK was lower than anticipated because the actual column concrete strength was lower than specified (3.3 ksi versus 4.0 ksi). Thus, Specimen CIP-SF-REF-SHK experienced lower ductility demand per displacement than Specimen PreT-SF-FIB-SHK.
- The measured displacement demand on Specimen CIP-SF-REF-SHK was nearly double that of Specimen PreT-SF-FIB-SHK in Earthquake 2. This caused the mild reinforcement in Specimen CIP-SF-REF-SHK to yield earlier in the test sequence.

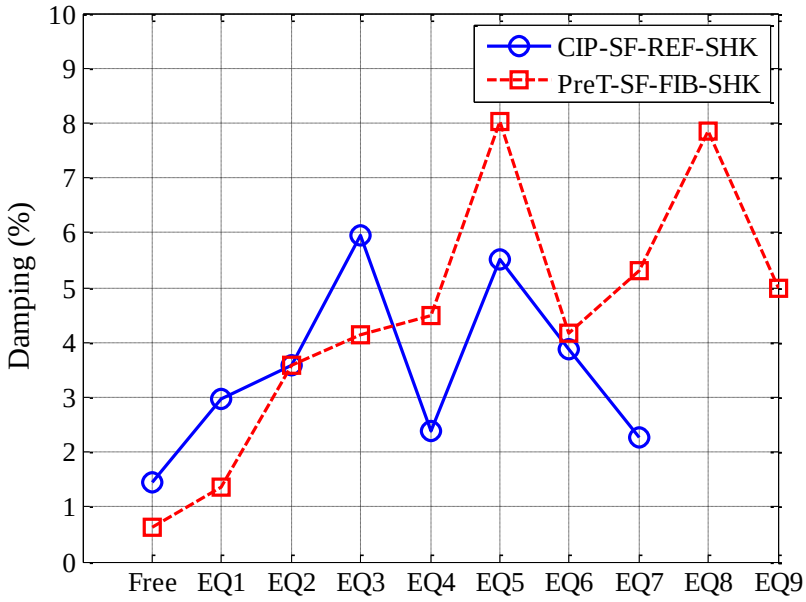

Figure 8-9. North-South variation of damping for specimens

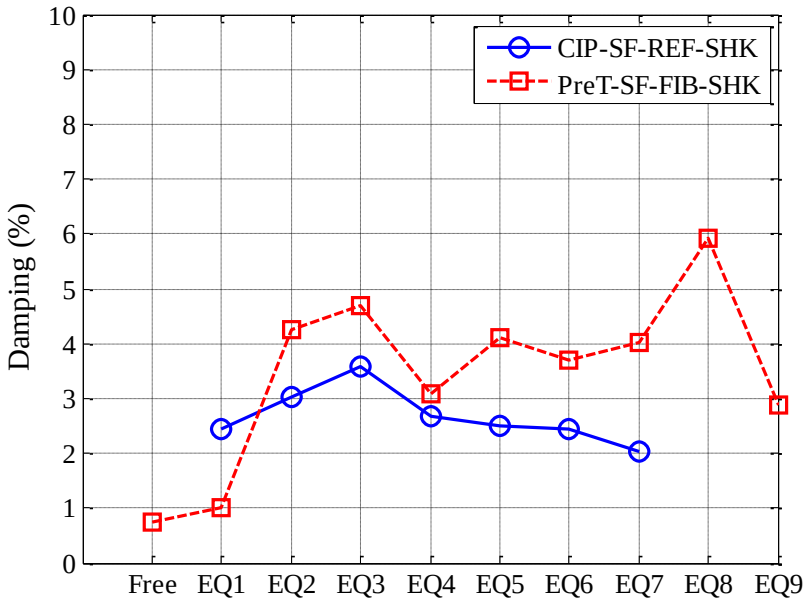

Figure 8-10. East-West variation of damping for specimens

8.4 Column Re-Centering

The ability of both specimens to re-center to their original plumb position after each earthquake test was evaluated by using Normalized Residual Displacement (NRD) and is calculated by dividing the vector sum column residual displacement by the vector sum peak displacement in the particular earthquake test. The normalized residual displacement was then calculated with Equation 8-6:

$$\boldsymbol{NRD} = \frac{\boldsymbol{\Delta_{peak,any\ dir}}}{\boldsymbol{\Delta_{res,any\ dir}}} \qquad 8\text{-}6$$

Figure 8-11 compares the Normalized Residual Displacements of the two specimens throughout the test program. Specimen PreT-SF-FIB-SHK shows superior re-centering capability compared to Specimen CIP-SF-REF-SHK.

In Chapter 4, the quasi-static test subassemblies were compared in terms of their re-centering ratio (see Section 4.5.4). Table 6-1 lists the shake-table specimens' re-centering ratio

and for convenience it is repeated in Table 8-3. The re-centering ratio for specimens CIP-SF-REF-SHK and PreT-SF-FIB-SHK were 0.26 and 1.39, respectively.

Table 8-3. Re-centering ratios for specimens CIP-SF-REF-SHK and PreT-SF-FIB-SHK

Reference	Specimen	λ_{re}
Schoettler et al. 2013	CIP-SF-REF-SHK	0.26
Haraldsson	PreT-SF-FIB-SHK	1.39

Figure 8-12 plots the normalized residual displacement versus re-centering ratio for both specimens. A line is added between data points to assist with interpreting the results. The figure shows that a higher re-centering ratio leads to better re-centering. Specimen PreT-SF-FIB-SHK re-centers better than Specimen CIP-SF-REF-SHK throughout the whole official test program. It is not until after Earthquake 7 (2 x Design Level Earthquake) that Specimen PreT-SF-FIB-SHK shows significant residual displacements. Testing on Specimen CIP-SF-REF-SHK was discontinued after Earthquake 7 since it showed a residual drift ratio of 6.7%.

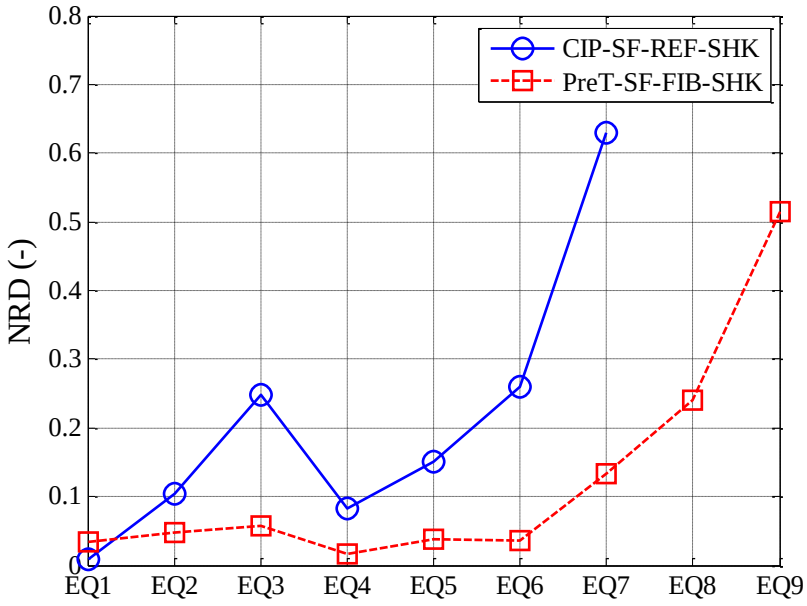

Figure 8-11. Normalized residual displacement versus earthquake no. for specimens CIP-SF-REF-SHK and PreT-SF-FIB-SHK

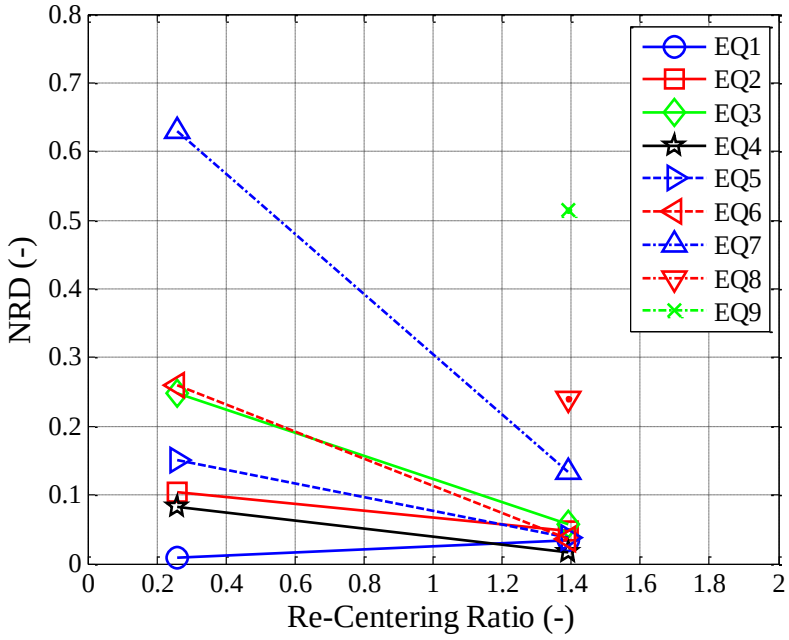

Figure 8-12. Normalized residual displacement versus re-centering ratio. for specimens CIP-SF-REF-SHK PreT-SF-FIB-SHK

8.5 Damage Progression Models

Berry and Eberhard (2003) proposed three semi-empirical damage equations for predicting the onset of spalling, bar buckling, and bar fracture. These equations were described in detail in Section 4.5.5 and are repeated here for convenience:

Spalling: $$\frac{\Delta_{sp}^{calc}}{L}\,(\%) = 1.6\left(1-\frac{P}{A_g f'_c}\right)\left(1+\frac{L}{10D}\right) \quad 8\text{-}7$$

Bar Buckling: $$\frac{\Delta_{bb}^{calc}}{L}\,(\%) = 3.25\left(1+150\rho_{eff}\frac{d_b}{D}\right)\left(1-\frac{P}{A_g f'_c}\right)\left(1+\frac{L}{10D}\right) \quad 8\text{-}8$$

Bar Fracture: $$\frac{\Delta_{bf}^{calc}}{L}\,(\%) = 3.5\left(1+150\rho_{eff}\frac{d_b}{D}\right)\left(1-\frac{P}{A_g f'_c}\right)\left(1+\frac{L}{10D}\right) \quad 8\text{-}9$$

where P is the axial load applied, L is the distance to the point of contraflexure (here 96 in.), D is the column depth (here 16 in.), A_g is the column gross-sectional area, d_b is the diameter of the longitudinal bars, f'_c is the concrete compressive strength, $\omega_s = \rho_s f_{ys}/f'_c$ where ρ_s is the

transverse volumetric ratio, and f_{ys} is the transverse reinforcement yield strength. The equations were developed for non-prestressed columns, but, for want of a better alternative, they are used here for the partially unbonded, pretensioned column.

Results from the three equations, using measured material properties, are compared to observed values in Table 8-4.

Table 8-4. Comparison of damage model predictions and observed occurrences

Specimen	Drift ratio at onset of spalling (%)			Drift ratio at onset of bar buckling (%)			Drift ratio at onset of bar fracture (%)		
	Pred.	Obs.	Obs./Pred.	Pred.	Obs.	Obs./Pred.	Pred.	Obs.	Obs./Pred.
CIP-SF-REF-SHK	2.36	3.65	1.55	9.52	10.68	1.12	10.25	0.00	0.00
PreT-SF-FIB-SHK	2.31	4.15	1.80	6.40	7.48	1.17	6.89	7.48	1.08
Mean	2.34	3.90	1.68	7.96	9.08	1.15	8.57	3.74	N/A

The observed values reported in Table 8-4 are the peak drift responses measured in any direction, (i.e., the vector sum) from the relevant earthquake for which the observation was made (see Section 7.1). The drift ratio at onset of spalling was observed in the same earthquake for both specimens (Earthquake 4, 4.2% target drift, μ_Δ = 4.2). In Specimen CIP-SF-REF-SHK the onset of bar buckling became visible for the first time after the last earthquake (Earthquake 7, 8.3% target drift, μ_Δ = 8.0) at which time spalling had penetrated through the cover. No longitudinal bars fractured in Specimen CIP-SF-REF-SHK. In Specimen PreT-SF-FIB-SHK both bar buckling and bar fracture were observed after the same earthquake (Earthquake 8: 10.4% target drift, μ_Δ = 10.0). Prior to being subjected to Earthquake 8, the column was subjected to Earthquake 7 (8.3% target drift, μ_Δ = 8.0) which displaced the column to 9.52% drift. Despite the fact that the equations were developed for non-prestressed columns with conventional materials, the peak drift associated with bar buckling and fracture were accurate within 20%. They may have been more accurate than this, because the exact times during the earthquake that the events occurred, and therefore value of the true peak drifts, are not known. The peak drifts during the relevant ground motions were used instead. It should be noted that inspection of the plastic hinge zone was difficult because the spalling was held in by steel and plastic fibers. During the test of

Specimen PreT-SF-FIB-SHK, it was noticed that the cracking of the HyFRC shell was very fine and distributed in the top 16 in. up the column from the footing surface. Not until after Earthquake 6 (6.3% target drift, μ_Δ = 6.0) was a dominant crack noticed. It formed 4 in. above the interface. That same crack kept opening in subsequent tests. It is unknown whether the bars had buckled earlier than was noticed.

The damage progression models under-predict the drift at the onset of spalling for both specimen by 68% on average. The models predict bar buckling and bar fracture reasonably well in Specimen PreT-SF-FIB-SHK using the HyFRC shell. The difference is 17% for the bar buckling and as low as 8% for the onset of fracture. The bar buckling model predicted bar buckling for Specimen CIP-SF-REF-SHK reasonably well with a difference of 12%. As mentioned previously, no column longitudinal bar fracture was observed in Specimen CIP-SF-REF-SHK.

The damage progression models were developed and calibrated for spirally reinforced circular columns without post- or pre-tensioning. As pointed out in Chapter 4, these same models over-estimated the drift by 30-40% in prior research conducted by Davis et al. 2012 on statically unbonded, pre-tensioned columns that did not include HyFRC shells (specimens PreT-CB-CONC and PreT-SF-CONC), but provided moderate predictions for the post-tensioned specimens (specimens PosT-CB-LOPT and PosT-CB-HIPT) and the unbonded, pre-tensioned column with HyFRC (Specimen PreT-SF-FIB).

8.6 Summary of Single-Column Shake-Table Tests

In 2011, Pacific Earthquake Engineering Research Center (PEER) initiated a research program to investigate some new resilient columns designed to re-center after being displaced from vertical . The research represented a collaboration between the University of California at Berkeley, the University of California San Diego, and the University of Washington). The research program included four single-column specimens, where one served as a reference specimen that was designed according to current standards and practice. The other three columns were three new designs using prestressed columns. In chapters 6 to 8, the research program, test results, and

evaluation of test results were presented. The discussion focused on the unbonded pre-tensioned specimen with HyFRC in the plastic hinge region (Specimen PreT-SF-FIB-SHK) that was designed and fabricated at the University of Washington and the reference column (Specimen CIP-SF-REF-SHK) that was detailed by Schoettler et al. 2013. Information about the other two resilient columns can be found in research report by Guerrini and Restrepo 2013 and Trono et al. 2013.

To complement Specimen PreT-SF-FIB-SHK, Finnsson et al. 2013 conducted quasi-static tests on a similar unbonded pre-tensioned cantilever column with HyFRC in the plastic hinge region, (Specimen PreT-SF-FIB in Chapter 4). It is clear both from both the quasi-static test (Specimen PreT-SF-FIB) and shake table test (Specimen PreT-SF-FIB-SHK) that adding HyFRC in the plastic hinge region delays spalling. Both the shake-table and quasi-static test specimen eventually formed a dominant crack plane at which the columns rocked, causing localized inelastic deformation in the mild reinforcement.

Finnsson et al. (2013) showed two features of the HyFRC column shell system:

- Including HyFRC shell in the plastic hinge region does not delay bar fracture.
- Including the HyFRC shell makes the column response more ductile than that of the pre-tensioned specimens with conventional concrete in the plastic hinge region. The specimen maintained strength above 80% of its peak strength during the whole test program.

Shake table testing of Specimen PreT-SF-FIB-SHK showed superior re-centering capability compared to Specimen CIP-SF-REF-SHK. The performance of the shell was robust throughout the test program but revealed the same weakness as observed the quasi-static test. As soon as a crack forms in the shell, the column tends to rock at it, and the cracking does not distribute, thereby causing a strain concentration in the column mild reinforcement. This weakness can potentially be counteracted with debonding of the mild reinforcement.

9 NUMERICAL MODELING STRATEGIES FOR RC SHAKE-TABLE TESTS

9.1 Introduction

The numerical strategies calibrated in Chapter 5 were applied to predict the responses measured during single-column shake table tests. The accuracy of the dynamic simulations was evaluated in terms of goodness-of-fit, as well as maximum and residual displacements.

A total of five specimens were simulated in OpenSees. Hachem et al. (2003) tested four identical reinforced concrete (RC) columns that were subjected to either unidirectional and bidirectional excitations using near-fault or far-field earthquakes. Schoettler et al. (2013) tested one RC column tri-axially using near-fault earthquakes as part of the shake table experimental program described in chapters 6 through 8.

In this chapter, a brief description of the test specimens, test setup and procedure will be given, the modeling strategy will be reviewed, and the simulation results will presented. For detailed information about the tests performed in 2003, the reader is referred to the report by Hachem et al. (2003).

9.2 Shake Table Column Data

9.2.1 Description of Test Specimens

All specimens met the same screening criteria for columns that represent modern day reinforced concrete construction, as outlined in Chapter 5. The criteria are repeated here for convenience:

- $P/A_g f'_c \leq 0.30$
- $\omega_s \geq 0.05$
- $\rho_l \leq 0.04$
- $s/d_b \leq 6.0$
- $cover/D \leq 0.10$

where P is the axial load, $A_g$is the gross cross-sectional area, f'_c is the specified concrete compressive strength, $\rho_s$is the transverse reinforcement ratio, ω_s is the reinforcement index, ρ_l is the longitudinal reinforcement ratio, s is the spacing of the spiral reinforcement, d_b is the diameter of the longitudinal reinforcement, $cover$ is the distance from column face to the transverse reinforcement, and D is the diameter of the column.

Table 9-1 lists key properties for the five cantilever specimens. All five specimens were circular 16-in. diameter (D) columns with height (L) from the foundation surface to center-of-mass (COM) of 96 in., resulting in a span-to-depth ratio (L/D) of 6.0. The axial load ratio ($P_{axial}/A_g f'_c$) was almost identical in specimens A1, A2, B1, and B2 but this ratio was significantly higher in Specimen CIP-REF-SHK, which was a result of a lower measured column concrete strength. The longitudinal mild reinforcement ratio (ρ_l) in specimens A1, A2, B1, B2 was kept at 1.20% with a reinforcement index, ω_s, of 8.48%. The longitudinal mild reinforcement ratio in Specimen CIP-REF-SHK was 1.59% with the reinforcement index of 21.1%.

Table 9-1. Shake table column dataset key properties

Reference	Specimen	L (in.)	L/D	$P/A_g f'_c$ (%)	ρ_l (%)	ω_s (%)	s/d_b
Schoettler et al. 2013	CIP-SF-REF-SHK	96	6.0	7.89	1.59	21.07	2.5
Hachem et al. 2003	A1	96	6.0	5.67	1.20	8.42	2.5
Hachem et al. 2003	A2	96	6.0	5.67	1.20	8.42	2.5
Hachem et al. 2003	B1	96	6.0	5.71	1.20	8.48	2.5
Hachem et al. 2003	B2	96	6.0	5.71	1.20	8.48	2.5

Figure 9-1 shows the elevation and key dimensions of specimens A1, A2, B1, and B2 tested by Hachem et al. 2003. Each specimen was a column-to-footing connection constructed with a top slab that supported three weight blocks. Figure 9-2 shows that the elevation and key dimensions of Specimen CIP-REF-SHK tested by Schoettler et al. (2013) differed from Hachem's specimens. First, instead of having a top slab to support the weight blocks, the specimen was constructed with a load stub for steel beams to be post-tensioned into. By having the load stub instead of the top slab, the clear height (L_{clear}) was 53 in. instead of 64 in.

Secondly, the cast-in-place spread footing was 60-in. x 60-in. x 20-in. instead of 96-in. x 96-in. x 16-in. In all specimens, the height (L) from the foundation surface to the center-of-mass (COM) was 96 in.

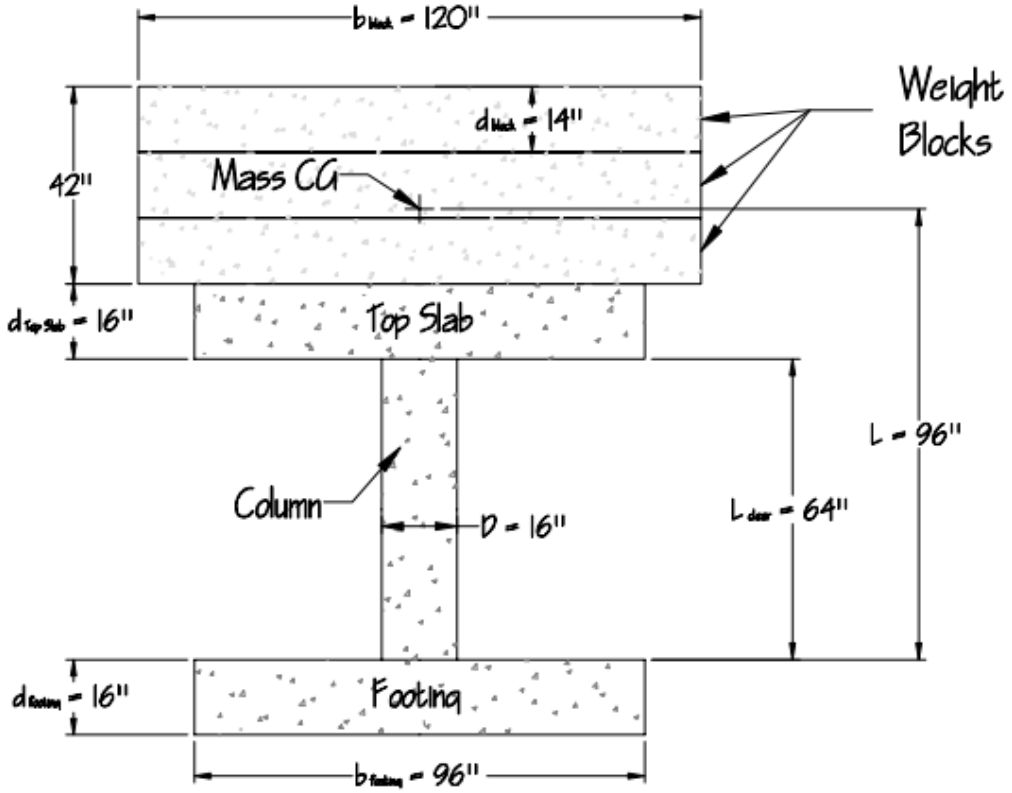

Figure 9-1. Elevation of specimens A1, A2, B1, and B2 (Hachem et al. 2013)

Table 9-2 lists the measured material properties for five column-to-footing cantilever RC specimens tested on the shake table at the Richmond Field Station Earthquake Simulation Laboratory of the University of California at Berkeley.

Table 9-2. Shake table bridge column dataset measured properties

Reference	Specimen Designation	$f'_{c,column}$ (psi)	$f_{y,l}$ (ksi)	$f_{y,s}$ (ksi)
Schoettler et al. 2013	CIP-SF-REF-SHK	3,278	63.0	79.0
Hachem et al. 2003	A1	5,707	73.0	89.0
Hachem et al. 2003	A2	5,707	73.0	89.0
Hachem et al. 2003	B1	5,664	73.0	89.0
Hachem et al. 2003	B2	5,664	73.0	89.0

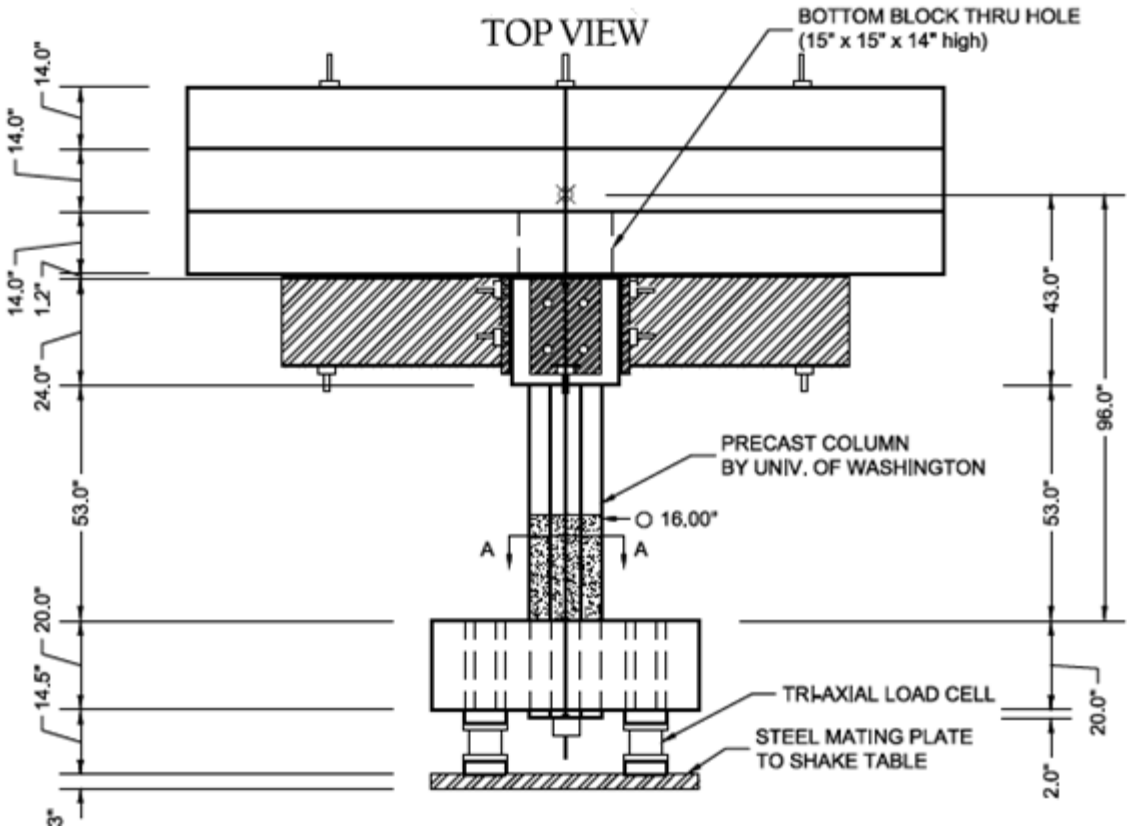

Figure 9-2. Elevation of Specimens CIP-SF-REF-SHK

All specimens had the same design strength of 4.0 ksi. As shown in Table 9-2, the test day concrete strength ($f'_{c,column}$) for specimens tested by Hachem et al. (2003) was nearly identical,

or about 5.7 ksi. The concrete strength in Specimen CIP-REF-SHK was significantly lower, at 3.3 ksi.

All longitudinal reinforcement in the test specimens conformed to ASTM A706 with a minimum specified yield strength of 60 ksi. In all specimens, the measured yield stress ($f_{y,l}$) exceeded the specified minimum. Coupons of the specimens tested by Hachem (A1, A2, B1, B2) had on average a yield stress of 73 ksi, whereas the coupons of Specimen CIP-REF-SHK measured 63 ksi. All specimens included a continuous smooth spiral. The yield stress ($f_{y,s}$) measured in Hachem's columns and in Specimen CIP-REF-SHK were 89 ksi and 79 ksi, respectively. The former was measured using the 0.5% offset method and the latter using the 0.2% offset method.

9.2.2 Test Setup and Procedure

Table 9-3 lists the earthquakes the specimens were subjected to. Specimens CIP-REF-SHK, A1, and A2 were all subjected to near-fault ground motions. Specimen CIP-REF-SHK was subjected to a total of seven tri-axial ground motions, in order of ascending severity. The earthquake ground motions were arranged such that the intensity level increased in five levels, as described in Chapter 6. Level 1 consisted of one earthquake that was intended to displace the column below first yield. Levels 3 and 4 each consisted of two ground motions and were designated as the Design and the Maximum Credible Earthquake (MCE) levels, respectively. For both the Design and Maximum Credible levels, the first earthquake in that specimen was the 1994 Northridge earthquake recorded at the Rinaldi receiving station. The test procedure for Specimen CIP-REF-SHK is discussed in more detail in Chapter 6.

Specimens A1 and A2 were subjected to variations of the Olive View record of the 1994 Northridge earthquake. Specimen A1 was only excited unidirectional, whereas Specimen A2 was excited in two horizontal directions. Both specimens were first subjected to one run below or at first yield. After the run, they were subsequently subjected to a Design Level earthquake and then the Maximum Credible Earthquake. The test program continued in both column tests after

the maximum level earthquake with scaled-up runs of the Design Level earthquake and the Maximum Credible Earthquake.

Specimens B1 and B2 were subjected to long-duration earthquake of the 1985 Chile earthquake recorded at the Llolleo station. Similarly to A1 and A2, Specimen B1 was excited unidirectional and B2 was excited in two directions. Both specimens were subjected to four earthquakes below or at yield before being subjected to the Design Level earthquake and the Maximum Credible Earthquake. Similarly to specimens A1 and A2, the test program continued after the Maximum Credible Earthquake.

Table 9-3. Ground motion peak acceleration for all specimens

Reference	Specimen	Run	History	Station	Scale factor	Peak ground acceleration (g)			Comment
						Long.	Lat.	Vert.	
Schoettler et al. 2013	CIP-SF-REF-SHK	1	Coalinga, 1983	46T07 Harris Ranch	2.50	0.37	0.11	0.09	Sub-yield
Schoettler et al. 2013	CIP-SF-REF-SHK	2	Imperial Valley, 1979	EC Meloland Overpass FF	0.80	0.38	0.08	0.09	½ Design
Schoettler et al. 2013	CIP-SF-REF-SHK	3	Morgan Hill, 1984	Coyote Lake Dam (SW Abutment)	0.70	0.88	0.25	0.36	½ Design
Schoettler et al. 2013	CIP-SF-REF-SHK	4	Northridge, 1994	Rinaldi Receiving Station	0.56	0.64	0.34	0.26	Design
Schoettler et al. 2013	CIP-SF-REF-SHK	5	Northridge, 1994	Sylmar, Olive View Med FF	-0.80	0.90	0.59	0.13	Design
Schoettler et al. 2013	CIP-SF-REF-SHK	6	Northridge, 1994	Rinaldi Receiving Station	0.90	1.31	0.53	0.62	MCE
Hachem et al. 2003	A1	1	Northridge, 1994	Olive View	0.30	0.16	-	-	Sub-yield
Hachem et al. 2003	A1	2	Northridge, 1994	Olive View	1.10	0.58	-	-	Design
Hachem et al. 2003	A1	3	Northridge, 1994	Olive View	1.65	0.90	-	-	MCE
Hachem et al. 2003	A2	1	Northridge, 1994	Olive View	0.30	0.16	0.19	-	Sub-yield
Hachem et al. 2003	A2	2	Northridge, 1994	Olive View	1.10	0.58	0.65	-	Design
Hachem et al. 2003	A2	3	Northridge, 1994	Olive View	1.65	0.91	0.95	-	MCE
Hachem et al. 2003	B1	1	Chile, 1985	Llolleo	0.13	0.03	-	-	Sub-yield
Hachem et al. 2003	B1	2	Chile, 1985	Llolleo	0.26	0.08	-	-	Sub-yield
Hachem et al. 2003	B1	3	Chile, 1985	Llolleo	0.39	0.14	-	-	Sub-yield
Hachem et al. 2003	B1	4	Chile, 1985	Llolleo	0.52	0.19	-	-	Sub-yield
Hachem et al. 2003	B1	5	Chile, 1985	Llolleo	1.30	0.48	-	-	Design
Hachem et al. 2003	B1	6	Chile, 1985	Llolleo	2.60	0.87	-	-	MCE
Hachem et al. 2003	B2	1	Chile, 1985	Llolleo	0.13	0.02	0.05	-	Sub-yield
Hachem et al. 2003	B2	2	Chile, 1985	Llolleo	0.26	0.07	0.15	-	Sub-yield
Hachem et al. 2003	B2	3	Chile, 1985	Llolleo	0.39	0.12	0.19	-	Sub-yield
Hachem et al. 2003	B2	4	Chile, 1985	Llolleo	0.52	0.17	0.21	-	Sub-yield
Hachem et al. 2003	B2	5	Chile, 1985	Llolleo	1.30	0.47	0.36	-	Design
Hachem et al. 2003	B2	6	Chile, 1985	Llolleo	2.60	0.90	0.67	-	MCE

9.3 Modeling Strategy

The analytical platform Open System for Earthquake Engineering Simulation (OpenSees v. 2.4.1 2013) was used for the dynamic simulation of the RC columns. A three-dimensional model was created for each specimen using the lumped-plasticity modeling methodology. The methodology is reviewed in Chapter 5 and described in detail by Berry and Eberhard (2007). Figure 9-3 shows the computer model schematically.

The mass block was represented with a lumped mass that included both the translational mass and rotational moment of inertia. The total mass of the mass blocks for Specimen CIP-REF-SHK was 0.135 kip·s^2/in., and the rotational moment of inertia was calculated to be 180.5 kip-in.-s^2 about the N-S and E-W axes. The corresponding values for specimens A1, A2, B1, and B2 were 0.169 kip·s^2/in. and 234 kip-in.-s^2, respectively. A rigid beam element was used to connect the lumped mass to the column. The column itself was modeled with a single lumped-plasticity fiber element (Scott and Fenvis 2006). The element consists of a plastic hinge in which the inelastic deformations are concentrated, and a second region that is elastic. The element's plastic hinge length (L_p) was calculated using Equation 9-1 (Berry and Eberhard 2007):

$$L_p = 0.05L + 0.1\frac{f_y d_b}{\sqrt{f_c'}} \leq \frac{L}{4} \qquad 9\text{-}1$$

where f_y, d_b, and f_c' are the measured yield stress, bar diameter of the tension reinforcement, and the measured concrete strength, respectively.

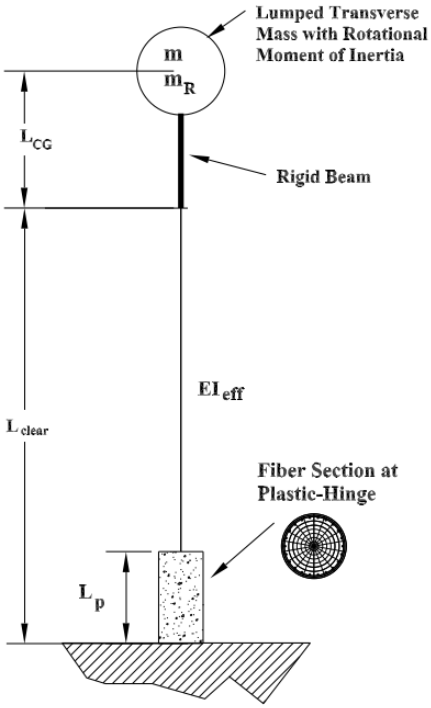

Figure 9-3. Modeling strategy for shake table tests (Berry and Eberhard 2007)

The effective stiffness (i.e., $(EI)_{eff}$ in Figure 9-3) of the elastic portion of the lumped-plasticity element was estimated three ways.

- Berry and Eberhard (2007) developed a methodology to estimate the effective stiffness. First, the secant stiffness (EI_{sec}) is calculated from a moment-curvature analysis up to the yield moment. The stiffness modification ratio, α_{sec}, is then calculated with Equation 9-2 (Berry and Eberhard 2007, Berry et al. 2008). This ratio adjusts the secant stiffness to take into account shear deformation, anchorage slip, and axial load (cracking).

$$\alpha_{sec} = 0.35 + 0.1\frac{L}{D} \leq 1.0 \qquad 9\text{-}2$$

  Since the element consists both of a plastic hinge and an elastic portion, the element has two stiffnesses. The pre-yield stiffness in the plastic hinge is determined from the fiber element assigned to it, and the stiffness of the elastic portion is user defined. To obtain the appropriate analytical stiffness for the full column, the elastic stiffness was modified (Berry and Eberhard 2007) using Equation 9-3:

$$\widehat{\alpha_{sec}} = \frac{\alpha_{sec}(L-L_p)}{L-3\alpha_{sec}L_p} \quad 9\text{-}3$$

where L is the height of the column, L_p is the height of the plastic hinge, and α_{sec} is the stiffness modification ratio.

The EI_{eff} was calculated as follows:

$$EI_{eff} = \widehat{\alpha_{sec}} EI_{sec} \quad 9\text{-}4$$

- Elwood and Eberhard (2006) proposed a model that predicts the effective secant stiffness of a full column. The model takes into account for deformations due to flexure and bar-slip. The EI_{eff} was calculated using Equation 9-5:

$$EI_{sec} = EI_g \left(\frac{0.45+2.5\left(\frac{P}{A_g f'_c}\right)}{1+110\left(\frac{d_b}{D}\right)\left(\frac{D}{a}\right)} \right) \quad 9\text{-}5$$

where, EI_g is gross modulus of rigidity, P is the axial load, A_g is the gross-sectional area of the column, f'_c is the unconfined concrete strength, d_b is the longitudinal bar diameter, D is the column diameter, and a is the cantilever length. This modeling strategy usually results in stiffnesses lower than those calculated with the Berry and Eberhard procedure, so it was applied with a value for $\widehat{\alpha_{sec}}$ equal to 1.0.

Even though the prediction from the Elwood and Eberhard (2006) model is for a full column, the results were used as an input on the elastic portion of the element. For comparison to the estimated stiffnesses from Berry and Eberhard (2007) and Elwood and Eberhard (2006), the effective stiffness for the full column was calculated after the last run intended to displace the column below or at yield. It was obtained using estimated periods and the two-degree-freedom (2DOF) model with a rigid end zone (discussed in Chapter 8).

Table 9-4 lists the effective stiffnesses using estimates described above for all the columns. In this table, the elastic modulus (E) was calculated with Equation 9-6. This is the expression that ACI uses to approximate the elastic modulus of concrete.

$$E = 57{,}000\sqrt{f'_c} \quad 9\text{-}6$$

Table 9-4. Effective stiffness, EI_{eff}, estimation

Specimen	Effective Stiffness		
	Berry and Eberhard (2007)	Elwood and Eberhard (2006)	As measured
	EI_{eff}(kip-in^2)	EI_{eff}(kip-in^2)	EI_{eff}(kip-in^2)
CIP-SF-REF-SHK	2,522 x 10^3	2,107 x 10^3	4,191 x 10^3
A1	2,920 x 10^3	2,771 x 10^3	3,927 x 10^3
A2	2,920 x 10^3	2,771 x 10^3	3,169 x 10^3
B1	2,909 x 10^3	2,760 x 10^3	4,529 x 10^3
B2	2,909 x 10^3	2,760 x 10^3	3,225 x 10^3

The fiber section assigned to the plastic hinge was discretized according to recommendations given by Berry and Eberhard (2007). The confined and the unconfined concrete fibers were modeled using the Concrete08 constitutive material model that was developed as part of this research. The longitudinal reinforcement was modeled in two ways. First, the columns were simulated by using the Steel02 constitutive model (Menegotto-Pinto) and then ReinforcingSteel. For a given effective stiffness assigned to the model, simulations were run four times using optimal values from Chapter 5 and using values proposed by Berry and Eberhard. Tables 9-5 and 9-6 list the values used as an input in the simulation.

Table 9-5. Constitutive model parameters input for Concrete08 and Steel02

Input	Concrete08		Steel02			
	α	C_{max}	R	cR_1	cR_2	b
Haraldsson (OH-Steel02)	~0.00	0.150	12.0	0.90	0.15	0.01
Berry and Eberhard (BE-Steel02)	0.00	0.000	18.5	0.925	0.15	0.01

Table 9-6. Constitutive model parameters input for Concrete 08 and ReinforcingSteel

Input	Concrete08		ReinforcingSteel	
	α	C_{max}	C_f	C_d
Haraldsson (OH-RS)	~0.00	0.100	0.28	0.41
Berry and Eberhard (BE-RS)	~0.00	0.100	0.26	0.45

In tables 9-5 and 9-6, the optimized values chosen from Chapter 5 were from the optimization up to 80% of the peak effective force (i.e., 80%-run). They were chosen because the measured peak drifts at the design level earthquake were within the range of still maintaining strength above 80% of the peak effective force.

Viscous damping was applied to the models. Rayleigh damping coefficients (α and β) were determined so that the damping for the first two periods were 1%, 2%, 2.5%, 3%, 3.5%, 4%, 5%, and 6%. Observed damping in the free-vibration tests ranged from 3.5% to 4%. The variation in the model effective stiffness (2), constitutive model assumptions (4), and damping ratios (8) resulted in a total of 64 simulations per column.

All columns were analyzed until the Maximum Credible Earthquake (MCE) was reached and model parameters were stored between runs. This meant that, in each run, the column properties took into account the damage accumulated in the previous runs. In the simulations, an additional 15 seconds of free vibration was added to each history to allow the column model to come to rest before being subjected to the next earthquake. In the analysis, the equation of motion was integrated using the Newmark method with constant average acceleration.

9.4 Measures of Dynamic Accuracy

The results of the dynamic analysis were evaluated in terms of goodness-of-fit of horizontal displacement histories in two principal directions, peak displacement, and residual displacement. The accuracy using each measure was evaluated using the average root mean square (RMS) error of all five columns.

RMS Peak Displacement Error (E_{peak}). The RMS peak displacement error was defined as:

$$E_{peak} = \frac{1}{L}\sqrt{\frac{\sum_{i=1}^{n}\left(\Delta_{meas}^{peak} - \Delta_{calc}^{peak}\right)^2}{n}} \quad 9\text{-}7$$

where Δ_{meas}^{peak} and Δ_{calc}^{peak} are the measured and calculated maximum displacements in any direction in the simulation run; n is the number of columns; and L is the height from the foundation to the center-of-mass (COM).

RMS Residual Displacement Error ($E_{residual}$). The residual RMS displacement error was defined as:

$$E_{residual} = \frac{1}{L}\sqrt{\frac{\sum_{i=1}^{n}\left(\Delta_{meas}^{res} - \Delta_{calc}^{res}\right)^2}{n}} \quad 9\text{-}8$$

where Δ_{meas}^{res} and Δ_{calc}^{res} are the measured and calculated residual displacements in any direction in the simulation run.

RMS Goodness-of-Fit RMS Error (E_{gof}). The goodness-of-fit error evaluated the full displacement histories. It was calculated in two steps. First, the error between the measured and calculated displacements in both horizontal principal directions at each time step was calculated for each specimen using Equation 9-9.

$$E_{x\ or\ y,gof} = \frac{1}{L}\sqrt{\frac{\sum_{i=1}^{n}\left(\Delta_{meas}^{i} - \Delta_{calc}^{i}\right)^2}{N_{step}}} \quad 9\text{-}9$$

where Δ_{meas}^{i} and Δ_{calc}^{i} are the displacements at a particular time for either of the horizontal principal directions; N_{step} is the number of data points in the history of interests per column

The goodness of fit is a more stringent measure than the peak or residual displacements, because it requires that the simulation track the true behavior accurately at all times, rather than just at the peak or end. For example, the peak measured and simulated displacements might happen at different time steps, but they are nonetheless compared in the RMS error calculation,

whereas a slight time-phase shift between measured and calculated values would cause a significant increase in the goodness-of-fit error. To minimize a large error term due to out of phase response post-peak displacement, the goodness-of-fit error was calculated from the point at which the displacement specimen reached one-third of the measured peak amplitude of the column in any direction, in the time history, to when the column last reached the one-third of the peak amplitude. The total goodness-of-fit was calculated as the mean of five columns over the vector sum of the errors in both principal directions:

$$E_{gof}^{total} = \frac{1}{n}\sum_{i=1}^{n}\left(\sqrt{E_{x,gof}^{2} + E_{y,gof}^{2}}\right) \quad 9\text{-}10$$

In Equation 9-10, n is the number of columns. The goodness-of-fit for the vertical history was not evaluated as only one column was excited in that direction (i.e., Specimen CIP-SF-REF-SHK).

9.5 Simulation Results

The following three subsections discuss the simulation results for the yield, design, and maximum levels, respectively. Results are given as the average root-mean-square (RMS) for five columns using accuracy measures discussed in Section 9-4. The discussions of the simulations are organized in terms of constitutive modeling inputs, peak and residual displacement predictions, and goodness-of-fit using effective stiffnesses calculated with the procedures proposed by Berry and Eberhard (2007) and Elwood and Eberhard (2006). The following legends are used throughout the next three subsections in figures 9-4, 9-6, and 9-8 using input parameters listed in tables 9-5 and 9-6:

- Steel02-BE := Recommended Steel02 parameters from Berry and Eberhard (2007)
- Steel02-OH := Optimized Steel02 parameters with early concrete reloading as developed in this thesis.
- ReinforcingSteel-BE := Optimized ReinforcingSteel from Berry and Eberhard (2007) parameters with no early concrete reloading.

- ReinforcingSteel-OH := Optimized ReinforcingSteel parameters with early concrete reloading as developed in this thesis.

The full set of calculated peak and residual displacements are summarized in Appendix E.

9.5.1 Yield Level

Figure 9-4 shows, for the Yield Level runs, the RMS errors for the three different criteria, Goodness-of-fit, Peak Displacement and Residual Displacement, as functions of the level of assumed viscous damping. Two different versions of the results are shown, using the EI_{eff}values developed by Berry and Eberhard (left three graphs), and Elwood and Eberhard (right three graphs), respectively. In each graph, four curves represent the results for the four sets of constitutive model assumptions listed above.

At the yield level, the results of the four simulations were insensitive to the cyclic parameters set for the constitutive models. At this level, the response was mainly sensitive to the level of damping and the assumed stiffness. The following observations were made for each fit measure:

- **Goodness-of-Fit (GOF):** Both graphs show that simulation error lowered to about 0.3% with increased viscous damping assumed for the model. The value of 0.3% was reached approximately at a damping ratio of 2.5% for the Berry and Eberhard assumptions, and 4% for the Elwood and Eberhard set of assumptions. This trend was a consequence of the effective stiffnesses assigned to the models. Both stiffnesses estimated by using Berry and Eberhard (2007), and Elwood and Eberhard (2006) were lower than the measured initial stiffness of each column (Table 9-4). Thus, the first-mode frequency all columns was lower than the measured value, which led to a phase shift and a significant GOF error. By increasing viscous damping, the cycles' peaks were lowered which reduced the errors. An example of this phenomenon is shown in Figure 9-5 for Specimen CIP-SF-REF-SHK using the Steel02-OH recommendations and early concrete reloading.

- **Peak Displacements:** The accuracy of the peak displacement decreased with increasing viscous damping. At 1.0% viscous damping, the model on average overestimated the peak drift while underestimating the drift using damping values larger than 3.0%.
- **Residual Displacements:** None of the models reproduced well the small residual displacements measured in the tests. At 1.0% viscous damping, the residual displacements were overestimated but at larger dampings the residuals were underestimated. This was expected since the models were excited in the elastic range of the constitutive models.

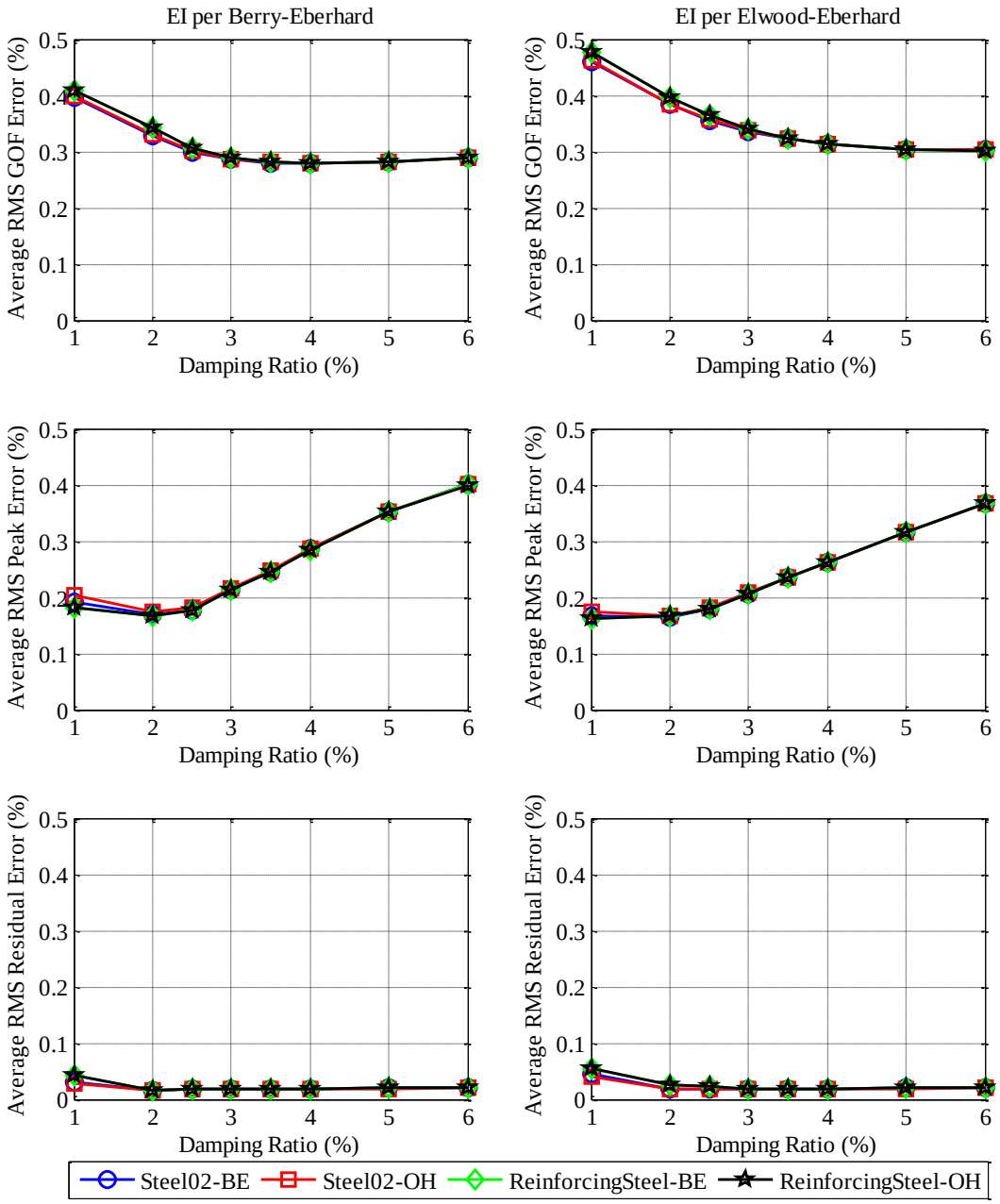

Figure 9-4. Yield level RMS errors for goodness-of-fit, peak and residual displacements for five RC columns

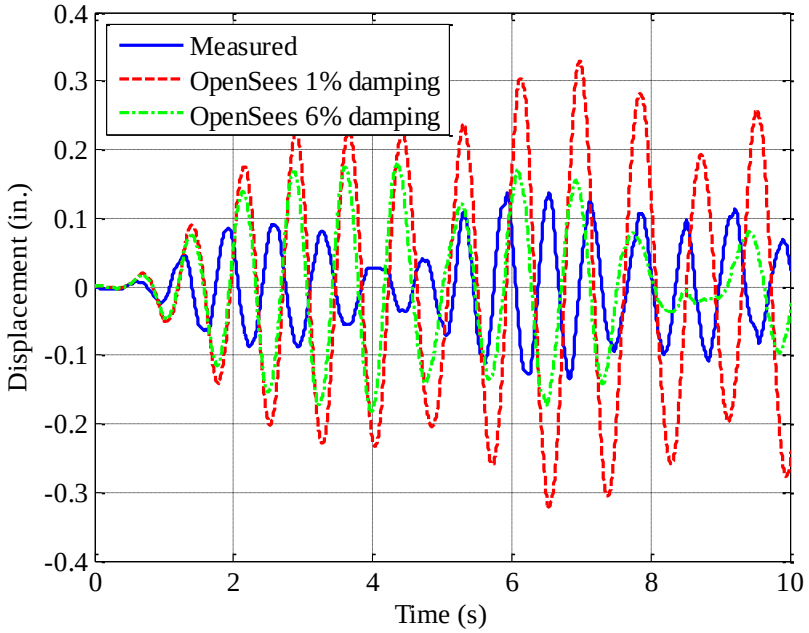

Figure 9-5. North-South displacement vs time for Specimen CIP-SF-REF-SHK for the first 10 seconds (Note: Measured peak displacement occurs later in the time-history)

9.5.2 Design Level

Figure 9-6 shows the results from the Design Level runs. Overall, the responses were relatively insensitive to the stiffness assumptions, and the differences among the fit measures were attributable mainly to the assumed constitutive strategy and the level of viscous damping. The following observations were made:

- **Goodness-of-Fit (GOF):** The error was identical for both ReinforcingSteel inputs using either the effective stiffness estimated using Berry and Eberhard (2007) and Elwood and Eberhard (2006). There is a difference between the two Steel02 simulations and was due to the difference in the unloading/reloading path constitutive model. Steel02 using recommendations by Berry and Eberhard (2007) unloaded with a larger stiffness ($R_{inf} \approx 1.4$) than Steel02 using optimized inputs from Chapter 5 ($R_{inf} = 1.2$) throughout the simulations. Using Steel02 with optimized inputs from Chapter 5 caused

both the simulation history to diverge from the measured response more and higher peak displacements were typically obtained. In general, the model was able to trace the cycle in which peak displacement was reached but failed to match the peaks in subsequent cycles. This was especially true in the columns that were subjected to near-fault earthquakes. Those columns experienced the peak cycle early in the ground motion history, while the columns subjected to far-field earthquakes experienced peak later in the history. An example of this is shown in Figure 9-7. All specimens accumulated large errors due to out-of-phase response. This was particularly noticeable in the two columns subjected to far-field earthquakes as they were long-duration ground motions.

- **Peak Displacements:** In contrast to the Yield Level excitation, the accuracy of the model predicting the peak displacement improved with increased viscous damping up until a damping ratio of about 4%. In general, specimens A1 and A2 contributed the largest errors using low viscous damping as the models overestimated the peaks. These two specimens experienced peak drift ratios of about 5.0%, while the other three experienced peak drift ratios of 3.5%. The models overestimated the peak displacements for the three columns subjected to near-fault earthquakes (specimen CIP-SF-REF-SHK, A1, and A2) while underestimating the peaks for the two columns subjected to far-field earthquakes (specimens B1 and B2). This behavior was attributed to the assigned effective stiffness (EI_{eff}) in the columns. It was lower than the measured value in each column, so the initial frequency content was lower. The columns that were subjected to near-fault earthquakes were subjected to a high-velocity pulse that which occurred at the beginning of the history. In contrast, in the Design Level far-field earthquake history, the peak occurred later, by which time the effective stiffness of the test column was closer to the predicted stiffness by Berry and Eberhard (2007), and Elwood and Eberhard (2006).
- **Residual Displacements:** Residual displacements were on average consistently underestimated in the simulation using Steel02. Similarly, ReinforcingSteel underestimated them using low viscous damping (i.e., below 3.5%) for specimens CIP-SF-REF-SHK, B1, and B2. The residual displacements predicted for Specimens A2 and

were consistently overestimated while Specimen A1 residual displacement got more accurate with more viscous damping imposed on the model.

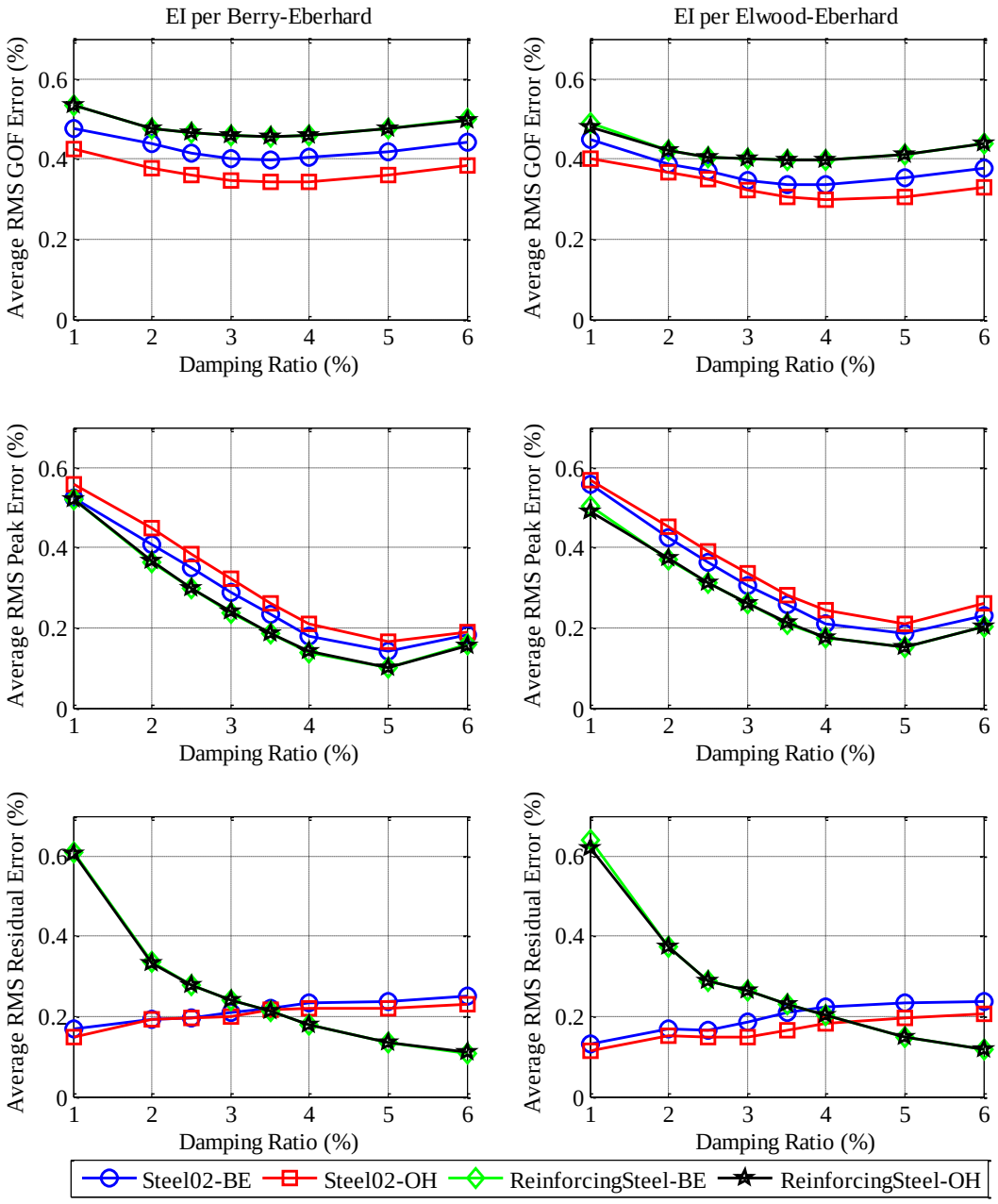

Figure 9-6. Design level RMS errors for goodness-of-fit, peak and residual displacements for five RC columns

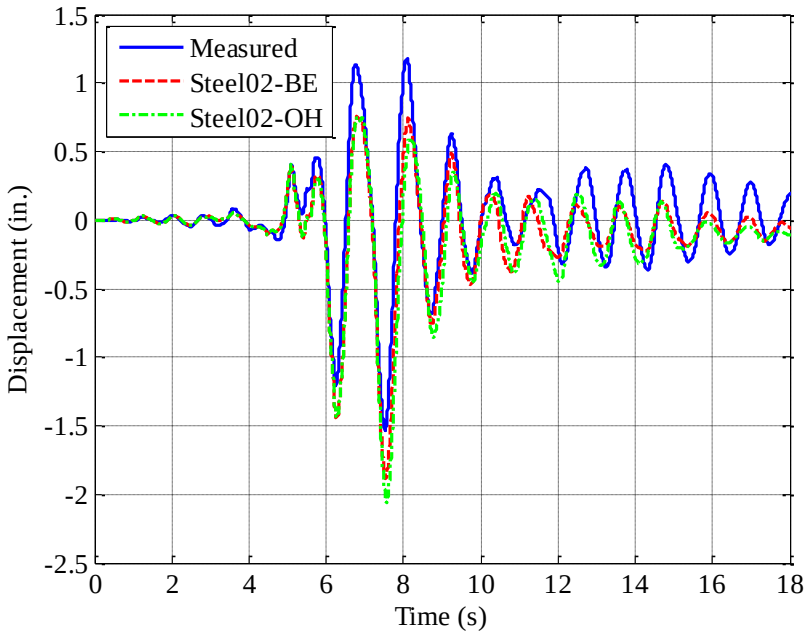

Figure 9-7. North-South displacement vs time for Specimen CIP-SF-REF-SHK for the first 18 seconds

9.5.3 Maximum Level

Figure 9-8 shows the average RMS results for the maximum level simulation. The Maximum Level peak ground motion acceleration intensity was about 1.5-2.0 greater than in the design level. Overall, the errors were remarkably insensitive to any of the model assumptions.

- **Goodness-of-Fit (GOF):** Similarly to Design Level, the out-of-phase response of the model was more pronounced. The error was slightly less using Elwood and Eberhard (2006) effective stiffness prediction. That was expected since that stiffness was closer to the measured effective stiffness before testing at maximum level.
- **Peak Displacements:** On average, the model on average systematically underestimated the peak displacements for all modeling inputs. However, Steel02 using optimized values from Chapter 5 yielded the closest peak displacement predictions. This was attributed to the low unloading/reloading stiffness of the steel.

- **Residual Displacements:** The model systematically underestimated the residual displacement using Steel02. In contrast, there was more scatter using ReinforcingSteel.

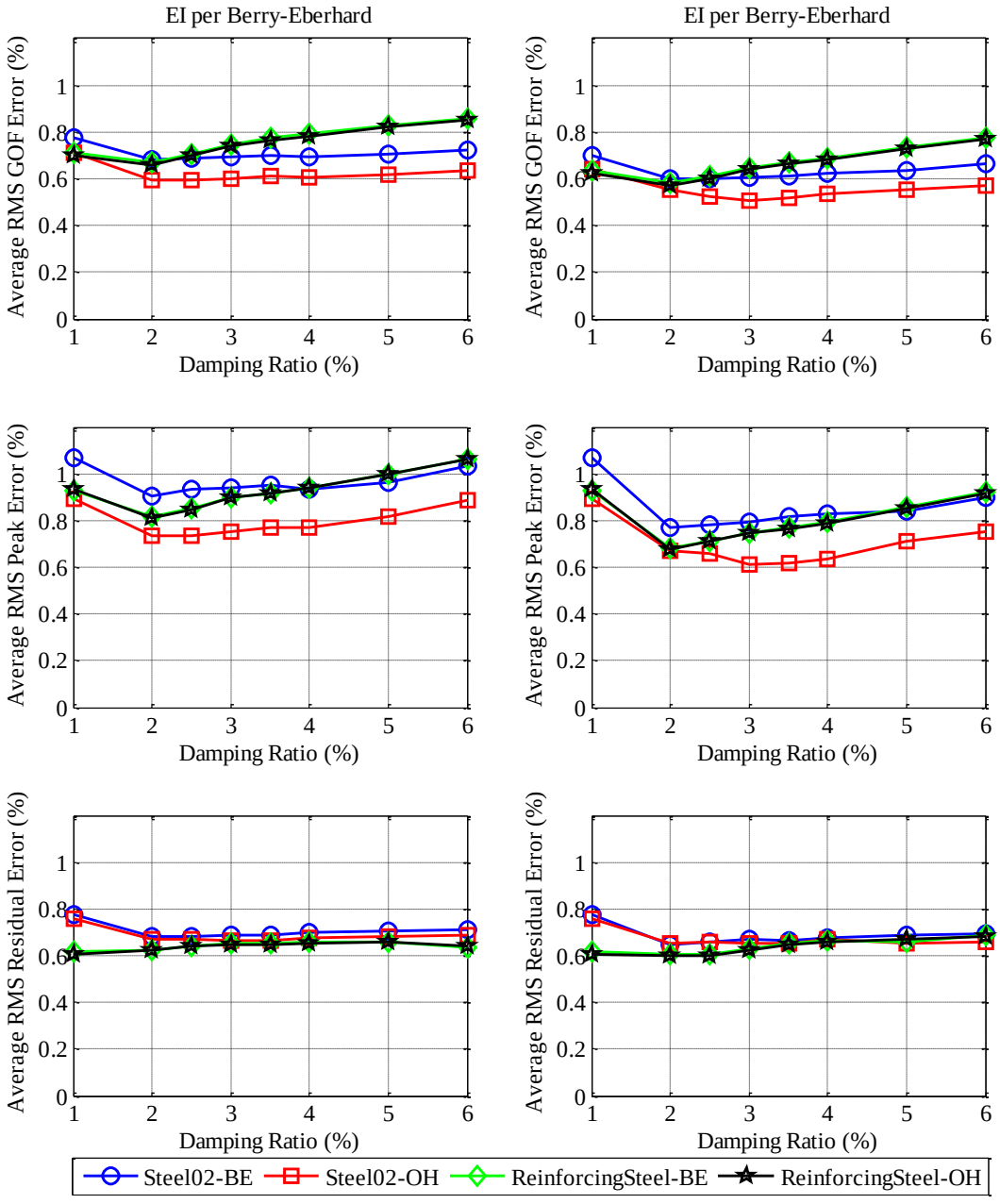

Figure 9-8. Maximum level RMS errors for goodness-of-fit, peak and residual displacements for five RC columns

9.6 Summary

In this chapter, the lumped-plasticity modeling strategy was evaluated using both calibrated constitutive model values from Chapter 5 and values used and/or calibrated in the research performed by Berry and Eberhard (2007). A total of five RC columns were simulated using two effective stiffness estimations, eight viscous damping ratios, and four constitutive modeling approaches.

Accurate measures of forces were not available from the shake table experiments, so comparisons of the force-displacement response were not possible. In the pseudo-static tests described in Chapter 5, the force-displacement response was well simulated by the OpenSees model. Matching responses at each time step is more difficult than matching responses in force displacement space.

The following conclusions were reached about the ability of the modeling strategies to reproduce the three key measures of response.

- **Goodness-of-Fit**: The GOF criterion compared measured and predicted results at each time step, so is sensitive to slight period shifts, which, in the end, do not matter much in terms of the bridge's ability to survive an earthquake.
- **Peak Displacements**: The various modeling strategies were able to predict the peak displacements of the columns accurately. When the parametric values were given values near the optimum, all four of the material models led to results that differed in detail but were about equally accurate in an overall sense. Peak displacements were predicted more accurately under the Design Level earthquake than under the Maximum Credible Earthquake. This difference was expected because the models' accuracy is likely to decrease at higher strains.
- **Residual Displacements**: The modeling strategies predicted residual displacements less successfully than peak displacements, despite the introduction of additional sophistication in the concrete model in the form of early re-loading. Berry and Eberhard (2007) concluded similarly. However, the scatter was greater at Maximum Credible Earthquake

Level than at Design Level. The results of the simulations show that, even though the concrete model was improved, the uncertainties in the unloading of the constitutive materials are still too great and needs to be investigated further.

The following conclusions were reached about the accuracy of the various modeling strategies.

- The lumped-plasticity modeling strategy using calibrated constitutive model inputs from Chapter 5 yielded matched the measured values as well as or better than the one used by Berry and Eberhard 2007. At the Yield Level, the four curves are nearly identical in all plots. At this stage, steel constitutive models responses were in the elastic range and concrete responses were quite similar, as expected.
- At Design Level, the simulations using ReinforcingSteel steel inputs were nearly identical since no bar fracture was obtained in any of the columns. In contrast, there was a slight difference between the simulations using Steel02. The difference is attributed to the unloading/reloading path of the steel constitutive model. Steel02 using recommendations by Berry and Eberhard (2007) unloaded with a larger stiffness ($R_{inf} \approx 1.4$) than Steel02 using optimized inputs from Chapter 5 ($R_{inf} = 1.2$) throughout the simulations. This phenomenon has been observed and evaluated by other researchers (e.g., Yazgan and Dazio 2011). Early concrete reloading was observed in concrete cover fibers in the extreme tension and compression but the early reloading effect was not enough to cause significant difference.
- At Maximum Credible Earthquake, the responses were quite similar using Steel02 and ReinforcingSteel using recommendations from Berry and Eberhard (2007) and optimized values from Chapter 5. Furthermore, the errors were independent from the viscous damping assigned to the models due to hysteretic damping.
- All simulations were performed using a plastic hinge model proposed by Berry and Eberhard (2007). Using the effective stiffness, EI_{eff}, estimation by Berry and Eberhard (2007) yielded more accurate results in terms of peak displacement at both Yield and

Design Levels. However, results were more accurate using the Elwood and Eberhard (2007) model and Maximum Credible Earthquake Level.

- In general, the appropriate viscous damping for a cantilever column was between 2-3%.

10 SUMMARY AND CONCLUSIONS

10.1 Summary

This thesis describes the development of a new bridge bent system that is intended to accelerate onsite construction, improve seismic performance and increase durability, as compared with conventional cast-in-place concrete construction.

- *Accelerated construction* is achieved by precasting the columns and cap beams, which are then joined by grouted connections on site. A "wet socket" connection between the column and spread footing is made by setting the column in the excavation and casting the footing concrete around it. No steel crosses the interface, and a roughened interface on the precast column ensures the integrity of the connection.
- The *seismic performance* is improved in two ways. First, the system includes pre-tensioned strands that are bonded at the ends of the column but unbonded over the free height of the column. They remain elastic up to the design drift ratio, and therefore return the column to vertical when the ground motion stops. The second improvement is intended to reduce the need for post-earthquake repair by using Hybrid-Fiber Reinforced Concrete (HyFRC) instead of conventional concrete in the plastic hinge region. The high fiber content makes the concrete tougher and is intended to reduce spalling in compression.
- The *durability* is increased by improving the columns resistance to steel corrosion. The prestressing places the concrete under permanent compression and inhibits ingress of moisture. The use of epoxy-coating on the strands further protects them from corrosion.

The system was evaluated using four approaches:

1. Rapid Constructions. This feature was evaluated in the laboratory by observing the ease with which the components could be assembled. A full-scale bridge was also built in the field using technology that lacked the prestressing in the columns but which otherwise was almost identical from the viewpoint of constructability.

2. Cyclic Lateral-Load Performance. The results of nine pseudo-static tests of 42%-scale precast column specimens were evaluated. Five were prestressed, and four contained only deformed bar reinforcement. All specimens had the same diameter (D = 20") and cantilever height (h = 60").
3. Dynamic Performance. Two column specimens, one conventional and one pre-tensioned with HyFRC in the plastic hinge region, were tested on a shake table. The results were compared to demonstrate the dynamic properties of the new system. Both had D = 16" and h = 60".
4. Numerical Simulation. Numerical simulations were undertaken to evaluate the ability of the OpenSees simulation software to reproduce the behavior measured in tests. The work focused on the concrete and steel material models, with the goal of selecting the features of each to best fit the measured results. During the work, a new concrete model (Concrete 08) was developed as an extension of a previous one, and it was incorporated into OpenSees. The results from 34 other column tests were also used as a database against which to compare the simulated results. The optimized models were used to predict the responses of five columns tested on the UC Berkeley shaking table.

10.2 Conclusions about Quasi-Static Behavior

The following conclusions were drawn from this research about the quasi-static behavior of the new system.

- **Failure mechanism and damage location.** In all cases the failure occurred in the plastic hinge region of the column. The adjoining elements (footing or cap beam) suffered either no damage at all or cosmetic cracking. This behavior satisfies the overall design goal for bridge bents in seismic regions.
- **Re-Centering.** All of the prestressed columns re-centered better than the non-pre-stressed systems. The extent to which they did so depended on the re-centering ratio, which is a design parameter related to the relative amounts of prestressed and non-prestressed reinforcement. The prestressed column with HyFRC performed the best, and returned to essentially zero residual drift after being displaced to 9% peak drift. After the

same peak drift, the non-prestressed columns had approximately 2% residual drift. The US has no formal guidelines but, in Japan, 1% residual drift is accepted as the cut-off after which repair is impractical and demolition is necessary.

- **Strength.** The pre-tensioned system can be detailed such that it has the same design strength as a conventional non-prestressed system.
- **Ductility.** When pre-tensioning was used with conventional concrete, the column strength dropped below 80% of its peak after about 5% drift. When HyFRC was used, the column strength remained above 80% of the peak throughout the whole test history, in which the largest drift ratio was above 10%. Past tests had shown that the ductility decreased with prestressing, mainly because larger reinforcing bars would be replaced with smaller ones. Based on the tests described here, it appears that the use of HyFRC provided sufficient additional toughness that the ductility lost by adding prestressing was more than fully restored.
- **Concrete damage and need for repair.** Prestressing caused spalling to occur earlier than in the specimens reinforced with deformed bars, while the addition of HyFRC in the plastic hinge region delayed spalling. It had been hoped that the HyFRC would have achieved a damage level low enough that repair would prove unnecessary, but this was not the case. Spalling due to compression was indeed reduced, although not eliminated entirely, but, contrary to expectations, the tensile deformations concentrated at a single crack, the width of which grew as loading progressed.
- **Bar buckling and fracture are affected by three features of the system.** Prestressing promotes them through early spalling, the use of HyFRC delays them by delaying spalling, and local debonding of the bars can delay fracture by reducing the local strain concentrations. The net outcome depends on the extent to which each feature is active. Bar buckling started at 6.1%, 3.3% and 4.0% drift ratio in the conventional, the prestressed, and the prestressed with HyFRC systems respectively. However, the HyFRC did not delay bar fracture. None of the specimens had their mild reinforcement debonded.

- **Energy dissipation.** The pre-tensioned and the post-tensioned specimens dissipate less energy per cycle than observed in the non-prestressed specimens. This is a result of replacing mild reinforcement with prestressing strands or bars. At a drift ratio of 4.0%, the average equivalent viscous damping for the pre-tensioned system with HyFRC and the non-prestressed system were about 13% and 20%, respectively.

10.3 Conclusions about Dynamic Response.

The following conclusions were made from the shake table study:

- **Maximum drift demand.** The reinforced concrete reference specimen and the HyFRC pre-tensioned specimen had similar maximum drift demands under all earthquake motions except two. In those two, the cast-in-place reference column displayed a higher peak drift than the pre-tensioned column.
- **Re-centering.** The pre-tensioned specimen showed superior re-centering capability compared to the reference specimen. It showed a residual drift of 0.23% after being displaced up to a peak drift of 5.5%. In comparison, the reference column had a residual drift of 0.83% after experiencing 5.7% peak drift.
- **Damage progression.** The use of HyFRC slightly delayed spalling. In tension, the pre-tensioned specimen showed the same behavior as was observed in the quasi-static specimen. As soon as the HyFRC cracked, the tensile deformations concentrated there and caused a strain concentration in the mild reinforcement, which led to premature bar fracture. Similarly to the quasi-static test with HyFRC, this specimen did not have its mild reinforcement debonded.

10.4 Conclusions on Numerical Modeling

The following conclusions were made:

- **Relative importance of constitutive models.** The response of the system is affected more by the properties of the steel model than by those of the concrete model. This conclusion is in accordance with the findings or other researchers who have studied columns with relatively low axial loads.

- **Steel models.** Two models (Steel02 and ReinforcingSteel) were evaluated. In each case, the model parameters were optimized to provide the best match with the database of test results. When the complete test data histories were used, ReinforcingSteel provided the better match, but when the histories were curtailed at the point where the strength had dropped to 80% of the peak, Steel02 gave better results. The difference is attributed to the fact that ReinforcingSteel takes into account degradation of the steel but Steel02 does not. The Bauschinger effect parameters (i.e., R_0, cR_1) in Steel02 proved to have greater impact on the accuracy of the numerical model than any other parameters. A procedure was developed Section 5.2.2.3 to determine the optimal values of these parameters.
- **Concrete models.** The new feature of the concrete model developed here (Concrete 08) was early re-loading, whereby compressive stress can exist across a crack that is not yet fully closed. This feature is intended to mimic the presence of rubble in the crack, or a slight shear offset of the two crack faces. The improvement in matching test results proved to be minimal.
- **Comparison with previous simulation research**. Berry and Eberhard (2007) performed a similar simulation exercise, but on a smaller database of column tests and with a different optimization procedure. The model parameters found here to be optimal were similar to those found by Berry and Eberhard.
- **Dynamic simulation accuracy.** The accuracy of the calibrated numerical models using either steel constitutive model was equally as good to that of Berry and Eberhard (2007) for all levels. Both provided accurate means of predicting the peak displacement at yield level and design level. The accuracy was the least at the maximum level of ground motion, for which the error ranged from 10% to 12% of the total peak displacements. However, neither approaches was successful in predicting accurately residual displacements.
- **Dynamic damping and effective stiffness.** Viscous damping in the range of 2 to 3% provided the most accurate results at the yield level. However, at the design level, the best results were obtained using 5% damping. This was a consequence of the effective stiffnesses given to the model. Both effective stiffness predictions underestimated the real

effective stiffness of the columns prior to be subjected to design level earthquake. The calculated effective stiffness using Berry and Eberhard (2007) provided slightly more accurate results than the one proposed by Elwood Eberhard (2006). By using viscous dampings from 2% to 3% the simulation accuracy at design level were 8% to 11% of the peak displacements.

10.5 Recommendations for Future Research

The following lists recommendations for future work:

- **Pre-tensioned bridge bent system plastic hinge regions.** This research evaluated the performance of the pre-tensioned bent system using HyFRC in the plastic hinge region. Both quasi-static test and shake table test revealed weakness of the HyFRC shell; as soon as a crack formed the specimen tended to rock on it, causing strain concentration in the mild reinforcement that caused premature bar fracture. The effect of debonding should be explored further to evaluate whether strain concentration and bar fracture would be delayed.
- **Pre-tensioned bridge bent system unbonded strand system.** All three pre-tensioned quasi-static test specimens encountered strand slipping from the connections. The same observation was made in the shake table test. It would be ideal to develop a chuck-system that is both safe for construction workers and allows it to be cast with the strands.
- **Numerical modeling.** Current numerical modeling methodologies provide accurate means of predicting peak displacements during seismic event. However, these same methodologies are not successful in predicting residual displacements. This shortcoming is a consequence of the fact the current constitutive models over-simplify the unloading and reloading of both the steel and concrete. This study showed that the behavior is more controlled by the steel model used in the simulations. Research should be conducted to more accurately predict the real steel behavior inside concrete columns.

11 REFERENCES

"AASHTO LRFD Bridge Design Specifications" (2010). 6th ed., with 2011 Interim Revisions. American Association of State Highway and Transportation Officials, Washington, DC.

"AASHTO Guide Specification for LRFD Seismic Bridge Design" (2011). 2nd edition. American Association of State Highway and Transportation Officials, Washington DC.

ACI Committee 318 (2011). "Building Code Requirements for Structural Concrete and Commentary." *ACI 318-11* American Concrete Institute, Farming Hills, MI.

Berry, M.P. and Eberhard, M.O. (2004). "Performance Models for Flexural Damage in Reinforced Concrete Columns," Pacific Earthquake Engineering Research Center Report PEER-2003-18, University of California, Berkeley, August, 156 pp.

Berry, M.P., and Eberhard, M.O. (2004). "PEER Structural Performance Database User's Manual." *Pacific Earthquake Engineering Research Center Report 2004*, <www.ce.washington.edu/~peeral>, University of California, Berkeley, CA.

Berry, M.P. and Eberhard, M.O. (2005), "A Practical Performance Model for Bar Buckling." *Journal of Structural Engineering, ASCE*, July, Vol. 131, No. 7, pp 1060-1070.

Berry, M.P. and Eberhard, M.O. (2007). "Performance Modeling Strategies for Modern Reinforced Concrete Columns." Pacific Earthquake Engineering Research Center Report, PEER 2007/7, University of California, Berkeley, July, 206 pp.

Billington, S.L., R.W. Barnes, and J.E. Breen (1999). "A Precast Segmental Substructure System for Standard Bridges," *PCI Journal*, Vol. 44, No. 4, August, pp. 56-73.

Billington, S.L., R.W. Barnes, and J.E. Breen (2001). "Alternate Substructure Systems for Standard Highway Bridges," *ASCE Journal of Bridge Engineering*, Vol. 6, No. 2, March/April, pp. 87-94.

Billington, SL, and JK Yoon (2004) “Cyclic Response of Precast Bridge Columns with Ductile Fiber-reinforced Concrete,” *ASCE J. Bridge Engineering*, **9**(4): 353-363.

Billington, SL, Lignos, DG, Hanson, JV, and Moreno-Luna, DM, (2011). "Response of high-performance fiber reinforced concrete infill panels retrofitting steel moment-resisting frames," *Proc. 8th Int'l Conf. Urban Earthquake Engineering*, Tokyo Institute of Technology, Tokyo, Japan, March.

Blunt, J. and C.P. Ostertag, (2009a). "A Performance-based Approach for the Design of a Deflection-Hardened Hybrid Fiber-reinforced Concrete," *ASCE J. Engineering Mechanics*, 135:978-986.

Blunt, J. and C.P. Ostertag, (2009b). "Deflection Hardening and Workability of Hybrid Fiber Composites," *ACI Materials Journal*, 106: 265-272.

Brearley Jr., Ladson M., and David W. Johnston (1990). "Pull-Out Bond Tests of Epoxy-Coated Prestressing Strand." *Journal of Structural Engineering* 116.8: 2236-252.

Brown, W. (2008). “Bar Buckling in Reinforced Concrete Bridge Columns.” MSCE Thesis, University of Washington, Seattle, WA.

Building Seismic Safety Council. (2003). “NEHRP Recommended Provisions for Seismic Regulations for New Buildings and Other Structures (FEMA 450).” *National Earthquake Hazards Reduction Program*, National Institute of Building Sciences, Washington, D.C.

Canbolat, B.A., Parra-Montesinos, G.J., and Wight, J.K. (2005). “Experimental study on the seismic behavior of high-performance fiber reinforced cement composite coupling beams, *ACI Structural Journal*, Vol. 102, No. 1, pp. 159-166.

Calderone, A.J., Lehman, D.E., Moehle, J.P. (2000). "Behavior of Reinforced Concrete Bridge Columns Having Varying Aspect Ratios and Varying Lengths of Confinement," Pacific Earthquake Engineering Research Center Report 2000/08.

Caltrans (2010). “*Seismic Design Criteria Version 1.6.*”. Caltrans, Sacramento, CA.

Cheok, G.S. and Stone, William C. (1986). "Behavior of 1/6-Scale Model Bridge Columns Subjected to Cycle Inelastic Loading." NBSIR 86-3494, Center for Building Technology, National Engineering Laboratory, National Institute of Standards and Technology, Gaithersburg, Maryland, 20899, November, 291 pages.

Cohagen, L.S., Pang, J.B.K., Eberhard, M.O., and Stanton, J. F. (2008). " A Precast Concrete Bridge Bent Designed to Re-center after an Earthquake." *Washington State Department of Transportation Report No. WA-RD 684.3*, Washington State Department of Transportation, Washington, 2008.

Cheok, G. S., Stone, W. C., and Kunnath, S. K. (1998). ''Seismic response of precast concrete frames with hybrid connections.'' *ACI Struct. J.*, 95~5!, 527–539.

Chronister, A. (2007). "Experimental Investigation of High Strength Concrete Filled Steel Tubes in Embedded Column Base Foundation Connections". MSCE thesis. University of Washington, Seattle, WA.

Davis, P.M., Janes, T.M., Eberhard, M.O., and Stanton, J.F., (2012a). "Unbonded Pre-Tensioned Columns for Bridges in Seismic Regions," Pacific Earthquake Engineering Research Center Report PEER-2012, 147 pp. (submitted)

Davis, P.M., Janes, T.M., Stanton, J.F., Eberhard, M.O., and Haraldsson, O.S. (2012b). "Unbonded Pre-Tensioned Columns for Accelerated Bridge Construction in Seismic Regions,' to be submitted to Journal of Bridge Engineering, ASCE.

El-Sheikh, M.T., R. Sause, S. Pessiki, and L. Lu (1999). "Seismic Behavior and Design of Unbonded Post-Tensioned Precast Concrete Frames," *PCI Journal*, Vol. 44, No. 3, May/June 1999, pp. 54-71.

FHWA (2008). "2008 Condition and Performance Report." U.S. Department of Transportation, Federal Highway Administration.

Finnsson, G. (2012), "Pre-Tensioned Column with HyFRC in the Plastic Hinge Region". MSCE thesis. University of Washington, Seattle, WA. (ongoing)

Grupp, J., C.P. Ostertag, T. Devine, (2007). “Effect of steel microfibers on corrosion of steel reinforcing bars.” Cement and Concrete Research, Vol. 37, pp. 1115-1126.

Gunnarsson, A.K., Lehman, D., Roeder, C., and Kuder, K. (2012). “Long-Term and Seismic Performance of Concrete-Filled Steel Tube Columns with Conventional and High-Volume SCM Concrete,” TRANSNOW final report, June, 238 pp.

Hachem, M., Mahin, S., and Moehle, J. (2003). "Performance of Circular Reinforced Concrete Bridge Columns under Bidirectional Earthquake Loading," Pacific Earthquake Engineering Research Center, PEER 2003/03, March.

Haraldsson, O.S., Eberhard, M.O., Stanton, J.F, Berry, Michael (2010), “Accelerating Bridge Construction to Reduce Congestion,” TRANSNOW final report, December, 49 pp.

Haraldsson, O.S., Janes, T.M., Eberhard, M.O., and Stanton, J.F. (2012a). *“Laboratory Tests of Column-to-Footing Socket Connections.”* U.S. Department of Transportation, Federal Highway Administration, Washington, DC.

Haraldsson, O.S., Janes, T.M., Eberhard, M.O., and Stanton, J.F. (2012b). “Seismic Resistance of Socket Connection between Footing and Precast Column.” Journal of Bridge Engineering. 10.1061/(ASCE)BE.1943-5592.0000413 (1 November 2012)

Hewes, J. T., and Priestley, N. (2002). “Seismic design and performance of precast concrete segmental bridge columns.” Rep. No. SSRP-2001/25, Univ. of California at San Diego.

Hieber, D., Wacker, J., Eberhard, M.O., and Stanton, J. F. (2005a). “Precast Concrete Pier Systems for Rapid Construction of Bridges in Seismic Regions.” *Washington State Department of Transportation Report No. WA-RD-611.1,* Washington State Department of Transportation, Washington, 2005.

Hieber, D., Wacker, J., Eberhard, M.O., and Stanton, J.F. (2005b). “State of the Art Report on Precast Concrete Systems for Rapid Construction of Bridges.” *Washington State Department of Transportation Report No. WA-RD-549.1,* Washington State Department of Transportation, Washington, 2005.

Ishizuka, T., Hawkins, N. M., and Stanton, J. F., (1984) "Experimental Study of the Seismic Resistance of a concrete Exterior Column Beam Sub-assemblage Containing Unbonded Post-Tensioning Tendons," *Dept. of Civil Engineering*, University of Washington, May.

Janes, T.M. (2011). "Precast Column Socket Connections for Thin Spread Footings". MSCE Thesis. University of Washington, Seattle, WA. 91 p.

Jen, G., Trono, W., Ostertag, C.P. (2011). Design and Properties of Self compacted Hybrid Fiber reinforced composites, CCC Journal, (submitted).

Jeong, H.I, Sakai, J., and Mahin, S.A, (2008). "Shaking Table Tests and Numerical Investigation of Self-Centering Reinforced Concrete Bridge Columns," Pacific Earthquake Engineering Research Center, PEER 2008/06, June.

Kanda, T., Watanbe, S., and Li. V.C., (1998). "Application of pseudo strain hardening, cementitious composites to shear resistant structural elements," *Fracture Mechanics in Concrete Structures: Proceedings of Framcos-3*, Eds. H. Mihashi and K. Rokugo. Volume III, pp. 1477-1490.

Keoleian, GA, Kendall, A, Dettling, JE, Smith, VM, Chandler, RF, Lepech, MD, and Li, VC (2005) "Life Cycle Modeling of Concrete Bridge Design: Comparison of ECC Link Slabs and Conventional Steel Expansion Joints," *Journal of Infrastructure Systems*, March 2005 pp 51-60.

O'Neill, K.A. (2012). "Experimental Investigation of Circular Concrete Filled Steel Tube Geometry on Seismic Performance". MSCE thesis. University of Washington, Seattle, WA.

Khalegi, B., Schultz, E., Sequirant, S., Marsh, L.M., Haraldsson, O.S., Eberhard, M.O., and Stanton, J.F. (2012), "Accelerated Bridge Construction in Washington State: From Research to Practice," *PCI Journal*, Vol. 57, No. 4, October/November, pp. 34-49.

Kowalsky, M.J., Priestley, M.J.N., and Seible, F (1999), "Shear and Flexural Behavior of Lightweight Concrete Bridge Columns in Seismic Regions," American Concrete Institute, ACI Structural Journal, Vol. 96, No. 1, January-February, pp. 136-148.

Kumar, P., Jen, G., Trono, W., Lallemant, D., Panagiotou, M., & Ostertag, C.P. (2011). Self Compacting Hybrid Fiber Reinforced Concrete Composites for Bridge Columns. Pacific Earthquake Engineering Research Center; PEER report 2011/106.

Kingsley, A. (2005). "Experimental and Analytical Investigation of Embedded Column Base Connections for High Strength Concrete-Filled Steel Tubes". MSCE thesis. University of Washington, Seattle, WA.

Kwan, WP and SL Billington (2003) "Unbonded Post-tensioned Bridge Piers: Part I-Monotonic and Cyclic Analyses" ASCE J. Bridge Eng., 8(2): 102-111.

Kwan, WP, and SL Billington (2003) "Unbonded Post-tensioned Bridge Piers: Part II - Seismic Analyses" ASCE J. Bridge Eng., 8(2): 92-101.

Kyriakides, MA and SL Billington (2008) "Seismic Retrofit of Masonry-Infilled non-ductile Reinforced Concrete Frames using Sprayable ECC," *Proceedings of the 14th World Conference on Earthquake Engineering (14WCEE)*, Beijing, China, October.

LeClaire, Philip J., and Abdul F. Shaikh. "Effect of Elevated Temperature on the Bond Strength of Epoxy-Coated Prestressing Strand." *Precast/Prestressed Concrete Institute*, July-Aug. (1996): 54-61.

Lee, W. and Billington, S. (2010). "Modeling Residual Displacements of Concrete Bridge Columns under Earthquake Loads Using Fiber Elements." *J. Bridge Eng.*, 15(3), 240–249.

Lee, J.R. (2011). "Experimental Investigation of Embedded Connections for Concrete-Filled Steel Tube Columns". MSCE thesis. University of Washington, Seattle, WA.

Lehman, D.E. and Moehle, J.P. (2000); "Seismic Performance of Well-Confined Concrete Bridge Columns," Pacific Earthquake Engineering Research Center, PEER 1998/01, Dec.

Lehman, D.E., and Roeder, C.R. (2012). "Foundation Connections for Circular Concrete-Filled Tubes." Journal of Constructional Steel Research, 78(8), 212-225.

LoBuono, Armstrong, & Associates, *Development of Precast Bridge Substructures* (1996), Florida Department of Transportation, Tallahassee, FL

Mander, J. Priestley, M., and Park, R. (1998). "Theoretical Stress-Strain Model for Confined Concrete." *Journal of the Structural Division ASCE 114(8)*, 1804-1826.

Marsh, L.M., Wernli, M., Garrett, B.E., Stanton, J.F., Eberhard, M.O., and Weinert, M.D. (2011). NCHRP Report 698: "Application of Accelerated Bridge Construction Connections in Moderate-to-High Seismic Regions." Transportation Research Board, Washington, DC.

Matsumoto, E., Waggoner, M., Sumen, G., Kreger, M., Wood, S., and Breen, J. (2001). *"Development of a Precast Bent Cap System,"* Center for Transportation Research, Research Project 0-1748, University of Texas at Austin.

Matsumoto, E., Waggoner, M., Kreger, M., Vogel, J., and Wolf, L. (2008). "Development of a Precast Concrete Bent-Cap System." *PCI Journal, 53(3),* 74-99.\

Matsumoto, E. (2009). "Emulative Precast Bent Cap Connections for Seismic Regions: Grouted Duct and Cap Pocket Test Results, Design and Construction Specifications, Design Examples, and Connection Details." Sacramento, CA: California State University, Sacramento. ECS Report No. ECS-CSUS-2009-05, 749 p.

Mole, A. (1994). "Seismic Response of Hybrid Connections in Precast Concrete Frames". MSCE thesis. University of Washington, Seattle, WA, 147 p.

Moehle, J. and Deierlein, G. (2004). "A Framework Methodology for Performance-Based Earthquake Engineering." *Proceeding of the 13th World Conference on Earthquake Engineering*, Vancouver, Canada, August, 2004, paper No. 679.

Motaref, S., Saiidi, M. S., and Sanders, D. (2010). Experimental Study of Precast Bridge Columns with Built-in Elastomer. *Transportation Research Record: Journal of the Transportation Research Board, 2202*, 109-116.

Nakaki, S.D., Stanton, J.F., Sritharan, S. (1999). "Overview of the PRESSS Five Story Precast Test Building." *PCI Jo., 44(2),* March-April 1999, pp 26-39.

OpenSees Development Team (2012). Opensees: Open system for earthquake engineering simulations. Version 2.4.0, Berkeley, CA.

Osanai, Y., Watanabe, F., and Okamoto, S., (1996). "Stress Transfer Mechanism of Socket Base Connections with Precast Concrete Columns." *ACI Structural Journal,* ACI, Chicago. IL. May-June, pp. 266-276.

Ostertag, C.P., Blunt, J., Grubb, J. (2007a), Mitigation of Expansive Deterioration Mechanisms through Crack Control" Proc. of 6th International Conference on Fracture mechanics of Concrete and Concrete Structures," pp. 1843-1849.

Ou, Y.-C., Chiewanichakorn, M., Aref, A. J., and Lee, G. C. (2007). "Seismic performance of segmental precast unbonded post-tensioned concrete bridge columns." Journal of Structural Engineering, ASCE, 133(11), 1636-1647.

Pang, J.B.K., Steuck, K., Cohagen, L., Stanton, J.F., Eberhard, M.O. (2008). "Rapidly Constructable Large-Bar Precast Bridge-Bent Seismic Connection." *Washington State Department of Transportation Report No. WA-RD 684.2*, Washington State Transportation Center.

Pang, J.B.K., Eberhard, M.O., and Stanton, J.F. (2010). "Large-Bar Connection for Precast Bridge Bents in Seismic Regions." *Journal of Bridge Engineering, ASCE*, May-June, pp. 231-239.

Parra-Montesinos, G.J., Peterfreund, S., and Chao, S.-H. (2005). "Highly damage tolerant beam-column joints through the use of strain-hardening fiber reinforced cement composites," *ACI Structural Journal*, **102**(3): 487-495

Priestley, M.J.N. and J.R. Tao (1993), "Seismic Response of Precast Prestressed Concrete Frames with Partially Debonded Tendons," *PCI Journal*, Vol. 38, No. 1, January/February, pp. 64-81.

Priestley M. J. N. and MacRae G. A. (1996) Seismic Tests of Precast Beam-to-Column Joint Subassemblages with Unbonded Tendons. *PCI Journal,* 64-80.

Precast/Prestressed Concrete Institute (2004). "*PCI Design Handbook*". 6th ed. PCI, Chicago, IL.

Porter, K.A. (2003). “An Overview of PEER’s Performance-Based Earthquake Engineering Methodology.” *Proceedings of the 9th Conference on Applications of Statistics and Probability in Civil Engineering.”* San Francisco, July.

Raynor, D.J., Lehman, D.E. and Stanton, J.F. (2002). “Bond-Slip Response of Reinforcing Bars Grouted in Ducts.” *ACI Str. Jo.* 99(5), Sept. pp. 568-576.

Restrepo, J., Matsumoto, E., Tobolski, M. (2010). Development of precast bent cap systems for seismic regions, Report No. NCHRP 12−74, National Cooperative Highway Research Program

Rouse, JM and Billington, SL (2003) “Behavior of Bridge Piers with Ductile Fiber Reinforced Hinge Regions and Vertical, Unbonded Post-Tensioning,” *Proc. fib Symposium on Concrete Structures in Seismic Regions*, Greece, May.

Sakai, J., and Mahin, S. (2004). "Analytical Investigations of New Methods for Reducing Residual Displacements of Reinforced Concrete Columns," Pacific Earthquake Engineering Research Center, PEER 2004/02, February.

Schoettler M.J., Eberhard M. (University of Washington), Mahin S. (UC Berkeley), Mosalam K. (UC Berkeley), Ostertag C. (UC Berkeley), Panagiotou M. (UC Berkeley), Restrepo J. (UC San Diego), Stanton J. (University of Washington), Terzic V. (UC Berkeley) (2012) *“Advancing the performance of bridge columns: Overview of a shake table test program,”* 7th National Seismic Conference on Bridges and Highways, Oakland, CA.

Stanton, J., and McNiven, H. (1979). “The development of a mathematicalmodel to predict the flexural response of reinforced concretebeams to cyclic loads, using system identification.” *Rep. No. EERC 79-02*, Earthquake Engineering Research Center, Univ. of California, Berkeley, Calif.

Stanton, J., Stone, W. C., and Cheok, G. S. (1997). Hybrid Reinforced Precast Frame for Seismic Regions. *PCI Journal*, 42(2), 20-32.

Steuck, K., Pang, J.B.K., Stanton, J.F. and Eberhard, M.O. (2007). "Anchorage of Large Bars in Grouted Ducts." *Washington State Transportation Center Report WA-RD 684.1*, Seattle, WA.

Steuck, K., Stanton, J.F. and Eberhard, M.O. (2009). "Anchorage of Large-Diameter Reinforcing Bars in Ducts." *ACI Str. Jo.*, July-August, pp 506-513.

Stone, W.C., Cheok, G.S., and Stanton, J.F. (1995). "Beam-Column Connections Subjected to Cyclic Loads". *ACI Str. Jo.*, Vol. 92(2), March-April, pp. 229-249.

Tobolski, M. J. (2010). "Improving the Design and Performance of Concrete Bridges in Seismic Regions". PhD thesis. University of California, San Diego, CA.

Tran, H.V., Eberhard, M.O., and Stanton, J.F (2012). "Seismic-Resistant Connections Between Precast Concrete Columns and Drilled Shafts," TRANSNOW final report, December, 128 pp.

Trono, W., Jen, G., Moreno, D., Billington, S.L., Ostertag, C.P. (2011). Confinement and Tension Stiffening Effects in High Performance Self-consolidated Hybrid Fiber Reinforced Concrete Composites, Proc. HPFRCC-6 Workshop, Ann Arbor Michigan.

Wacker, J., Hieber, D., Eberhard, M., and Stanton, J. (2005). "Design of Precast Concrete Piers for Rapid Construction of Bridges in Seismic Regions." *Washington State Department of Transportation Report No. WA-RD-629.1*, Washington State Department of Transportation, Washington, 2005.

Weinert, M.D. (2011). "Substructure Connections for Accelerated Bridge Construction in Seismic Regions". MSCE thesis. University of Washington, Seattle, WA, 239 p.

Williams, T. (2006). "Experimental Investigation of High Strength Concrete Filled Steel Tubes in Embedded Column Base Foundation Connections". MSCE thesis. University of Washington, Seattle, WA.

WSDOT (2008). *"Bridge Design Manual Version M23-50.02."* Washington State Department of Transportation, Olympia, WA.

Xiao, Y., Priestley, M.J.N., and Seible, F. (1996). "Seismic Assessment and Retrofit of Bridge Column Footings." *ACI Str. Jo.,* ACI, Farmington Hills, MI. Jan-Feb., pp. 79-94.

Yazgan U. and Dazio A. (2011). Simulating Maximum and Residual Displacements of RC Structures: I. Accuracy, *Earthquake Spectra,* Vol. 25, Iss. 4, pp. 1187-1202

Yazgan U. and Dazio A. (2011). Simulating Maximum and Residual Displacements of RC Structures: II. Sensitivity, *Earthquake Spectra*, Vol. 25, Iss. 4, pp. 1203-1218

Yi, C.K. and C.P. Ostertag, (2004), Mechanical Approach in Mitigating Alkali Silica Reaction, Cement and Concrete Research, Vol. 35, pp. 67-75.

APPENDIX A: SPECIMEN CONSTRUCTION DRAWINGS

A.1 Conventional Cast-In-Place Shake Table Column

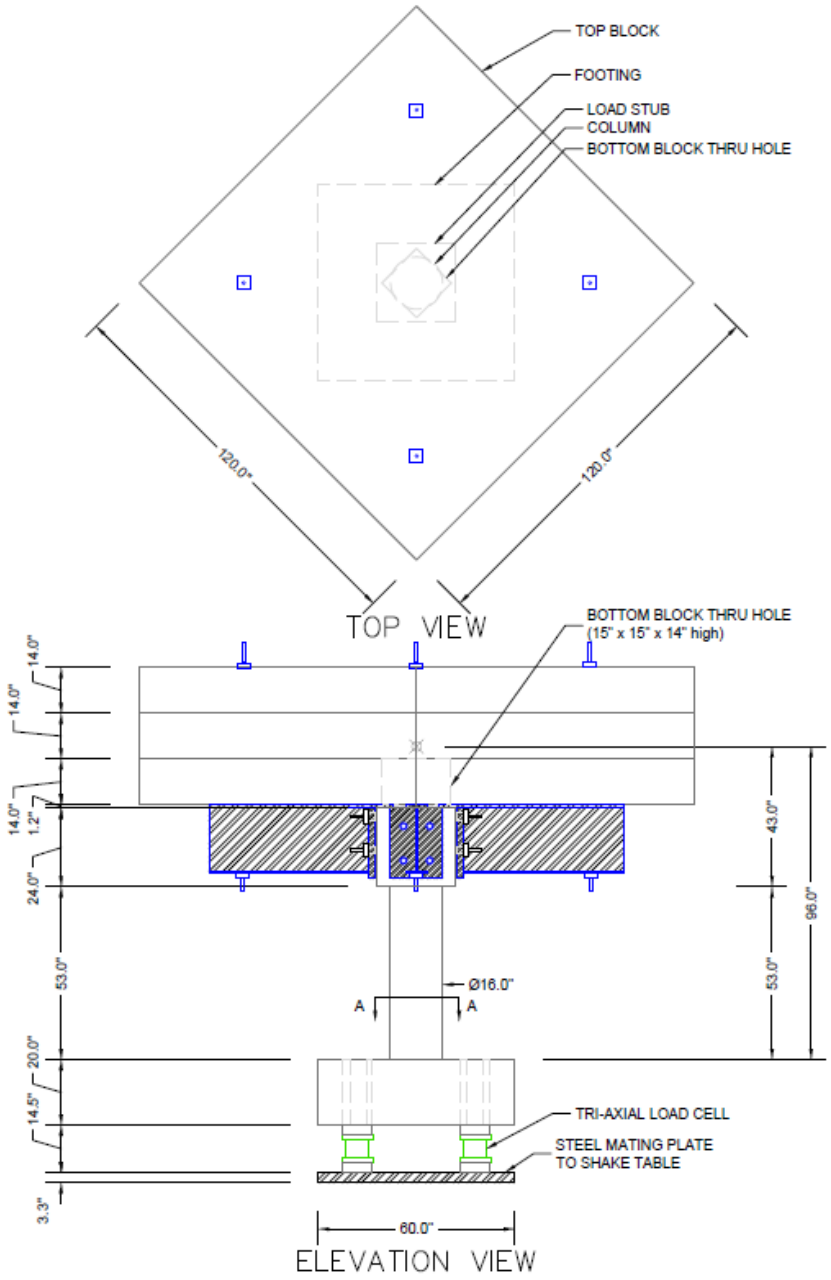

Figure A-1. Conventional cast-in-place shake table specimen: elevation

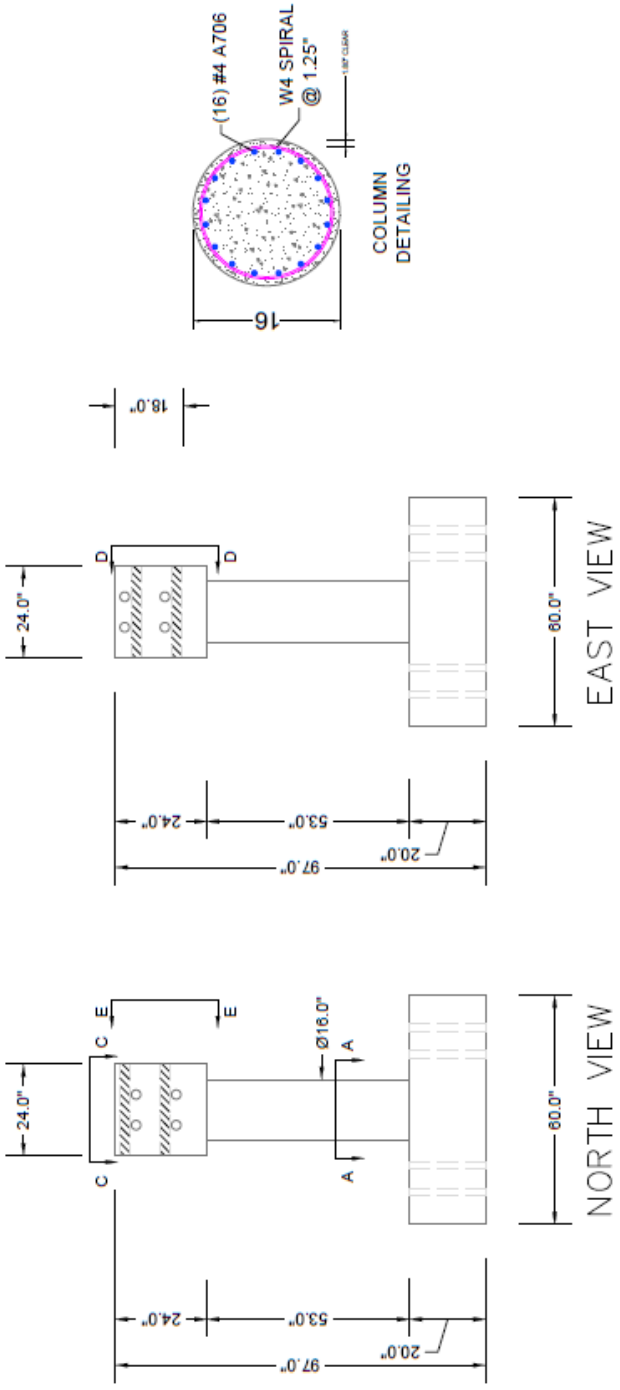

Figure A-2. Conventional cast-in-place shake table specimen: elevation and cross section

A.2 Unbonded Pre-Tensioned Shake Table Column with HyFRC in the Plastic Hinge Region

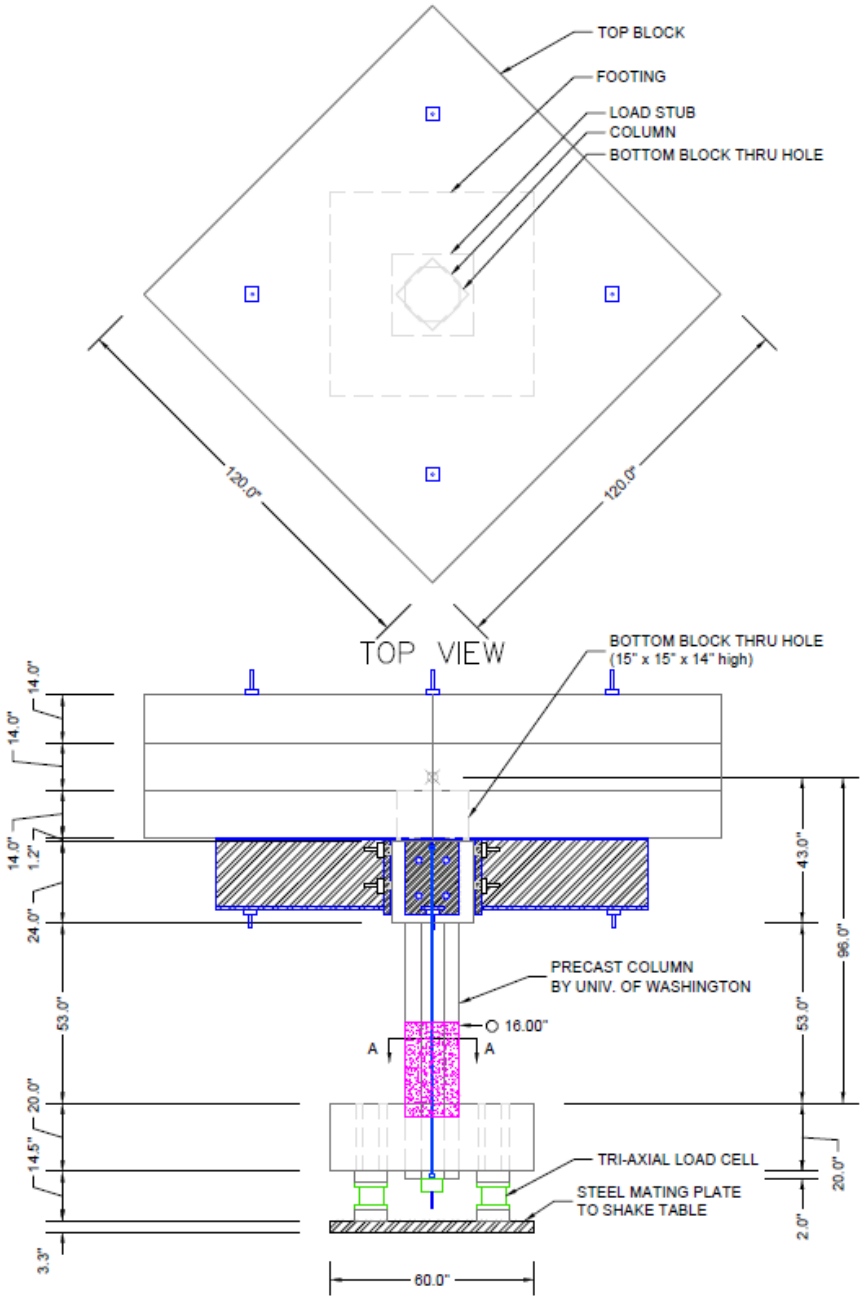

Figure A-3. Unbonded pre-tensioned shake table specimen: elevation

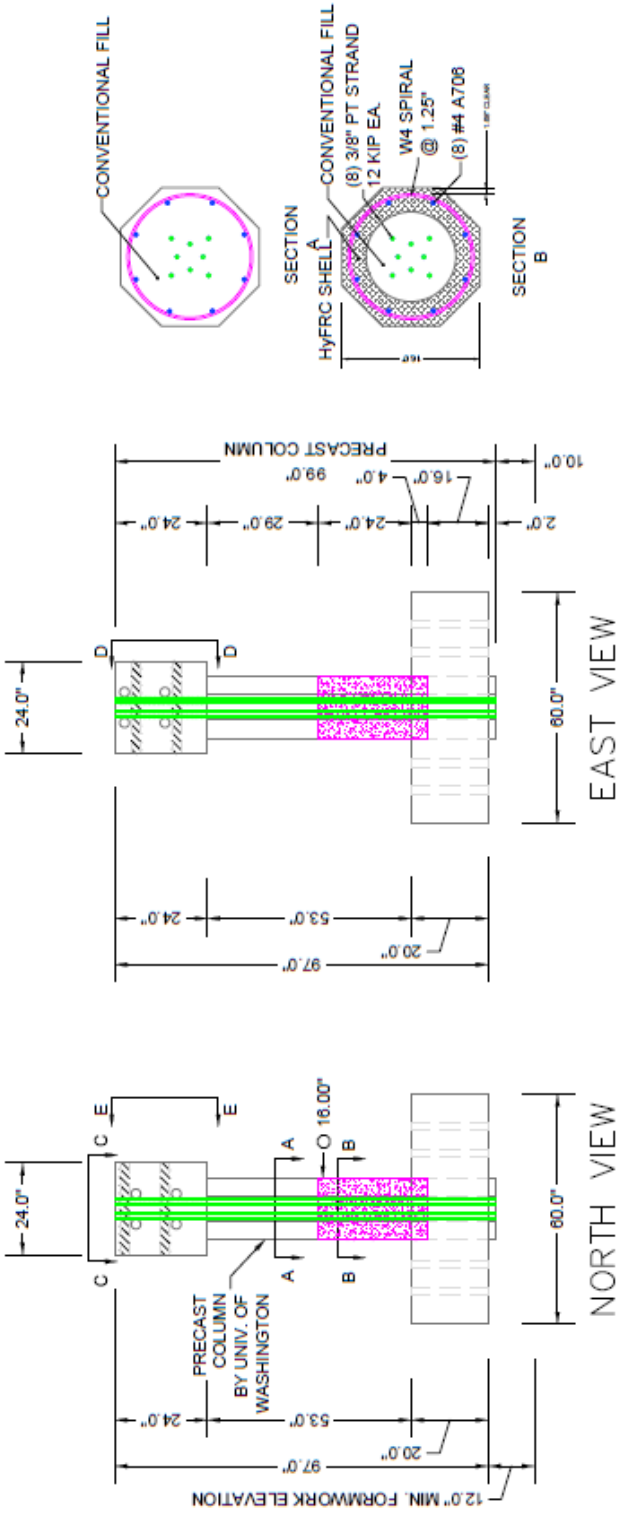

Figure A-4. Unbonded pre-tensioned shake table specimen: elevation and cross-sections

A.3. Unbonded Pre-Tensioned Quasi-Static Column with HyFRC in the Plastic Hinge Region

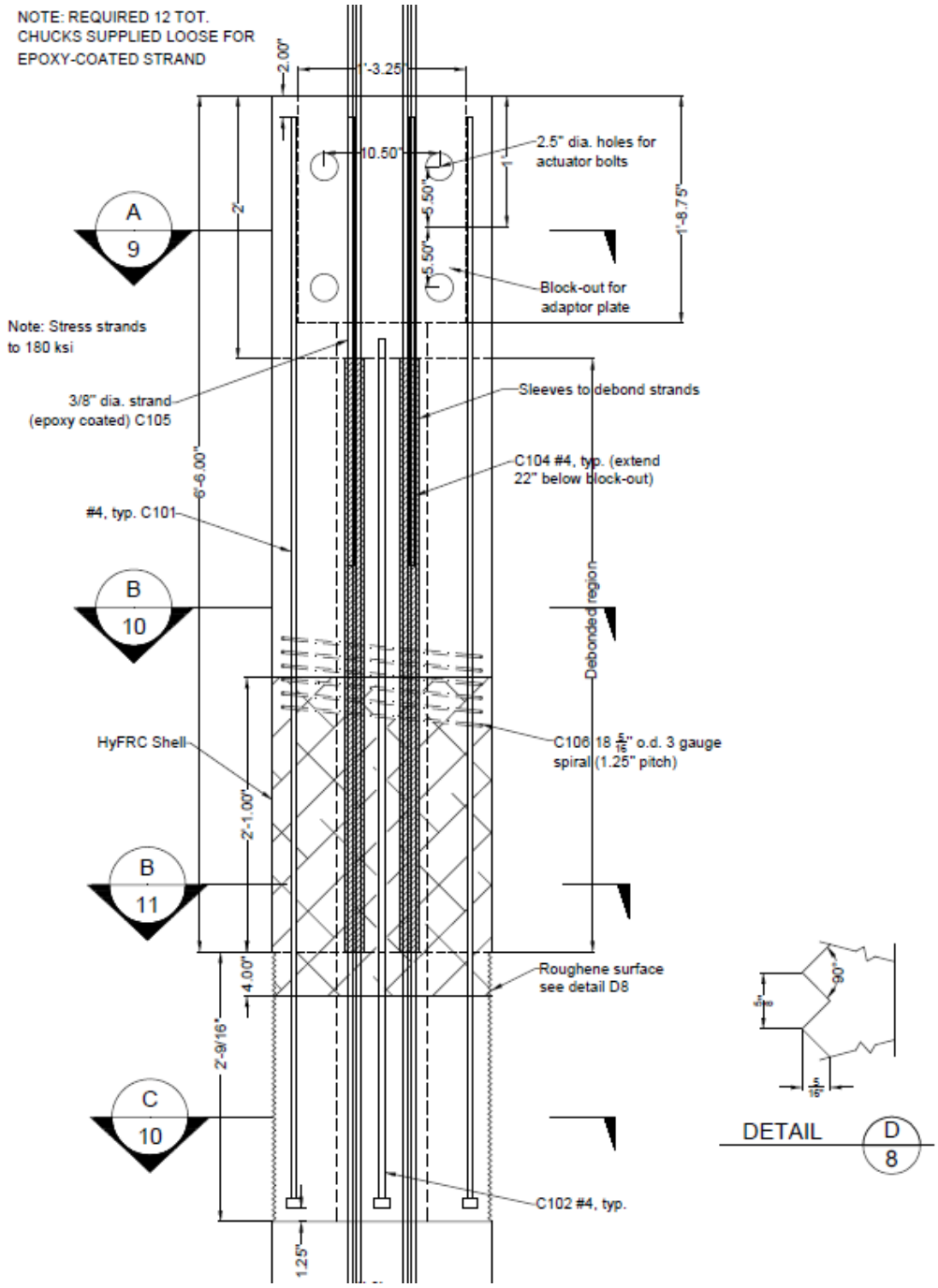

Figure A-5. Unbonded pre-tensioned quasi-static specimen: elevation (Finnsson et al. 2012)

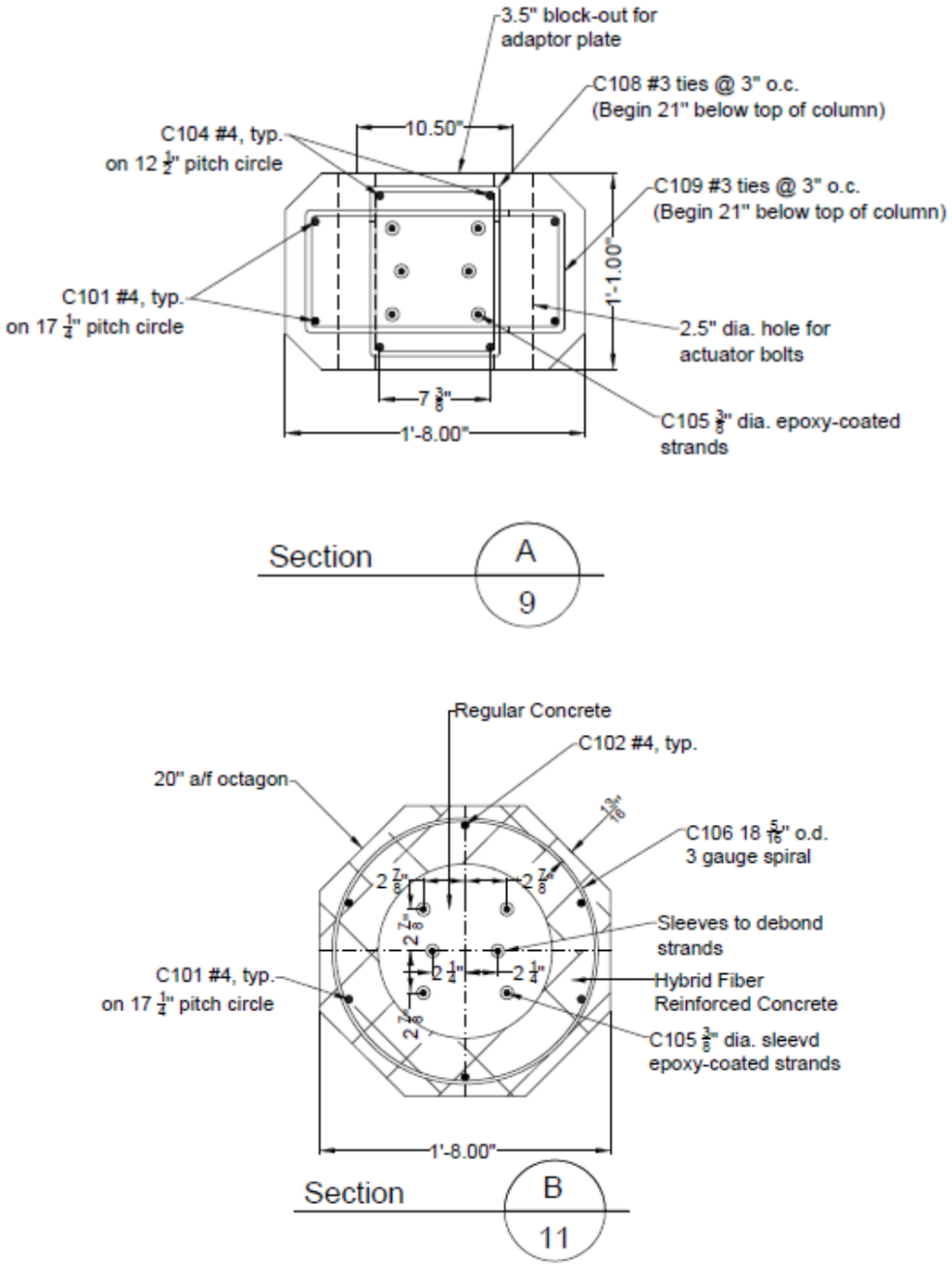

Figure A-6. Unbonded pre-tensioned quasi-static specimen: cross-sections (Finnsson et al. 2012)

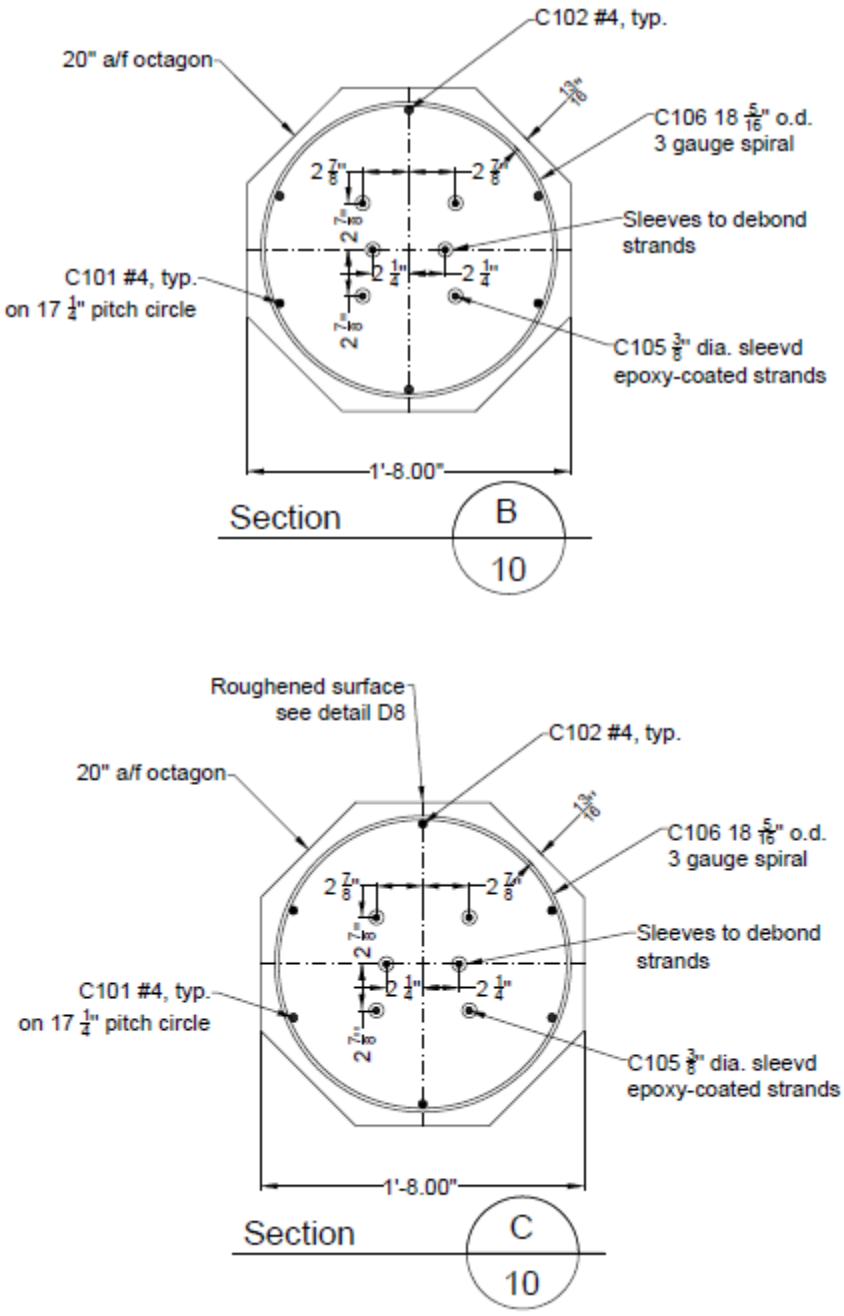

Figure A-6 (cont.). Unbonded pre-tensioned quasi-static specimen: cross-sections (Finnsson et al. 2012)

APPENDIX B: MATERIAL TESTS

B.1 Hybrid Fiber Reinforced Concrete (HyFRC)

Specimen PreT-SF-FIB-SHK consisted of both conventional concrete and Hybrid Fiber Reinforced Concrete (HyFRC), a composite material developed at the University of California-Berkeley. A HyFRC shell was constructed for the column hinge region. Once the HyFRC shell had cured, the reinforcing cage was completed by adding transverse reinforcement outside the shell, it was then placed in a custom-built horizontal octagonal wood form lying inside a prestressing rig. The construction procedure and the dimensions of the shell are discussed in Chapter 6. HyFRC has two types of fibers: Dramix ZP 305 steel and Kuralon RECS 15x8 polymer fibers. The dosages were 4.4% and 0.1% of the total weight, respectively. The mechanical properties of the fibers are discussed in detail in Finnsson (2013). The design compression strength of HyFRC was specified 4.0 ksi. Table B-1 gives the mix proportions of HyFRC for one cubic yard.

Table B-0-1. Mix proportions of HyFRC for one cubic yard[1]

Material	Design Quantity
Fine Aggregate	692.86 lb
Pea Gravel	1,764.19 lb
Cement Type I/II	652.60 lb
Fly Ash	214.29 lb
Water	311.24 lb
Superplasticizer	105.57 oz
Viscosity Modifying Admixture	293.09 oz
Steel Fibers	3121.97 lb
Polymer Fibers	0.37 lb

1. Weights were adjusted for aggregate moisture

Before the HyFRC shell was cast, the air content of the HyFRC was measured according to ASTM C231. The air content was measured to be 5.5%. Cylinders (4-in. by 8-in.) were fabricated according to ASTM C31 and stored in a curing room. Tables B-2 and 0-3 list the HyFRC average compressive strength and average elastic modulus (of two cylinders) at 7 days, 14 days, 28 days, and at one day before the shake table test, respectively. Split cylinder tests were conducted according to ASTM C496 and the result is presented in Table B-4.

Table B-2. HyFRC average compressive strengths

Reference	Specimen	Cylinder Sample	7 Days (psi)	14 Days (psi)	28 Days (psi)	174 Days[1] (psi)
Haraldsson	PreT-SF-FIB-SHK	HyFRC Shell	4,408	5,100	5,778	8,065

1. One day prior to testing

Table B-3. HyFRC average elastic modulus

Reference	Specimen	Cylinder Sample	7 Days (ksi)	14 Days (ksi)	28 Days (ksi)	174 Days[1] (ksi)
Haraldsson	PreT-SF-FIB-SHK	HyFRC Shell	2,334	3,617	3,535	4,775

1. One day prior to testing

Table B-4. HyFRC average split cylinder strength

Reference	Specimen	Cylinder Sample	174 Days[1] (psi)
Haraldsson	PreT-SF-FIB-SHK	HyFRC Shell	1,068

1. One day prior to testing

B.2 Concrete Strength

The design concrete compressive strength for both specimens CIP-SF-REF-SHK and PreT-SF-FIB-SHK was specified as 4.0 ksi, for both the columns and the footings. The course aggregate used was 3/8-in., and the specified slump for the columns and the footings were 8 in. and 5 in., respectively. PreT-SF-FIB-SHK column was fabricated at the University of Washington Structural Laboratory and transported to the Richmond Field Station Earthquake Simulation Laboratory of the University of California at Berkeley, where the footing was cast around it.

Before casting the column in concrete in Specimen PreT-SF-FIB-SHK, the slump and air content were measured. The slump test was conducted according to ASTM C143, and the air content according to ASTM C231. The slump was measured to be 8 in. and the air content was 2.3%. Cylinders were fabricated according to ASTM C31 (6-in. by 12-in. cylinders). The cylinders were stored in a curing room. Table B-5 lists the average compressive strengths of both the column concrete and the footing concrete up to 29 days. Table B-6 lists the average compressive strengths measured at test day. For convenience, the compressive strength for Specimen CIP-SF-REF-SHK on test day is included.

Table B-7 lists the average column concrete elastic modulus measured at 1 day, 3 days, 7 days, 10 days, 14 days, 28 days, and at test day. The elastic modulus test was conducted according ASTM C469. Table B-8 lists the average split cylinder test on test day. The tests were conducted according to ASTM 496.

Table B-5. Concrete compressive strengths up to 29 days for Specimen PreT-SF-FIB-SHK

Reference	Specimen	Cylinder Sample	1 Day (psi)	3 Days (psi)	7 Days (psi)	10 Days (psi)	11 Days (psi)	14 Days (psi)	28 Days (psi)	29 Days (psi)
Haraldsson	PreT-SF-FIB-SHK	Column	2,527	4,844	5,738	6,117	N/A	6,786	7,150	N/A
		Footing	N/A	N/A	N/A	N/A	3,900	N/A	N/A	3,900

Table B-6. Concrete compressive strengths on test day

Reference	Specimen	Cylinder Sample	Days	Test Day (psi)
Schoettler et al. 2013	CIP-SF-REF-SHK	Column	139	3,278
		Footing	143	5,032
Haraldsson	PreT-SF-FIB-SHK	Column	70	7,203
		Footing	38	4,860

Table B-7. Concrete modulus of elasticity

Reference	Specimen	Cylinder Sample	1 Day (psi)	3 Days (psi)	7 Days (psi)	10 Days (psi)	14 Days (psi)	28 Days
Haraldsson	PreT-SF-FIB-SHK	Column	2,665	3,930	4,424	4,810	4,735	N/A

Table B-8. Split cylinder tests

Reference	Specimen	Cylinder Sample	Days	Test Day (psi)
Haraldsson	PreT-SF-FIB-SHK	Column	70	1,068

B.2 Reinforcement

The prototype reinforcement in both specimens CIP-SF-REF-SHK and PreT-SF-FIB-SHK conformed to ASTM A706. All main reinforcement was scaled down appropriately (33 %). Scaling down the transverse reinforcement proved to be difficult since the smallest reinforcement conforming to ASTM A706 is No. 3 bar. A smooth W4-wire conforming to ASTM A82 was used instead. Table B-9 lists the results from the tension tests for both specimens CIP-SF-REF-SHK and PreT-SF-FIB-SHK. The No. 4 longitudinal bars in both specimens exceeded their minimum specified yield stress, f_y, of 60 ksi. The yield strength of the spiral in Specimen PreT-SF-FIB-SHK was measured to be 64 ksi (yield strain was taken to be 0.35% to be consistent with earlier spiral tests at the University of Washington) which is less than the specified strength of 70 ksi for ASTM A82. This low value is attributed to the fact that the spiral was coiled up and

needed to be straightened out before tensile testing. Schoettler et al. 2013 report the wire yield stress of Specimen CIP-SF-REF-SHK was 79.0 ksi, using a 0.20% strain offset method.

Table B-9. Measured mild reinforcement properties

Reference	Specimen	Bar	f_y (ksi)	ε_y (%)	f_u (ksi)	ε_{su} (%)
Schoettler et al. 2013	CIP-SF-REF-SHK	No. 4	63.0	0.44	94.4	11.7
		W4-wire	79.0[1]	0.52	93.9	1.1
Haraldsson	PreT-SF-FIB-SHK	No. 4	68.0	0.52	99.1	10.9
		W4-wire	64.0[2]	0.51	94.6	1.1

1. 0.20% offset method
2. 0.35% offset method

APPENDIX C: SHAKE TABLE RESULTS

C.2 Column Drift-Time Response

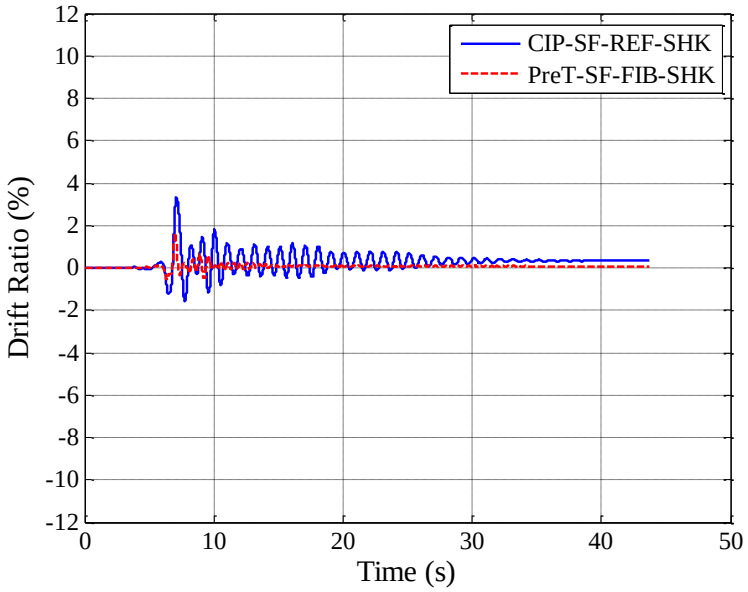

Figure C-1. North-South drift ratio vs time. Earthquake 2

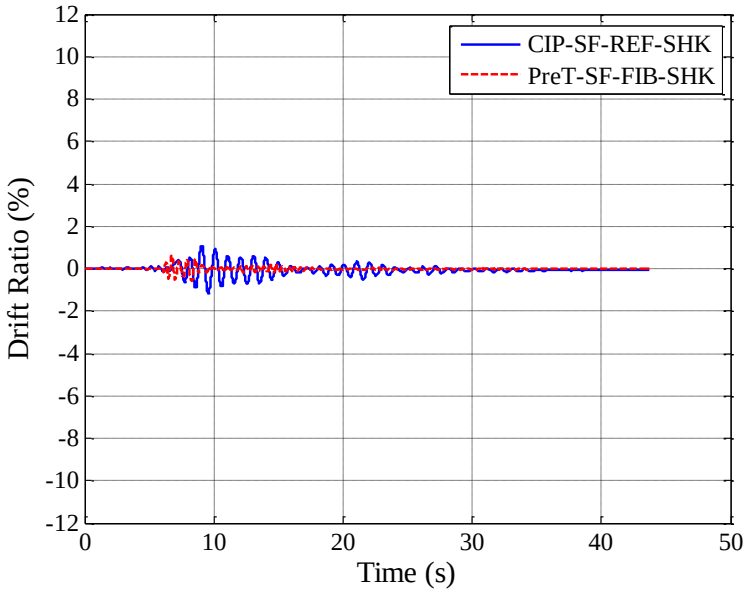

Figure C-2. East-West drift ratio vs time. Earthquake 2

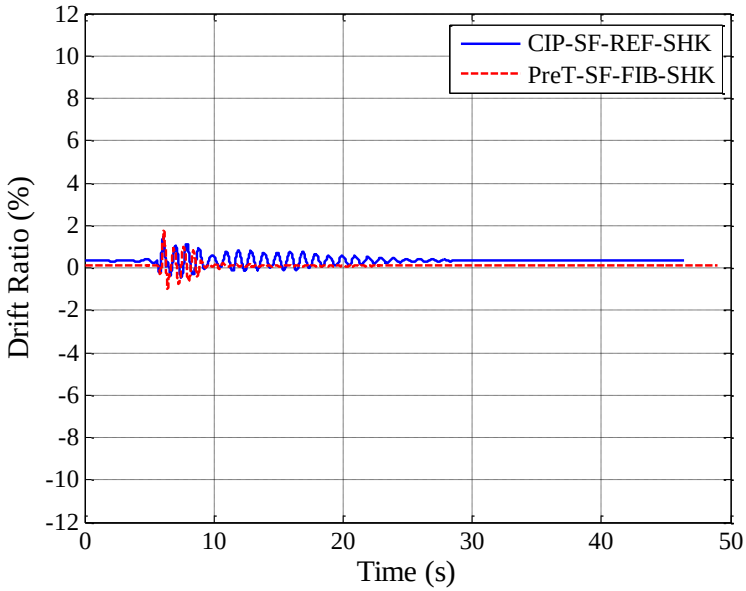

Figure C-3. North-South drift ratio vs time. Earthquake 3

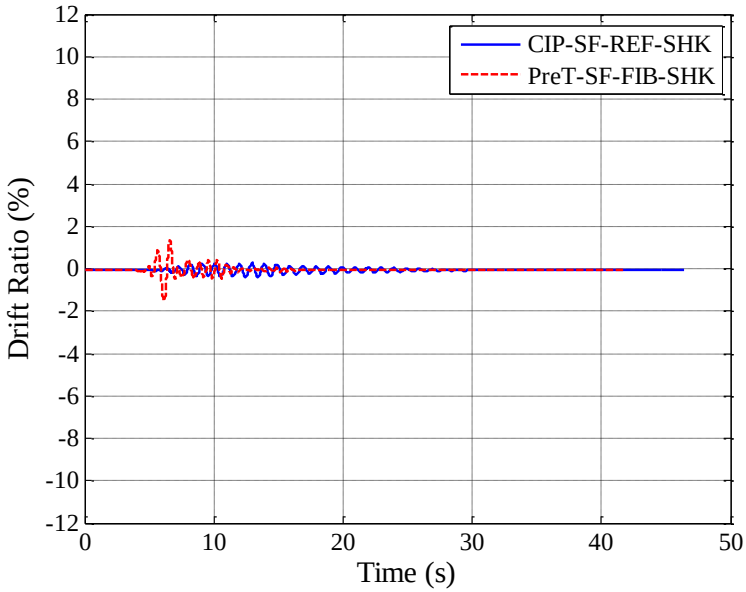

Figure C-4. East-West drift ratio vs time. Earthquake 3

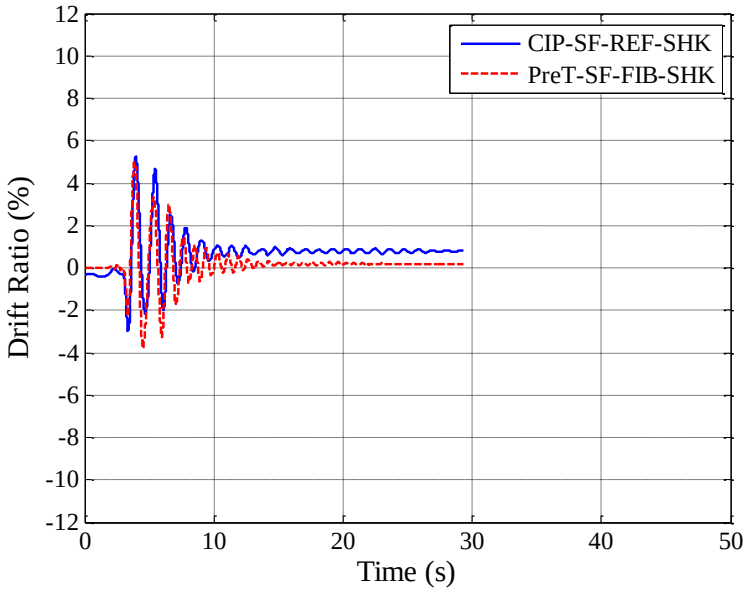

Figure C-**5.** North-South drift ratio vs time. Earthquake 5

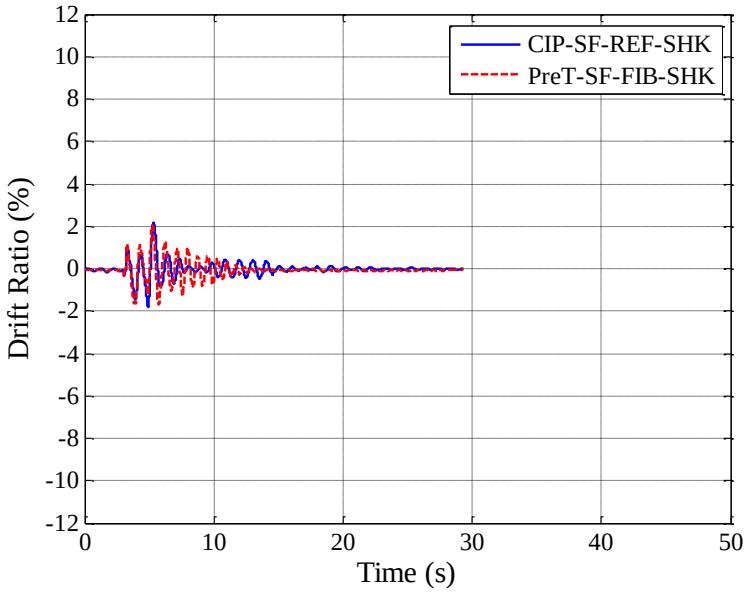

Figure C-6. East-West drift ratio vs time. Earthquake 5

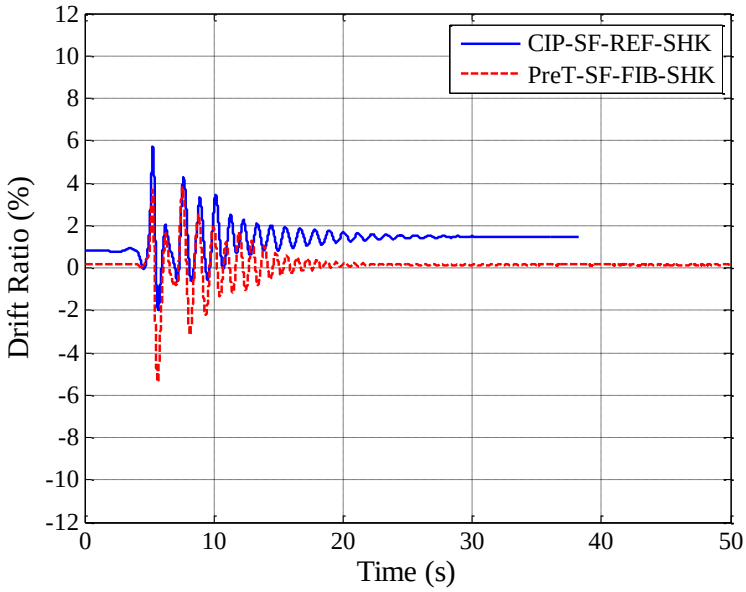

Figure C-7. North-South drift ratio vs time. Earthquake 6

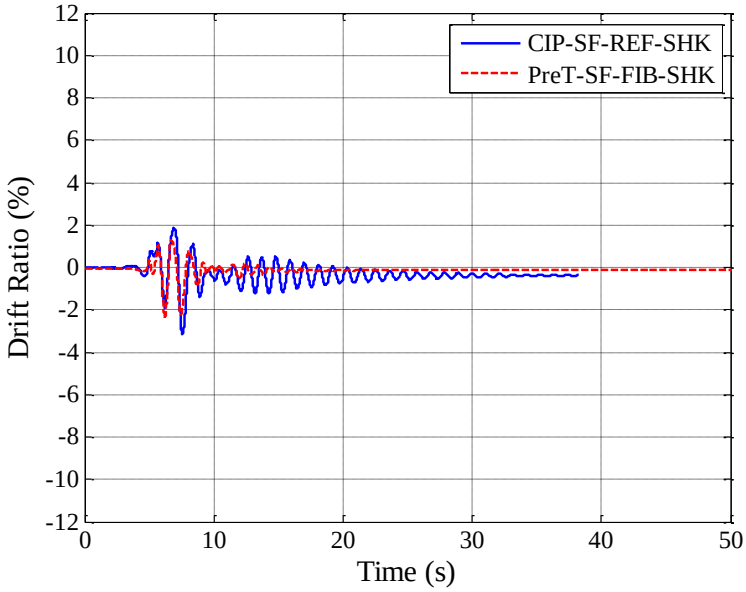

Figure C-8. East-West drift ratio vs time. Earthquake 6

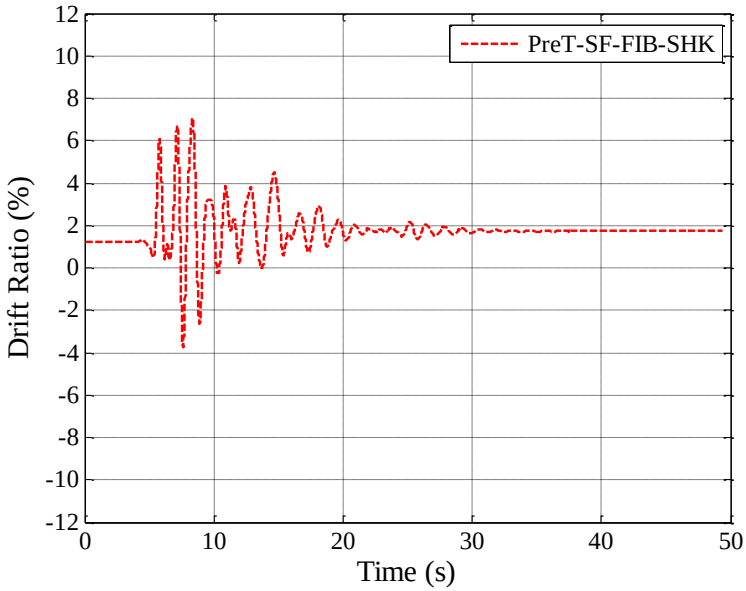

Figure C**-9.** North-South drift ratio vs time. Earthquake 8

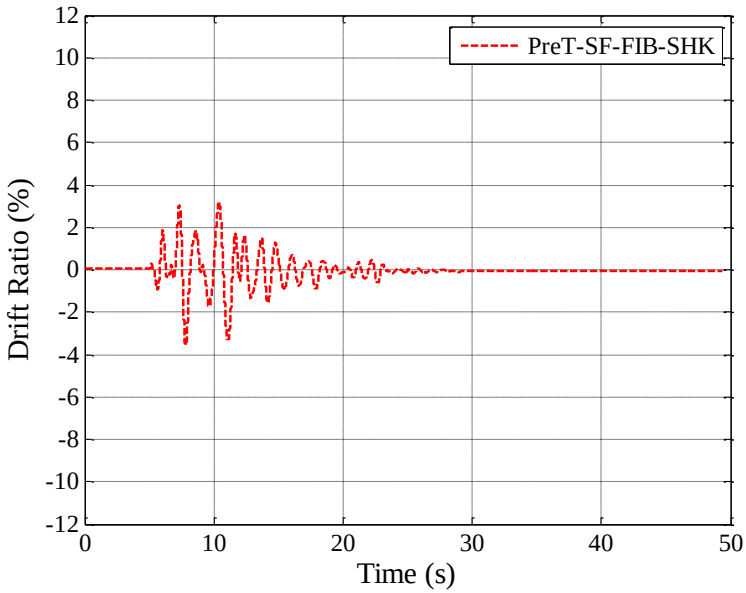

Figure C-10. East-West drift ratio vs time. Earthquake 8

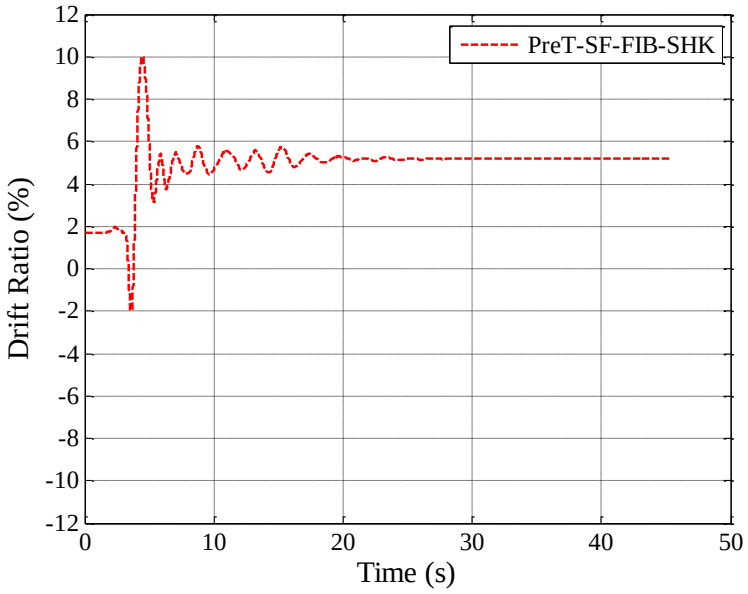

Figure C-11. North-South drift ratio vs time. Earthquake 9

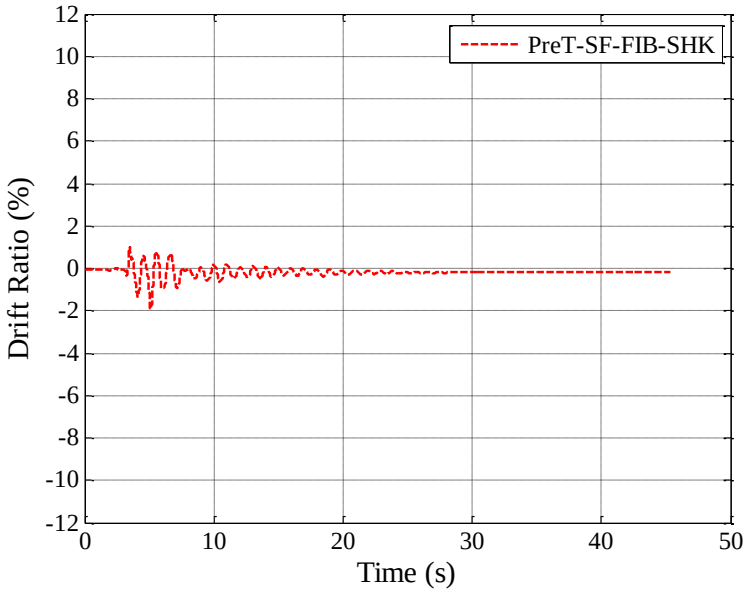

Figure C-12. East-West drift ratio vs time. Earthquake 9

C.2 Moment-Drift Response

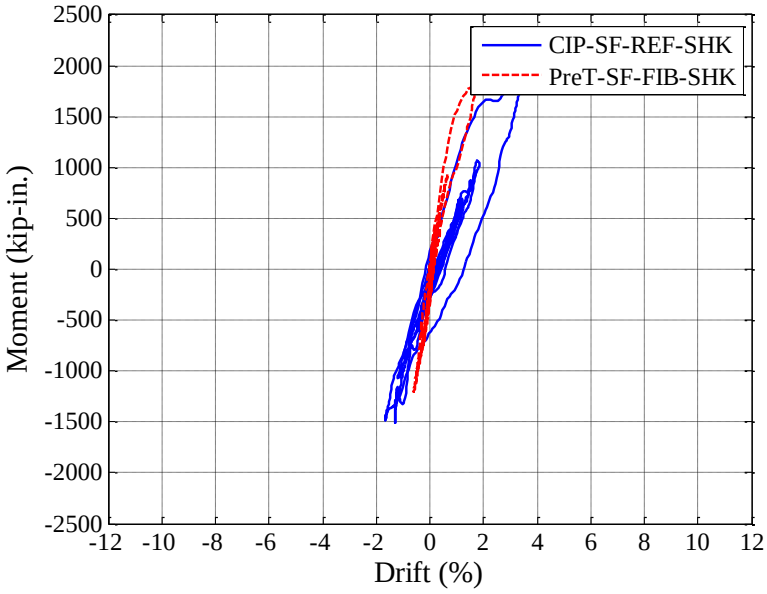

Figure C-13. North-South moment vs drift ratio. Earthquake 2

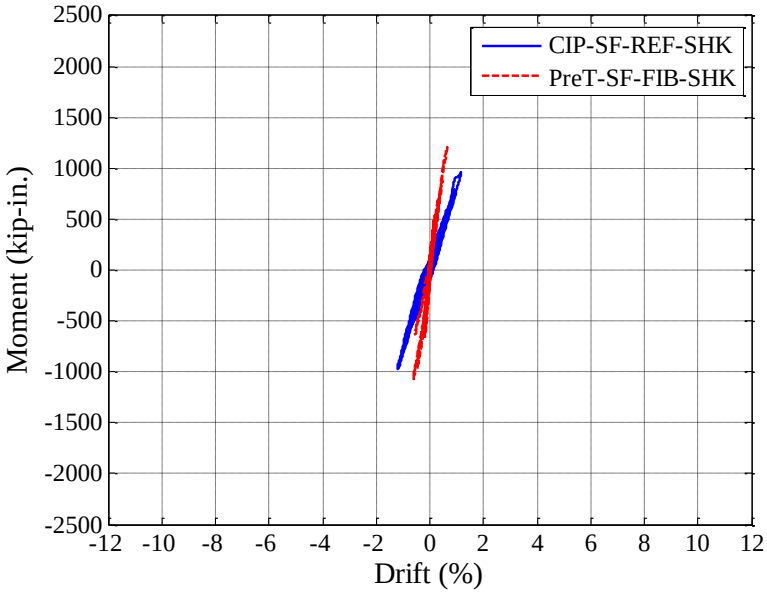

Figure C-14. East-West moment vs drift ratio. Earthquake 2

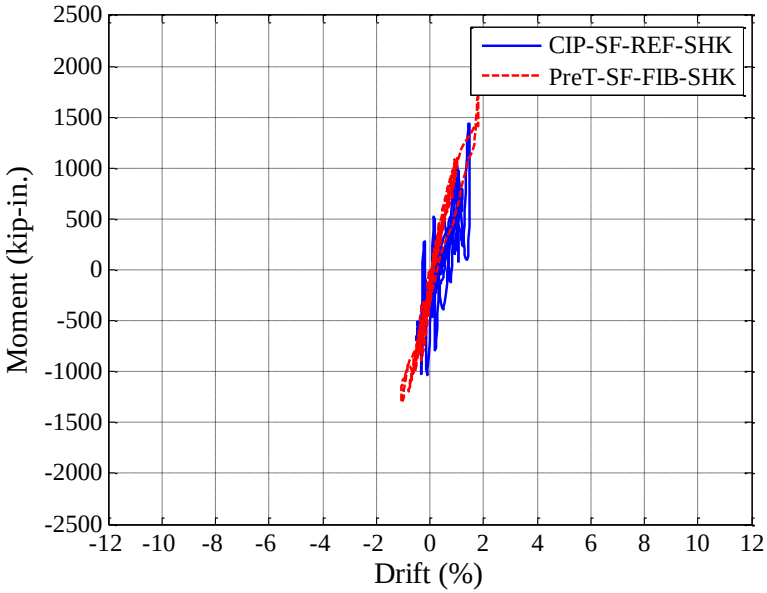

Figure C-15. North-South moment vs drift ratio. Earthquake 3

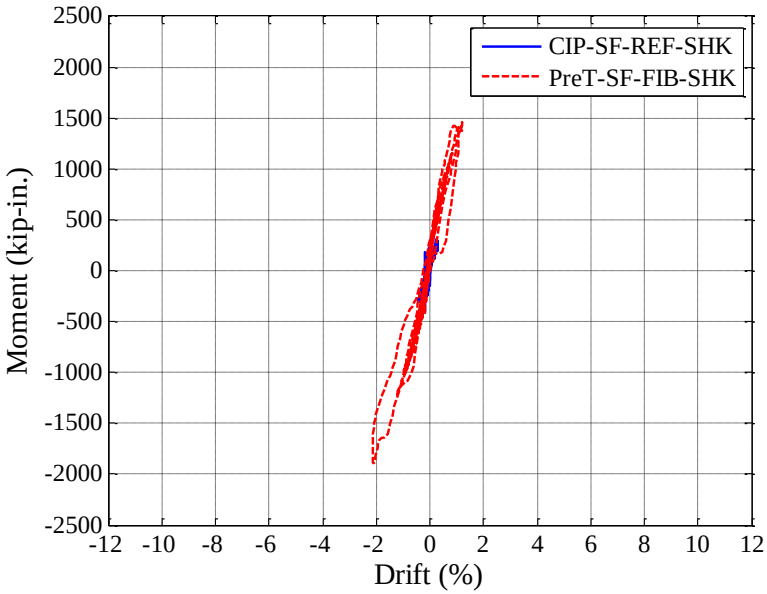

Figure C-16. East-West moment vs drift ratio. Earthquake 3

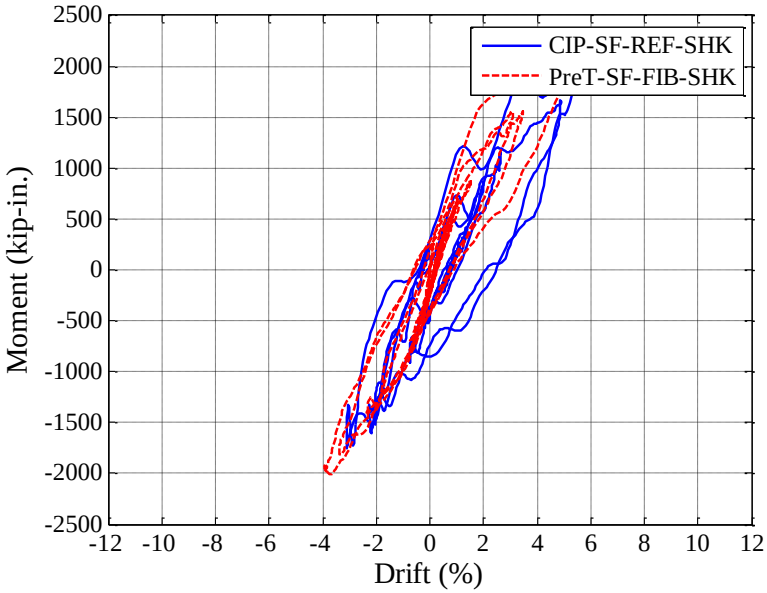

Figure C-17. North-South moment vs drift ratio. Earthquake 5

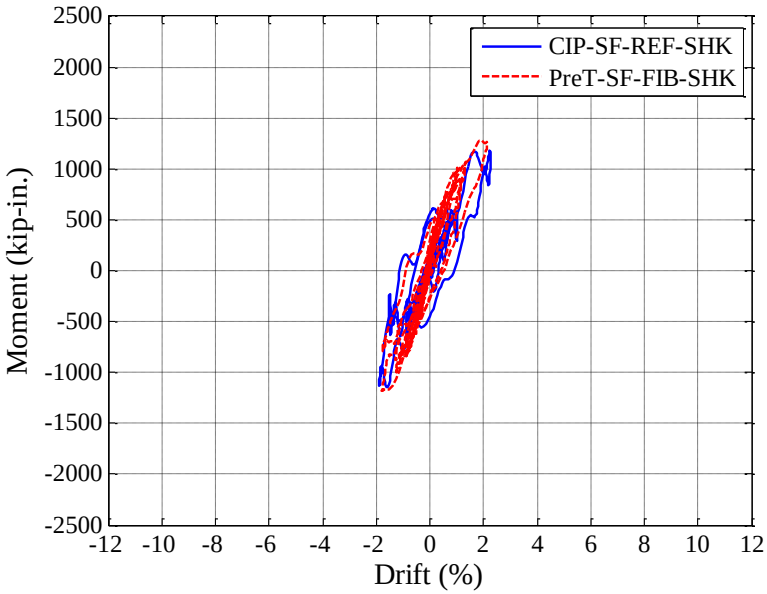

Figure C-18. East-West moment vs drift ratio. Earthquake 5

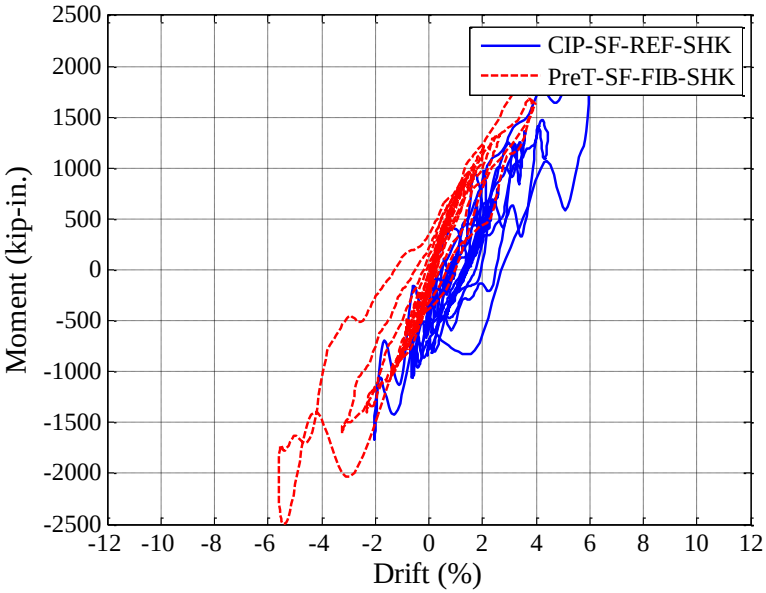

Figure C-19. North-South moment vs drift ratio. Earthquake 6

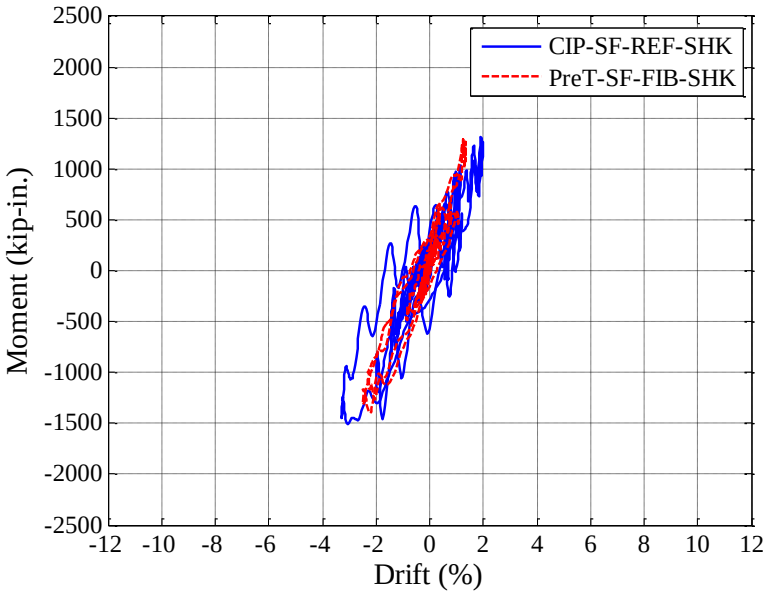

Figure C-20. East-West moment vs drift ratio. Earthquake 6

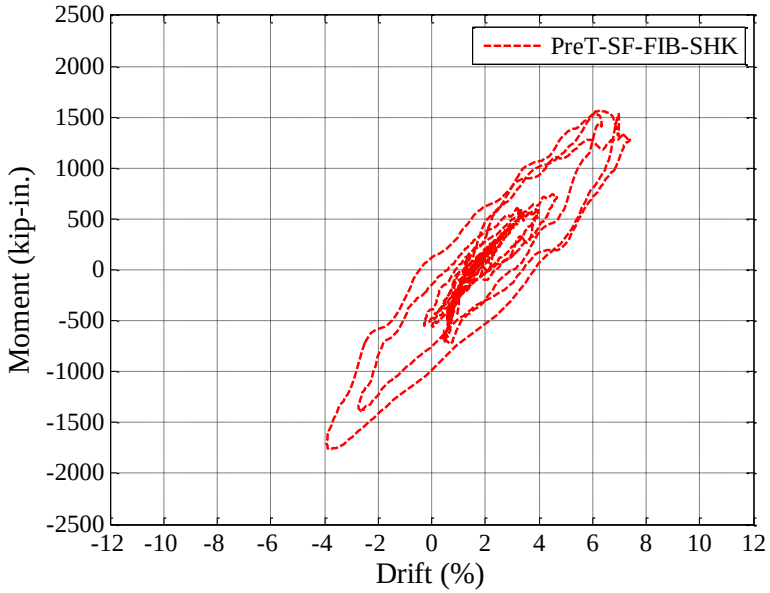

Figure C-21. North-South moment vs drift ratio. Earthquake 8

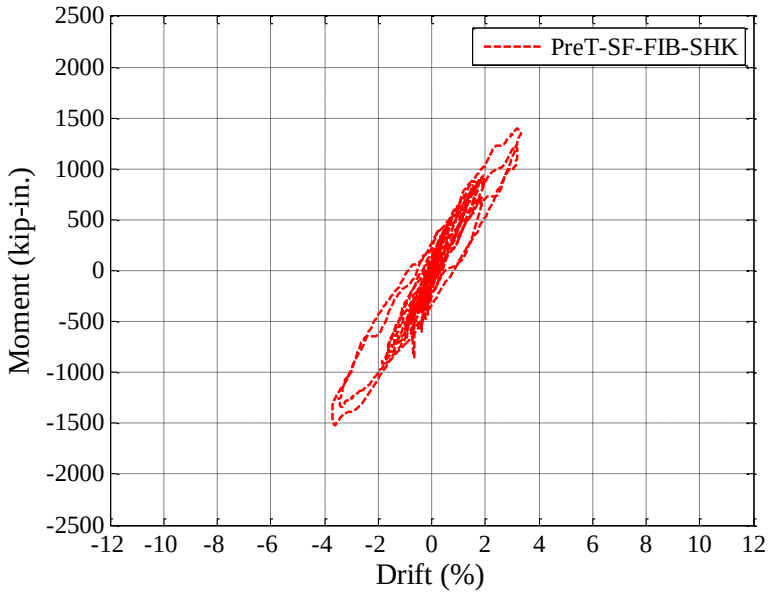

Figure C-22. East-West moment vs drift ratio. Earthquake 6

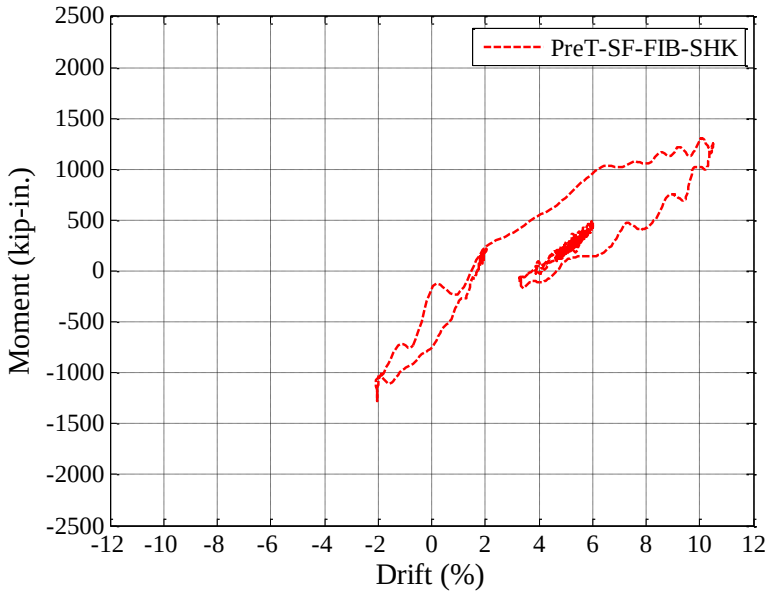

Figure C-23. North-South moment vs drift ratio. Earthquake 9

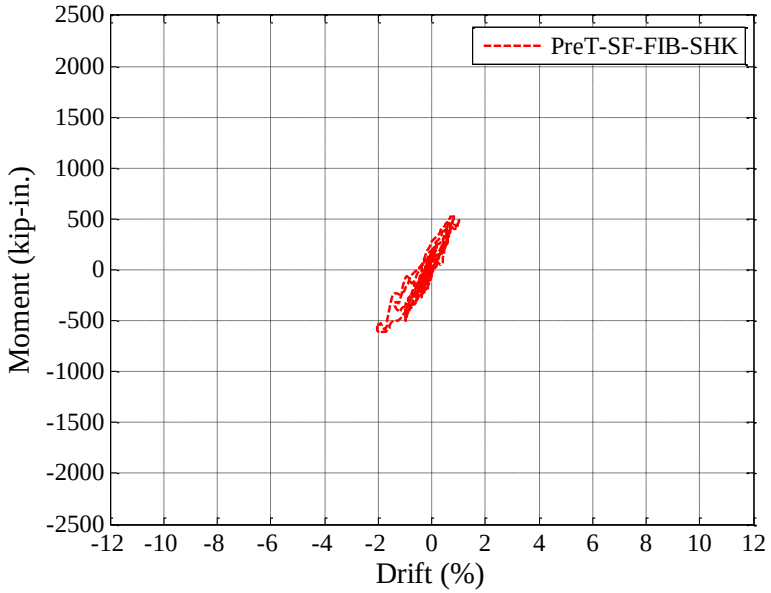

Figure C-24. East-West moment vs drift ratio. Earthquake 9

APPENDIX D: CONCRETE CONSTITUTIVE MODEL

This appendix contains a command description of Concrete08 constitutive material and source codes in C++ for implementation in OpenSees.

D.1 Command Description

The following command is used in OpenSees to construct a uniaxial concrete material object.

uniaxialMaterial Concrete08 $matTag, $fc, $ec, $ecu, $Ec, $fct, $et, $beta, $alfa, $Cmax

$matTag:	integer tag identifying material
$fc:	floating point value defining concrete compressive strength at 28 days
$ec:	floating point value defining concrete strength at maximum strength
$ecu:	floating point value defining concrete strain at crushing strength
$Ec:	floating point value defining initial stiffness
$fct:	floating point value defining the maximum strength of concrete
$et:	floating point value defining ultimate tensile strength of concrete
$beta:	floating point value defining the exponential curve parameter to define the residual stress (as factor of ***$ft***) at ***$etu***
$alfa:	floating point value defining the power of the quotient of the relative strain difference (strain difference from concrete compressive unloading strain to tensile reloading strain) and ***$Cmax***. Only used in calculation if relative strain does not exceed ***$Cmax***
$Cmax:	floating point values defining the largest relative strain that early reloading will occur.

D.2 File: Concrete08.h

```
#ifndef Concrete08_h
#define Concrete08_h

#include <UniaxialMaterial.h>
#define MAT_TAG_Concrete08 6004

class Concrete08 : public UniaxialMaterial
{

 public:

  //  Concrete08 (int tag, double fpc, double eco, double ecu, double Ec0,
double fct);

  Concrete08 (int tag, double fpc, double eco, double ecu, double Ec0, double
fct, double etu, double beta, double alfa, double Cmax);

  Concrete08 ();

  ~Concrete08();
  int setTrialStrain(double strain, double strainRate = 0.0);
  double getStrain(void);
  double getStress(void);
  double getTangent(void);
  double getInitialTangent(void) {return Ec0;}
  int commitState(void);
  int revertToLastCommit(void);
  int revertToStart(void);
  UniaxialMaterial *getCopy(void);
  int sendSelf(int commitTag, Channel &theChannel);
  int recvSelf(int commitTag, Channel &theChannel, FEM_ObjectBroker
&theBroker);
  void Print(OPS_Stream &s, int flag =0);
  double getDamage(void) {return 0;}
  /*// LOWES: add function for use with variable hinge lnegth model*/

  int getMaterialType(void);


  /*// LOWES: end*/

 protected:

private:

  /*** Material Properties ***/
  double fpc;    /*// Compressive strength*/
  double epsc0;  /*// Strain at compressive strength*/
  double epscu;  /*// Strain at crushing strength*/
  double Ec0;    /*// initial tangent*/
```

```
  double fct;   /*// Concrete tensile strength*/
  double etu;   /*// ultimate tensile strain*/
  double beta;  /*// exponential curve parameter, residual stress (as a
factor of ft)*/

  /*** CONVERGED History Variables ***/
  double CminStrain;   // Smallest previous concrete strain (compression)

  double CmaxStrain;
  double CunloadSlope; // Unloading (reloading) slope from CminStrain
  double CendStrain;   // Strain at the end of unloading from CminStrain
  double CcompStrain;   // strain value at which the compression unloading
intersects the
  // zero stress value or the strain value at which tensile reloading starts.
  double CUtenStress;      // tensile stress value at which unloading begins
  double CUtenSlope;      // unloading tensile slope value
  double Ceps1;
  double Cf1;
  double Ceps2;
  double Ceps3;
  double Ceps4;
  double Cf4;
  /*** CONVERGED State Variables ***/
  double Cstrain;
  double Cstress;
  double Ctangent;

  /*// Don't need Ctangent other than for revert and sendSelf/recvSelf

  // Storing it is better than recomputing it!!!*/

  double TminStrain;
  /*** TRIAL History Variables ***/

  double TmaxStrain;
  double TunloadSlope;
  double TendStrain;
  double TcompStrain;
  double TUtenStress;
  double TUtenSlope;

  double Teps1;
  double Tf1;
  double Teps2;
  double Teps3;
  double Teps4;
  double Tf4;
  double alfa;
  double Cmax;


  /*** TRIAL State Variables ***/
```

```
  double Tstrain;
  double Tstress;
  double Ttangent; /*// Not really a state variable, but declared here for
convenience*/
  //double TempTensionStrain;

  void CompReload(void);
  void CompEnvelope(void);
  void setCompUnloadEnv(void);
  void TensReload(void);
  void TensEnvelope(double e);
  void setTenUnload(double e);

};

#endif
```

D.3 File: Concrete08.cpp

```
/* ****************************************************************** **
**    OpenSees - Open System for Earthquake Engineering Simulation    **
**          Pacific Earthquake Engineering Research Center             **
**                                                                     **
**                                                                     **
** (C) Copyright 1999, The Regents of the University of California    **
** All Rights Reserved.                                                **
**                                                                     **
** Commercial use of this program without express permission of the   **
** University of California, Berkeley, is strictly prohibited.  See   **
** file 'COPYRIGHT'  in main directory for information on usage and   **
** redistribution,  and for a DISCLAIMER OF ALL WARRANTIES.           **
**                                                                     **
** Developed by:                                                       **
**   Frank McKenna (fmckenna@ce.berkeley.edu)                          **
**   Gregory L. Fenves (fenves@ce.berkeley.edu)                        **
**   Filip C. Filippou (filippou@ce.berkeley.edu)                      **
**                                                                     **
** ****************************************************************** */

// $Revision: 1.1 $
// $Date: 2005/09/23 22:51:27 $
// $Source: /usr/local/cvs/OpenSees/SRC/material/uniaxial/Concrete08.cpp,v $


// File: ~/material/Concrete08.cpp
//
// Written: N.Mitra (nmitra@u.washington.edu)
// Created: 09/04
// Revision: A
//
```

```
// Description: This file contains the class implementation for
// Concrete08 based on Popovics pre and post compression curve
// for concrete.
//

// What: "@(#) Concrete08.C, revA"
// Revision 1. Adding in exponential tensile envelope for concrete
// Dt. 05-16-05
//// Revision 1. Adding in exponential tensile envelope for concrete - M.
Mitra 2005
//// Revision 2. Adding Substances In the Cracks (SITC) per Stanton and
McNiven (1979) - M. Berry //// 2007
//// Revision 3. Modify the SITC feature so it can reload in compression when
in tensile region //// (Tstrain > 0) per Stanton and McNiven (1979) - O.
Haraldsson 2013
//// Revision 4. Modify tensile envelope so it can transfer along the strain
axis(i.e. concrete //// loads first in compression, when cracks are closed it
goes into tension given its tensile //// capacity has not been reached) - O.
Haraldsson 2013
//// Reference:  Stanton, J.F. and McNiven, H.D. (1979). "The Development of
a Mathematical Model //// to Predict the Flexural Response of Reinforced
Concrete Beams to Cyclic Loads, Using System //// Identification."

//// Earthquake Engineering Research Center, Berkeley, CA.
//// Dt. 05-16-05

#include <elementAPI.h>
#include "Concrete08.h"
#include <Vector.h>
#include <Matrix.h>
#include <Channel.h>
#include <Information.h>
#include <math.h>
#include <float.h>

#ifdef _USRDLL
#define OPS_Export extern "C" _declspec(dllexport)
#elif _MACOSX
#define OPS_Export extern "C" __attribute__((visibility("default")))
#else
#define OPS_Export extern "C"
#endif

OPS_Export void *
OPS_Concrete08()
{
  // Pointer to a uniaxial material that will be returned
  UniaxialMaterial *theMaterial = 0;

  //
  // parse the input line for the material parameters
  //
```

```
  int    iData[1];
  double dData[9];
  int numData;

  numData = 1;
  if (OPS_GetIntInput(&numData, iData) != 0) {
    opserr << "WARNING invalid uniaxialMaterial Concrete08 tag" << endln;
    return 0;
  }

 numData = 9;
 if (OPS_GetDoubleInput(&numData, dData) != 0) {
  opserr << "WARNING invalid material input(s)";
  return 0;
}

  theMaterial = new Concrete08(iData[0], dData[0], dData[1], dData[2],
dData[3], dData[4], dData[5], dData[6], dData[7], dData[8]);


  return theMaterial;
}



Concrete08::Concrete08
(int tag, double FPC, double EPSC0, double EPSCU, double EC0, double FCT,
double ETU, double BETA, double ALFA, double CMAX)
  :UniaxialMaterial(tag, MAT_TAG_Concrete08),
   fpc(FPC), epsc0(EPSC0), epscu(EPSCU), Ec0(EC0), fct(FCT), etu(ETU),
   CminStrain(0.0), CendStrain(0.0), CcompStrain(0.0), CUtenStress(FCT),
   Cstrain(0.0), Cstress(0.0), CmaxStrain(0.0), Ceps1(0.0), Ceps2(0.0),
   Ceps3(0.0), Ceps4(0.0), Cf4(0.0), Cf1(0.0),alfa(ALFA), Cmax(CMAX),
beta(BETA)
{

  // Make all concrete parameters negative
  if (fpc > 0.0 || epsc0 > 0.0 || epscu > 0.0) {
    opserr << "error: negative values required for concrete stress-strain
model" << endln;
  }

  if (fct < 0.0) {
    fct = 0.0;
    opserr << "warning: fct less than 0.0 so the tensile response part is
being set to 0" << endln;
  }
  Ctangent = Ec0;
  CunloadSlope = Ec0;
  CUtenSlope = Ec0;
```

```
  // Set trial values
  this->revertToLastCommit();
}

Concrete08::~Concrete08()
{
  // Does nothing
}



int
Concrete08::setTrialStrain (double strain, double strainRate)
{
  /* // Set trial strain*/
  this->revertToLastCommit();
  Tstrain = strain;

  TminStrain = CminStrain;
  TmaxStrain = CmaxStrain;
  TendStrain = CendStrain;
  TunloadSlope = CunloadSlope;
  TUtenSlope = CUtenSlope;
  Teps1 = Ceps1;
  Teps2 = CendStrain;
  Teps3 = Ceps3;
  Teps4 = Ceps4;
  Tf1 = Cf1;
  Tf4 = Cf4;

  /*// Determine change in strain from last converged state*/
  double dStrain = Tstrain - Cstrain;

  if (fabs(dStrain) < DBL_EPSILON)
    return 0;
  double TmaxStrainTemp = Tstrain - Teps2 + DBL_EPSILON;
  /*// Calculate the trial state given the change in strain
  // determineTrialState (dStrain);*/

  //TunloadSlope = CunloadSlope;
  //TUtenSlope = CUtenSlope;

  if (dStrain <= 0.0) {
    /*// Material can be either in Compression-Reloading // or Tension-
Unloading state. */

    //Teps2 = Ceps2;
    //TmaxStrain = CmaxStrain;
    //Teps2 = CendStrain;
    //double TmaxStrainTemp = Tstrain - Teps2 + DBL_EPSILON;

    if (TmaxStrainTemp >= 0.0 && TmaxStrain <= etu) {
```

```
    /*// Material is in Tension-Unloading State*/

    Ttangent = TUtenSlope;
    Tstress = TmaxStrainTemp * TUtenSlope;

  } else {
    /*// Material is in Compression-Reloading State*/

    TminStrain = CminStrain;
    TendStrain = CendStrain;
    TunloadSlope = CunloadSlope;

    Teps1 = Ceps1;
    Teps2 = Ceps2;
    Teps3 = Ceps3;
    Teps4 = Ceps4;
    Tf1 = Cf1;
    Tf4 = Cf4;

    CompReload();
  }

} else {

  /*// Material can be either in Compression-Unloading
  // or Tension-Reloading State.*/

  //TmaxStrain = CmaxStrain;
  //Teps2 = CendStrain;

  double tempTeps2 = -Cstress / TunloadSlope + Cstrain;

  if (Tstrain <= TendStrain && Tstrain < 0.0) {

    Ttangent = TunloadSlope;
    Tstress = Cstress + Ttangent * (Tstrain - Cstrain);
    Teps4 = Tstrain;
    Tf4 = Tstress;

  }   else if (Tstrain <= tempTeps2 && Cstress < 0.0) {

    Ttangent = TunloadSlope;
    Tstress = Cstress + Ttangent * (Tstrain - Cstrain);
    Teps4 = Tstrain;
    Tf4 = Tstress;

  } else {

    TmaxStrain = CmaxStrain;
    //double TmaxStrainTemp = Tstrain - Teps2 + DBL_EPSILON;
    if (TmaxStrainTemp < 0.0) {
```

```
      opserr << "PROBLEM" << TmaxStrainTemp << endln;
      }
      if (TmaxStrainTemp <= TmaxStrain && TmaxStrain <= etu) {

      Tstress = TmaxStrainTemp * CUtenSlope;
      Ttangent = CUtenSlope;

      } else {

      if (TmaxStrainTemp > TmaxStrain) {
        TmaxStrain = TmaxStrainTemp;
        //opserr << "TmaxStrain" << TmaxStrainTemp << endln;
      }

      TensEnvelope(TmaxStrainTemp);
      setTenUnload(TmaxStrainTemp);
      }
    }

  }
  // opserr << "Teps2 " << Teps2 << endln;
  /*opserr << "TendStrain " << TendStrain << endln;
    opserr << "Teps3 " << Teps3 << endln;
    opserr << "Teps4 " << Teps4 << endln;
    opserr << "TmaxStrain " << TmaxStrain << endln;
  */
  return 0;

}

void
Concrete08::CompReload(void)
{

  if (Tstrain <= TminStrain) {

    TminStrain = Tstrain;
    //opserr << "her 1" << endln;
    /*// Determine point on envelope*/
    CompEnvelope ();
    setCompUnloadEnv ();
    Teps1 = Tstrain;
    Tf1 = Tstress;
  }

  else if (TmaxStrain <= etu) {
    Ttangent = TunloadSlope;
    Tstress = Ttangent * (Tstrain - Teps2);
    //opserr << "her 2" << endln;
  }

  else if (Tstrain <= Teps4) {
```

```
    if (Teps1 == Teps4) {opserr << "may be propblem" << endln;
    } else {

      Ttangent = (Tf1 - Tf4) / (Teps1 - Teps4);

      if (Ttangent == 0) {
      Ttangent = 0.0000000001 * Ec0;
      }
      //opserr << "her 3" << endln;
      //  opserr << "may be propblem" << Ttangent << endln;
      Tstress = Tf4 + Ttangent*(Tstrain-Teps4);
    }
  } else {
    //opserr << "her 4" << endln;
    Tstress = 0.0;
    Ttangent = 0.0000000001 * Ec0;
  }
}


void
Concrete08::CompEnvelope(void)

{
  if (Tstrain >= epscu) {
    double Esec = fpc/epsc0;
    double r2 = 0.0;
    if (Esec >= Ec0) {
      r2 = 400.0;
    } else {
      r2 = Ec0/(Ec0-Esec);
    }
    double eta = Tstrain/epsc0;
    Tstress = fpc*eta*r2/(r2-1+pow(eta,r2));
    Ttangent = fpc*r2*(r2-1)*(1-pow(eta,r2))/(pow((r2-
1+pow(eta,r2)),2)*epsc0);
    //      opserr << "Cstate 1: Compression Envelope" << endln;
  } else {
    Tstress = 0.0;
    Ttangent = 0.0000000001 * Ec0;
  }

}

void
Concrete08::setCompUnloadEnv(void)
{

  double tempStrain = TminStrain;

  if (tempStrain < epscu)
```

```
    tempStrain = epscu;

  double eta = tempStrain/epsc0;

  double ratio = 0.707*(eta-2.0) + 0.834; // unloading parameter as per
Karsan-Jirsa

  if (eta < 2.0)
    ratio = 0.145*eta*eta + 0.13*eta;

  TendStrain = ratio*epsc0;

  double temp1 = TminStrain - TendStrain;

  double temp2 = Tstress/Ec0;

  if (temp1 > -DBL_EPSILON) { // temp1 should always be negative
    TunloadSlope = Ec0;
    //double Teps2 = -Cstress / TunloadSlope + Cstrain;
  }
  else if (temp1 <= temp2) {
    TendStrain = TminStrain - temp1;
    TunloadSlope = Tstress/temp1;
    //double Teps2 = -Cstress / TunloadSlope + Cstrain;
  }
  else {
    TendStrain = TminStrain - temp2;
    TunloadSlope = Ec0;
    //double Teps2 = -Cstress / TunloadSlope + Cstrain;
  }


}


//void Concrete08::TensReload()
//
//{
//    //opserr << "her 6" << endln;
//  TensEnvelope (double e);
//  setTenUnload (double e);
//}


void
Concrete08::TensEnvelope(double e)
{

  // double TempTensionStrain = Tstrain - Teps2 + DBL_EPSILON;

  double ect = fct / Ec0;
  double fctn = fct * (TunloadSlope / Ec0);
```

```
  if (e <= ect && TmaxStrain <= etu) {

    Tstress = e  * TunloadSlope;
    Ttangent = TunloadSlope;

  } else if (TmaxStrain > etu) {

    Tstress = 0.0;
    Ttangent = 0.0000000001 * Ec0;
    Tf4 = 0.0;

  } else {

    Tstress = fctn * pow(beta, (e- ect) / (etu - ect));
    Ttangent = fctn * pow(beta, (e - ect) / (etu - ect)) * log(beta) / (etu -
ect);
  }
}


void
Concrete08::setTenUnload(double e)
{
  //double TempTensionStrain = Tstrain - Teps2 + DBL_EPSILON;
  double ect = fct / Ec0;

  if (e <= etu && TmaxStrain <= etu) {

    TUtenStress = Tstress;
    TUtenSlope = Tstress / e;

  } else {
    TUtenStress = 0.0;
    TUtenSlope = 0.0000000001 * Ec0;

    Teps3 = Tstrain;
    double diff;
    if ((Teps3 - Teps2) > Cmax) {
      diff = Cmax;
    } else {

      double temp = (Teps3-Teps2) / Cmax;
      double tempsee = pow(temp,alfa);
      diff = (Teps3 - Teps2) * tempsee;
    }

    Teps4 = Teps2 + diff;
  }

}
```

```
double
Concrete08::getStress (void)
{
  return Tstress;
}



double
Concrete08::getStrain (void)
{
  return Tstrain;
}



double
Concrete08::getTangent (void)
{
  return Ttangent;
}



int
Concrete08::commitState (void)
{

  /*// History variables*/
  CminStrain = TminStrain;
  CmaxStrain = TmaxStrain;
  CunloadSlope = TunloadSlope;
  CendStrain = TendStrain;
  CUtenSlope = TUtenSlope;
  Ceps1 = Teps1;
  Ceps2 = Teps2;
  Ceps3 = Teps3;
  Ceps4 = Teps4;
  Cf1 = Tf1;
  Cf4 = Tf4;

  /*// State variables*/
  Cstrain = Tstrain;
  Cstress = Tstress;
  Ctangent = Ttangent;

  return 0;

}
```

```
int
Concrete08::revertToLastCommit (void)
{

  /*// Reset trial history variables to last committed state*/

  TminStrain = CminStrain;
  TmaxStrain = CmaxStrain;
  TendStrain = CendStrain;
  TunloadSlope = CunloadSlope;
  TUtenSlope = CUtenSlope;

  Teps1 = Ceps1;
  Teps2 = Ceps2;
  Teps3 = Ceps3;
  Teps4 = Ceps4;
  Tf1 = Cf1;
  Tf4 = Cf4;



  /*// Recompute trial stress and tangent*/
  Tstrain = Cstrain;
  Tstress = Cstress;
  Ttangent = Ctangent;

  return 0;

}



int
Concrete08::revertToStart (void)
{
  /*// History variables*/

  CminStrain = 0.0;
  CmaxStrain = 0.0;
  CunloadSlope = Ec0;
  CendStrain = 0.0;
  CUtenSlope = Ec0;

  Ceps1 = 0.0;
  Ceps2 = 0.0;
  Ceps3 = 0.0;
  Ceps4 = 0.0;
  Cf1 = 0.0;
  Cf4 = 0.0;


  /*// State variables*/
```

```
  Cstrain = 0.0;
  Cstress = 0.0;
  Ctangent = Ec0;

  /*// Reset trial variables and state*/
  this->revertToLastCommit();

  return 0;

}



UniaxialMaterial*
Concrete08::getCopy ()
{

  Concrete08* theCopy = new Concrete08(this->getTag(),

                                fpc, epsc0, epscu, Ec0, fct, etu, beta, alfa,
Cmax);



  /*// Converged history variables*/

  theCopy->CminStrain = CminStrain;
  theCopy->CmaxStrain = CmaxStrain;
  theCopy->CunloadSlope = CunloadSlope;
  theCopy->CendStrain = CendStrain;
  theCopy->CUtenSlope = CUtenSlope;
  theCopy->Ceps1 = Ceps1;
  theCopy->Ceps2 = Ceps2;
  theCopy->Ceps3 = Ceps3;
  theCopy->Ceps4 = Ceps4;
  theCopy->Cf1 = Cf1;
  theCopy->Cf4 = Cf4;


  /*// Converged state variables*/
  theCopy->Cstrain = Cstrain;
  theCopy->Cstress = Cstress;
  theCopy->Ctangent = Ctangent;

  return theCopy;

}



int
```

```
Concrete08::sendSelf (int commitTag, Channel& theChannel)
{
  int res = 0;
  static Vector data(13);
  data(0) = this->getTag();



   /* Material properties*/
  data(1) = fpc;
  data(2) = epsc0;
  data(3) = epscu;
  data(4) = Ec0;
  data(5) = fct;
  data(20) = alfa;
  data(21) = Cmax;



  /*// History variables from last converged state*/

  data(6) = CminStrain;
  data(7) = CunloadSlope;
  data(8) = CendStrain;
  data(9) = CUtenSlope;
  data(10) = CmaxStrain;



  /*// State variables from last converged state*/
  data(11) = Cstrain;
  data(12) = Cstress;
  data(13) = Ctangent;

  data(14) = Ceps1;
  data(15) = Ceps2;
  data(16) = Ceps3;
  data(17) = Ceps4;
  data(18) = Cf1;
  data(19) = Cf4;



  /*// Data is only sent after convergence, so no trial variables
  // need to be sent through data vector*/


  res = theChannel.sendVector(this->getDbTag(), commitTag, data);
  if (res < 0)
    opserr << "Concrete08::sendSelf() - failed to send data\n";

  return res;
```

```
}


int
Concrete08::recvSelf (int commitTag, Channel& theChannel,
                  FEM_ObjectBroker& theBroker)
{

  int res = 0;

  static Vector data(13);

  res = theChannel.recvVector(this->getDbTag(), commitTag, data);



  if (res < 0) {

    opserr << "Concrete08::recvSelf() - failed to receive data\n";

    this->setTag(0);

   }

  else {

    this->setTag(int(data(0)));



    /*// Material properties */

    fpc = data(1);
    epsc0 = data(2);
    epscu = data(3);
    Ec0 = data(4);
    fct = data(5);
    alfa = data(20);
    Cmax = data(21);


    /*// History variables from last converged state*/

    CminStrain = data(6);
    CunloadSlope = data(7);
    CendStrain = data(8);
    CcompStrain = data(9);
    CmaxStrain = data(10);
```

```
    /*// State variables from last converged state*/
    Cstrain = data(11);
    Cstress = data(12);
    Ctangent = data(13);

    Ceps1 = data(14);
    Ceps2 = data(15);
    Ceps3 = data(16);
    Ceps4 = data(17);
    Cf1 = data(18);
    Cf4 = data(19);



    /*// Set trial state variables*/
      this->revertToLastCommit();
  }
  return res;
}



void Concrete08::Print(OPS_Stream& s, int flag)
{

  s << "Concrete08, tag: " << this->getTag() << endln;
  s << "  fpc: " << fpc << endln;
  s << "  epsc0: " << epsc0 << endln;
  s << "  fct: " << fct << endln;
  s << "  epscu: " << epscu << endln;
  s << "  Ec0:  " << Ec0 << endln;
  s << "  etu:  " << etu << endln;
  s << "  beta: " << beta << endln;
  s << " alfa: " << alfa << endln;
  s << " Cmax: " << Cmax << endln;
}



/*// LOWES: add functions for variable hinge-length model*/

int
Concrete08::getMaterialType(void)
{
  return 0;
}

/*// LOWES: end*/
```

APPENDIX E: NUMERICAL RESULTS

The following legends are used throughout the figures from E-1 through E-16 using input parameters listed in tables 9-5 and 9-6 in Chapter 9:

- Steel02-BE := Recommended Steel02 parameters from Berry and Eberhard (2007)
- Steel02-OH := Optimized Steel02 parameters with early concrete reloading as developed in this thesis.
- ReinforcingSteel-BE := Optimized ReinforcingSteel from Berry and Eberhard (2007) parameters with no early concrete reloading.
- ReinforcingSteel-OH := Optimized ReinforcingSteel parameters with early concrete reloading as developed in this thesis.
- EI_{eff}^{BE} := Effective stiffness per Berry and Eberhard (2007)
- EI_{eff}^{EE} := Effective stiffness per Elwood and Eberhard (2006)

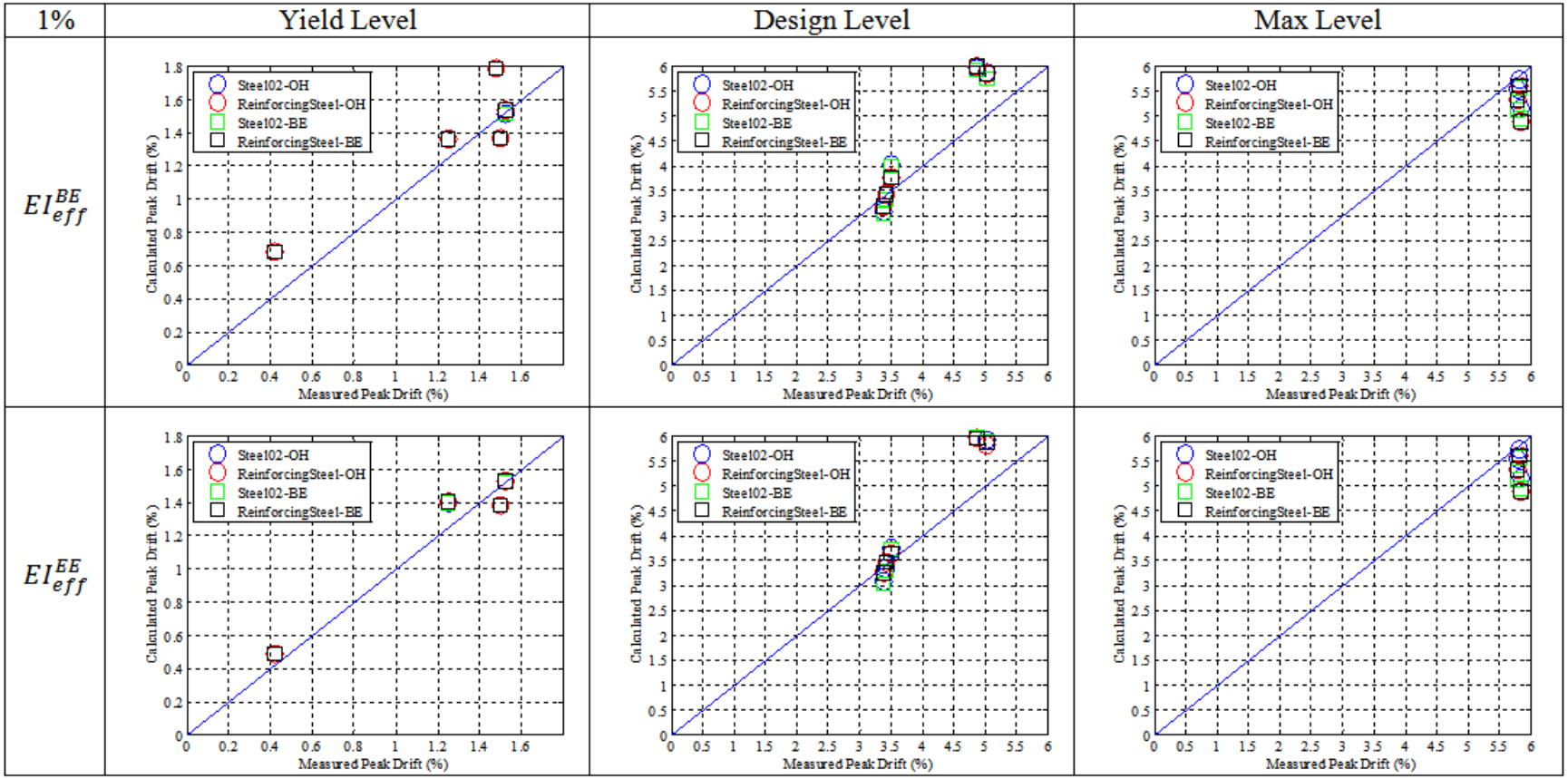

Figure E-1. Comparison of measured and calculated peak displacement using 1% viscous damping

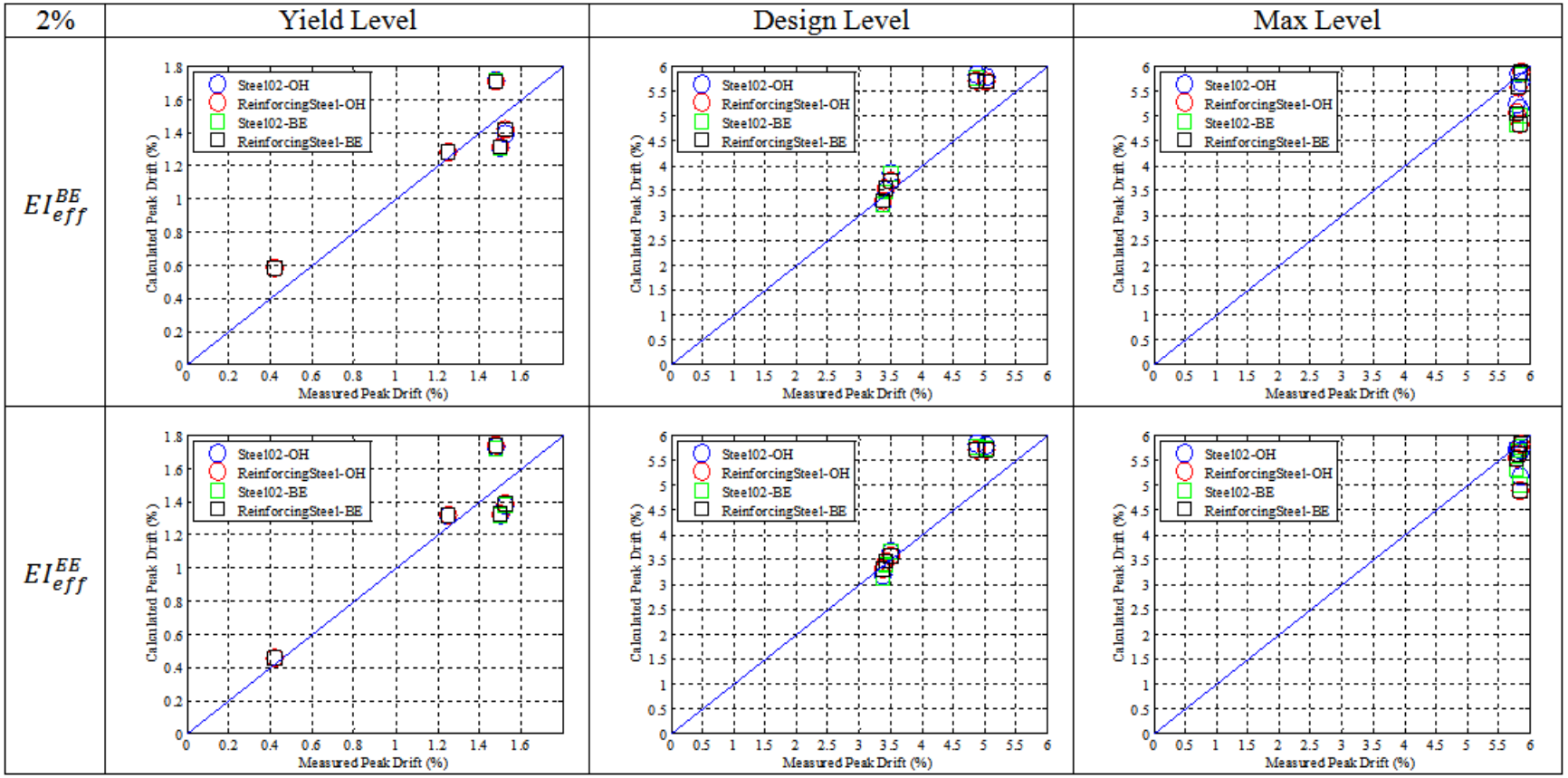

Figure E-2. Comparison of measured and calculated peak displacements using 2% viscous damping

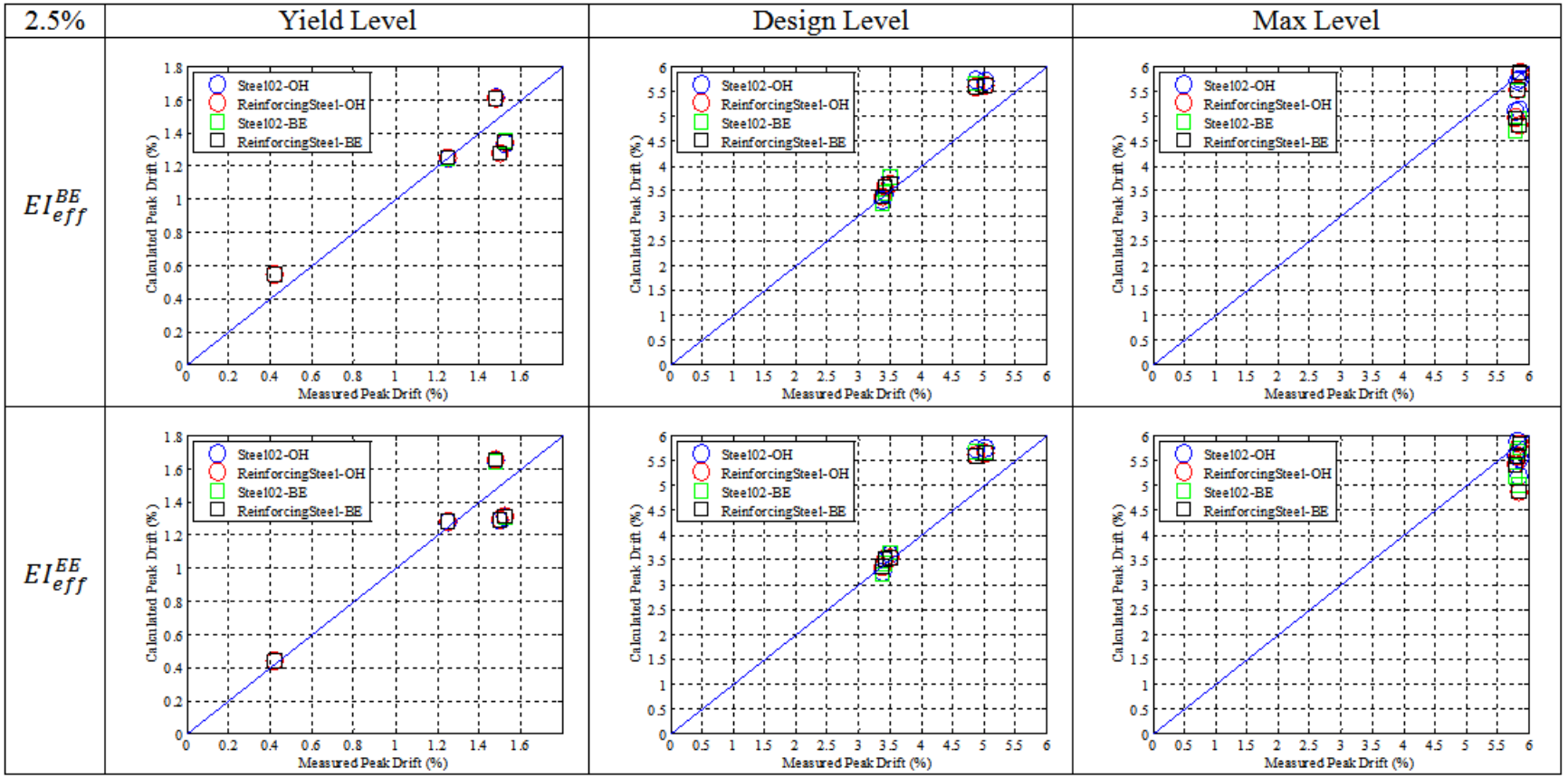

Figure E-3. Comparison of measured and calculated peak displacements using 2.5% viscous damping

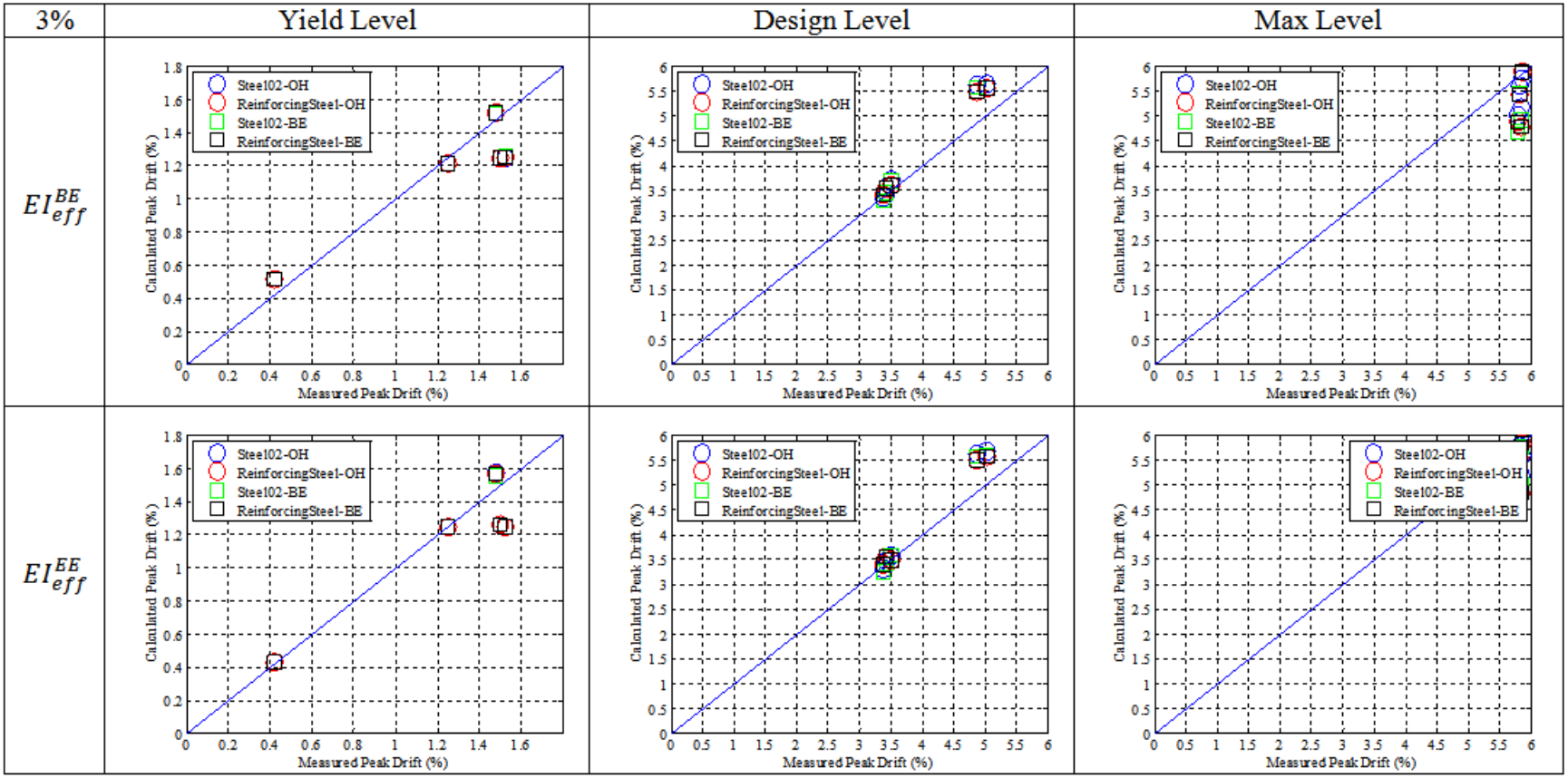

Figure E-4. Comparison of measured and calculated peak displacements using 3.0% viscous damping

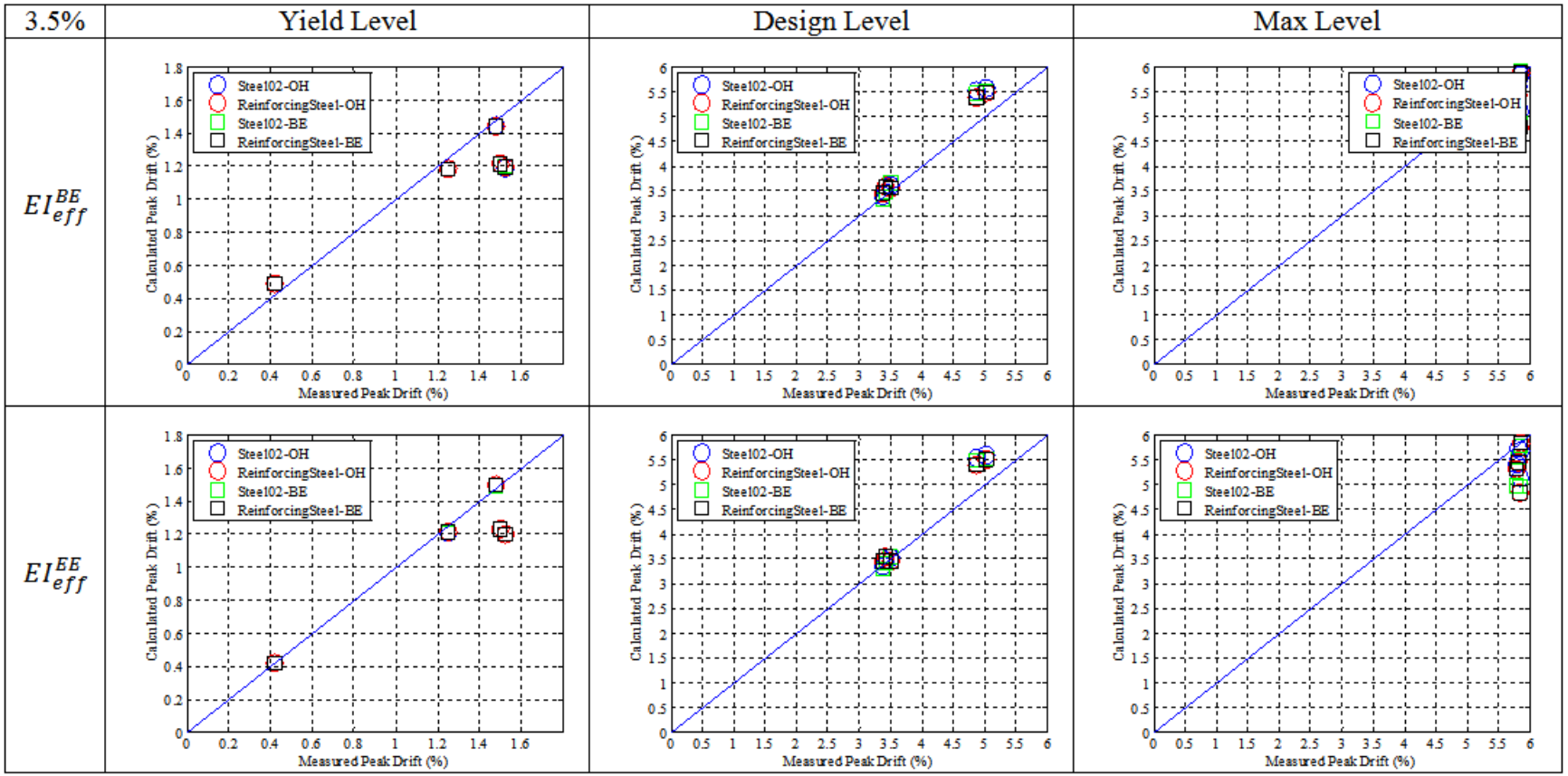

Figure E-5. Comparison of measured and calculated peak displacements using 3.5 % viscous damping

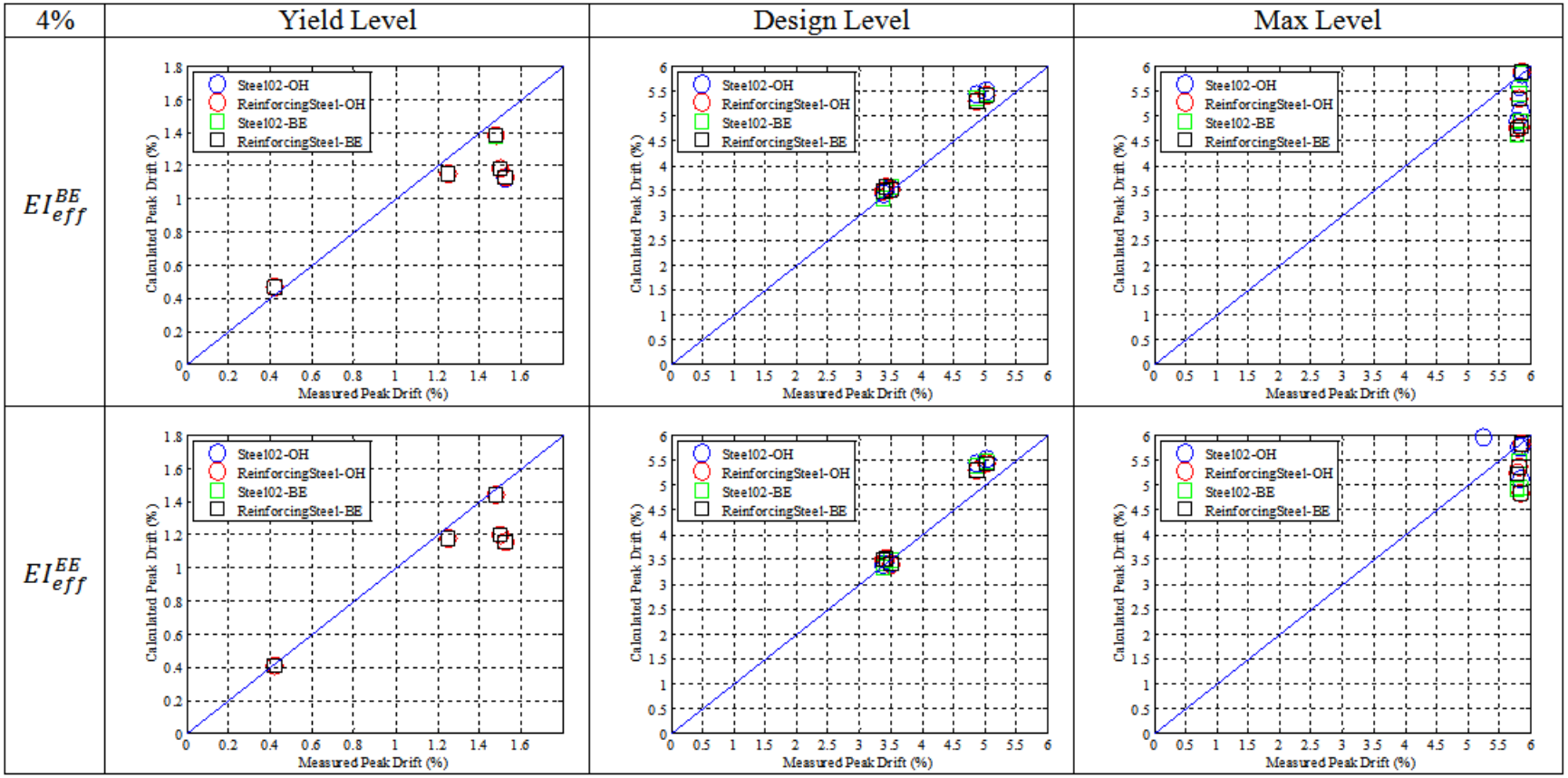

Figure E-6. Comparison of measured and calculated peak displacements using 4.0 % viscous damping

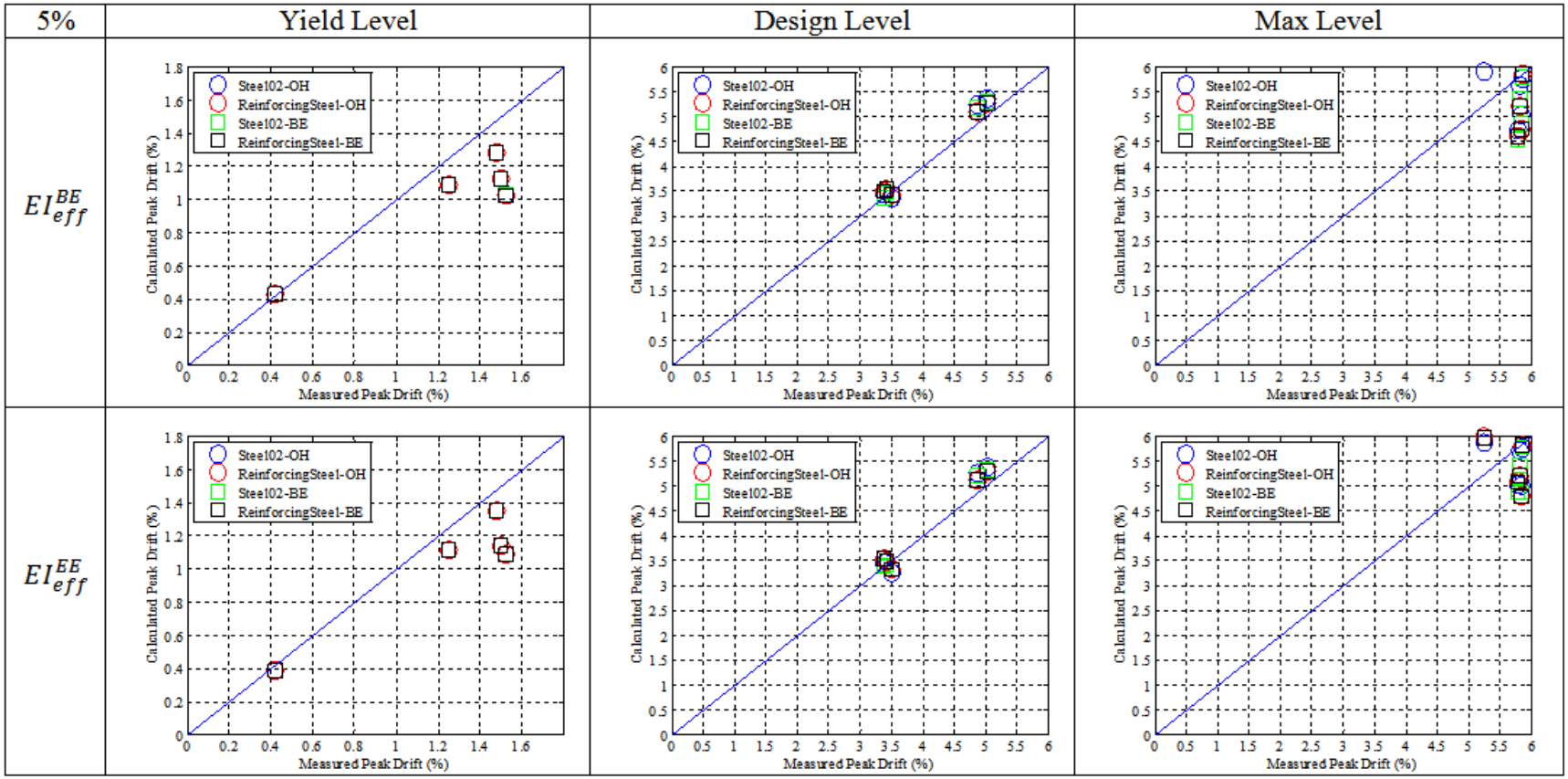

Figure E-7. Comparison of measured and calculated peak displacements using 5.0 % viscous damping

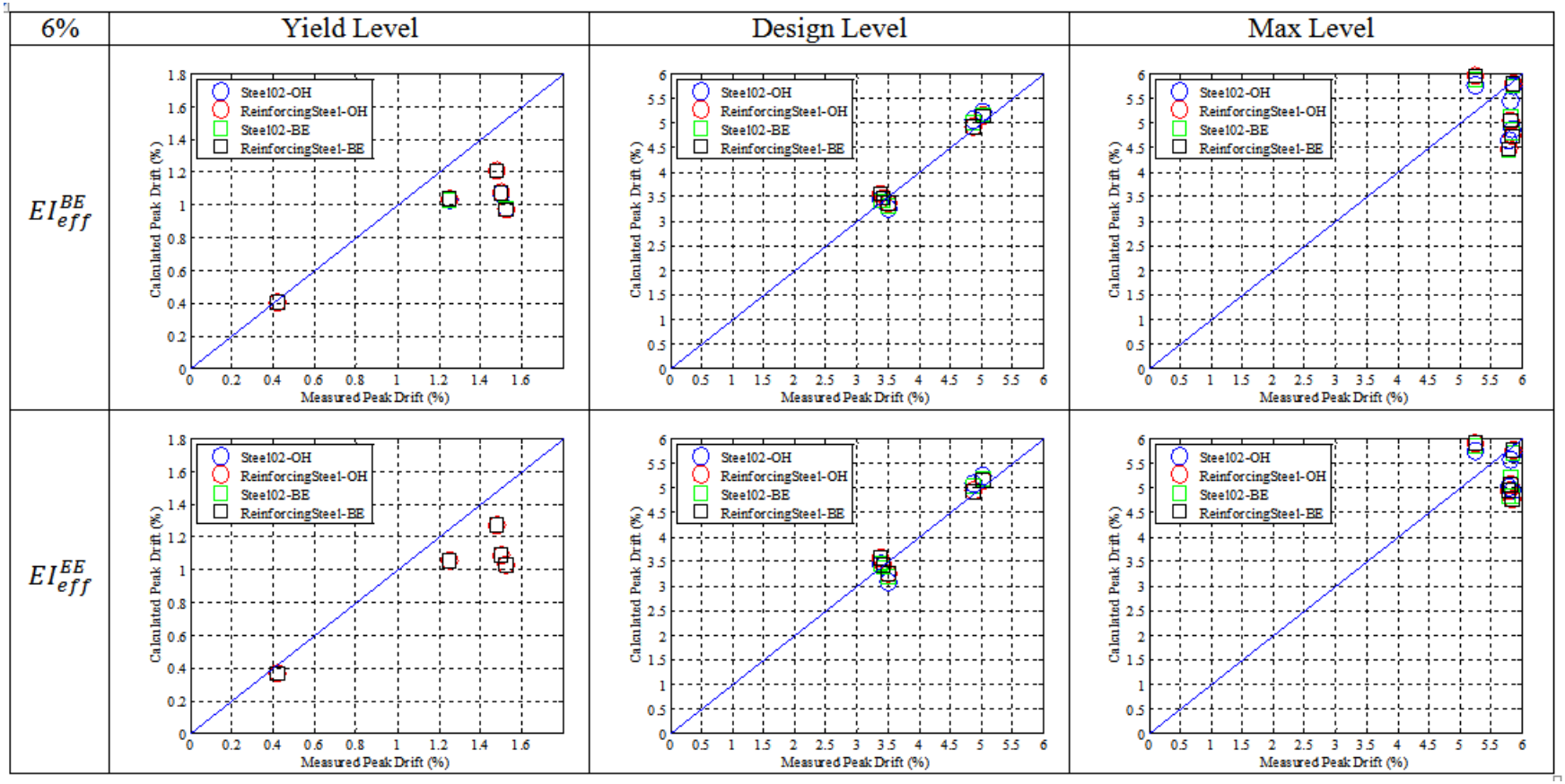

Figure E-8. Comparison of measured and calculated peak displacements using 6.0 % viscous damping

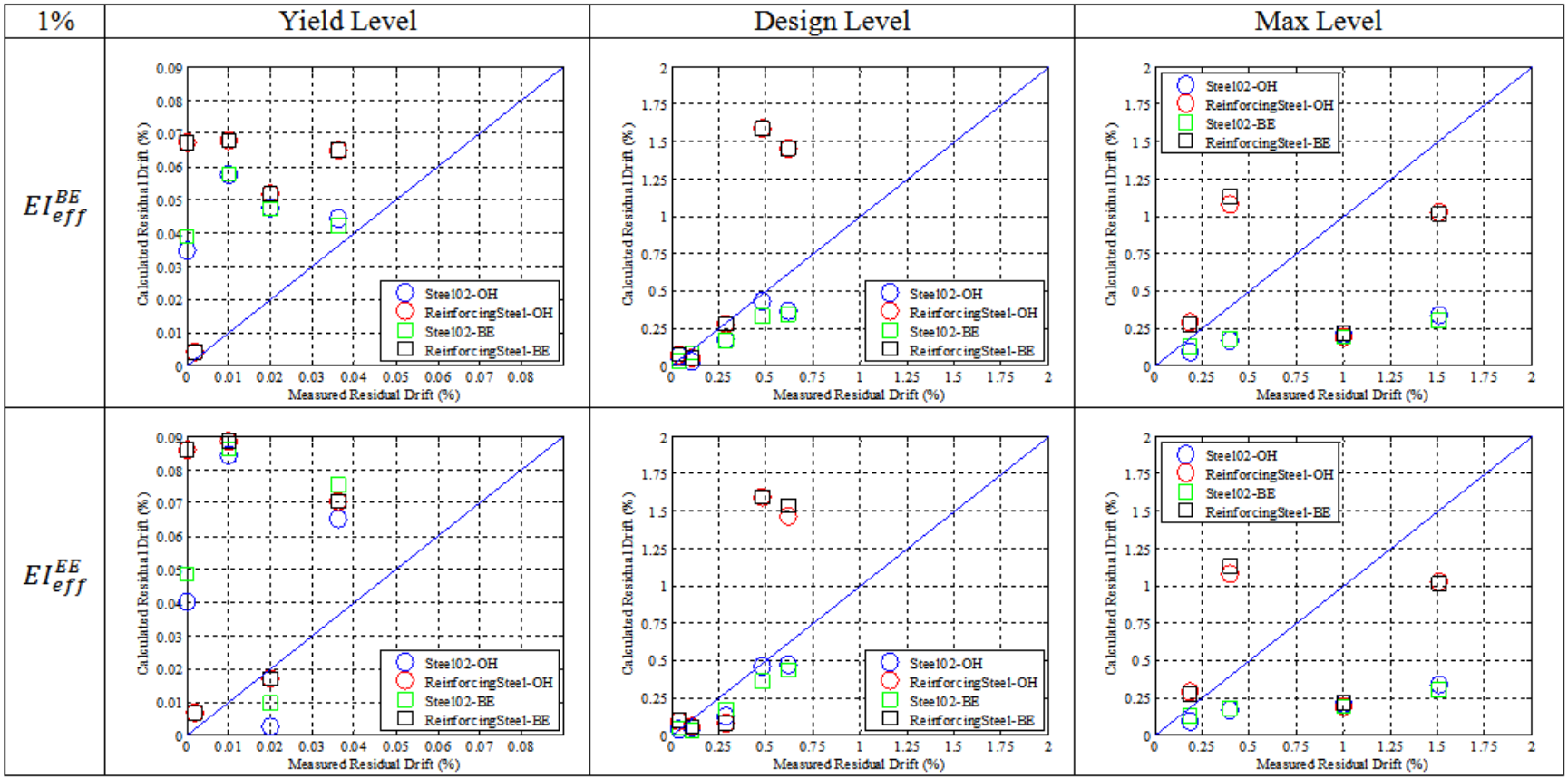

Figure E-9. Comparison of measured and calculated residual displacements using 1.0 % viscous damping

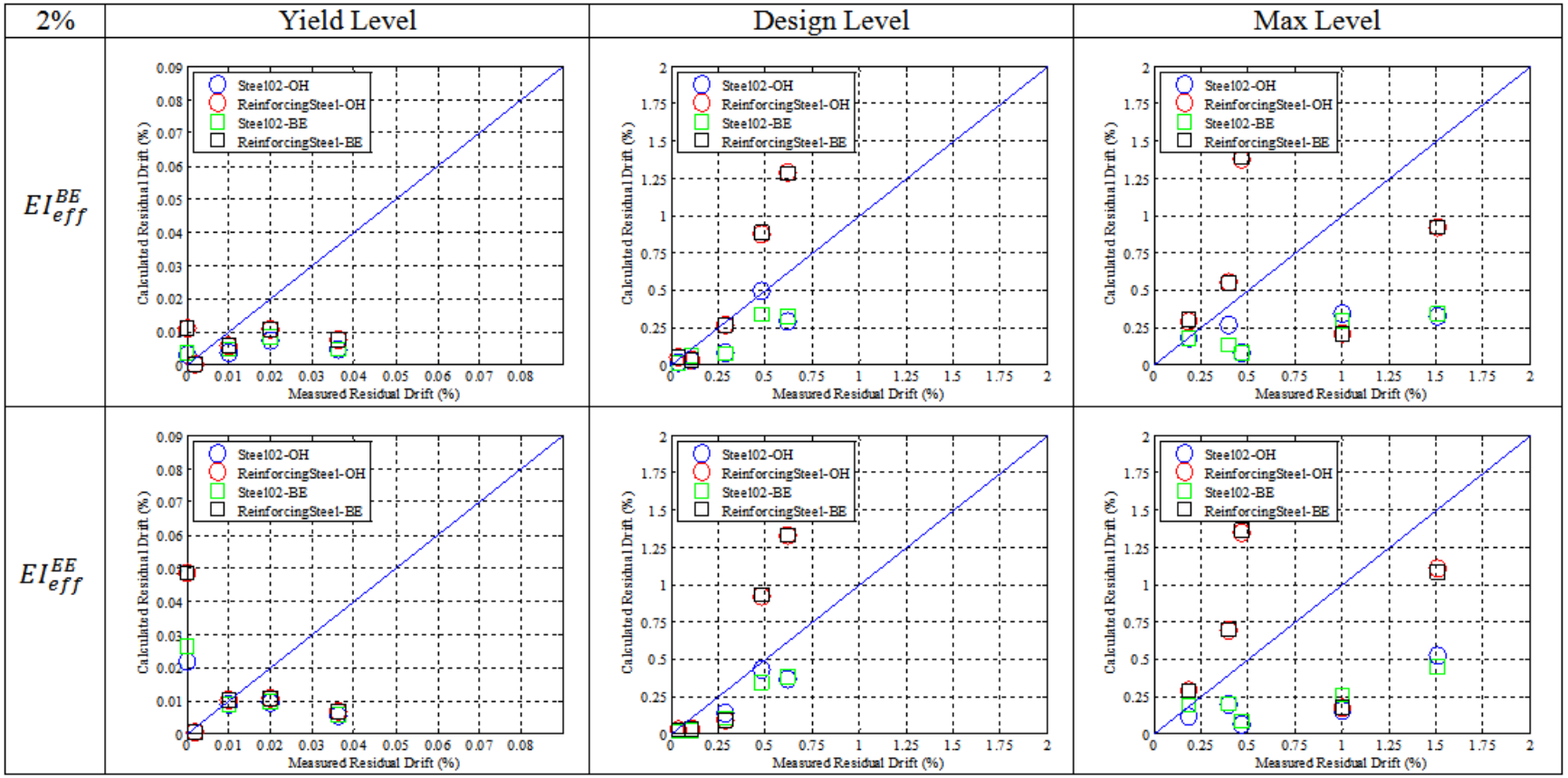

Figure E-10. Comparison of measured and calculated residual displacements using 2.0 % viscous damping

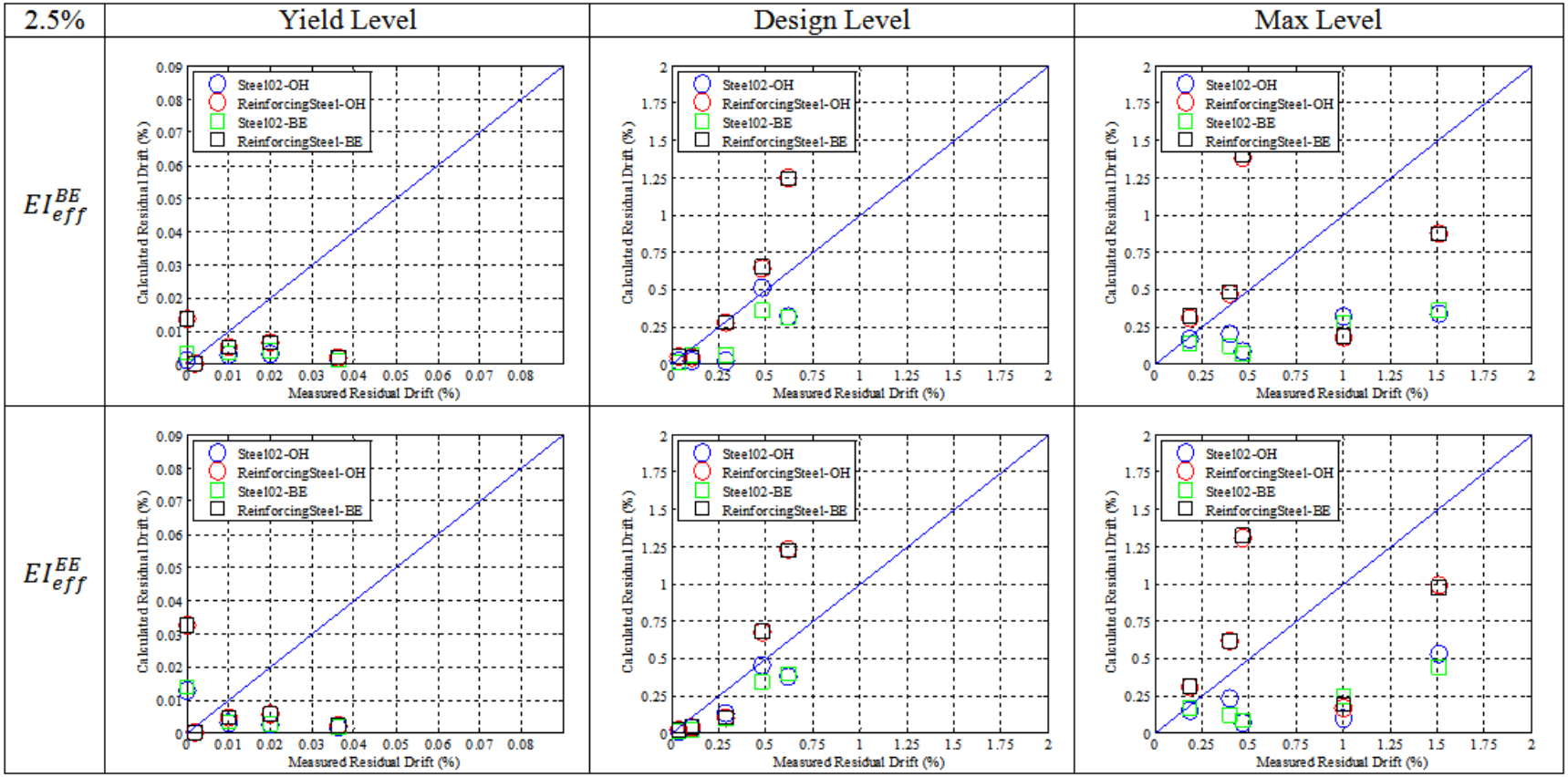

Figure E-11. Comparison of measured and calculated residual displacements using 2.5 % viscous damping

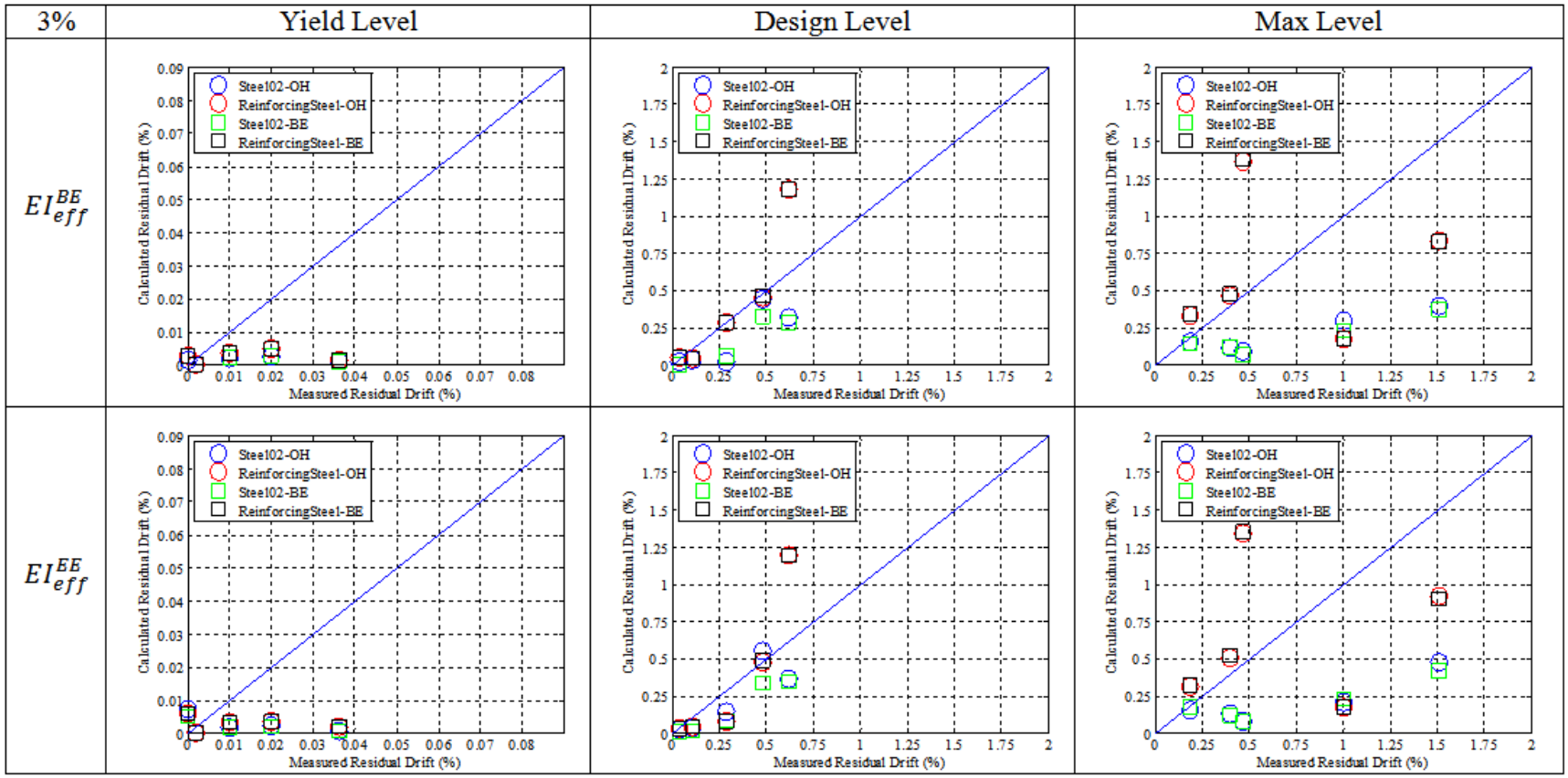

Figure E-12. Comparison of measured and calculated residual displacements using 3.0% viscous damping

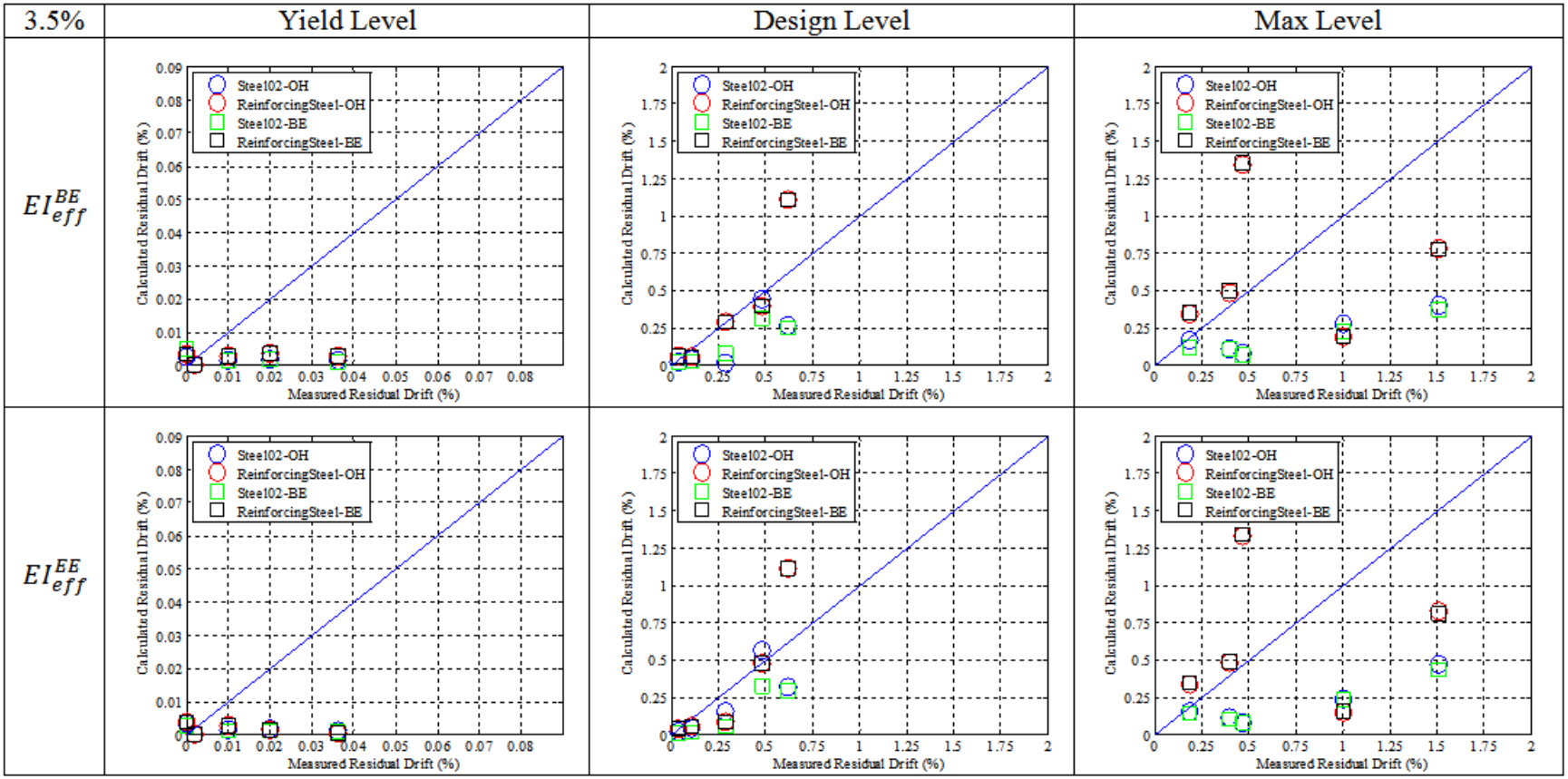

Figure E-13. Comparison of measured and calculated residual displacements using 3.5% viscous damping

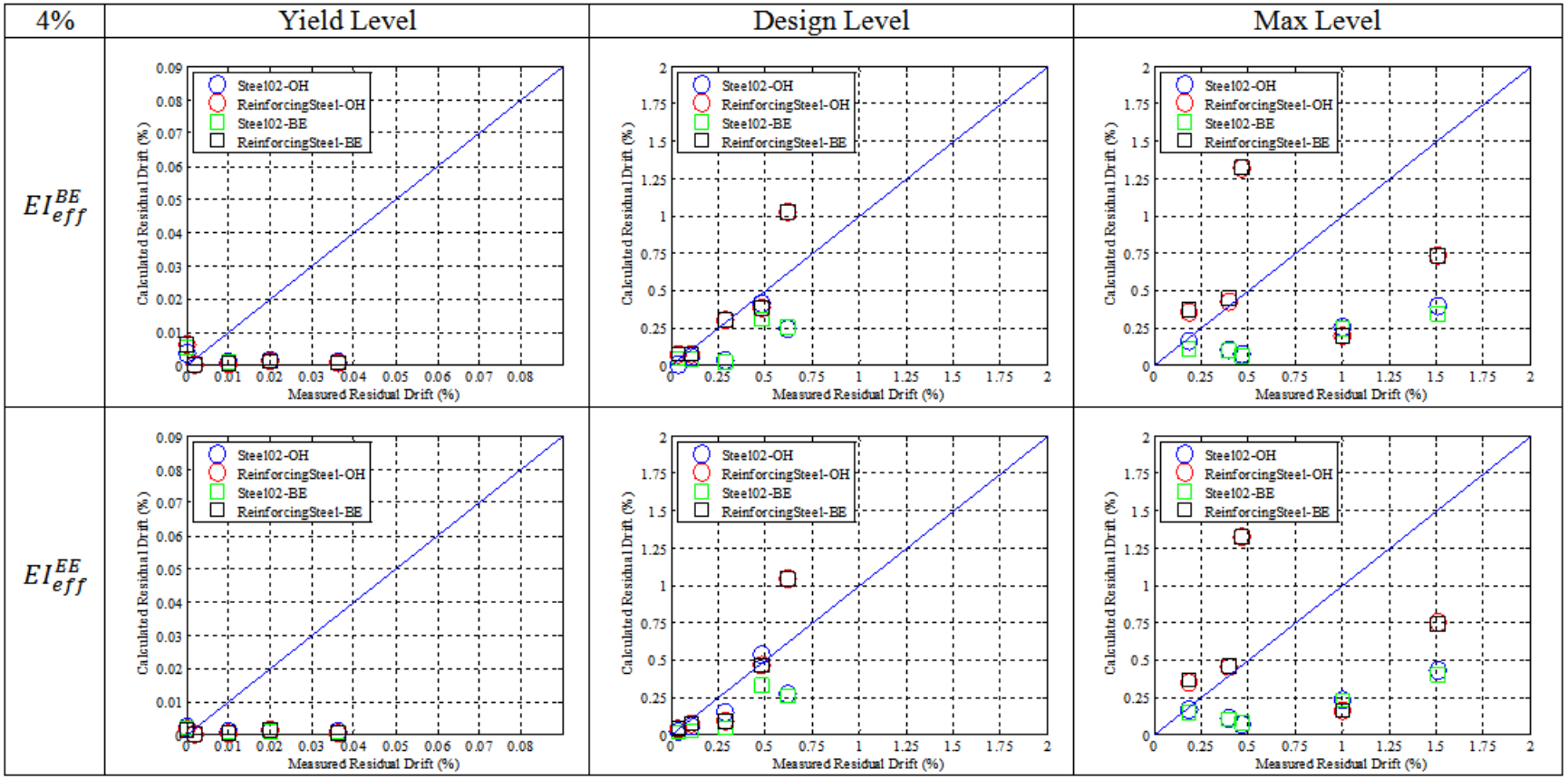

Figure E-14. Comparison of measured and calculated residual displacements using 4.0% viscous damping

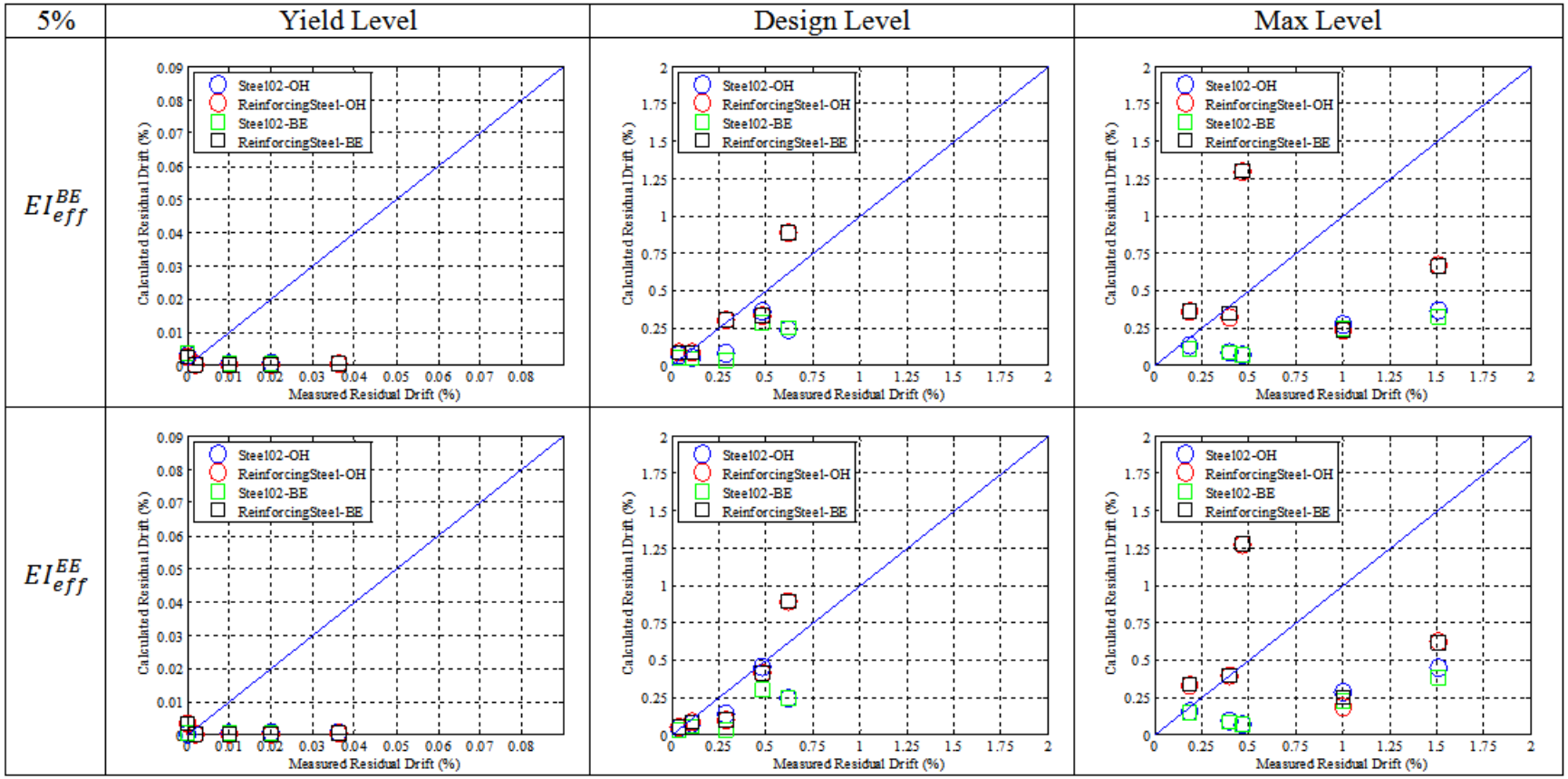

Figure E-15. Comparison of measured and calculated residual displacements using 5.0% viscous damping

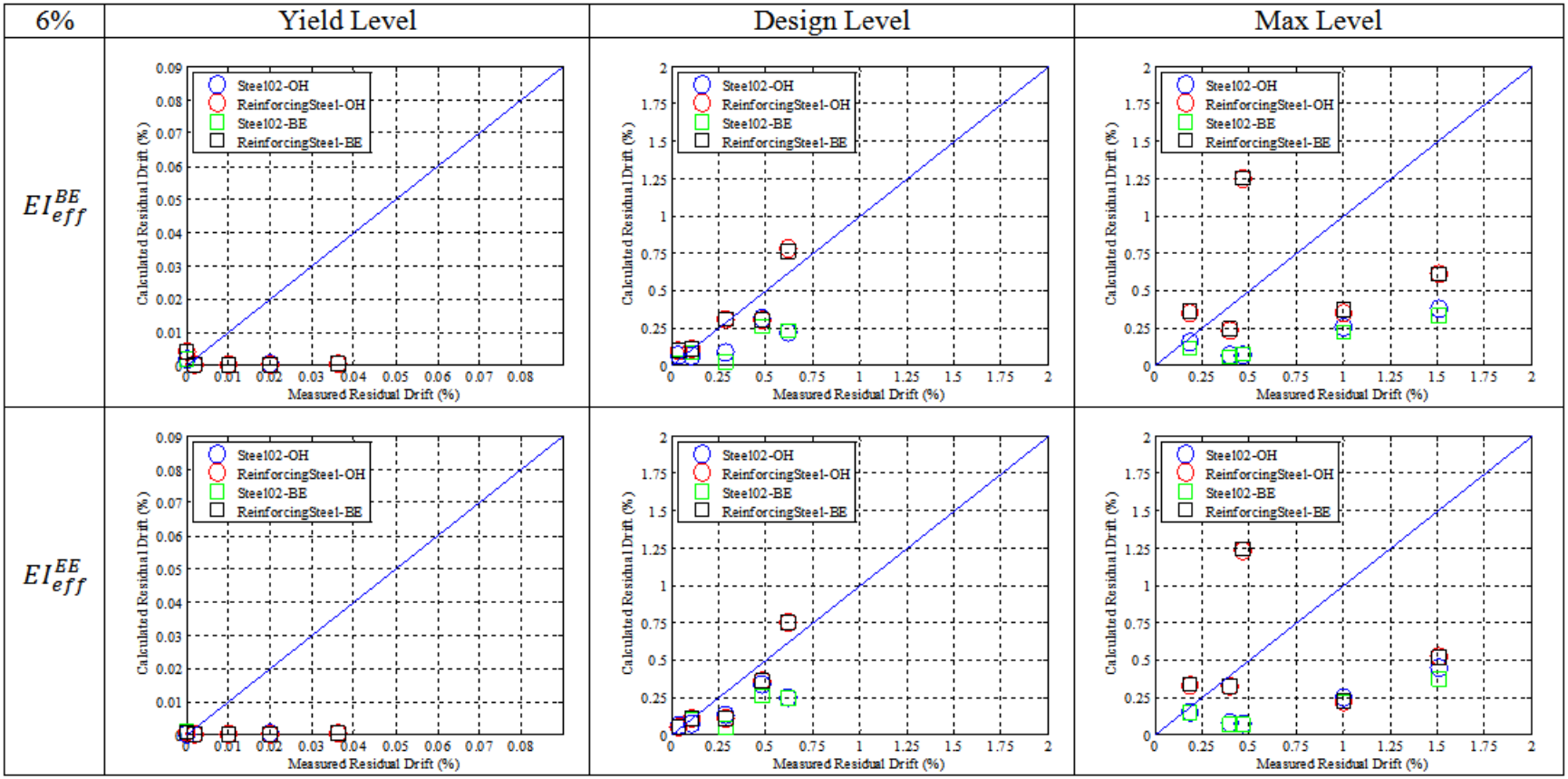

Figure E-16. Comparison of measured and calculated residual displacements using 6.0% viscous damping